Time-Resolved Terahertz Spectroscopy of Water

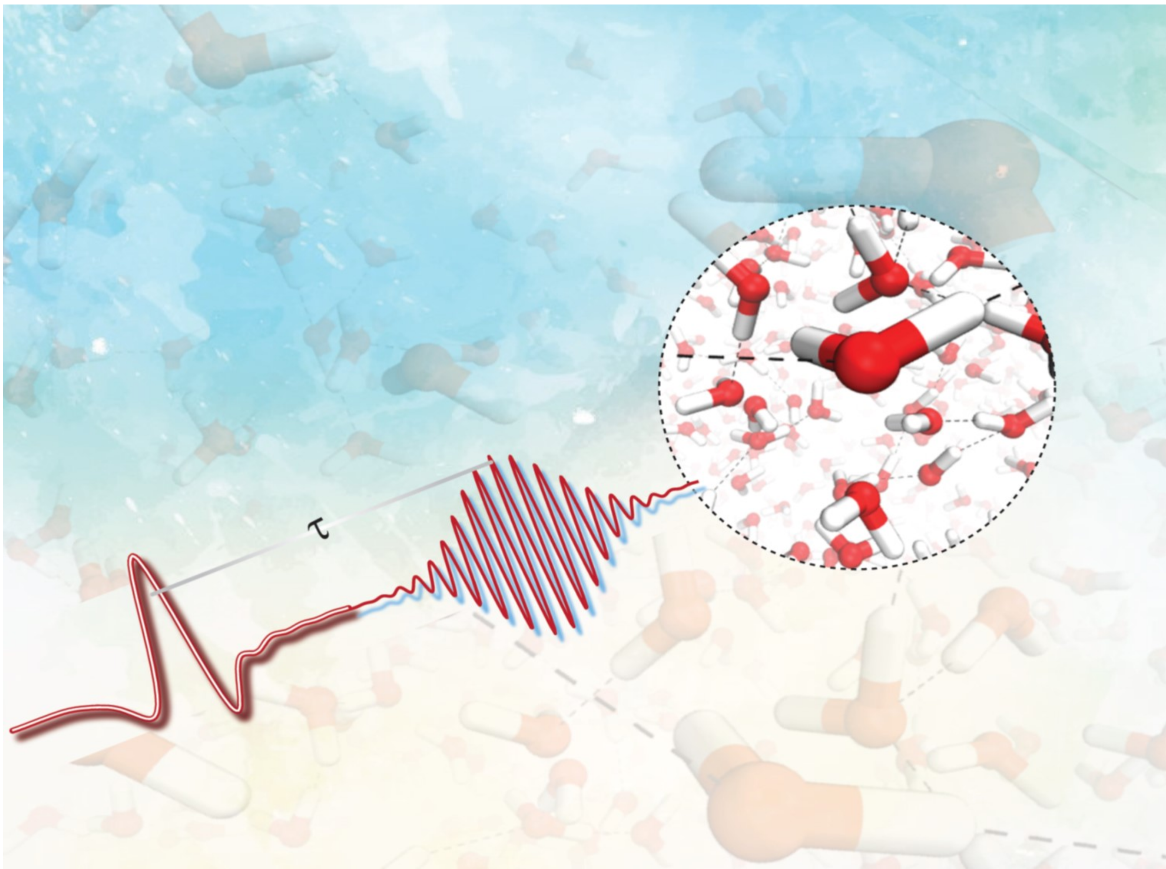

Dissertation by Saima Nafees Ahmed
Zürich, 2018

University of Zurich UZH

CMSZH CHEMICAL MOLECULAR SCIENCES ZURICH GRADUATE SCHOOL

Time-Resolved Terahertz Spectroscopy of Water

Dissertation
zur
Erlangung der naturwissenschaftlichen Doktorwürde
(Dr. sc. nat.)

vorgelegt der
Mathematisch-naturwissenschaftlichen Fakultät
der
Universität Zürich

von
Saima Nafees Ahmed
aus
Indien

Promotionskommission
Prof. Dr. Peter Hamm (Vorsitz)
Prof. Dr. Thomas Feurer
Prof. Dr. Jürg Hutter

Zürich, 2018

“The whole of science is nothing more than the refinement of every day thinking.”

-Albert Einstein

List of Publications

The following publications are consequences of the research carried out in the context of this dissertation, some of which are reproduced in this thesis.

Journal Publications

- Saima Ahmed, Andrea Pasti, Ricardo J. Fernández. Terán, Gustavo Ciardi, Andrey Shalit, P. Hamm
  Aqueous Solvation from the Water Perspective.
  (to be published)

- Andrey Shalit, Saima Ahmed, Janne Savolainen, P. Hamm
  THz Echoes Reveal the Inhomogeneity of Aqueous Salt Solutions.
  Nature Chemistry,**(9)**:273-278(2016).

- Saima Ahmed, Janne Savolainen, P. Hamm
  The Effect of the Gouy Phase in Optical-pump-THz-probe Spectroscopy.
  Optics Express, 22**(4)**:4256(2014).

- Saima Ahmed, Janne Savolainen, P. Hamm
  Detectivity Enhancement in THz Electrooptical Sampling.
  The Review of Scientific Instruments, 85**(1)**:013114(2014).

- Janne Savolainen, Frank Uhlig, Saima Ahmed, Pavel Jungwirth, P. Hamm
  Direct Observation of the Collapse of the Delocalized Excess Electron in Water.
  Nature Chemistry, 6**(8)**:697-701(2014).

- Janne Savolainen, Saima Ahmed, P. Hamm
  Two-dimensional Raman-terahertz Spectroscopy of Water.
  Proceedings of the National Academy of Sciences of the United States of America, 110**(51)**:20402-20407(2013).

Contents

Abstract

Regardless of the tremendous efforts and investigations performed over centuries to understand the most elementary and most important liquid of life, 'water', it still poses many unanswered questions. One particular question relates to the collective nature of the hydrogen bond network in water. The research work presented in this dissertation mainly focuses on studying the low frequency hydrogen bond dynamics of water by time-resolved Terahertz spectroscopy. Specifically, two experimental concepts were realised. One is related to the solvation dynamics of water, studied by one dimensional UV-pump THz probe spectroscopy and the other is associated with the behaviour of the hydrogen bond network in bulk water, for which a novel two dimensional Raman-THz spectroscopic method was introduced, developed and successfully realized.

Prior to the actual studies, the experimental setup was reviewed in order to achieve the high detection sensitivity necessary to detect weak signals emitted from the water. Hence, a simple scheme has been discussed and implemented, which significantly enhances the detection sensitivity (factor of ≈20) of the THz electro-optical sampling by introducing a sequence of four ZnSe Brewster windows along the detection path. Furthermore, it was shown in a pump-probe experiment, that the Gouy phase shift, which depends on the exact positioning of the sample in relation to the focus of the single cycle THz-probe beam, can alter the shape and size of a pump-probe signal. To avoid such perturbations in the desired signal, the generation and detection crystals as well as the sample were placed precisely to their corresponding focii.

To study the aqueous solvation from the water perspective, a fluorescent probe molecule (Coumarin 343) was used as a solute and the response of water upon photoexcitation of the dye was measured. Because of the change of dipole moment of the solute, water molecules are expected to reorient after excitation to accommodate the new configuration. Significant conclusions can be drawn from the experiment by evaluating the time scales. The observed response of water can be described as the biexponential decay with two time constants which agree well with the Debye relaxation related to reorientation of water molecules and the life time of the solute measured independently with the Time Correlated Single Photon Counting.

In the 2D Raman-THz experiment, intermolecular modes of water molecules were excited and then probed directly in a low frequency regime in order to explore the hydrogen bonded dynamical network. An echo in the 2D Raman-THz response was identified, indicating the inhomogeneous distribution of the hydrogen bond network with the inhomogeneity existing for a short time of ≈100 fs. These findings, have been a direct observation of heterogeneous behaviour of the hydrogen bond network in bulk water, providing important insights into the long-standing debate on the structure of water and life time related to it.

Zusammenfassung

Ungeachtet des enormen Aufwandes und der zahlreihen Untersuchungen, die über Jahrhunderte hinweg unternommen wurden um die elementarste und für das Leben wichtigste aller Flüssigkeiten, nämlich Wasser, zu erforschen, bleiben immer noch viele unbeantwortete Fragen. Eine zentrale davon betrifft das kollektive Verhalten des Netzwerkes von Wasserstoffbrückenbindungen. Die Messungen, die in dieser Doktorarbeit zu diesem Thema präsentiert werden, fokussieren sich auf die Untersuchung niederfrequenten Dynamiken der Wasserstoffbrücken mittels zeitaufgelöster Terahertz-Spektroskopie. Zwei wesentliche Experimente wurden in diesem Kontext realisiert: das erste untersucht die Solvatationsdynamik von Wasser mittels UV-Pump-THz-Probe-Spektroskopie, das zweite bezieht sich auf das Verhalten des Wasserstoffbrücken-Netzwerkes in Wasser als Flüssigkeit, wofür zweidimensionale Raman-Terahertz Spektroskopie konzipiert, entwickelt und erfolgreich angewendet wurde.

Vor den eigentlichen Messungen wurde der experimentelle Aufbau auf eine hohe Detektionsempfindlichkeit hin optimiert, um das von Wasser emittierte, schwache Signal messen zu können. Dazu wurde ein relativ einfaches Schema implementiert, das die Detektierbarkeit des THz-elektro-optischen Probensignals durch die Einführung von vier ZnSe Brewster Fenstern signifikant verbessert. Wir konnten damit eine ca. 20-fache Signalverstärkung erreichen. Weiters zeigte sich, in einem Pump-Probe-Experiment, dass die Gouy Phasenverschiebung, die von der exakten Positionierung der Probe relativ zum Focus des einfach zyklisierten THz-Messstrahls abhängt, die Form und die Grösse des Pump-Probe-Signals verändern kann. Um solche Einflüsse im Signal zu vermeiden, wurden die zur Erzeugung und Detektion verwendeten Kristalle sowie die Probe sehr präzise in den jeweiligen Fokuspunkten platziert.

Um die Solvatation aus der Sicht des Wassers zu messen, wurde ein fluoreszierendes Probemolekül, Coumarin 343, verwendet. Die Antwort des Wassers auf die elektronische Anregung des Farbstoffs wurde mit UV-Pump-THz Probe Spektroskopie gemessen. Nach der Anregung ändert sich das Dipolmoment des Solvats, die Wassermoleküle in der Solvatationshülle ändern daraufhin ihre Orientierung, um die neue Elektronenkonfiguration zu stabilisieren. Der beobachtete Response des Wassers zeigt eine exponentielle Relaxation mit zwei Zeitkonstanten, die kürzere davon beschreibt die Debye Relaxation der Umorientierung der Wassermoleküle, die zweite die Lebensdauer der Anregung von C343, die auch unabhängig mit TCSPC (time correlated single photon counting) gmessen wurde.

Im 2D Raman-THz-Experiment werden die intermolekularen Bewegungen der Wassermoleküle bei Normalbedingungen direkt im niederfrequenten Bereich detektiert, um das dynamische Wasserstoffbrückennetzwerk zu untersuchen. Es wurde ein Echo in der 2D-Raman-THz-Messung identifiziert, die auf eine inhomogene Verteilung des H-Brücken Netzwerkes hindeutet.

Es zeigte sich, dass diese Inhomogenität eine Zeitkonstante von ungefähr 100 fs aufweist. Diese Beobachtungen sind ein direkter Hinweis auf das heterogene Verhalten der Wasserstoffbrücken in Wasser als Flüssigkeit und leistet einen Beitrag zur langanhaltenden Debatte über die Struktur des Wassers und der damit verbundenen Lebensdauern.

List of Figures

List of Abbreviations

2D–Raman THz	two dimensional Raman terahertz spectroscopy
TRTS	time resolved terahertz spectroscopy
a.u.	arbitrary units
Ti:Sa	titanium–doped sapphire (Al_2O_3)
Nd:YVO_4	neodymium–doped yttrium vanadate
cw	continuous wave
abs	absorbance
BBO	beta barium borate
NA	numerical aperture
FWHM	full width half maximum
IR	infrared
MD	molecular dynamics
UV	ultraviolet
ZnSe	zinc selenide
GaP	gallium phosphide
ZnTe	zinc telluriod
IRF	instrument response function
LDL	low density liquid
HDL	high density liquid
TDFSS	time dependent fluorescence Stokes shifts
TCSPC	time correlated single photon counting
DFT	density functional theory

Chapter 1

Introduction

Water is a unique and important liquid that has never ceased to fascinate scientists over many years. It plays a crucial role in physics, chemistry, biology and many different fields across the sciences. It is often perceived to be simple as it is colourless, odourless, tasteless and encountered everywhere in everyday life. However, from the physical and chemical point of view, the properties exhibited by water are far from simple to comprehend. The central theme of this dissertation is an attempt to understand water by investigating the intermolecular hydrogen bond network and its dynamics.

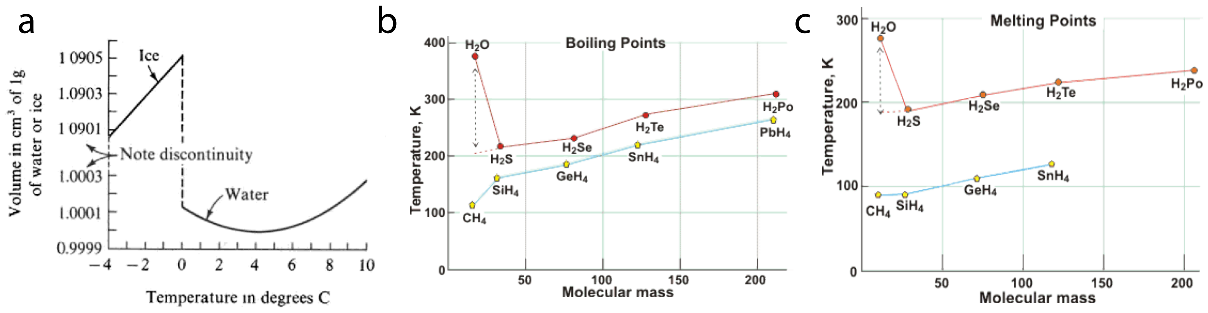

Figure 1.1: a)Dependence of the volume of ice and water with temperature. Fig. Adapted from ref. [1]. b) and c) Melting and boiling points of hydrides of group 6A and 4A elements respectively, showing abnormally high value for water. Fig. adapted from *http : //www1.lsbu.ac.uk/water.html*

When water is compared to other substances, it becomes clear that it deviates in many properties. For example, water is liquid at room temperature while the other compounds of similar molecular weight are gaseous; most of the liquids diminish in volume when temperature is decreased but in contrast, water expands upon freezing and has density maximum at 4°C as shown in Fig.1.1 a [1]; it has unusually higher melting and boiling points than expected extrapolation of other group 6A hydrides. Fig.1.1 b and c show trends of boiling and melting points of group 6A and other comparable 4A hydrides respectively. The variation for the sequence CH_4, SiH_4, GeH_4 and SnH_4 is normal and the curve through H_2Te, H_2Se and H_2S shows the expected behaviour but water does not follow the trend; instead it shows higher melting and boiling points than the expected values of 173K and 193K. Typically water behaves as a simple liquid when it is hot, but close to ambient temperatures and upon further cooling, many of its properties such as compressibility, heat capacity and density begin to deviate [2]. One can learn about all different kinds of anomalies in water listed at $http : //www1.lsbu.ac.uk/water.html$.

Apparantly, the anomalous properties of water, most of which make it suitable for life, have their origin in only one underlying property: the ability of water molecules to form a dense spatial network of hydrogen bonds [1, 3].

1.1 Water anomalies and hydrogen bond

When the hydrogen atom is attached to an electronegative atom such as O, N or F by a covalent bond, the binding electron is attracted more towards the electronegative atom and this causes the hydrogen atom to acquire a small positive charge. As a result the hydrogen atom is attracted towards the lone pair of electronegative elements of the neighbouring molecule, thereby making hydrogen bonds. Hydrogen bonds are found not only in water but also in a majority of chemical and biological molecules such as formic acid, proteins and DNA etc. Hydrogen bonds shapes the structure and functions of these molecules and provide required flexibility to them.

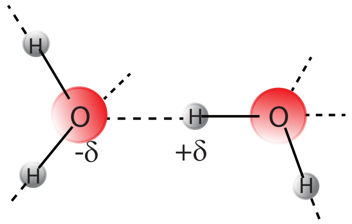

Figure 1.2: Existence of hydrogen bond between water molecules.

Water is a small molecule, which consists of two light hydrogen atoms attached to a 16-fold heavier oxygen atom. The partial positive and negative charges on hydrogen and oxygen atoms respectively make it polar in nature. Thus hydrogen atoms of one water molecule are attracted towards the oxygen atom of neighbouring molecules and form a hydrogen bond. Fig.1.2 shows a hydrogen bond between two water molecules. The strength of the hydrogen bond is apprximately 20 KJ mol^{-1} which is considerably stronger than a regular dispersive force but ≈20 times weaker than a covalent bond[1]. Because of its geometry and polarity, individual water molecules can participate in four hydrogen bonds simultaneously, leading to a tetrahedral arrangement of molecules through a continuous network (see Fig.1.3, which depicts the two possible arrangments of tetraheral network). In ice, these tetrahaderal structure in which each water molecule is four fold coordinated by the other water molecule is indeed observed but in liquid phase the ordered structure collapses and acquires some degree of disorder. However, the average tetrahedral coordination is retained and the x-ray analysis of the structure of water by J.Morgan et al. [5] shows that liquid water is highly structured and coordinated. This transient tetrahedral arrangement provides added energetic stability in which bond strength and directionality establish a low local density and cause a loss of orientational entropy. Therefore, at sufficiently low temperatures, hydrogen bonds force negative correlation between energy and volume, as well as entropy and volume [1]. In most of the other liquids these correlations are positive. Thus, water anomalies have direct relation with the intermolecuar hydrogen bond network which ultimately demands the need to understand hydrogen bonds in detail. The collective environment of this three-dimensional network of hydrogen bonds in liquid water is highly dynamic. Hydrogen bonds stretch, contract, break and reform on picosecond time scales and have been studied

---

[1] energy of a covalent bond $\approx 400KJmol^{-1}$ and enrgy dispersive inteaction $\approx 1KJmol^{-1}$ [4]

extensively with very many experimental techniques [6–12]. The dynamic nature of hydrogen bonds leads to further anomalous properties related to solvation e.g ultrafast solvation of the transient charge distribution and high mobility of protons [13–16]. This has a huge impact on all chemical reactions occurring in the solution phase.

1.2 Aqueous solvation dynamics

In solute-solvent assembly, solvation is a process which defines the equilibrium interaction between the molecules of the bulk solvent and the molecules or ions of the solute. These interaction can be of ionic nature, dipole-dipole interactions, van der Waals forces, and, of particular interest of this thesis, hydrogen bonding [17–19]. These interactions are dynamic in liquid phase in contrary to solids. The effect of these forces depends on the choice of the substances used as solvent and solute. Among various solvents, water is often considered to be especial solvent as it can dissolve not a wide variety of solutes. It is of paramount importance, in particular because it can dissolve ions and polar molecules, but it is poor at dissolving nonpolar molecules because of its own polarity. The reason that water is so good at dissolving salts is that it has a large dielectric constant(ϵ)(about 80 at room temp.) which is related to the large dipole moment of water molecules. Besides polarity it exhibits its liquid properties over a convenient range of temperatures as its boiling and freezing temperatures are far apart.

Solvation can have a profound influence in chemical reactions. Especially for the reactions involving charged species and polar solvent, the time scale of the response of solvent molecules to electronic rearrangement of the solute has a dramatic effect on rate of reaction. For more than half a century, considerable efforts have been made in the domain of both experimental and theoretical studies to understand the role of solvation dynamics in chemical reactions [20–23]. Early solvation studies were mostly focused on equilibrium solvent effect such as the effect of solvent polarity on reaction potential energy surface [24–26]. Subsequently the focus shifted to understand the role of time dependent response of polar solvent to a changing charge distribution in a polar solute molecule that takes place during the reaction. During the late 70's and 80's, solvation dynamics studies were restricted to slow dipolar liquids like higher alcohols, propelene carbonates etc. [20, 20, 27, 28] because of the limited temporal resolution available by laser spectroscopy.

Invention of ultrafast laser spectroscopy enabled the real-time study of dynamical processes in liquids. The general approach is to induce a change in the chemical solute using short pulses of light and then to interrogate the medium with the second pulse of light. The time dependence of the intensity, polarization or phase of the second laser pulse with respect to photoinitiating light pulse provides information on the dynamical evolution of the reacting system. Various linear and nonlinear spectroscopies (involving more than two light pulses) have been developed to probe the dynamical properties of chemical systems. These spectroscopic methods gave new insight into the fine processes at the subpicosecond to femtosecond timescale resolution to study the instantaneous dynamics of solvation in solvents like water [14], acetonitrile [29] and alcohols [30].

Solvation dynamics have been extensively studied by monitoring the time dependent fluorescence Stokes shifts (TDFSS) of the emission spectrum of a fluorescent probe (solute) whose charge distribution is instantaneously changed by optical excitation. Jimenez *et al.* [14] reported a solvent(water) response of a few tens of fs with the subsequent relaxation in ps uning TDFSS. Another complementary technique, photon echo peak shift spectroscopy, has also been used to study the solvation dynamics of water. The key idea behind the photon echo peak shift spectroscopy is that after the optical excitation, the transition frequencies of different absorbers in an inhomogeneous ensemble of absorbers become uncorrelated in time. A second pulse rephases them after a fixed time, resulting in the appearance of an echo. Fleming and coworkers [31] showed three kinetic components (17 fs, 400 fs and 2.7 ps) and an average solvation time of 400 fs using this technique. All these studies were done from the solute perspective and pointed towards the fact that water is one of the many fastest solvents. Before going into the details of the solvation studies of water, it is important to have some idea about the established understanding of transient water structure and its dynamics, which is addressed in the subsequent paragraph.

1.3 Structure of liquid water

In order to understand the unusual behaviour of water at ambient and low temperature, it is important to elucidate the instantaneous local structure and dynamical motion of water molecule and establish the relation between them. Over the period of a century, from the days of Röntgen [32] untill now, we have accumulated a great deal of knowledge about the molecular structure of water and its connection to anomalies, although this topic is still extremely controversial [33–35]. Water on a larger scale is homogeneous but locally does it show heterogeneity? Theories related to the liquid-liquid phase transition between high and low density water have been proposed to account for the low temperature anomalies [34]. Water at ambient conditions has traditionally been considered as a homogeneous distribution of hydrogen-bonded tetrahedral structures with thermal fluctuations increasing with temperature. This picture has been challenged by recent studies based on conventional X-ray absorption spectroscopy (XAS) [35], X-ray emission spectroscopy (XES) [36] and small-angle X-ray scattering (SAXS) [37]. These have suggested the 'two-state model' of water with patches of local structures of high density liquid(HDL) and low density liquid (LDL) as depicted in Fig.1.3. a) and b) respectively, whereas other researchers have interpreted essentially the same experimental result as continuous density fluctuation of water as expected from isothermal compressibility [38].

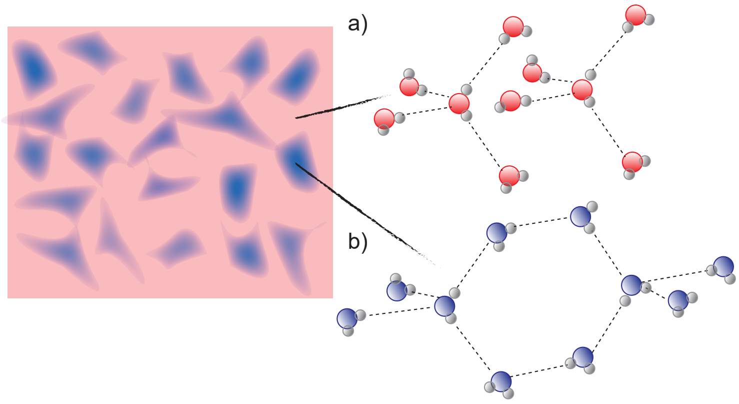

Figure 1.3: Simple dipiction of heterogenous nature of water consisting of tetrahedral structure of water proposed to explain a)HDL and b)LDL of water [33]. Dotted lines represent hydrogen bond network.

Any of the above mentioned X-ray techniques, are 'linear spectroscopies' in the sense that they use one photon to probe water structure and essentially take static instantenous snapshots of the distribution. In contrast, multidimensional IR spectroscopies [7, 9, 11, 12] and hole burning or photon echo experiments [39–41] examine the system twice and deduce the correlation between the inter-converting structure. Most of these experiments employ intramolecular OH or OD stretch vibrational frequency as sensitive measure of the strength of hydrogen bonding to the environment. Due to multiple interaction these techniques can elucidate the inhomogeneous broadening of OH or OD stretch vibrations and thus the heterogeneity in hydrogen bond strength [42]. It is well established from these experiments that inhomogeneity in OH/OD vibrations is of the order of ≈1ps which is interpreted as the typical life time of hydrogen bonds. In order to disentangle the ambiguity between homo and heterogeneity of water, one needs a spectroscopic method which is sensitive to the inhomogeneity of low frequency, intermolecular and collective modes of water.

1.4 Context of this work: Research orientation

In this dissertation, the prime focus is on liquid water. Fig.1.4 explains the basic theme of the research work. Studies to understand the low frequency, intermolecular and collective hydrogen bond dynamics are carried out by conducting two fundamental experiments related to solvation and structural aspects of water. The technique used to explore the dynamic behaviour of water imposed by solvation and structure is time-resolved THz spectroscopy.

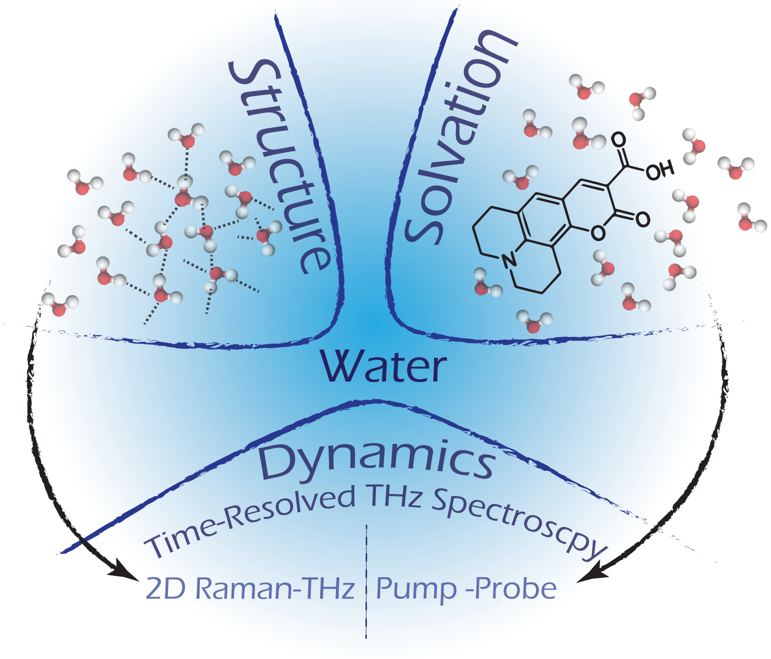

Figure 1.4: Basic theme of the dissertation: Water being the core of this research, the dynamical behaviour of its collective intermolecular modes related to the solvation and the structure is studied by time-resolved THz spectroscopy. Black arrows point towards the UV-pump-THz probe and 2D-Raman THz spectroscopic techniques used to investigate the solvation and structural properties of water respectively.

The study of the dynamics of solvation of a newly created ion or a dipole in polar liquids is now a well-established methods to obtain molecular-level information about the collective solvent response of both orientational and translational motions of the solvent molecules around the probe [21,43–46]. However, a consistent picture of solvation and the standard experimental approaches to investigate the solute-solvent assembly are yet to emerge. Most of the studies on the solvation dynamics were carried out from the solute perspective. The research domain of solvation dynamics from the solvent perspective needs noticeable attention. Therefore the fundamental questions addressed in this experiment are: Can we measure solvation dynamics from the solvent perspective, especially in water by directly probing the hydrogen bond network and can we deduce the time scale of relaxation? Thus, to study how quickly the water adapts and rearranges itself around the probe molecule (Cumarine 343), when it is excited by a UV pump, we used one-dimensional transient THz spectroscopy. A detailed description of the solvation dynamics of water is given in chap.4.

The second crucial experiment of this research is regarding the heterogeneity of hydrogen bond network in water. Unravelling the ambiguity about the structure of water remains extremely difficult, as the different experimental techniques used to study it e.g. small angle x-ray scattering (which emphasize the structure of water) and multidimensional IR spectroscopy (focusing on dynamics), do not provide a conclusive picture. The questions we ask in this section are: on a larger scale liquid water is homogeneous, but locally does it show heterogeneity? Does the two state model of water exist at ambient temperature, and if it does, then what is the relevant time scale of its survival? To address these questions, we used two-dimensional Raman-THz spectroscopy, which directly probes the intermolecular motions of water molecules. A detailed description of the heterogenity of water is given in chap.5.

As mentioned, the basic technique used to explore the above problems is based on time-resolved THz spectroscopy.

1.5 Time-resolved terahertz spectrscopy

Terahertz radiation (0.1 -10 THz, 30 pm -3 mm in free space, 3 cm^{-1} to 330 $^{-1}$ or 0.4 meV to 40 meV) of the electromagnetic spectrum, its generation, detection and interaction with matter have been of considerable interest to the scientific community of late. Since the introduction of THz time-domain spectroscopy (THz-TDS) in the late 1980's [47], it has found widespread use as a simple and versatile method for obtaining the low frequency response of solids, liquids and gases. The THz range covers a wide range of physical phenomena, spanning many different fields of study. Physical phenomena that can be probed in this spectral range include molecular and material excitations like those in semiconductors, biological molecules and molecular crystals [48–50], charge transfer [51, 52] and plasma dynamics [53].

Time-resolved THz spectroscopy (TRTS) is a vast field that includes very many different experimental techniques e.g.THz emission spectroscopy[2] of bulk semiconductors, superconductors and other materials, pump/probe technique and coherent control etc. Optical pump/THz probe technique is used to study systems in which a visible excitation initiates a change in

---

[2] In Terahertz emission spectroscopy, the sample itself is the source of THz emission and the THz waveform is analyzed to extract the information about the process responsible for the emission (optical rectification, shift currents, charge transfer etc.) [54]

far-infrared absorption properties on a sub-picosecond timescale. One of the most powerful aspects of THz spectroscopy is that it provides subpicosecond pulses in the far-infrared region of the spectrum. As THz pulses are created and detected using short-pulsed lasers with pulse widths ranging from ≈100 down to ≈10 fs making it possible to carry out time-resolved far-IR studies with subpicosecond temporal resolution. On the contrary other sources of far-IR radiation such as arc lamps or globars are continuous, and pulsed sources such as free electron lasers or synchrotrons typically produce far-IR pulses with ≈3 ps duration or greater. This capability has been exploited in several ways. For example, one can monitor a single point on the THz waveform, and pump-probe delay can be varied to map out the average response of the material. Alternatively the entire THz waveform can be obtained at one or several fixed delay times after photoexcitation. In a most comprehensive way one can map out a two dimensional picture by varying pump probe delay throughout the entire THz waveform. We used TRTS to study the low frequency vibrations of the water molecular network. The THz spectrum obtained from the experimental setup used for the purpose of our investigations covers the region from 0.1 to 6 THz, corresponding to H-bond bending and stretching vibrations, indicated in the yellow shaded area of Fig.1.5

1.5.1 Need for multidimensional spectroscopy

Spectroscopy is the fundamental tool in condensed phases to understand molecular structures, interactions, relaxations and dynamics. In traditional linear spectroscopy, these information can be extracted from the spectral features like resonance frequencies, spectral amplitude and lineshape as a function of the light field (amplitude, frequency, phase, polarization, etc.) or modification of the sample. Absorption or emission spectroscopies are referred to as linear spectroscopy, because they involve one primary light-matter excitation interaction, typically characterized by a single frequency axis. Fig.1.5 shows the linear absorption spectrum of water at low frequency, based on thermally excited intermolecular degrees of freedom.

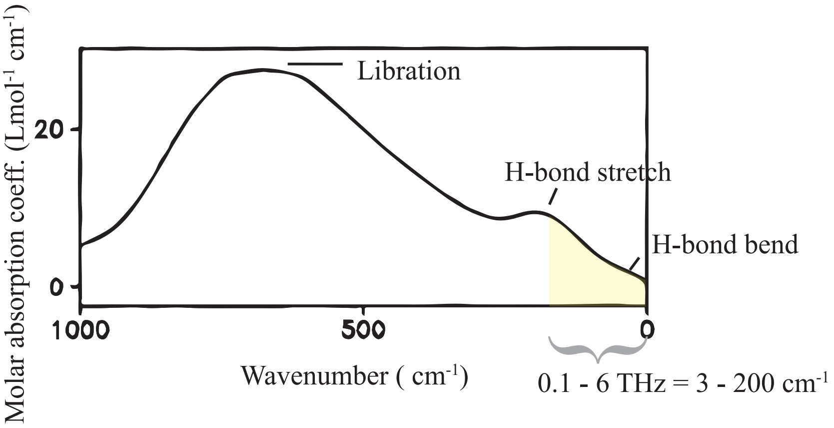

Figure 1.5: Low frequency absorption spectrum of water, showing absorption due to hydrogen bond bending (60 cm^{-1})and stretching vibrations (200 cm^{-1}). Main peak around 600 cm^{-1} appears because of libration (hindered rotation) of water molecules. Fig. adapted from ref. [55]

When two water molecules connected by hydrogen bonds vibrate against each other, there is a charge flow along the hydrogen bond resulting into the vibrating dipole showing a broad peak at 200 cm^{-1} in the spectrum, while the more promienent peak at 600 cm^{-1} is assigned to hindered rotation or libration of water molecules and the one at 60 cm^{-1}is often referred to hydrogen bond bending motions. [56]. The linear spectrum of water looks very broad, featureless and the broadening mechanism of the bands is unclear. i.e. one cannot disentangle whether the modes are homogeneous or heterogeneous. Moreover, it is also not clear if the there is correlation between hydrogen liberation, stretching and/or bending mode.

In other words, the linear spectroscopic approach is tormented by a number of ambiguities in their interpretation such as:

- Absorption spectrum with multiple peaks: If the absorption spectrum is comprised of multiple peaks as shown below (right), it poses uncertainty whether these resonances arise from different, non-interacting molecules, or are these coupled quantum states of the same molecule? One cannot resolve spectral correlation and couplings directly.

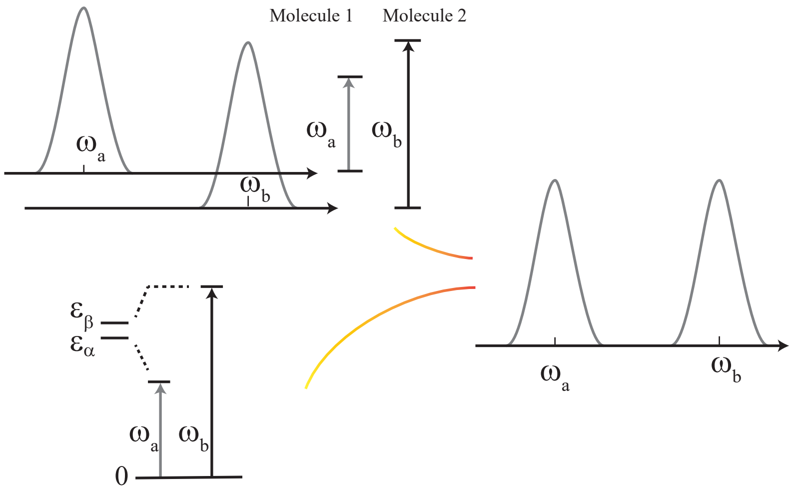

- Broad lineshape : Linear spectra cannot uniquely interpret line-broadening mechanisms. e.g. in linear infrared spectroscopy, like Fourier Transform IR (FTIR), the spectral absorption profile can be homogeneously or inhomogenously broadened, indicating that all contributing oscillators experience the same local environment or distinct subensembles contributing to one vibrational band respectively.

  Fig.1.6 a) shows nearly identical 1D-FTIR spectra (vibrational lineshapes) of amorphous ice and liquid water, which do not yield any information about the broadening mechanism of the line shapes obtained for these two samples. On the contrary 2D IR spectra (Fig.1.6 b)) of same samples are distinctly different. For amorphous ice we get a characteristically tilted line shape along the diagonal indicating the heterogeneous nature of vibrational lineshape while water shows nearly circular line shape representing its homogeneous character on longer time scale.

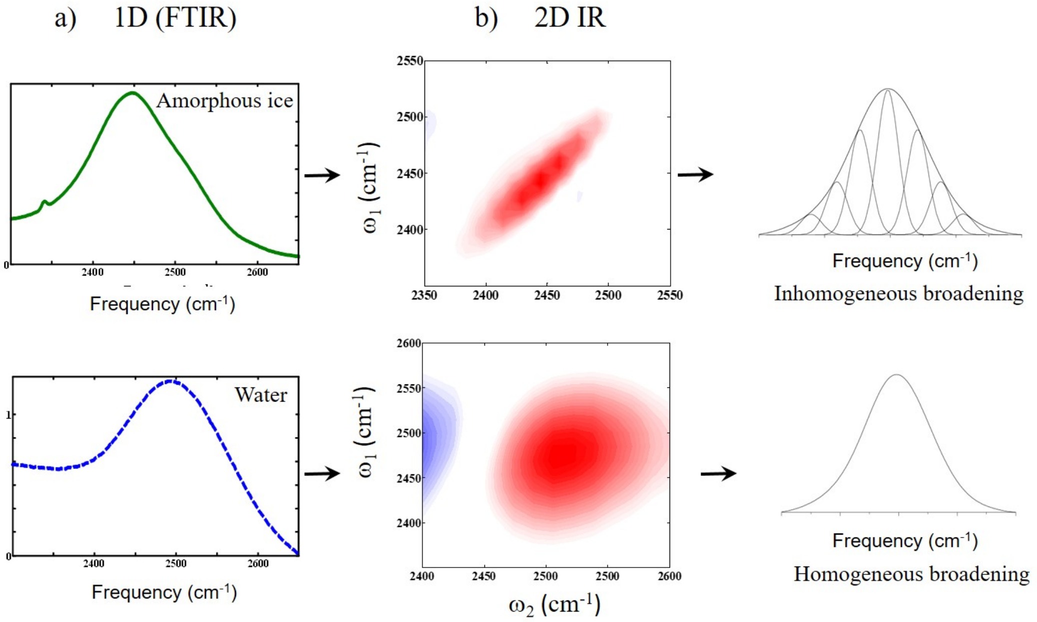

Figure 1.6: a) FTIR Spectra and b) 2D IR spectra of OH stretch vibrations of amorphous ice and liquid water. Fig. adapted and modified from ref. [11, 57]

This tells us that 2D spectroscopy can separate the underlying molecular contributions of broad featureless 1D lineshapes providing a sensitive measure of conformational heterogeneity. Therefore, multidimensional spectroscopy is required to get the informations regarding the dynamics of particular modes, possible couplings between them and changing local and collective environments as it uses multiple light field interactions with independent control over frequency and time ordering. Here, for the purpose of investing collective hydrogen bond dynamics in liquid water, 2D- Raman- THz spectroscopy is developed.

1.6 Dissertation outline

The research questions mentioned in section 1.4 constitute a set of ideas that have provided the motivation to use transient TRTS to study the behaviour of collective intermolecular H-bond motions of water. In particular, we focus on understanding the solvation dynamics upon photoexcitation of a dipole in water, the structure of bulk water, its heterogenous behaviour and the time scales related to these processes.

Chapter 2 is concerned with the experimental technique and apparatus used. It also describes basic spectroscopic concepts essential for the construction of experimental setups, including the generation and detection scheme of THz pulses. In general the desired THz signal coming from water is very small and very difficult to measure. It also deals with the technical improvements in the experimental setup to enhance the sensitivity of THz detection by a significant amount, without which the measurement of a transient THz field coming from the water sample would have been impossible. Chapter 3 describes another type of technical improvement related to the effect of the Gouy phase observed in THz pulses when they are focused with high NA optics. It also shows how the Gouy phase affects the pump-probe signal, and finally concludes that exact positioning of the sample in relation to the focus of the probe beam is important in pump probe experiments involving single cycle pulses.

The aim of the first experiment described is to probe the relaxation of the low frequency hydrogen bond network of water surrounding the solute molecule when the solute molecule is photoexcited. To facilitate this goal, a one-dimensional UV pump- THz probe experiment on Coumarin 343 dye in water has been designed and performed. In chapter 4 the solvation dynamics of water molecules upon photoexcitation of Coumarine dye is demonstrated and it is argued that the response of water is close to the Debye relaxation time rather than the solvation time.

After performing one-dimensional pump probe spectroscopy, the investigations proceed further to two-dimensional Raman-THz spectroscopy of neat water at ambient temperature. The target formulated in the second experiment is to acquire some additional insight regarding the structure of water, its heterogeneity and related time scale. To accomplish this goal, a hybrid two-dimensional Raman THz spectroscopy on neat water is designed and implemented. In chapter 5, with the help of this multidimensional spectroscopic technique, the appearance of an echo in 2D Raman-THz response and its indication towards the heterogeneous nature of the hydrogen-bond network is presented.

The concluding Chapter 6 provides a summary of the presented work. This dissertation also includes an appendix A that contains all the research works published with the supporting material. Last two publications are not described in this dissertation but are the part of the research.

Chapter 2

Experimental techniques

This chapter discusses the experimental setup and the basic spectroscopic concepts that are applied to the experiments described in this thesis. It also discusses a simple scheme that is used to enhance the sensitivity of electro-optic detection of the THz pulses. Conceptually, the experimental setup is developed from an optical pump THz probe setup [54, 58].

2.1 Ultrafast pulse generation

A commercially available Titanium-doped sapphire (Ti:Sa) oscillator (Tsunami from Spectra Physics) delivers 80 fs pulses centered at 800 nm at 80 MHz repetition rate with ≈ 10 nJ energy. A diode pumps a intracavity doubled Nd:YVO_4 cw laser (Millennia, Spectra Physics), which in turn pumps the oscillator. The energy output of the oscillator is low, and in order to study non-linear and non-equilibrium physical phenomena, high peak power is required. Thus, to get high peak power, the oscillator output is fed to a chirped-pulse regenerative amplifier (Spitfire, Spectra Physics) where pulses are first stretched and then get amplified. After amplification it undergoes compression resulting into 800 nm, 110 fs long pulses with a repetition rate of 2.5 to 5 kHz and a output power of $\sim$ 5W. These ultrashort pulses are used to generate and detect THz radiation.

2.2 Generation and detection of THz pulses

2.2.1 Optical rectification: Generation

A typical broadband THz radiation shows the shape of single-cycle pulse. These extremely short THz pulses are obtained by using nonlinear optical responses of bound electrons in non-linear crystals induced by ultrashort optical pulses from femtosencond lasers. In general, an electric field $E(t) = E_0 cos(\omega t)$ induces a polarization $P(t)$ inside a dielectric can be represented by a Taylor series as follows:

$$\bar{P}(t) = \sum_{n=1}^{N} \chi^{(n)} \bar{E^n}(t) \tag{2.1}$$

where $\chi^{(n)}$ is an electric susceptibility of the order n (which varies from 1 to N). For n=1, eq.2.2 represent the linear response. For n= 2 the second order polarization $P^{(2)}$ becomes

$$P^{(2)}(t) = \chi^{(2)} E^2(t) = \chi^{(2)} E_0 \frac{1 + cos(2\omega t)}{2} \tag{2.2}$$

The second order nonlinearity leads to a DC electric field $E_0/2$, as well as a second harmonic generation (SHG, 2ω) of the fundamental frequency ω. The SHG and DC fields are the result of sum and difference frequency generation, respectively. Because the near-IR pulse has a duration of ≈100 fs, a 'dc' pulse corresponding to the envelope of the optical pulse is generated rather than a constant dc level. Alternatively, this generation mechanism can be understood by considering the fact that the optical pulses have significant bandwidths. Thus, the high-frequency components can mix with the low-frequency components within a given pulse to produce a pulse at the difference frequency. Since the optical pulses have a bandwidth of a few THz, the difference frequencies fall in the THz range [54, 58].

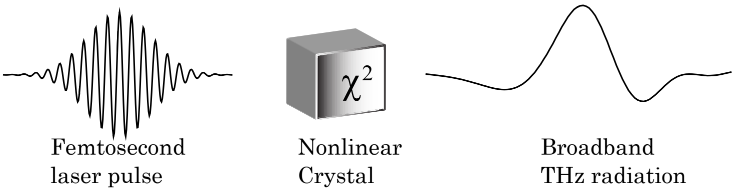

Figure 2.1: THz generation in nonlinear media by optical rectification.

2.2.2 Electro-optical sampling: Detection

Electro-optic sampling is a coherent THz detection technique, which exploits the second order nonlinear susceptibility $\chi^{(2)}$ of non centro-symmetric crystals to induce birefringence upon exposition to an electric field. This is called the linear electro-optic (EO) effect or the Pockels effect.

When a voltage is applied across a material possessing $\chi^{(2)}$ response, it will lead to a change in the refractive index of that material. Thus the total (up to second order) polarization can be written as

$$P(t) = [\chi^{(1)} + \chi^{(2)}_{DC}] E^0 cos(\omega t) \tag{2.3}$$

where the quantity in the bracket corresponds to an effective linear susceptibility. The induced change of the refractive index is:

$$\triangle n \simeq \frac{1}{2} \chi^{(2)} E_{DC} \tag{2.4}$$

As a result of the induced birefringence, an optical probe pulse or gating pulse experiences a change of its polarization state, which is linear in the electric field applied on the crystal. Thus, by measuring the small change of refractive index, a field-resolved THz radiation measurement scheme can be implemented.

Fig.2.2 illustrates the commonly used coherent detection schemes. When the THz field is applied to the non-linear medium (here, detection crystal: 0.1 mm GaP [110] crystal), it induces birefringence in the material which can be sampled by analysing the polarization of an optical probe or gating pulse. Thus, the entire waveform is determined by measuring the field-induced birefringence as a function of the relative time delay between the THz and optical probe (or gating) pulses. An initially s-polarized 800 nm probe beam will thus become elliptically polarized with a small p-polarization component. In a standard electro-optic sampling scheme [58], the light would then be passed through a $\lambda/4$ wave plate, which results in a distorted circular polarized beam, and then through a Wollaston polarizer, which separates p- and s-polarization components, whose difference is measured by two balanced photodiodes. The p-polarization component introduced in the probe pulse after the detection crystal depends on THz field and the rotation sense of the elliptically polarized light reflects the sign of the THz field.

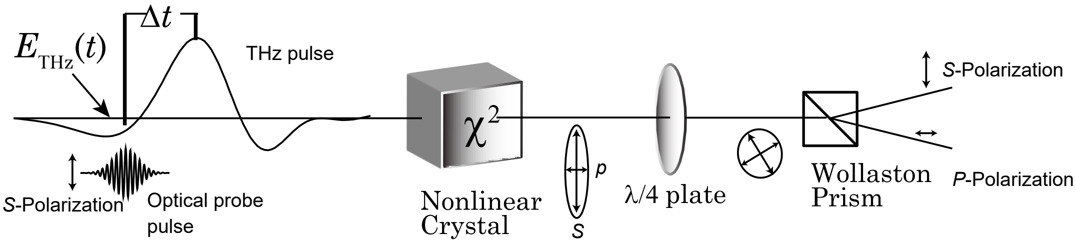

Figure 2.2: Coherent electro-optic detection of THz radiation. Entire THz wave form can be mapped by monitoring the altered polarisation of probe pulse as function of time delay between probe and THz pulse.

Probe pulses coming from amplified laser system have large energies that can saturate the detector. Therefore, we introduced a scheme that makes use of extra amount of single-pulse energy to increase the sensitivity of the THz detection by using a sequence of Brewster windows. This scheme plays a significant role in the measurement of very small, transient THz fields in connection with low-repetition rate amplified Ti:Sa laser systems.

2.3 Detectivity enhancement in THz electrooptical sampling

This work has been published in *The Review of Scientific Instruments*, see Ref. [59].

2.3.1 Experimental scheme and results

The ellipticity of probe or gating pulses just after the detection crystal mentioned above in section2.2.2, can be very small, depending on the strength of the THz field. In order to reduce the large s-polarization component, the beam was first passed through a set of four ZnSe Brewster windows before the Wollaston polarizer (see Fig. 2.3). These Brewster windows ideally transmit 100% of the p-polarization component, but reflect a certain fraction of the s-polarization component, thus increasing the ellipticity of the beam and, in a relative sense, the p-polarization component.

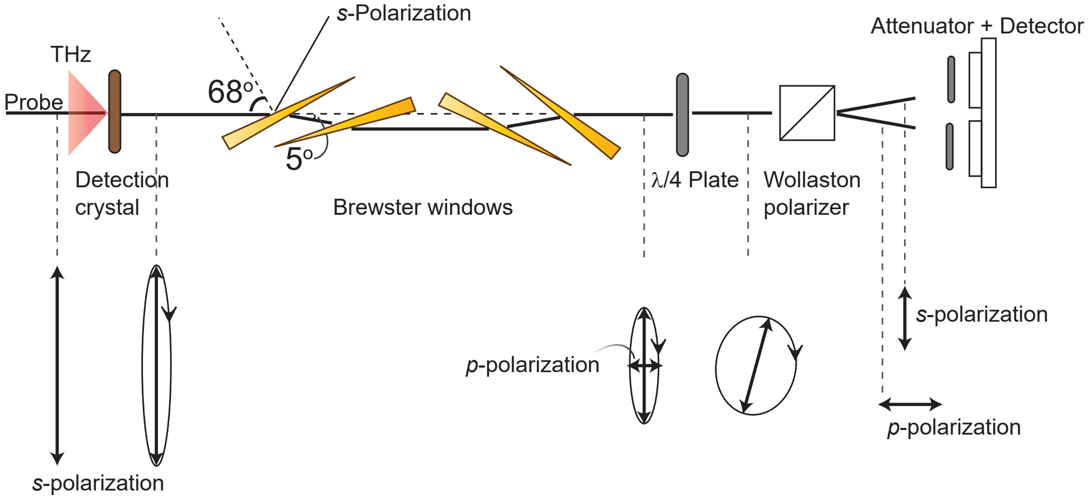

Figure 2.3: Electro-optical sampling setup with four Brewster windows in order to decrease the ellipticity of the probe beam. The bottom row shows the polarization states at various positions along the beam path.

The Brewster windows have a small wedge of $\alpha = 1°$ to avoid multiple reflections from hitting the detector. This wedge causes a deflection dθ of the beam of $d\theta \approx (n^2 - 1)\alpha \approx 5°$ (where α is the wedge angle, and n is the index of refraction). Since it is critical for the overall performance of the setup that every ZnSe surface is hit at the Brewster angle as closely as possible, the tilt of second and third Brewster windows is corrected for that deflection angle (see Fig. 2.3). The overall transmission through the four Brewster window setup was measured to be $t = 0.24\%$, which perfectly matches the expected value for the index of refraction of $n = 2.52$ for ZnSe at 800 nm with a Brewster angle of 68°.

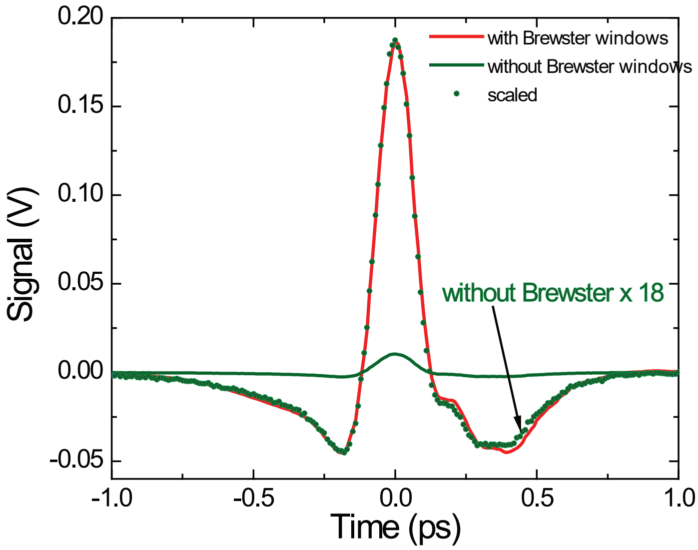

Figure 2.4: THz pulses measured with (red) and without (green) Brewster windows. The amount of light at the two photodiodes of the balanced detection was the same in both measurements. The green solid line shows the raw data without Brewster windows, the green dots the data up-scaled by a factor 18.

Fig. 2.4 shows the THz pulses measured with (red line) and without (green line) Brewster windows by scanning the 800 nm probe pulse relative to the THz pulse. In these two experiments, the amount of light at the two photodiodes of the balanced detection was kept constant with the help of additional attenuators in front of the photodiodes, which compensated the effect of the Brewster windows in the measurement without them. Comparing both measurements, we obtain an enhancement factor of ≈18 (Fig. 2.4, green dots).

2.3.2 Polarization states in the setup

To describe the polarization states at the various positions in the setup, we use the Jones matrix formalism. We start from linearly s-polarized probe light:

$$p_{in} = \begin{pmatrix} 1 \\ 0 \end{pmatrix} \tag{2.5}$$

The detection crystal acts as a phase retarder with small retardation ϕ, that is proportional to the THz field [60]:

$$C = \frac{1}{2} \begin{pmatrix} e^{i\phi} + e^{-i\phi} & e^{i\phi} - e^{-i\phi} \\ e^{i\phi} - e^{-i\phi} & e^{i\phi} + e^{-i\phi} \end{pmatrix}. \tag{2.6}$$

The Brewster windows reduce the s-polarization component by a field attenuation factor a, while they fully transmit the p-polarization component:

$$B = \begin{pmatrix} a & 0 \\ 0 & 1 \end{pmatrix}, \tag{2.7}$$

and the quarter-wave plate is described as:

$$Q = \frac{1}{\sqrt{2}} \begin{pmatrix} 1 & i \\ i & 1 \end{pmatrix}. \tag{2.8}$$

The final polarization state thus becomes:

$$p = Q.B.C.p_{in} = \frac{1}{\sqrt{2}} \begin{pmatrix} a\cos\phi - \sin\phi \\ i(a\cos\phi + \sin\phi) \end{pmatrix} \tag{2.9}$$

The balanced detection measures the difference in intensity of the s- and p-polarization components, which we normalize to the total amount of light on the two detectors:

$$S = \frac{|p_s|^2 - |p_p|^2}{|p_s|^2 + |p_p|^2} \approx \frac{2\phi}{a} \tag{2.10}$$

where the last step is valid for $\phi \ll a$. We see that the relative signal is enhanced by a factor $1/a = 1/\sqrt{t}$ (where t is the corresponding intensity attenuation factor). For the concrete situation in our experiment, we would expect an enhancement factor of ≈ 20; slightly higher than the experimental value of ≈ 18. We attribute the small deviation from the theoretical value to the fact that we do not hit all surfaces of the Brewster windows at the perfect Brewster angle due to small misalignments and the wedges of the Brewster windows.

The enhancement factor can be changed by selecting a different window material and varying the number of Brewster windows. Four ZnSe windows turned out to be a good compromise for significant enhancement as well the available probe pulse energies due to the saturation limit of the photodiodes. The maximum enhancement factor is also limited by the condition $\phi \ll a$ (Eq. 2.10); if a is set too small, the signal no longer scales linearly with the THz field. In the limit of $a = 0$, when only the p-polarization component is transmitted, one could no longer distinguish the signs of the THz field and only the absolute-square of the THz field could be detected.

In the end, by introducing this simple scheme for enhancing the sensitivity of the THz detection, we are able to detect the small signal coming from water in both 1D and 2D time resolved THz experimets.

2.4 Measured THz pulse

Here, we use two identical 0.1-mm-thick (110) GaP or ZnTe crystals as nonlinear mediums to generate and detect THz pulses. Pulses with $\sim$ 10 μJ energy are focused on the THz generation crystal (GaP) with a spot size of $\sim$ 50 μm. The incident energy is just below the damage threshold of the crystals. Fig.2.5 shows a typical THz pulse measured in time and frequency domain, along with the phase. The generation crystal delivers half-cycle THz pulses extending from $\approx$0.3 - 7 THz having a peak at $\approx$1.4 THz. Thus, it covers the hydrogen-bond bend mode at 60 cm^{-1} and a significant part of the hydrogen-bond stretch mode at 200 cm^{-1} as indicated by yellow shaded region of low frequency absorption of water in Fig.1.5. They however miss the librational band at 600 cm^{-1}. The phase of the pulse is almost flat across the spectrum.

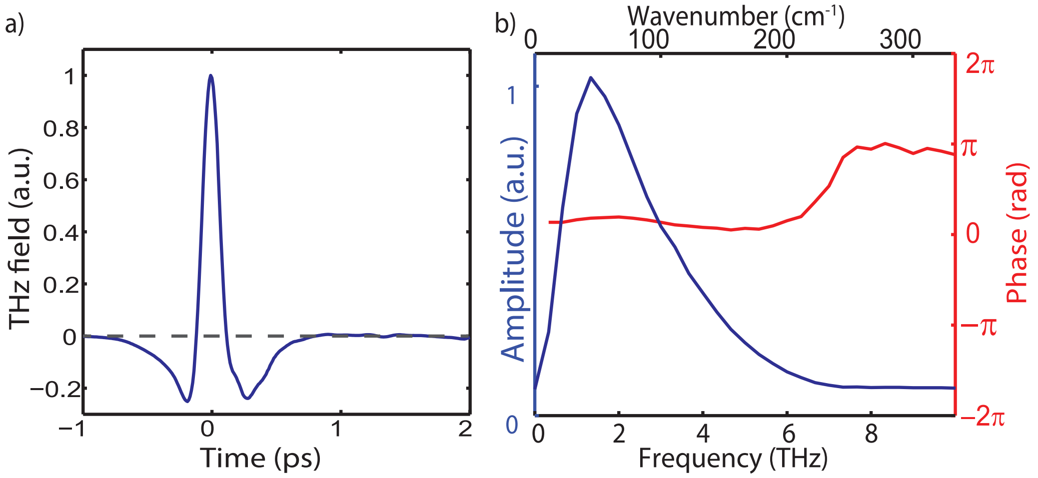

Figure 2.5: a) Measured THz transient in time domain sampled by the probe pulse. b) THz amplitude and phase in frequency domain.

2.5 Optical pump-THz probe experimental setup

A complete description of time resolved optical pump- THz probe spectroscopic method is discussed in this section. Fig.2.6 shows the general optical pump-THz probe experimental setup. The initial laser output is split into two parts with a beam splitter, generating the pump and probe paths. The pump beam is much more intense than the probe beam. The probe beam is split again in two parts. One part is used to generate the THz pulse and the other one is used to detect it. THz is generated by optical rectification and it is detected by electro-optic sampling, as described in the section 2.2.

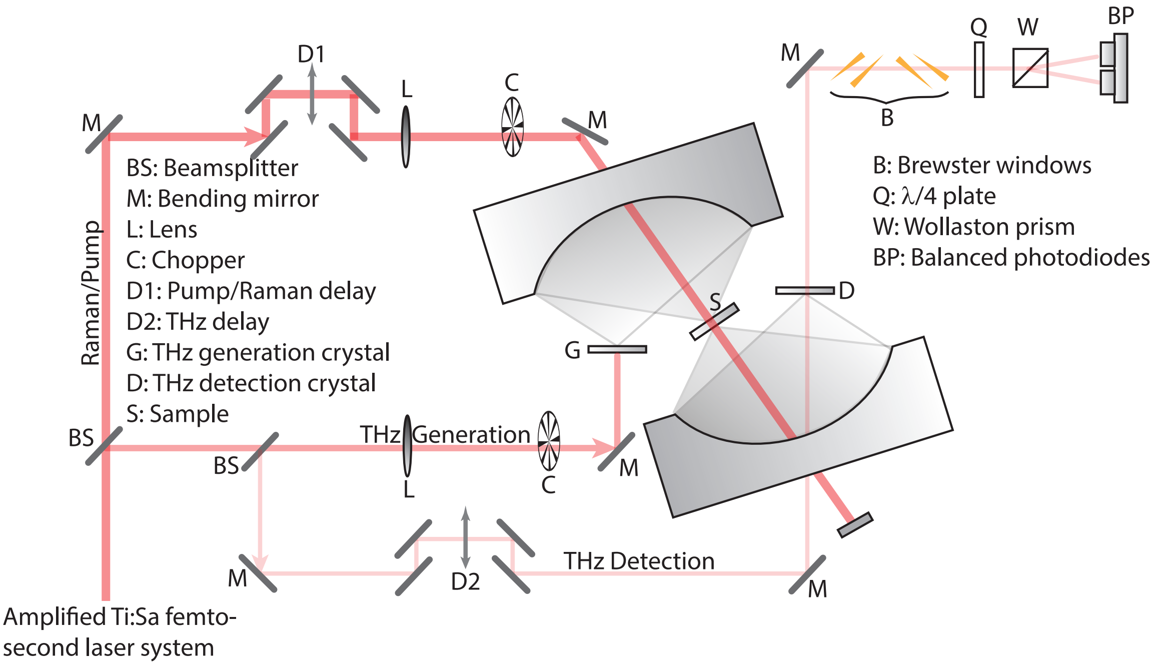

Figure 2.6: Experimental setup used for time-resolved THz spectroscopy of water. For 1D UV pump- THz probe measurement a SHG crystal is placed along the pump path after the delay line D1 to obtain 400 nm pulses.

The THz pulses from the generation crystal are collected and focused on the sample and then onto the detection crystal by two ellipsoidal mirrors. These ellipsoidal mirrors are home-machined and made of aluminium (2f = 83 mm) (see fig.2.7). The two elliptical mirrors are mounted (without possibility of further alignment) in a way that we know the position of their foci with the help of an additionally designed alignment tool (i.e., a thin Al plate with a small pinhole of ≈200 μm positioned on a magnetic retention base). The estimated error in the positioning of the mirrors and the alignment tools is on the order of 100 μm. THz generation and detection crystals as well as the sample are placed at the focii of ellipsoidal mirror arrangement. This arrangement of ellipsoidal mirror has a numerical aperture of about unity, which gives a near-diffraction-limited THz field spot size of about 200 μm on the sample and the detection crystal.

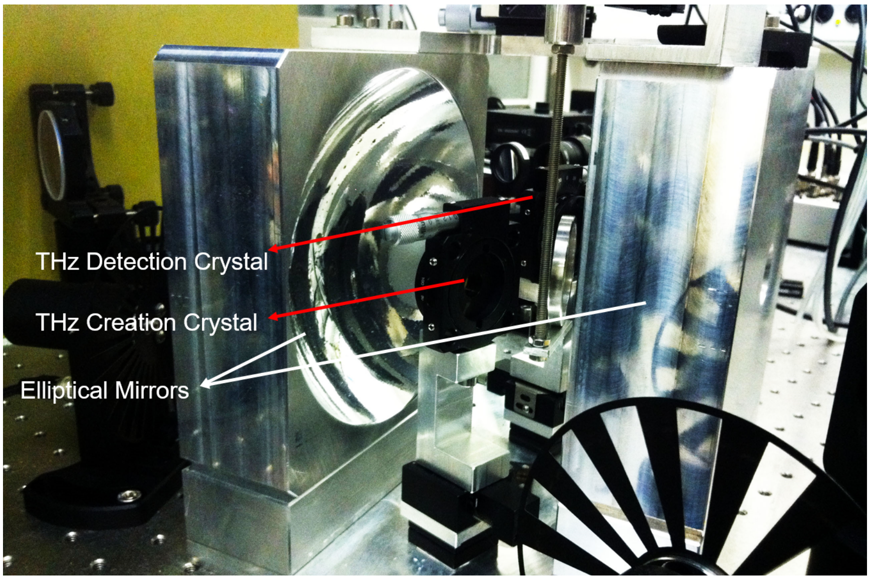

Figure 2.7: Home-built ellipsoidal mirror arrangement made of aluminium.

The detection beam (800 nm) is passed through an optical delay stage (t_2) and a small central hole in the second elliptical mirror. Then it is spatially and temporally matched to the detection crystal. THz pulses carrying information from the sample upon perturbation are focused on the detection crystal, making it birefringent and changing the original polarisation of the gating beam. The gating beam is then passed along the detection path following sensitivity enhancement scheme by Brewster windows as described in the section 2.3. The photodiode signals are then amplified, integrated in a boxcar integrator, and recorded in a computer on a single-shot basis.

The pump beam could be either second harmonic (400 nm, 3μJ) pulses or 800 nm pulses (ca.200 μJ used as Raman pump pulse). Pump pulses are passed through an optical delay stage (D1) controlling t_1. These pulses are focused with a lens (f=1 m) onto the sample, collinearly with the THz radiation, through a small hole in the first ellipsoidal mirror. The spot size of the pump beam is set to 250 μm by adjusting the focus to $\approx$ 8 cm after the sample. The pump pulse has a duration of ca. 110 fs. For 1D pump-probe measurements, optical delay stage (t_2) is fixed to the peak of the THz pulse and pump delay (t_1) is varied whereas for 2D Raman-THz both delays are varied.

THz generation pulses are modulated at a quarter of the laser frequency and pump pulses at half of the laser frequency by using two optical choppers. Electro-optic sampling directly measures the field rather than intensity. The transmitted THz field and generated THz fields after perturbation are added and thus the signals are calculated as the difference between pumped and un-pumped sample as follows:

$$S_{\text{signal}} = (S_{11} - S_{10}) - (S_{01} - S_{00}) \tag{2.11}$$

Where, S stands for the measured signal at the detector and

S_{11} = Pump On THz On.
S_{10} = Pump On THz Off.
S_{01} = Pump Off THz On.
S_{00} = Pump Off THz Off.

The THz pulse itself was measured constantly during scanning by recording all four types of data independently. The whole THz section of the setup was enclosed in a nitrogen-purged box to remove water vapour.

Chapter 3

The effect of the Gouy phase in THz pump-probe spectroscopy

This chapter discusses the effect of the Gouy phase shift observed in THz pulses and its consequence on the shape of the pump-probe signal. The Gouy phase shift depends on the exact positioning of a sample in relation to the focus of the probe beam in a pump-probe experiment.

This work has been published in *Optics Express*, see Ref. [61].

3.1 Introduction

With the advent of THz based systems used for spectroscopic and imaging purposes, there has been growing interest to know how the spatial and temporal evolution of such pulses occur [62]. Due to the large bandwidth of THz pulses, they undergo significant temporal reshaping. One such important process is the Gouy phase shift [63].

Gouy phase:

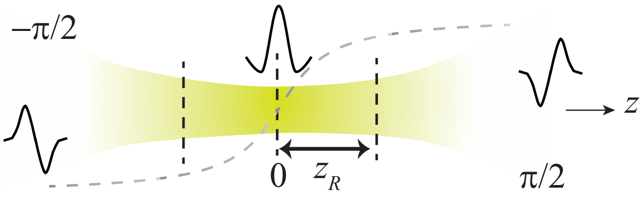

Figure 3.1: Illustrative schematic for Gouy phase.

When a laser pulse travels through a focus, it experiences a phase shift from -$\pi/2$ before the focus, 0 in the focus, and $+\pi/2$ after the focus as shown in the Fig.3.1. This phenomenon is called Gouy phase shift [63]. The Gouy phase of the beam propagating along z - direction is given by:

$$\psi(z) = arctan(\frac{z}{z_R}) = arctan(\frac{\lambda z}{\pi {\omega_0}^2}) \tag{3.1}$$

where z_R is the Rayleigh length and ω_0 is the beam waist. This phase anomaly was first observed by Gouy and was shown to exist for any waves, including acoustic waves, that pass through a focus. THz pulses have been used elegantly to visualize the Gouy phase effect [64–66]. In these studies the importance of the Gouy phase shift is discussed and a direct observation of the π Gouy phase shift through a spherical focus with THz pulses was reported. We also observed the Gouy phase shift in a focused single cycle THz pulse by varying the position of the detection crystal through the focus i.e. at the sample position (see Fig.3.4 top panels).

Here, we demonstrate the effect of the Gouy phase on the outcome of optical pump-THz probe experiments. Let us consider a prototype optical pump-THz-probe experiment as schematically shown in Fig. 3.2. A single-cycle THz pulse is generated by optical rectification in a non-linear crystal such as ZnTe, GaP, or GaSe, imaged by some optics onto the sample, where it is overlapped with an optical pump-pulse, and the generated 3rd-order field $E^{(3)}(t)$ is imaged another time onto the detection crystal. The one dimensional nonlinear interaction in the sample can be described by the usual convolution of the laser pulses with a system response function $R(t', t'')$ [42]:

$$P^{(3)}(t) \propto \int_0^\infty \int_0^\infty E_{THz}(t - t'') I_{pu}(t - t') R(t', t'') dt' dt'' \tag{3.2}$$

Here, $I_{pu}(t) = |E_{pu}(t)|^2$ is the intensity profile of the pump pulse, $E_{THz}(t - t'')$ is the THz pulse. We want to measure the system response function as it gives information about the system. In order to deduce the system response function, deconvolution of the measured field is required, which means we need to know very accurately the THz pulse i.e $E_{THz}(t)$ at the sample position, including its phase. This is where the Gouy phase shift comes into play.

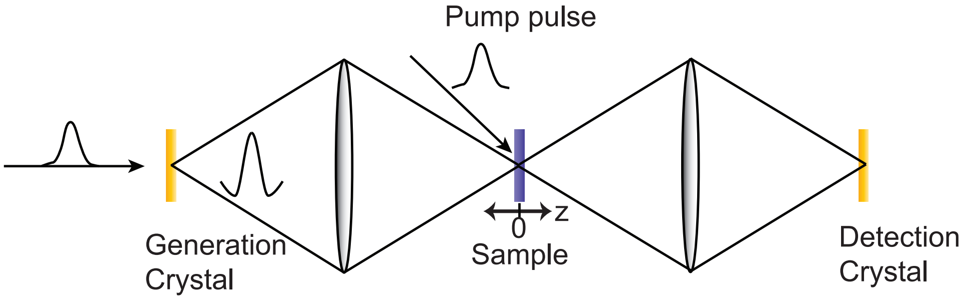

Figure 3.2: Scheme of a optical-pump-THz-probe experiment. The displacement z is measured relative to the middle focus.

In an idealized realization of Fig. 3.2, the Gouy phase shift would not matter since both generation and detection crystal as well as the sample are in the focus of the imaging optics and typically are thin, so the Gouy phase is the same in all three positions.

3.2 Relevance of the Gouy phase

In the context of our experimental consideration, one can assume that the exact positioning of the sample does not matter, since a Gouy phase introduced in $E_{THz}(t)$ is compensated by the corresponding Gouy phase that the emitted field $E^{(3)}$ accumulates on its way to the detection crystal. Mathematically, the Gouy phase can be described by adding a phase ϕ to a propagating field in a 1D description. Hence, one would just add a phase factor $e^{i\phi}$ to Eq. 3.2

$$e^{i\phi}P^{(3)}(t) \propto \int_0^\infty \int_0^\infty e^{i\phi}E_{THz}(t-t'')I_{pu}(t-t')R(t',t'')dt'dt'' \tag{3.3}$$

$e^{i\phi}$ can be pulled in front of the integral and and hence would cancel with a compensating phase $e^{-i\phi}$ for the emitted field. However, physical electric fields are real-valued. Using complex electric fields simplifies many calculations, but is rigorously correct only as long as linear optics is considered.

In the case of slowly varying envelope approximation (SVEA), the envelope of the forward moving pulse varies slowly in time and space as compared to the period/wavelength of the carrier wave. Electric field of the pulse can be expressed as:

$$E(t) = E_0(t)cos(\omega_0 t) \tag{3.4}$$

But for very short pulses, it is no longer meaningful to write them as an envelope times a carrier frequency (as Eq.3.4) because such a pulse would have a non-vanishing amplitude at zero frequency and whenever the time duration of $E_0(t)$ gets in the same order of magnitude as $1/\omega_0$. Consequently, we can not introduce a phase by simply writing:

$$E(t) = E_0(t)cos(\omega_0 t + \phi) \tag{3.5}$$

Alternatively, we can transform the real field into the complex field $\Re E(t) \to \Re E(t) + i\Im E(t)$ (as in a Hilbert transformation)[1]. That means, the field is Fourier-transformed into the frequency domain, the negative frequencies are zeroed, and the field is Fourier-transformed back into the time-domain, which will result in a complex-valued representation of the field (tilde indicates a field is complex). The phase factor may then be added and the real part be taken:

$$E(t) \xrightarrow{FT} E(\omega) \to \Theta(\omega)E(\omega) \xrightarrow{FT^{-1}} \tilde{E}(t) \to \Re(e^{i\phi}\tilde{E}(t)) \tag{3.6}$$

where $\Theta(\omega)$ is Heaviside step function[2]. Now, this sequence of operations is not equivalent to Eq.3.5, if the slowly varying envelope approximations breaks down. In other words, the operation Eq. 3.2 and Eq.3.6 do not commute. If they would commute, then one could first transform $E_{THz}(t)$ into a complex field $\tilde{E}_{THz}(t)$, plug it into Eq.3.2 including the phase factor $e^{i\phi}$, add a phase factor $e^{-i\phi}$ to the generated third order polarization $\tilde{P}^{(3)}(t)$ in order to describe the compensating Gouy-phase, which then would cancel:

$$E_{THz}(t) \to e^{i\phi}\tilde{E}_{THz}(t) \xrightarrow{Eq.3.2} e^{i\phi}\tilde{P}^{(3)}(t) \to e^{-i\phi}e^{i\phi}\tilde{P}^{(3)}(t) \to \Re(\tilde{P}^{(3)}(t)) \tag{3.7}$$

---

[1] Hilbert transform is linear operator that transforms a real valued function to its imaginary counter parts.

[2] It is a discontinuous function, whose value is zero for negative argument and one for positive argument.

The correct treatment of the problem is first transforms $E_{THz}(t)$ into a complex field $\tilde{E}_{THz}(t)$, adds a phase factor, but then plugs only the real part $\Re(e^{i\phi}\tilde{E}_{THz}(t))$ into Eq. 3.2, and finally repeats the compensating phase shift for $P^{(3)}(t)$:

$$E_{THz}(t) \rightarrow Re(e^{i\phi}\tilde{E}_{THz}(t)) \xrightarrow{Eq.3.2} P^{(3)}(t) \rightarrow e^{-i\phi}\tilde{P}^{(3)}(t) \rightarrow \Re(e^{-i\phi}\tilde{P}^{(3)}(t)) \tag{3.8}$$

Both lines of operations do not necessarily reveal the same result. Thus, the Gouy phase effect does not cancel out when slowly varying approximation breaks down as in case of single cycled THz pulses.

3.2.1 Linear Response

In the case of linear response the effect of Gouy phase vanishes. In the most simple approximation of linear response, the first order polarization in the time domain is:

$$P^{(1)}(t) \propto \int_0^{\infty} E_{THz}(t-t'')R(t'')dt'' \tag{3.9}$$

The above integral is a convolution of 1D functions, hence convolution theorem[3] applies. In frequency domain, it can be written as:

$$\tilde{P}^{(1)}(\omega) \propto \tilde{E}_{THz}(\omega)\tilde{R}(\omega) \tag{3.10}$$

where $\tilde{E}(\omega)$ and $\tilde{R}(\omega)$ are the Fourier transformations of the corresponding functions in Eq. 3.9. Treating the above equation according to Eq.3.6, the negative frequencies are then zeroed:

$$\tilde{P}^{(1)}(\omega) \propto \Theta(\omega)\tilde{E}_{THz}(\omega)\tilde{R}(\omega) \tag{3.11}$$

As they are simple product in the frequency domain, hence all the operation in Eq.3.11 commute in frequency domain as well as time domain. Therefore Eq.3.7 and Eq.3.8 give similar results and the Gouy phase induced in input field is compensated by that of the emitted field. Thus the measured linear response does not depend on the exact positioning of the sample in the focus in Fig.3.2.

3.2.2 Pump-probe Response

To simplify matters in a pump-probe response, we consider the system response function to be infinitesimally fast so that it can be approximated to δ-function:

$$R(t', t'') = \delta(t')\delta(t'') \tag{3.12}$$

The third order polarization in time domain described in Eq.3.2 reduces to:

$$P^{(3)}(t) \propto E_{THz}(t)I_{pu}(t) \tag{3.13}$$

---

[3] Convolution theorem states that, Fourier transform of a convolution is the product of the Fourier transforms i.e. FT(f⊗g) = FT(f).FT(g) / The Fourier transform of a product is the convolution of the Fourier transforms i.e FT(f.g) = FT(f)⊗FT(g)

According to the convolution theorem, a simple product in the time domain will become convolution in the frequency domain:

$$\tilde{P}^{(3)}(\omega) \propto \tilde{E}_{THz}(\omega) \otimes \tilde{I}_{pu}(\omega) \tag{3.14}$$

Here, applying the Hilbert transformation before and after the convolution does not yield similar result.

$$\Theta(\omega) \left(\tilde{E}_{THz}(\omega) \otimes \tilde{I}_{pu}(\omega) \right) \neq \left(\Theta(\omega) \tilde{E}_{THz}(\omega) \right) \otimes \tilde{I}_{pu}(\omega) \tag{3.15}$$

Hence, the Hilbert transformation and nonlinear interaction described in Eq.3.2 do not commute. Thus the Gouy phase in the input field is not compensated by that of the emitted field and the nonlinear (pump-probe) interaction does depend on the exact positioning of the sample at the focus. However, the Gouy phase effect is not relevant in pump-probe studies where multi-cycle pulses are used.

For a typical THz experiment, one wants to achieve high intensities of the pump-light in the sample to explore its nonlinear response, the THz pulse is often imaged with high-aperture optics to achieve a small focus as shown in the Fig.3.3. The Gouy phase changes on a scale that equals the Rayleigh length, which in turn is of the order of the wavelength of the THz light if the aperture approaches 1. That is, the accumulated Gouy phase shift in the input THz field $E_{THz}(t)$ before the sample does not cancel out in the signal propagation after the sample. Consequently, the positioning of the crystals and the sample is critical within $\approx 100\ \mu$m for these THz experiments.

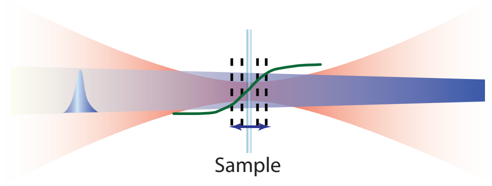

Figure 3.3: Optical (blue) and THz pulses (red) at the focus. Green curve indicates the Gouy phase change.

3.3 Experimental verification

The experimental setup which has been discussed in chapter 2 is used to study the effect of Gouy phase on a pump-probe signal. Here, we used Raman pump- THz probe response of water as an illustrative example. The relevance of such experiment for water structure and dynamics will be explored in much more detail in chapter 5. Briefly, in this experiment a Raman interaction induced by 800 nm pulse excites a coherence in low frequency modes of hydrogen-bonded water network that is switched to another coherence by subsequent THz pulse and finally read out by the emission of THz field. The experiment is termed as 2D Raman- THz spectroscopy as it allows one to determine the correlations among the various degree of freedom. A full 2D data set has been measured in chapter 5, while here, we show only 1D scans along the pump-probe delay time (t_1 or t_{pp}) with the detection time (t_2) kept fixed to the position where the signal is maximal.

As discussed in section 2.5 of chapter 2, a half-cycled THz pulse was imaged by ellipsoidal mirror onto 40 μm thick water jet, which was pumped by an intense 800 nm pulse through a non-resonant Raman process. Due to the high-aperture of the ellipsoidal mirror (NA $\approx$

1), the THz pulse could be focused onto a spot of diameter ≈240 μm. The beam size of the Raman-pump pulse (diameter 300 μm) was adjusted to match the spot size of the THz pulse in the focus. Because of its much shorter wavelength, the beam size can be considered to be essentially constant in the range around the focus which is relevant for the present discussion.

In order to measure the induced Gouy phase in the input THz field $E_{THz}(t)$ directly at the sample position, the detection crystal was put at the sample position instead of water jet. In that case, the positioning of the detection crystal relative to the water jet was measured with the help of a confocal chromatic measurement sensor (ConfocalDT, micro-epsilon) that provides a few micrometers resolution.

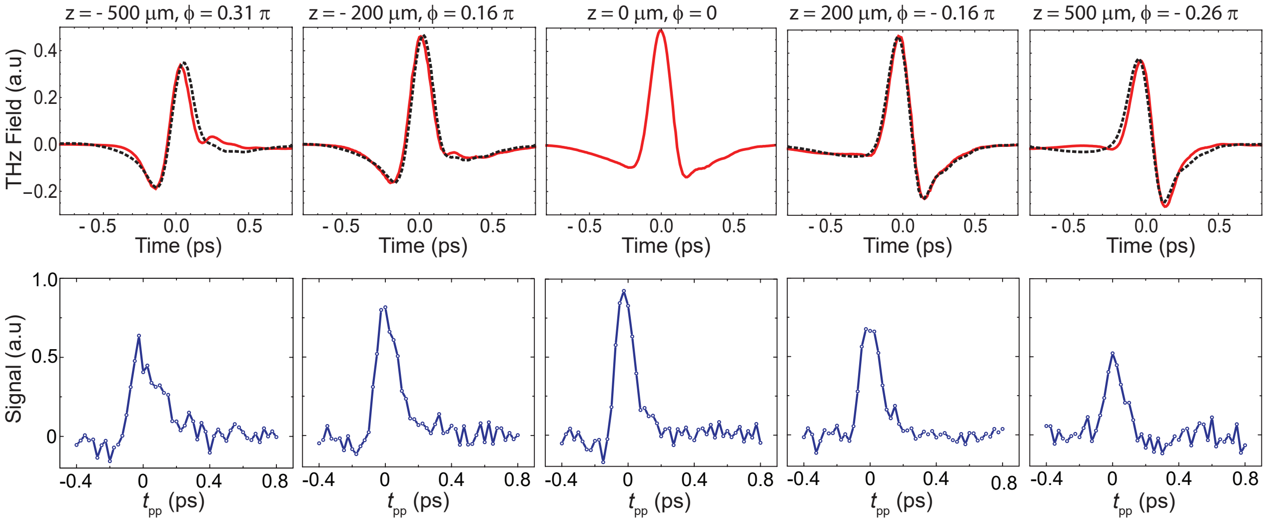

Figure 3.4: Top panels: THz pulses (red) at various positions relative to the focus from -500 μm to +500 μm. The phases ϕ of these pulses have been estimated by taking the pulse at z=0 μm and adding a phase that has been varied to give the best fit (black dotted lines). Bottom panels: Raman pump-THz probe signal (blue) from water at various z positions in dependence of pump-probe delay t_{pp} between the peaks of the Raman-pump and the THz probe pulse. The detection time t was kept fixed at 50 fs relative to the peak of the transmitted THz pulse, where the signal is maximal.

The red lines in the Fig.3.4, top row, show the measured input THz pulse at various positions relative to the focus from z=-500 μm to z=500 μm, where we assumed the focus z=0 μm to be the position where the pulse is symmetric (the displacement z is defined in Fig.3.2). As we move away from the focus in both directions, the phase of the THz pulse changes. Here, the black dotted lines take the pulse at z=0 μm and add a phase ϕ that was varied to give the best match with the red lines. As can be seen, a simple phase shift can very well describe the Gouy phase of the THz pulse as the crystal is moved through the focus. Between z=-500 μm to z=500 μm, the Gouy phase changes from ≈0.3π to ≈-0.3π.

The fact that a simple Gouy phase shift can indeed describe the effect of moving the detection crystal through the focus quite well proves that effects of a changing frequency-dependent overlap between pump pulse and the THz probe pulse do play only a minor role, owing to the high-aperture THz optics (red and black dotted lines in Fig.3.4 would match exactly if the spectral amplitude would not change at all.)

Fig.3.4 bottom row, shows the effect of the Gouy phase shift on the resulting Raman pump-THz probe signal. Between the various measurements of Fig.3.4, bottom row, nothing has been touched in the experimental setup except for the crystal or the jet that has been moved by the indicated distance. As a trivial result, when the water jet is moved off-focus, the signal size diminishes due to the smaller spatial overlap between pump and probe pulses. More importantly, however, the shape of the response changes quite a bit. For example a quite sharp response is found at z=0 μm, the signal at z=-500 μm might be misinterpreted as relatively slow decay. Interestingly, it is these z=-500 μm data which exhibit the slowest decay, despite the fact that the THz pulse is slightly shorter (Fig.3.4, top row) due to a somewhat smaller overlap of the lower frequency components when being off-focus. Hence the effect is opposite to what would be expected if a frequency-dependent overlap would be the origin. Fig.3.4, bottom row, clearly shows that the exact positioning of the sample does matter for the outcome of optical pump-THz probe experiments.

3.4 Conclusion

We show experimentally that the Gouy phase plays a significant role in altering the strength and shape of the desired signal, particularly when high-aperture imaging optics are used. Thus, in order to avoid the severe perturbation of measured signal in optical pump-THz probe spectroscopy, great care should be taken to precisely position the generation and detection crystals as well as the sample in their corresponding foci.

As discussed in section 3.2, the Gouy phase effect occurs only when single-cycle probe pulses are used, i.e. when the slowly varying envelope approximation breaks down, while it disappears for multi-cycle pulses. The effect is thus most relevant in THz time-resolved spectroscopy, where such single cycle pulses are most commonly used, but it should not be overlooked also in other spectral regimes when correspondingly short pulses are involved.

Chapter 4

Dipole solvation in water measured in the THz regime

This chapter presents the experiments to investigate aqueous solvation upon photoexcitation of Coumarin 343, which shows a charge transfer in the excited state. In particular, the rearrangement of the hydrogen bond network of water around the dye is addressed and the difference between the solvation time (τ_s) and Debye relaxation time (τ_D) is pointed out. The aim of the experiment is to demonstrate how the low frequency hydrogen bond dynamics in water can be reached directly by using UV-pump THz-probe spectroscopy. The measured THz response of water is analysed with particular emphasis on the Debye relaxation of water.

4.1 Introduction

Solvation of molecules in water is at the heart of countless molecular phenomena and of critical importance to understand diverse issues of chemical reactivity or biomolecular functions. In many important chemical and biological processes, it is essential to understand the time-dependent response of polar solvents upon changing charge distributions in polar solute molecules in order to study the rate of reaction. Since the availability of ultrashort laser pulses, various linear and nonlinear spectroscopies (involving more than two pulses) have been developed to investigate the solvation dynamics of many solvents [13, 14, 27, 67]. Among these techniques, time dependent fluorescence Stokes shift spectroscopy is extensively used to study the polar solvents like water in which solvation relaxation is studied by measuring the time-resolved emission spectra of fluorescing probe molecules that have significantly different dipole moments in the excited state (S_1) upon excitation as compared to the dipole moment in ground state (S_0). Relaxation of solvent polarisation around the excited dipole results in the time-dependent red shift of the fluorescence spectrum.

A simple depiction of dynamic Stokes shift is represented in Fig.4.1. Physically, the process of solvation of a solute can be understood as follows. Initially, a solute chromophore in its ground state S_0 is in equilibrium with the surrounding solvent molecules. When the solute-solvent assembly undergoes an optical Franck-Condon transition upon excitation to S_1, the equilibrium charge distribution of the solute is instantaneously changed but the solvent molecules still retain their previous spatial and orientational configuration. This configuration results in a non-equilibrium situation for the system because the free energy curves are displaced with respect to each other. Therefore subsequent to the excitation, the solvent molecules rearrange and reorient themselves to stabilize the new charge distribution in the excited state S_1 on time scale denoted as solvation time τ_S.

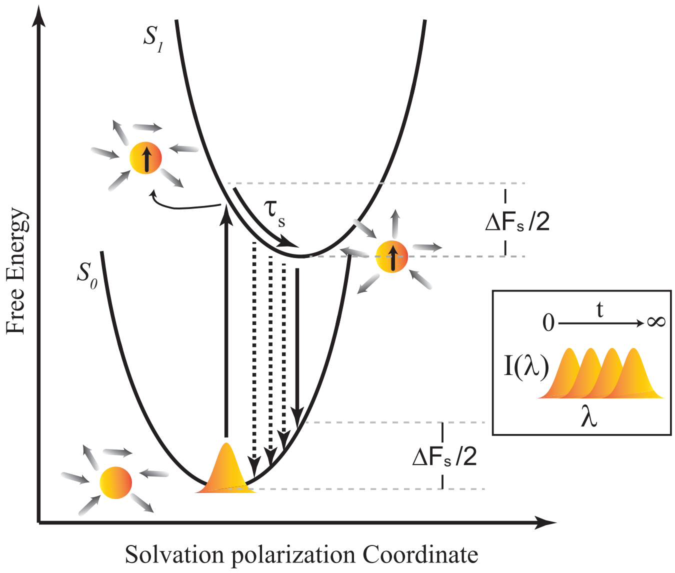

Figure 4.1: Schematic illustration of the dynamic Stokes shift of a dye molecule (orange sphere) in a polar solvent. The grey thick arrows indicate the arrangement of solvent molecule around the solute. After promoting a thermalized ensemble onto the excited S_1 state, it relaxes with the solvation time τ_S, resulting in a time-dependent red-shift of the fluorescence (dashed arrows). The inset (bottom right) shows the red shift of the fluorescence spectrum with respect to time by the virtue of the decrease in the energy of the solute due to progressive solvation.

As the ensemble relaxes, the energy gap between the S_1 and S_0 free energy surfaces decreases, which can be observed experimentally as a time-dependent red-shift of the fluorescence or stimulated emission.

A dynamic Stocks shift technique for studying solvation dynamics of a Cumarine dye in water had already been formulated by Maroncelli and coworkers [14]. They reported the initial part of the solvent response of water to be extremely fast (few tens of fs) with subsequent relaxation in ps which is further complemented by other related studies concluding that water is among the fastest of solvents. However, all these studies on the solvation dynamics are done from a solute perspective. To investigate the solvation dynamics of water with completely different angle, with the solvent perspective, we implemented transient THz spectroscopy to probe directly the relaxation of hydrogen bonded network of water as the solvation proceeds. Both perspectives might actually be very different, which can be seen from the fact that the solvation time τ_S (obtained from dynamic Stokes shift) and the Debye relaxation time τ_D may deviate significantly. The Debye relaxation time is related to the orientational relaxation of solvent molecules.

A continuum model has been applied to explain the time dependence of the solvation energy in terms of macroscopic properties of the solvent, such as the dielectric constant and Debye relaxation time. Assuming a continuum model for solvation and a single Debye process of the solvent, solvation is proportional to so called longitudinal relaxation time, τ_L [23, 68, 69] which is given by:

$$\tau_L = \frac{2\epsilon_\infty + 1}{2\epsilon_0 + 1}\tau_D \tag{4.1}$$

where ϵ_0 is the dielectric constant of the solvent including orientational polarizability and ϵ_∞ the dielectric constant from only the electronic polarizability of the molecule. Thus τ_L is derived via theoretical relation from experimental value of the dielectric relaxation time τ_D. For polar solvents, $\epsilon_0 \gg \epsilon_\infty$, thus Eq.4.1 predicts large separation between τ_L and τ_D. The time scale separation between solvation time and the orientational relaxation of solvent molecules is based on the very nonlinear dependence of the reaction field R on the dielectric constant ϵ in Onsager's reaction field model:

$$R = \frac{2}{r^3}\frac{\epsilon - 1}{2\epsilon + 1}\mu \tag{4.2}$$

where r is the radius of the assumed Onsager sphere and μ the dipole of the molecule. Eq.4.1 can be obtained by plugging in frequency dependent dielectric constant of a single Debye process(Eq.4.3) to the Onsager reaction field from the quasi static boundary value calculation [69].

$$\epsilon(\omega) = \epsilon_\infty + \frac{\epsilon_0 - \epsilon_\infty}{1 - i\omega\tau_D} \tag{4.3}$$

The nonlinear dependence in Eq.4.2 describes the saturation of the solvent response due to screeing effect;i.e., if ϵ is larger than 1 (like water), already the first solvation layer solvates a solute by generating a reaction field R in such a way that the field of the solute's dipole is no longer seen by molecules beyond the first solvation layer. If the ϵ gets smaller, the size of the solvation layer will get larger, but in a way that R will stay almost the same (except $\epsilon \to 1$). In 1977 Onsager suggested that solvation (of an electron) proceeded on range of time scales in such a way that the polarization relaxation of solvent molecules closer to a newly created ion occurs slower than those which are far away [70]. A detailed Mean Sphere Approximation (MSA) theory by Rips et al. [71] suggested that for a single Debye response, nonexponential solvation occurres with short-time response close to τ_L and long time response close to τ_D. Water is considered among the fasest solvents. According to the continuum model, Eq.4.1 predicts a longitudinal relaxation time for water τ_L=240 fs (with $\epsilon_0 \approx 80$ and $\epsilon_\infty \approx 1.8$ and τ_L = 8.3 ps [72]), which is quite close the experimentally observed average solvation time of 400 fs [31]. From that one may conclude that the reason for the fast solvation time in water is in fact its large dielectric constant, and not its orientational dynamics per se, the latter of which not being particularly fast with τ_D = 8.3 ps [72].

In order to study aqueous solvation from the water perspective, we optically excite a dye molecule and observe the response of water by transient THz spectroscopy. The THz spectrum of water is related to the dipole-dipole correlation function, whose long-time tail decays exponentially with the Debye relaxation time τ_D. When transiently measuring the THz spectrum of water after exciting a dissolved dye molecule, the expectation is that we observe τ_D rather than τ_S.

4.2 Solute of choice: Coumarin 343 as fluorescent probe

For rigid dye molecules with high fluorescence quantum yield in polar solvents such as water, the dynamic Stokes shift is dominated by the relaxation of the solvation degrees of freedom, rather than by intramolecular degrees of freedom, which is why it does not really matter which particular dye is used as a sensor of the solvent response. However, for the purpose of the experiment presented here, the solute needs to satisfy certain criteria stated below. Coumarin dyes have been shown to be excellent fluorescent probes for studying solvation dynamics [13, 14, 73] in dynamic Stokes shift studies. Therefore we chose Coumarin 343 as solute. Its molecular structure is shown in Fig.4.2. Upon photo-excitation it shows intramolecular electron transfer from the tertiary amine region to the carboxylic region of the molecule.

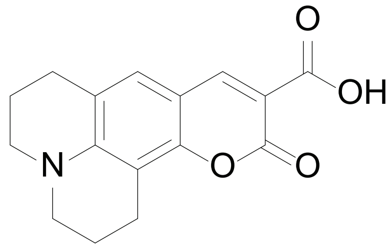

Figure 4.2: Molecular structure of Coumarin 343.

The reasons for selecting Coumarin 343 are therefore as follows:

- It has a high extinction coefficient at 400 nm as shown in its absorption spectrum in Fig.4.3. Hence UV pump is used to excite the dye molecule.
- It is soluble in water to a certain extent. (Solubility is discussed in the subsequent paragraph.)
- Upon photo excitation, it shows a significant change in dipole moment (5.3 D) due to intramolecular charge transfer.
- It is relatively rigid and stable and shows neither photoproduct nor isomerization during the course of the experiment.

The solubility of Coumarin 343 in water is relatively low ($\sim$ 1 mM) as it starts to form dimers [74]. In order to increase its solubility to 5mM, we deprotonated the dye by adding a base (1,4-diazabicyclo[2.2.2]octane, DABCO, 10 mM) to the solution. DABCO is a weak nucleophilic base and it helps the Coumarin to remain intact, thus preventing the degradation caused by the ring opening of the dye.

We measured the absorption and fluorescence spectra of Coumarine 343 at the concentration used in transient THz measurement (i.e 5 mM) as shown in Fig.4.3. From the peaks of the absorption and emission spectra, the Stokes shift is determined. i.e. 3200 cm^{-1}.

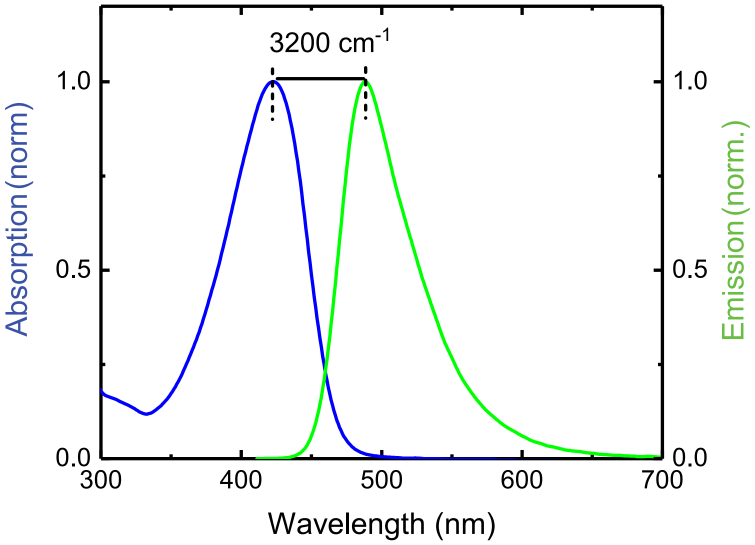

Figure 4.3: Normalized absorption and emission spectra of a solution of deprotonated Coumarin 343 (5 mM) with 10 mM DABCO in water at room temperature are represented by blue and green colour respectively. The Stokes shift, as determined by the peaks of the spectra, is 3200 cm $^{-1}$.

Time dependent DFT calculations show that the dipole changes by ≈5.3 D when exciting from the ground to the electronically excited state, which agrees well with values reported for the protonated form [75, 76]. Note that the absolute dipole-moments of ground and excited state are ill-defined since the molecule is charged; when one chooses the center of nuclear charge as origin, the dipole increases from 35.2 D in the S_0 to 40.5 D in the S_1 and both are essentially parallel.

4.3 Experimental methods

4.3.1 Life times and quantum yields

Time-correlated single photon counting (TCSPC):

The sample was excited using a 394 nm pulsed picosecond diode laser source (Horiba Scientific, DeltaDiode DD-395L) operating at a repetition rate of 8 MHz. The emission polarization was adjusted to the magic angle (54.7°) to minimize anisotropy contributions to the observed decays. The emitted light was passed onto the emission monochromator and detection system from the Fluorolog 3 instrument, which also allowed selection of a precisely detected wavelength. The monochromator bandpass was adjusted to a photon count rate of ca. 1% or less of the excitation frequency to avoid pulse pile-up effects.

The dilute solutions of C343 with DABCO in water were measured in standard 1x1 cm quartz cuvettes while the concentrated solutions of 5 mM C343 with 10 mM DABCO in water were measured in a 1 mm path length quartz cuvette to minimize reabsorption, and were excited at ca. 30° and measured in front face mode. Fig.4.4 shows the fluorescence decays and single exponential fits of deprotonated Coumarin 343 in the dilute case (blue) and the concentration used in transient THz experiment (red, 5mM). Fitting in the case of the diluted solution reveals a lifetime of 4.7 ns while for the concentrated solution it reduces to 3.9 ns. The fluorescence quantum yield of a dilute solution of deprotonated Coumarin 343 has been determined to ϕ_F=85% with the help of a Quanta-ϕ integrating sphere calibrated with respect to the reported quantum yield of Coumarin 153 in air-saturated ethanol at room temperature ($\phi_F = 53 \pm 4\%$) [77]. For the concentrated solution the quantum yield could not be reliably measured due to the re-absorption of the fluorescence light. However it can be assumed that it is reduced by the same factor as the fluorescence lifetime, i.e., $\eta \approx 70\%$.

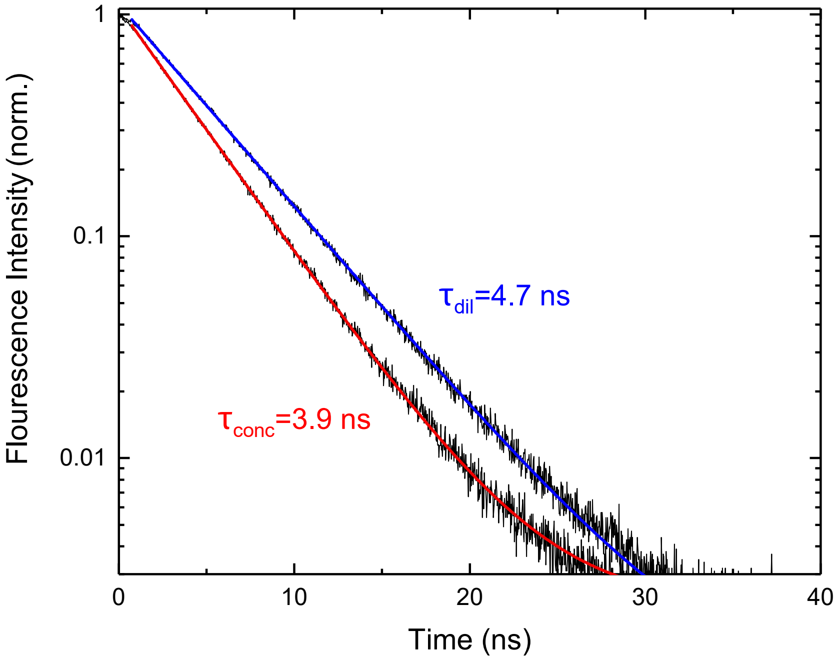

Figure 4.4: Fluorescence decay of deprotonated Coumarin 343 in the dilute case (blue) and at the concentration used in the transient THz experiment (red, 5 mM). The data were fitted to single exponential functions (thick lines), revealing lifetimes of 4.7 ns and 3.9 ns, respectively.

4.3.2 Transient THz spectrosscopy

Fig.4.5 shows a schematic illustration of the UV pump-THz probe experiment. A 400 nm beam initially excites the deprotonated 5 mM Coumarin with 10 mM DABCO in water at ambient conditions. Upon excitation the dipole moment of the dye instantaneously changes because of the intramolecular charge transfer, and than surrounding water molecules re-arrange themselves to accommodate the new configuration of the dye. Thus, the response of the water can be recorded by monitoring the peak of the THz electric field (probe) as a function of the pump-probe delay.

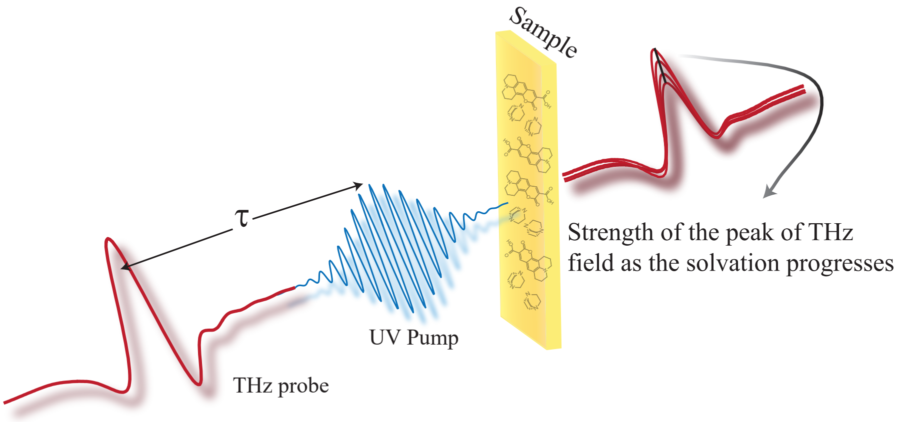

Figure 4.5: Schematic illustration of UV-pump THz probe experiment: 400 nm beam excites the sample (5 mM Coumarin 343 + 10 mM DABCO). Single peak point of the THz waveform is monitored by varying the time delay between pump and probe to map out the response of water subsequent to excitation of the dye.

For the transient THz spectroscopy we essentially used the same setup as described in chapter 2. 400 nm pump pulses were generated via frequency doubling in 0.5 mm thick BBO crystal placed along the pump path. THz probe pulses were produced in a 0.1 mm thick GaP (110) crystal, generating an almost perfect half-cycle pulse with a FWHM of ∼180 fs (see Fig. 4.8), and detected in a 0.5 mm thick ZnTe (110) crystal. The pump and probe spot sizes in the focus were ∼ 200 μm. The sample, Coumarin 343 in DABCO solution was measured in a 40 μm thick wire-guided jet [78] to avoid any contamination of the signal from window materials. In order to check the linearity of the signal, the signal strength as a function of the pump energy was measured as shown in Fig.4.6. The signal shows linear dependence until 4 μJ and starts to behave non-linearly afterwords. Therefore energy of the pump pulses was set to 3.5 μJ, which was safely within the linear regime of the detected signal (See Fig.4.6).

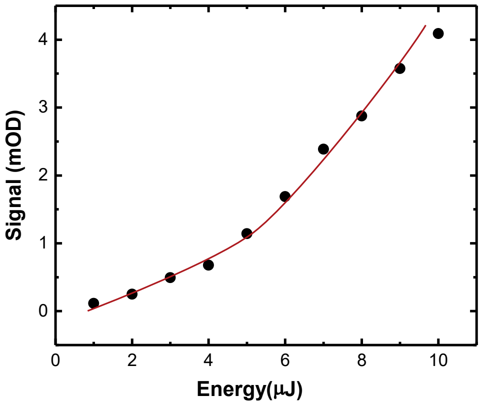

Figure 4.6: Effect of Pump-pulse energy at the peak of UV pump- THz probe signal. Signal shows linear behaviour until 4 μJ and behaves non-linearly afterwords. Red line is drawn for visual guide only and is not a fit.

Two different pump sources were used. For experiments with ~120 fs time resolution, pump and probe pulses were derived from the same Ti:Sa laser system, and the pump-pobe delay was changed with an optical delay line. For experiments with delay times up to 50 ns, two Ti:Sa amplifier systems were electronically synchronized [79], revealing an effective time resolution of 10 ps due to the jitter in the synchronization.

4.4 Results

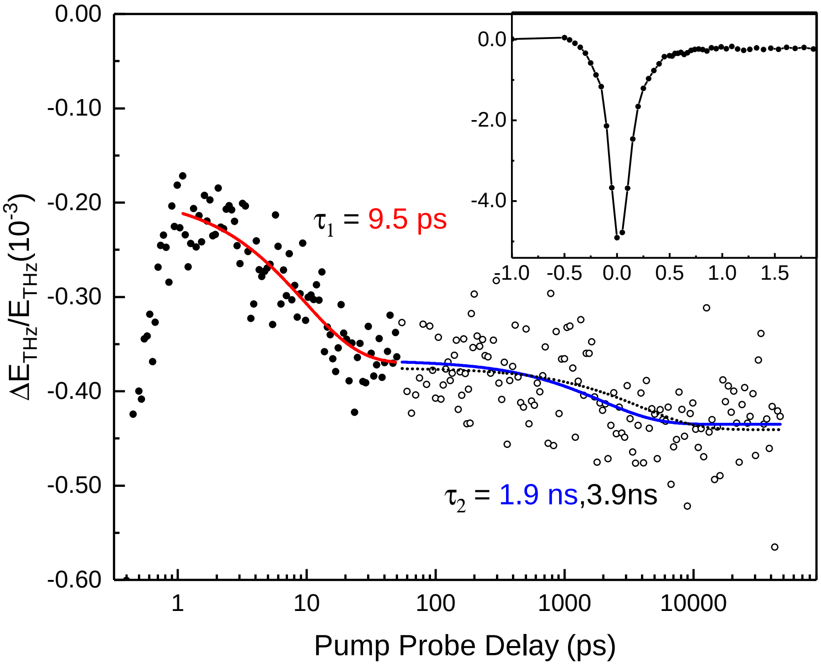

Figure 4.7: Relative change of the transmitted THz field E_{THz} measured at the peak of the half-cycle THz pulse after photoexcitation of Coumarin 343 (5 mM) and DABCO (10 mM) in water at ambient conditions. The filled circles show the data measured with high time resolution up to 50 ps, and the open circles those measured with two synchronized laser systems from 20 ps up to 50 ns. The red and blue solid lines show multi-exponential fits, leaving all time constants as free fit parameters, while the fit shown as a dashed red line fixes the slowest time constant to 3.9 ns, as determined from the fluorescence decay (see Fig.4.4). The two data sets have been stitched together by slightly scaling the second one, with the scaling factor determined from the solid line fits. The inset shows the spike around delay zero.

The transient THz signal from water after photoexcitation of the dye molecule is shown in Fig.4.7, which is measured at the peak of the half-cycle THz pulse. Two data sets are stitched together in this plot, obtained with the two different pump sources described in experimental methods, thereby covering the time-range from 100 fs to 50 ns. Around delay-zero, a pulse-width-limited spike of increased THz absorption is observed (see Fig.4.7, inset). The spike does not decay to zero completely, but leaves a small pedestal, which is hardly seen in the inset of Fig.4.7. When looking closely and enlarging the data from 0 ps onwards as exhibited in the main panel of Fig.4.7, we noticed that pedestal subsequently increases in two steps. The first step, occurring with a time constant of 10± 3 ps, agrees within error with the Debye relaxation time of water [72], while the second step can be fitted to a process with 1.9 ns (Fig.4.7, solid blue line). The signal stays constant from thereon.

4.5 Discussion

The transient THz signals from water after photoexcitation of the dye clearly show that the surrounding water molecules relax with time scale of 9.5 ps, with a subsequent very slow decay component of 1.9 ns and long lived constant signal. Let us first consider the non zero signal appearing at the later time of 10- 50 ns. Water is fully thermalized on a time scale of ns over the distances that exceed the typical separation of neighbouring molecules [80]. Thus, the non-zero signal remained at later time around 50 ns is attributted to the heating of the sample. Indeed, it is established from stationary spectroscopy that the THz absorption cross-section of water increases as a function of temperature [81]. In order to quantify the heating of the sample, the calibration of this effect for our experimental conditions was required. Therefore, we measured the transmission of the THz pulse through a thermostated water cuvette of equal thickness at various temperatures.

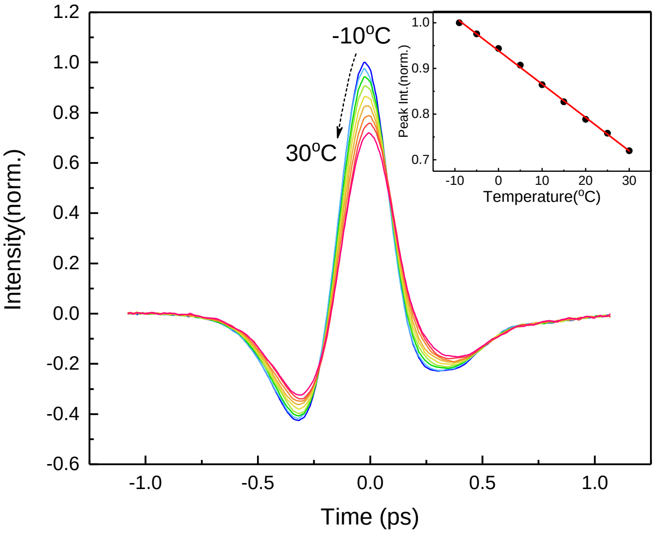

Figure 4.8: Normalized THz pulse after transmitting through a thermalized 40 μm water cuvette with the temperature varied from -10°C to 30°C in steps of 5°C. The inset shows the peak intensity of the THz pulse together with a linear fit (red line) that reveals a slope of $\triangle$T/T = -7.5 x 10^{-3} K^{-1}.

We observed a linear dependence of peak intensity with respect to temperature with a slope of $\triangle$T/T = -7.5. 10^{-3} K^{-1} (see Fig.4.8). With that, one can estimate a total temperature jump of $\approx$ 0.07 K from the size of the late-time pedestal of the transient THz data (Fig. 4.7). That number agrees very well with an independent estimate (0.06 K) obtained from the number of absorbed photons per sample volume, their energy, the heat capacity of water and the fluorescence quantum yield of the dye.

Calculation of temperature jump:

$\mathrm{E} = \mathrm{m}.C_v.\triangle\mathrm{T}$
$\mathrm{E}_{input} = 3.5\ \mu\mathrm{J}$; but Abs = 0.5 OD
$\mathrm{E}_{input} = 60\% \times 3.5\ \mu\mathrm{J} = 2.1\ \mu\mathrm{J}$
$\mathrm{E} = \mathrm{E}_{input} \times (1\text{-}\phi)$; ϕ = quantum yield = 85%;
$\mathrm{E} = 2.1\ \mu\ \mathrm{J} \times (1\text{-}0.85) = 0.315\ \mu\mathrm{J}$
$\mathrm{m}= \rho \times \mathrm{vol.} = \pi \times \mathrm{r}^2 \times \mathrm{h} = 1.25 \times 10^{-6}\ \mathrm{g}$
where r= radius of the the pump beam and h= thickness of the sample

C_v = heat capacity at const. vol. = 4.18 J/ mg °C
$$\triangle\ \mathrm{T} = \frac{E}{m.C_v} = 0.06\ \mathrm{K}$$

Thus, the long-term constant signal and the second step indicate the electronic relaxation of the dye. Since the fluorescence quantum yield of the dye is not 100% (we determined a quantum yield of $\eta = 70\%$), the remaining fraction of dye molecules dissipate their electronic excitation energy into the solvent by radiationless relaxation, thereby heating the solvent. The fluorescence lifetime, which can be measured much more accurately by TCSPC (3.9 ns, see Fig. 4.4), deviates from the value obtained from the fit of the transient THz data (1.9 ns). We therefore also show in Fig.4.7 a fit that fixes the time constant of that process to 3.9 ns (black dashed line), evidencing that this is still consistent with the relatively poor signal-to-noise ratio of the transient THz data.

We believe that the observation of second process with the time-constant agreeing well with the Debye relaxation of water is the most crucial part of the study. To discuss that we come back to Fig.4.1. However, one should be cautious about the definition of different terms involved. The solvation time τ_S indicated in Fig.4.1 is not same as the Debye timescale τ_D observed in the transient THz experiment. Fig.4.1 plots 'free energy', while heating measures 'energy'. Since solvation is largely entropy-driven, both terms may be very different. But, the entropy is function of solvation polarization coordinate and therefore free energy differences along that coordinate are, in fact, the same as energy differences [23]. Thus, the dashed arrows in Fig.4.1 indeed indicate the energy of the emitted fluorescence photons. Note that the total solvation free energy $\triangle\mathrm{F}_s$ is the same as the Stokes shift $\triangle\mathrm{E}_s$. However, the total solvation free energy splits half/half for the solvation of the excited state and the re-solvation of the ground state,(according to the linear response that reveals identical curvatures of the S_0 and S_1 free energy surfaces) that is not necessarily true for the splitting of the total solvation energy.

Clearly, in Fig.4.7, the amplitude of the 10 ps step upon solvation of the excited state is larger than the 3.9 ns step, despite the fact that the latter has contributions from both re-solvation of the ground state and the radiationless relaxation of the $(1\text{-}\eta)\approx 30\%$ of molecules that do not emit a photon. The temperature jump at late delay times (0.07 K) results from an energy of $\approx 9300\ \mathrm{cm}^{-1}$ per excited molecule (i.e., $\triangle\mathrm{E}_S + (1\text{-}\eta)\mathrm{E}_F$), where E_F is the energy of the fluorescence photons. From the amplitude of the 10 ps process relative to the late-time pedestal, one can then estimate that it dissipates $\approx 3800\ \mathrm{cm}^{-1}$, which coincides with roughly the total amount of the Stokes shift $\triangle\mathrm{E}_s$ (i.e., $3200\ \mathrm{cm}^{-1}$).

In conclusion, it is demonstrated that solvation dynamics of water can be measured directly by probing the hydrogen bond network by transient THz spectroscopy. As anticipated in the introduction, one fact that the response time of water is close to its Debye relaxation time rather than solvation time is indeed observed. This is clearly related to orientational motion of water molecules around the altered dipole moment of the dye. The THz response also verifies the lifetime of the dye molecule, which was measured independently by TCSPC. Thus to a certain extent, the solvation dynamics measured from the water perspective complements the investigations done from the solute perspective.

Chapter 5

Two-Dimensional Raman-THz Spectroscopy of Water

This chapter introduces the novel two-dimensional Raman-THz spectroscopy which is used to explore the dynamics of low frequency, intermolecular modes of water in a collective manner.

This work has been published in *Proceedings of National Academy of Sciences*, see Ref. [82].

Water shows many anomalies in its nature due to its ability to form tetrahedral structure with the hydrogen bonds as discussed in the introductory chapter. The discussion about the origin of these anomalities is extremely controversial. It started already more than 100 years ago [32], when the properties of water were attributed to two polyamorphic states of water, a low-density liquid (LDL) and a high-density liquid (HDL). From the experimental point of view, as mentioned in section 1.3 of the introductory chapter, two techniques have provided many insights into the structure and dynamics of water: X-ray absorption [35] and scattering [37,38] techniques as well as ultrafast multidimensional IR spectroscopy [7–10,40]. Multidimensional IR spectroscopies generally exploit the OH (or OD) stretch vibration as local sensors to the strength of the hyrogen bond network [6,83] and it has been established from these techniques that the typical lifetime of the hydrogen bond is ≈1 ps. This is very local way of probing the hyrogen bonded environment. On the other hand, the low-frequency spectrum of water using Raman or THz absorption reports on the intermolecular degrees of freedom in a much more direct manner [72,84–86].

However, in order to uncover the ambiguity regarding the homo- or hetrogeneity within the collective motions of the water network, multidimensional spectroscopy in the low frequency regime is required [87]. Along this direction, 2D-Raman spectroscopy has been proposed [88], but turns out to be experimentally very challenging [89–92] and has not been realized for water. With the advances in the generation of strong THz fields [93] required for a nonlinear interaction, various multidimensional THz techniques have emerged recently, but their applicability is currently limited to semiconductor solids [94] or molecules in the gas phase [95]. A hybrid 2D Raman-THz spectroscopy has been proposed [96,97] by our group, based on MD simulations that circumvents the technological limitations of both 2D Raman and 2D THz spectroscopy. Here, we present the experimental 2D Raman-THz response of liquid water.

5.1 Experimental method

Before going into technical details of the experimental method, it is important to understand certain spectroscopic concepts which are used for this investigation.

5.1.1 Pulse sequences

In 2D Raman-THz spectroscopy, two short laser pulses hit the sample: a nonresonant 800 nm pulse (Raman) and a resonant half-cycle THz pulse. The first laser pulse that hits the sample (this can be the Raman or THz pulse), but if it is Raman pulse, it induces a Raman transition and excites an intermolecular vibrational coherence. After time t_1, the second pulse (THz or Raman, respectively) interrogates the molecular system a second time, and the resulting coherence state is read out at time $t_1 + t_2$ by the emission of a THz field. In terms of pulse sequencing, two possibilities can appear, i.e Raman-THz-THz and THz-Raman-THz pulse sequences, respectively as shown in Fig.5.1. Both pulse sequences, may in principle induce the same coherence pathways with varying probabilities due to the different selection rules of Raman and THz interactions [97].

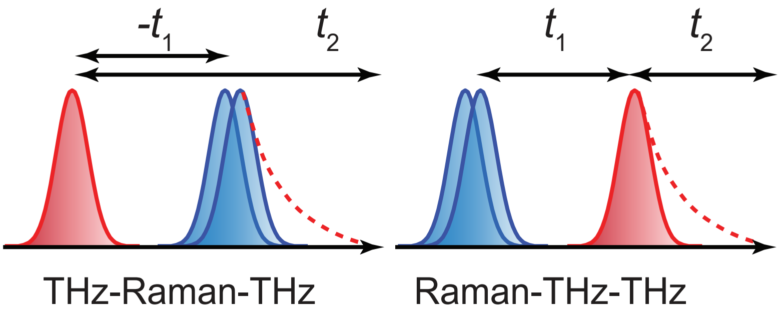

Figure 5.1: 2D Raman-THz Pulse Sequences. (Red: THz Pulses; Blue: Raman Pulses)

The most significant aspect of any of these pulse sequences is the switching of coherences induced by the second pulse, which ultimately allows one to correlate various degrees of freedom with each other. Most importantly, if the spectrum of collective intermolecular modes is inhomogeneously broadened due to hydrogen-bond network patterns, the second pulse may rephase the coherence induced by the first pulse, giving rise to an echo [98].

5.1.2 Appearance of an echo

The concept of an echo can be understood as follows. When the first pulse interacts with the sample, it generates coherence i.e the spectroscopic transitions of all molecules starts to oscillate in phase. As the time progresses, these oscillations run out of phase, resulting in the dephasing of coherences with respect to time and the oscillations become out of phase. Then a second pulse arrives at time t_1 after the first pulse and interact with the sample. This pulse inverts the coherence of the molecules. Thus, after the second pulse, fast molecules before the inversion will catch up to the speed of the molecules which were slower resulting in rephasing of the coherence. Rephasing signal appears at time $t_1 = t_2$ and hence it is called as an echo. Appearance of an echo is a hallmark of inhomogeneity in various degrees of freedom.

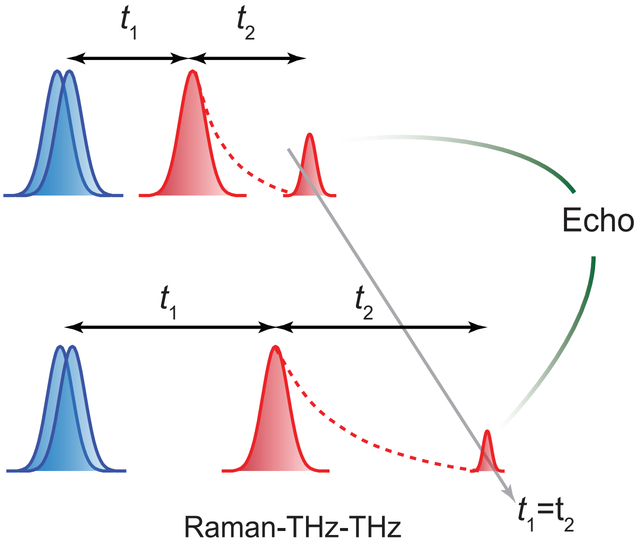

Figure 5.2: Raman-THz-THz pulse sequence: The appearance of an echo at t_1=t_2 represents the ability of the system to rephase the coherence after second light perturbation. Fig. adapted from ref. [99]

In the context of the discussion above, consider Raman-THz-THz pulse sequence shown in Fig.5.2. Two non-resonant field interactions induce a Raman transition and excite an intermolecular vibrational coherence, which quickly dephases. After a time t_1, the system is perturbed a second time by a THz field interaction, and is then read out along t_2 by the emission of a THz field. The amount of inhomogeneity can be monitored through the extent of the signal along the diagonal $t_1 = t_2$ in terms of 'echo', which reflects the ability of the system to rephase the coherence after the second perturbation [87].

5.1.3 Experimental technique

We measured the 2D Raman-THz response of liquid water at ambient conditions. We used the same experimental setup which is described in chapter 2. It is not different from an optical-pump-THz-probe experiment [54], except that the Raman pump pulse is non-resonant and, as such, excites a vibrational coherence. For the generation of THz pulses two identical 0.1 mm thick (110) GaP crystals are used. GaP crystals generate almost perfect half-cycle THz pulses without any ringing (unlike ZnTe crystals) as shown in Fig.2.5. The appearance of ringing in the THz pulses would make it difficult to differentiate between the 2D Raman-THz response and the IRF (Fig.5.5 and 5.6). GaP crystals produce significantly less THz light than the more commonly used ZnTe, making it harder to measure the small signal, but we considered the cleanness of the pulses to be more important. The setup was optimized for a high detection sensitivity (the peak of the emitted 3rd-order field was $\approx 4 \times 10^{-4}$ of that of the input THz pulse) and low dispersion for as close an approximation as possible to a half-cycle THz pulse.

Approximately 200 μJ per pulse of the laser output was used as the Raman pump pulse, which was passed through an optical delay stage controlling time t_1. The Raman pulses were focused to a spot size of 250 μm and coupled to the sample collinearly with the THz pulses. An auto-correlation measurement (using an AC-1PS auto-correlator from UVisIR Inc.) and a Gaussian fit with a FWHM of about 150 fs of the Raman pulse are shown in Fig.5.3. Assuming

Gaussian pulses, this corresponds to a pulse duration of ≈110 fs FWHM. Importantly, the Raman pulses are very clean with essentially no wings. If wings were present, they would show up in the diagonal cut of the IRF in Fig.5.5b because is in fact the convolution of molecular response function with the laser pulses. The same pulse is also used to generate the THz-pulse in the first GaP crystal.

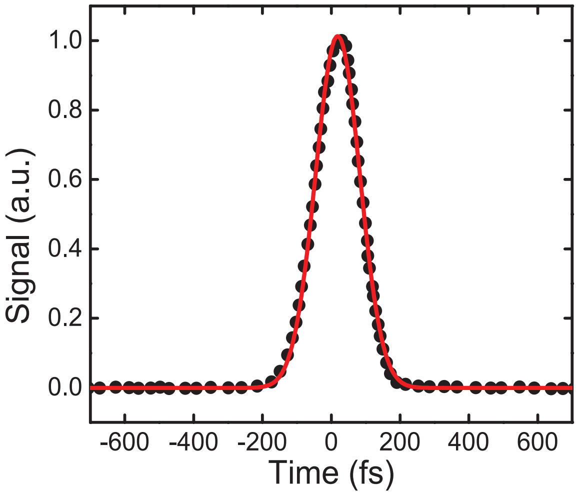

Figure 5.3: Raman pulse measured by autocorrelation setup (black dots) and Gaussian fit (red line).

The transmitted THz field and the generated 2D Raman-THz field are additive and thus the 2D Raman-THz signal can be calculated as a difference between the pumped and un-pumped sample.(see eq2.11 of chapter 2)

5.1.4 Sample: Water jet

The water sample (triple-distilled water) flowed in a windowless 40-μm thick gravity-driven jet to avoid any extra artifacts from windows as well as any accumulative thermal effects in the excitation volume. Thickness of the jet was calculated by [100]:

$$\Delta t = t_{\text{sample}} - t_{\text{ref}} = \frac{(n-1)}{c} D \tag{5.1}$$

Where t_{sample} and t_{ref} are the temporal positions of peak maximum of THz signals with and without sample respectively, n = 2 is the refractive index of water at THz wavelength, c is the velocity of light and D is the thickness of the sample.

The thickness of the jet gets modulated during the time of scanning due to water evaporation, which in turn changes the water level in the reservoir and hence the pressure of water delivered to the jet. In order to avoid such modulations, the amount of water in the reservoir was controlled by continuously adding small amounts of water with a syringe pump. All measurements were performed at room temperature.

5.2 Results

Fig.5.5 shows the experimental results of the 2D Raman-THz response of liquid water at ambient temperature. In order to make sure that the response measured is the desired one, signal strength as a function of the Raman pump pulse irradiance needed to be checked.

5.2.1 Raman pump power dependence

In order to obtain a measurable signal, high irradiance is required, but it may photoionize the water, resulting in the generation of solvated electrons. These solvated electrons may interact with the sample and/or the THz pulses leading to unwanted signals. The generation of solvated electrons is a multiphoton process, and thus the appearance of the signal shows nonlinear behaviour with respect to pump pulse intensity as shown in Fig.5.4 a. When increasing the pump pulse irradiance beyond 1 TW/cm^2, we do observe a signal that looks qualitatively very different from the Raman signal (Fig.5.4 c). This signal is due to the solvated electrons resulting from the photoionization of the water, with a threshold of above 1 TW/cm^2 for 800 nm pulses. Detailed descriptions of the generation of solvated electrons and their interactions are described in the publication included in Appendix A.5 [101].

On the other hand, the 2D Raman-THz signal has two field interactions with the Raman pulse, thereby showing linear dependence on pump pulse intensity. Therefore we critically verified the linearity of the desired signal by varying the Raman pulse intensity with a variable neutral density filter. The result in Fig.5.4 b indeed reveals a linear behaviour in a regime below ca.1 TW/cm^2, indicating that the signal is the desired 2D Raman-THz response. We thus conclude that it is possible to detect the 2D Raman-THz signal free from the response of solvated electrons in the water sample. The 2D Raman-THz response of Fig. 5.5 a has been measured at a pump irradiance of 0.6 TW/cm^2, which is safely within the linear regime.

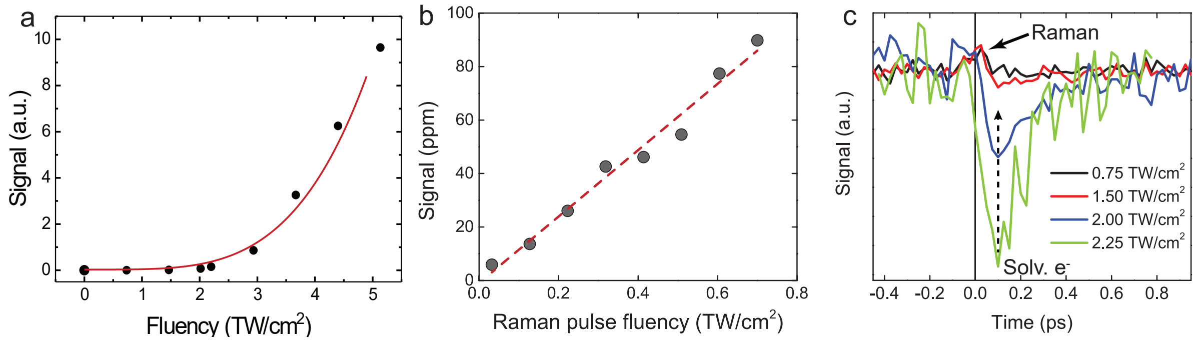

Figure 5.4: a) Peak of the signal with respet to pump-pulse irradiance showing nonlinear behaviour beyond 1 TW/cm^2 b) Raman-pulse irradiance dependency of the peak of the 2D Raman- THz signal. c) Disappearance of solvated electron signal and emergence of Raman induced signal upon reducing the Raman pump pulse irradiance.

5.2.2 2D Raman-THz response of water

The generated half-cycle THz pulses cover the hydrogen-bond bend mode at 60 cm^{-1} and a significant part of the hydrogen-bond stretch mode at 200 cm^{-1}. They however miss the librational band at 600 cm^{-1}(see Fig.1.5). The Raman pump pulses with a length of 110 fs

FWHM (Fig.5.3) cover a somewhat larger frequency range up to ~9 THz (300 cm^{-1}).

In order to get the required 2D Raman- THz response we used two delay stages in the experimental setup (Fig.2.6). D1 scans the delay between the Raman and THz pulses at the sample (t_1), and D2 scans the delay between the THz input pulse at the sample and the emitted field (t_2). In the experiment we scan t_1 from negative to positive times, which means that the signal before t_1=0 comes from the THz-Raman-THz sequence and that after t_1=0 comes from the Raman-THz-THz sequence. The time t_2 is defined as the delay between the THz input pulse and the emitted field, and not necessarily between the second pulse and the emitted field, so that $t_2 \leftarrow t_1 + t_2$ for $t_1 < 0$. Therefore, the Raman-THz-THz sequence appears in the upper-right quadrant with $t_1 > 0$ and $t_2 > 0$ (shaded in green in Fig. 5.5b), whereas the THz-Raman-THz sequence appears in the upper triangle of the upper-left quadrant with $t_1 < 0$ and $t_1 + t_2 > 0$ (shaded in gray in Fig. 5.5b).

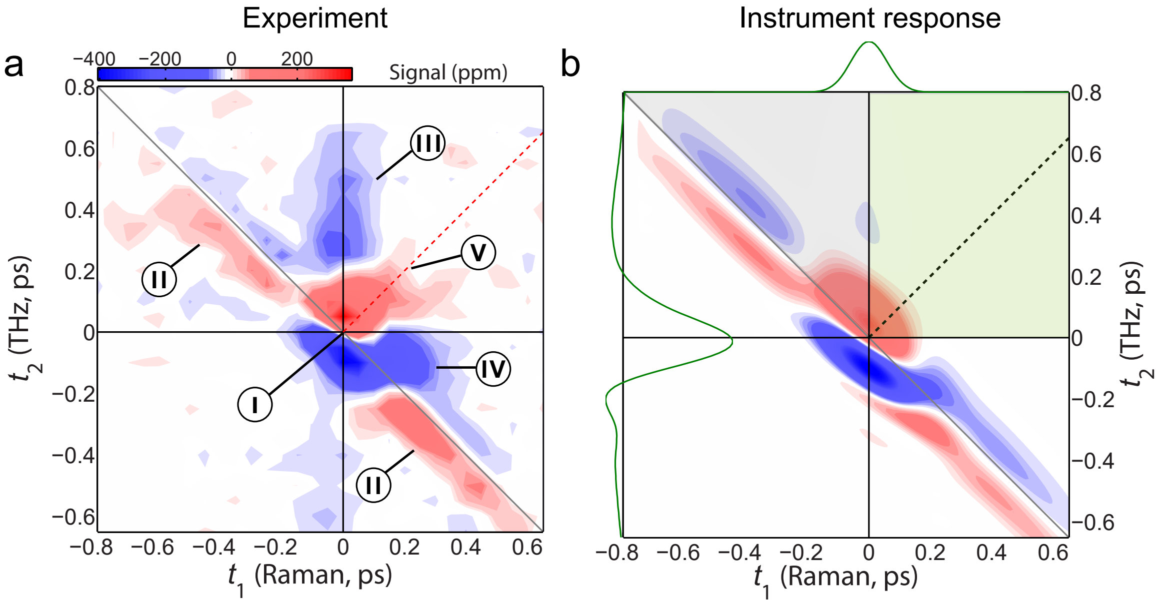

Figure 5.5: a) 2D Raman-THz response of water. The intensity scale is given in parts per million (ppm) with respect to the maximum of the THz pulse field transmitted through the water sample. The red dotted line indicates the diagonal ($t_1 = t_2$), where the appearance of an echo is expected. The origin $t_2 = 0$ is defined as the peak of the transmitted THz pulse, which is also measured during scanning. The origin $t_1 = 0$ has been adjusted to fit with the instrument response function. Labels I -V indicate features discussed in the text. b)The IRF, Raman ($I_{Raman}(t)$) and input THz ($E_{THz}(t)$) pulses have been determined experimentally and are shown as green lines on the top and left side, respectively. The black dotted line indicates the diagonal, the grey shaded area is where the THz-Raman-THz sequence appears. The light green-shaded area is where the Raman-THz-THz sequence is expected.

The nonlinear interaction in the sample can be described by the usual convolution of the laser pulses with a molecular response function $R(t', t'')$ [42]:

$$P^{(3)}(t_2; t_1) \propto \int_0^\infty \int_0^\infty E_{THz}(t_2 - t'') I_{Raman}(t_2 + t_1 - t'' - t') R(t'', t') dt' dt'' \tag{5.2}$$

where $E_{THz}(t_2 - t'')$ is the THz pulse, $I_{Raman}(t)$ the intensity profile of the Raman pump pulse, and t_1 accounts for the experimentally controlled delay time between the peaks of the two pulses.

The molecular response function $R(t'', t')$ is the property we ultimately want to measure, because it contains the molecular information. In order to extract $R(t'', t')$, we need to precisely know the input THz and Raman pulses entering Eq. 5.2, as well as how the emitted field propagates to the detection crystal [102]. In order to know about the emitted field through the detection crystal, we describe the generated 3^{rd} order field as a time-derivative of the 3^{rd} order polarization:

$$E^{(3)}(t_2; t_1) = \frac{d}{dt_2} P^{(3)}(t_2; t_1), \tag{5.3}$$

Eq.5.3 is valid when the effect of dispersion and absorption is neglected. Dispersion and absorption from the water jet can be introduced via a linear transfer function in the frequency domain. That transfer function can be combined with those of the imaging optics and the detection crystal [103], revealing a total transfer function $T_{total}(\omega_2)$, with which we obtain for the detected field:

$$E_{det}(\omega_2; t_1) = T_{total}(\omega_2) E^{(3)}(\omega_2; t_1). \tag{5.4}$$

The input pulses $E_{THz}(t)$ and $I_{Raman}(t)$ as well as the transfer function $T_{total}(\omega)$ have been determined experimentally (See supporting material Appendix A.4).

Evaluating Eqs. 5.2-5.3 for a hypothetical instantaneous response function $R(t'', t') = -\delta(t'')\delta(t')$ reveals the instrument response function (IRF) of the setup(see Fig.5.5 b), for which the integrals in the convolution Eq. 5.2 disappear:

$$P^{(3)}(t_2; t_1) \quad = \quad -E_{THz}(t_2) \cdot I_{Raman}(t_2 + t_1). \tag{5.5}$$

Thus this third-order polarization, which is a product of the two pulses, extends along the antidiagonal in the 2D representation of Fig.5.5b due to the argument $t_2 + t_1$ in I_{Raman}, reflecting the arrangement of delay lines in the experimental setup, while Eq.5.4 is stretched toward the positive t_2. The time derivative Eq.5.3 is responsible for the minus-plus (blue-red) pattern in the IRF in the t_2 direction. One can see that the IRF in Fig.5.5b stays quite narrow in the diagonal direction with $t_1 = t_2$, because the Raman pump pulse is significantly shorter than the THz pulse and it is clean without wings.

5.3 Discussion

Certain parts of the experimental data (Fig.5.5a) are similar to the IRF (Fig.5.5b). The common feature in both the experimental data and the IRF, i.e., the spikes around $t_1 = t_2 = 0$ labeled as "I" in Fig.5.5a and the antidiagonal ridge labeled as "II," originates from a part of the water response that is much faster than our laser pulses. This fast response is considered a result of electronic polarizability as well as librational motion of water with a typical frequency of 600 cm^{-1}. In contrast, any feature beyond the IRF originates from a water response that is slow enough to be observed with our time resolution. Three such features labeled III-V can indeed be identified.

Features III and IV extend along the positive t_1 and t_2 axes, and the simulation results from ref. [96] suggest that these features essentially reflect the 1D Raman and 1D THz responses respectively. The 1D Raman response decays on a typical timescale of 350 fs at room temperature [84], which is in reasonable agreement with the decay of feature III. The long time relaxation tail of the 1D THz response, on the other hand, decays much slower with 8 ps [72]. Due to the time derivative in Eq.5.3, we are very insensitive to such slow processes, so feature IV probably reflects some of the oscillatory contribution of the 1D THz response. Hoeowever, the feature V which extends along the diagonal $t_1 = t_2$ in the upper-right quadrant and contains additional substructure is the most interesting feature.

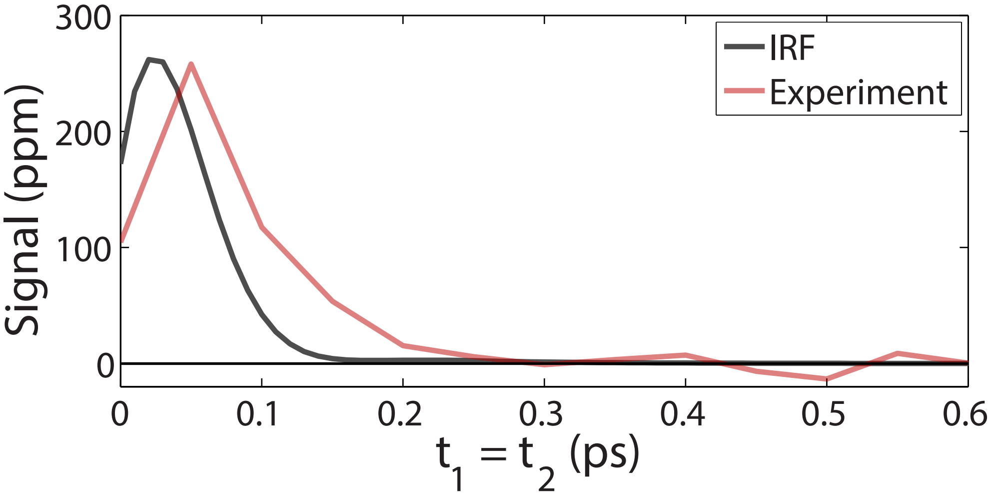

Figure 5.6: Cuts along the diagonal for the Raman-THz-THz pulse sequence, red for the experimental data and black for the IRF. The data beyond 0.3 ps give an idea of the signal-to-noise ratio.Experimental signal (red) decays with time constant of 100 fs.

Fig.5.6 highlights that feature by showing a cut along the diagonal with the decay of the experimental data (red) being slower than that of the IRF (black). The diagonal $t_1 = t_2$ is where an echo is expected. Echoes appear when a multimode system gets synchronized twice by two perturbations separated by a time t_1. As mentioned in section 6.1.2. an echo is emitted at $t_2 = t_1$ revealing that the modes rephase upon a second perturbation. Thus, the feature V is attributed to an echo, which suggests an inhomogeneous distribution among the collective intermolecular hydrogen-bond modes in water. The decay of this echo is found out to be 100 fs. This indicates the extent of inhomogeneity of low frequency modes in water. In order to verify this interpretation we measured the inhomogeneity of water structure by adding different salts with significant concentrations. Detailed 2D Raman-THz study of various salts in water is described in the publication included in Appendix A.6 [99].

If the lifetime of a single hydrogen bond is 1 ps as concluded from 2D-IR and related experiments on the OH stretch (or OD-stretch) vibration [9, 11, 12, 40], then the lifetime of a tetrahedral water cluster with four hydrogen bonds can be as short as 250 fs agreeing with the decay time observed in Fig.5.6.

5.4 Conclusion

In conclusion, we demonstrated that 2D Raman-THz spectroscopy is experimentally accessible with good signal to noise ratio. We believe that this represents the most decisive spectroscopy as of today of the intermolecular structure and dynamics of liquid water. Certainly, in order to support these interpretations, more refined theoretical attention is required. The observed echo with the decay of 100 fs reveals the extent of inhomogeneity of the hydrogen bonded network of water. However, 100 fs seems to be too fast to be compatible with the more extended and persistent structure within the two state model has been deduced from X-ray scattering experiments.

For future experiments, in order to cover larger frequencies of the absorption spectrum of water, shorter Raman and THz pulses are required in an improved instrument. This can be achieved by following a plasma generation and detection scheme [104] to fully cover the 200-cm^{-1}- band as well as the librational band. Another approach could be to measure the 2D-Raman THz response of supercooled water, as the dynamics are expected to be slower and thus easier to measure.

Chapter 6

Concluding Remarks

6.1 Dissertation summary

The aim of this work was to contribute to a deeper understanding of the solvation and structural dynamics of water, specifically by probing the low frequency intermolecular hydrogen bond mode of water directly by time-resolved THz spectroscopy as presented in introductory chapter 1. With the rising awareness of solvent-solute interactions, it is evident that the most of the solvation dynamics studies are limited to solute degrees of freedom, and the area of investigations from the solvent perspective remain void. Similarly, the controversies regarding the existence of the bimodal structure of water, its heterogeneity and the lifetime associated with its structural dynamics needed to be addressed. To shed some light on these curiosities, we used time-resolved THz spectroscopy. To investigate ultrafast dynamics, high temporal resolutions were required. The experimental verification of the solvation and structural dynamics of water in this dissertation leads to solid and unambiguous conclusions.

In particular, the experimental studies of this thesis contributed to the knowledge of aqueous solvation process and structure of water by:

- conducting UV pump-THz probe experiments of a dye molecule in water, which allowed us to record the relaxation time of water upon photoexcitation of the dye.

- performing a hybrid 2D Raman-THz spectroscopy on neat water, in which the appearance of an echo in 2D Raman-THz response allowed us to reveal the inhomogeneous behaviour of hydrogen bond networks.

In order to catch the weak signal emanating from water, prior technical modifications were required to the experimental setup. THz pulses, which serve as an indirect probe were, generated by optical rectification and detected by electro-optical sampling by GaP or ZnTe crystals. In order to achieve near-diffraction-limited THz field spot size of about 200μm on the sample and the detection crystal, an arrangement of two home-machined ellipsoidal mirrors were implemented in the experimental setup. The sensitivity of electro-optic detection was enhanced by introducing a sequence of Brewster windows mounted appropriately along the detection path. We demonstrated that this arrangement of four ZnSe Brewster windows enhances the signal by a significant factor ($\sim$20) in comparison to standard detection without Brewster windows.

The scheme is particularly useful when very small THz fields are to be measured in connection with low-repetition rate amplified Ti:Sa laser systems. Further more, the experimental setup was optimised to avoid perturbations caused by the Gouy phase shift. The Gaussian beam acquires a total phase shift of π along the propagation direction when it travels through the focus. This effect is called the Gouy phase shift. It is seen when high aperture optics are used and is related to the single cycle pulses typically used in THz spectroscopy. We observed that the Gouy phase shift significantly alters the strength and shape of the desired signal. In order to avoid such severe perturbation of the measured signal, we positioned the generation and detection crystals, as well as the sample, precisely to their corresponding focii.

Using this novel modifications of the experimental setup, we performed a series of experiments, focused on understanding the collective behaviour of hydrogen bonds and underlying physical phenomena in water.

Water is a special solvent. Studies of its solvation dynamics have been pursued for the past few decades using various techniques as described in the section 1.2 of the introductory chapter. All those studies essentially demonstrated relaxation dynamics of water from a solute's perspective. They reveal very fast dynamics of the order of a few tens of fs and later decay of ps time scale. On the contrary, in chapter 5, solvation dynamics was studied from solvent (water) perspective. Upon photo-excitation the dye molecules undergo intramolecular charge transfer resulting in the reorientation of the surrounding water molecules. Here, hydrogen bonded water molecular network was probed directly. One dimensional UV-pump-THz probe spectroscopy was utilised to measure the relaxation of water molecules upon photoexcitation of the dye. The transient THz signal in the time domain was measured with a time delay between the pump and probe pulses ranging from 50 fs to 50 ns. The THz response from the water shows multi-exponential decay of the order of 10 ps and a few ns. The first decay is associated with the Debye relaxation of water rather than solvation time and the second decay corresponds to the life time of the dye (Coumarin 343). During the solvation process, the relaxation of the water molecules occurs within the Debye relaxation time as a result of the complete reorientation of the molecules. Thus in a way these findings complement the previous studies.

The next experiment described in chapter 6 used 2D Raman-THz technique to investigate the intermolecular structure and dynamics of liquid water at ambient conditions. To disentangle the complexity regarding the homo- or heterogeneous nature of the hydrogen bond network of water, a development of 2D Raman-THz spectroscopy was realised, which essentially utilizes the non-resonant Raman pump to excite the vibrational coherence and multiple perturbations of the system leading to emission of THz fields. The 2D Raman-THz response of water was measured by varying the time delay between Raman-THz pulse (t_1) and the input-emitted THz fields(t_2). The appearance of an echo, observed at $t_1 = t_2$ reflects the ability of the heterogeneous system to rephase the coherence after the second perturbation. Thus, it demonstrated the heterogeneous distribution of intermolecular hydrogen bond modes in water. Decay of the echo was found to be 100 fs exhibiting the extent of inhomogeneity of low frequency modes of water molecular network. Not unreasonably, with a $\sim$ 1ps life time of a single hydrogen bond established from the 2D IR and related experiment (section 1.3 of the introduction), then the lifetime of a tetrahedral water cluster with four hydrogen bonds can be calculated as 250 fs asserting well with our experimental findings. However, the observed time scale at ambient temperature in our experiment seems too fast to be compatible with the two steady structures assumed within the two state model of water.

Both experiments used the novel methods to tackle the problem of probing structural and solvation dynamics of water in the low frequency regime. A direct probing approach of low frequency vibrational modes by THz time-domain and time-resolved spectroscopy should help to understand more complex systems.

6.2 Outlook for further studies

The direct studies of solvation and behaviour of the hydrogen bond network of water, pioneered in this dissertation provide a basis for extending these experimental methods to other solutions as well as further development of the methodology itself.
Potential ideas to be brought into consideration include:

Water dynamics surrounding biomolecules:

Solvation plays an important role not only in chemical processes but also in most of the important biochemical reactions which form the basis of life on this planet. The behaviour of water in the proximity of biomolecules such as proteins [105], lipids and DNA, can be probed to understand how their structural and functional properties are modified and the time scales of such structural or functional modification.

2D Raman-THz response of supercooled water:

The 2D Raman-THz response of supercooled water could be of immense interest because the dynamics is going to be slower and more pronounced [11], and thus easier to measure. Proteins has been shown to modify the THz spectrum [86]. It would be interesting to understand this behaviour using 2D time-resolved THz technique.

From a technical aspect, to cover the larger frequencies of absorption spectrum of water, shorter Raman and THz pulses are required in an improved instrument which can be achieved by following a plasma generation and detection scheme [104] to fully cover the 200-cm^{-1}- band as well as the librational band.

Appendix A

Publications

This Appendix is collection of all published journal articles which are the part of the research work. A Description of the contributions to these publications by the author of this thesis is given for each article.

A.1 Detectivity enhancement in THz electrooptical sampling

Reprinted from ref. [59], with the permission of AIP Publishing LLC.

A.1.1 Contribution to this paper

- Sequence of Brewster windows in detection path of experimental setup was designed and built by Saima Ahmed.
- Saima Ahmed performed the experiments.
- Saima Ahmed analysed the experimental data.

REVIEW OF SCIENTIFIC INSTRUMENTS **85**, 013114 (2014)

Detectivity enhancement in THz electrooptical sampling

Saima Ahmed, Janne Savolainen, and Peter Hamm
Department of Chemistry, University of Zurich, Zurich, Switzerland

(Received 19 December 2013; accepted 7 January 2014; published online 24 January 2014)

We demonstrate and discuss a simple scheme that significantly enhances the detectivity of THz electro-optical sampling by introducing a sequence of Brewster windows that increases the ellipticity of the probe beam. By varying the window material or the number of Brewster windows, the enhancement factor can be adjusted; we demonstrate an enhancement factor of ≈20 with four ZnSe Brewster windows. The scheme is particularly useful when very small THz fields are to be measured in connection with low-repetition rate amplified Ti:S laser systems. © *2014 AIP Publishing LLC*. [http://dx.doi.org/10.1063/1.4862657]

I. INTRODUCTION

In recent years, there has been a tremendous development in single cycle THz pulses produced from femtosecond lasers[1–4] with applications, for example, in imaging,[5–7] in the non-destructive detection of explosives,[8] as well as in other fields of spectroscopy.[9,10] In time-domain THz spectroscopy, one often uses the generated single cycle THz pulses only as bright light source with coherent detection, but one does not make explicit use of the fact that it is also a short pulse. Optical pump-THz-probe experiments, on the other hand, do so and have been applied to study, e.g., phonon dynamics,[11,12] ultrafast carrier dynamics in various materials,[13–19] other excitations in strongly correlated materials,[20,21] as well as low frequency vibrational dynamics in molecular liquids.[10,22,23] Most time-resolved THz setups use light from a laser oscillator for THz generation and detection, where the high repetition rate and high stability of the laser help tremendously to achieve very good signal-to-noise ratios. But as the field moves towards nonlinear THz experiments and optical-pump-THz-probe experiments, higher laser powers are needed that call for amplified laser systems with much lower repetition rates. At the same time, the emitted THz fields originating from a nonlinear interaction might be very weak. On the other hand, too much of single pulse energy is available from amplified laser systems as probing light for electro-optical sampling that would saturate any detector. Here, we describe a scheme that makes use of the extra amount of single pulse energy and thereby enhances the THz detectivity by a significant factor ≈20.

II. RESULTS

We used a typical optical-pump-THz-probe experimental setup[24] based on an amplified Ti:S laser system, but for the purpose of this discussion, only the THz-detection part is relevant, which used a 0.1 mm GaP [110] crystal for electro-optic sampling (see Fig. 1). A THz field at the detection crystal renders it birefringent with an optical axis 45° to the laser polarization. An initially s-polarized 800 nm probe beam will thus become elliptically polarized with a small p-polarization component. In a standard electro-optic sampling scheme,[4] the light would then be passed through a quarter wave plate, which results in a distorted circular polarized beam, and then through a Wollaston polarizer, which separates p- and s-polarization components whose difference is measured by two balanced photo diodes. The p-polarization component after the detection crystal is proportional to the THz-field and the rotation sense of the elliptically polarized reflects the sign of the THz field, but the ellipticity can be very small, depending on the strength of the THz field. Therefore, in order to reduce the large s-polarization component, the beam is first passed through a set of four Brewster windows before the Wollaston polarizer in our implementation (see Fig. 1). These Brewster windows (ideally) transmit 100% of the p-polarization component, but reflect a certain fraction of the s-polarization component, thus increasing the ellipticity of the beam and, in a relative sense, the p-polarization component.

The Brewster windows have a small wedge of 1° to avoid that multiply reflected beams hit the detector. This wedge causes a deflection dθ of the beam of $d\theta \approx (n^2 - 1)\alpha \approx 5°$ (where α is wedge angle and n is the index of refraction). Since it is critical for the overall performance of the setup that every ZnSe surface is hit at the Brewster angle as closely as possible, the tilt of second and third Brewster windows is corrected for that deflection angle (see Fig. 1). The overall transmission through the four Brewster window setup was measured to be $t = 0.24\%$, which perfectly matches the expected value for the index of refraction of $n = 2.52$ for ZnSe at 800 nm with a Brewster angle of 68°.

Fig. 2 shows the THz pulses measured with (red line) and without (blue line) Brewster windows by scanning the 800 nm probe pulse relative to the THz pulse. In these two experiments, the amount of light at the two photodiodes of the balanced detection was kept the same with the help of additional attenuators in front of the balanced detection, which compensated the effect of the Brewster windows in the measurement without them. Comparing both measurements, we obtain an enhancement factor of ≈18 (Fig. 2, blue dots).

III. DISCUSSION

To describe the polarization states at the various positions in the setup, we use the Jones matrix formalism. We start from

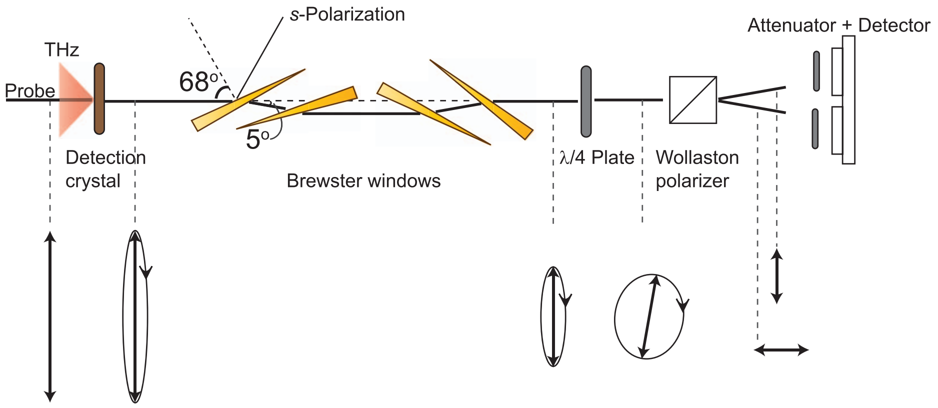

FIG. 1. Electro-optical sampling setup with four Brewster windows in order to increase the ellipticity of the probe beam. The bottom row shows the polarization states at various positions along the beam path.

linearly s-polarized probe light:

$$p_{in} = \begin{pmatrix} 1 \\ 0 \end{pmatrix}. \tag{1}$$

The detection crystal acts as a phase retarder with small retardation ϕ, that is proportional to the THz field:

$$C = \frac{1}{2}\begin{pmatrix} e^{i\phi} + e^{-i\phi} & e^{i\phi} - e^{-i\phi} \\ e^{i\phi} - e^{-i\phi} & e^{i\phi} + e^{-i\phi} \end{pmatrix}. \tag{2}$$

The Brewster windows reduce the s-polarization component by a field attenuation factor a while it fully transmits the p-polarization component:

$$B = \begin{pmatrix} a & 0 \\ 0 & 1 \end{pmatrix}, \tag{3}$$

and the quarter-wave plate is described as

$$Q = \frac{1}{\sqrt{2}}\begin{pmatrix} 1 & i \\ i & 1 \end{pmatrix}. \tag{4}$$

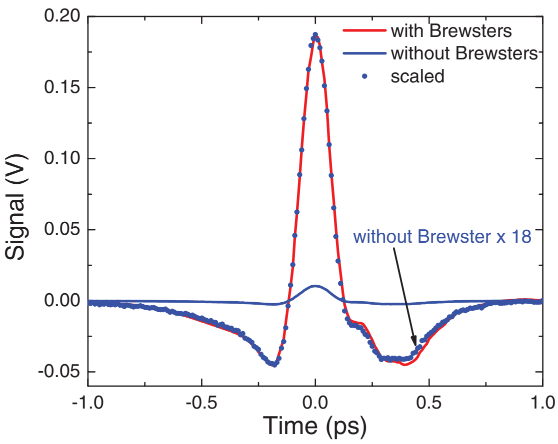

FIG. 2. THz pulses measured with (red) and without (blue) Brewster windows. The amount of light at the two photodiodes of the balanced detection was the same in both measurements. The blue line shows the raw data without Brewster windows, the blue dots the data up-scaled by a factor 18.

The final polarization state thus becomes

$$p = Q.B.C.p_{in} = \frac{1}{\sqrt{2}}\begin{pmatrix} a\cos\phi - \sin\phi \\ i(a\cos\phi + \sin\phi) \end{pmatrix}. \tag{5}$$

The balance detection measures the difference in intensity of the s- and p-polarization components, which we normalize to the total amount of light on the two detectors:

$$S = \frac{|p_s|^2 - |p_p|^2}{|p_s|^2 + |p_p|^2} \approx \frac{2\phi}{a}, \tag{6}$$

where the last step is valid for $\phi \ll a$. We see that the relative signal is enhanced by a factor $1/a = 1/\sqrt{t}$ (where t is the corresponding intensity attenuation factor). For the concrete situation in our experiment, we would expect an enhancement factor of ≈20; slightly higher than the experimental value of ≈18. We attribute the small deviation from the theoretical value to the fact that we do not hit all surfaces of the Brewster windows with perfectly the Brewster angle due small to misalignments and the wedges of the Brewster windows.

With the choice of the window material and the number of Brewster windows, one can adjust the enhancement factor. Four ZnSe windows turned out to be a good compromise between enhancement factor on the one hand, and the available probe pulse energies in connection with the saturation limit of the photo diodes on the other hand. The maximum enhancement factor is also limited by the condition $\phi \ll a$ (Eq. (6)); if a is set too small, the signal no longer scales linearly with THz-field. In the limit of $a = 0$, when only the p-polarization component is transmitted, one could in fact no longer distinguish the signs of the THz field and only the absolute-square of the THz field would be detected.

One may think of the sequence of Brewster windows as a polarizer with an extinction ratio of 1:2.4×10^{-3}. Before implementing these Brewster windows, we tested a combination of two film-polarizers with a comparable extinction ratio of 1:10^{-3} (other types of polarizers tend to have a too large extinction ratio). However, the enhancement factor was only ≈6, significantly smaller than the theoretical value $1/\sqrt{t}$, presumably since the small amount of transmitted s-polarization is no longer in a clean polarization state afterwards.

In conclusion, we have introduced and discussed a simple scheme that significantly enhances the detectivity of THz electro-optical sampling. The scheme is particularly useful when very small THz fields are to be measured in connection with low-repetition rate amplified Ti:S laser systems. For example, the 2D-Raman-THZ experiments of Ref. 24 would not have been possible without that enhancement of the THz detectivity.

ACKNOWLEDGMENTS

The work has been supported by the Swiss National Science Foundation (SNF) through the NCCR MUST.

[1] B. Ferguson and X. C. Zhang, Nat. Mater. **1**, 26 (2002).
[2] K. Reimann, Rep. Prog. Phys. **70**, 1597 (2007).
[3] J. Faure, J. van Tilborg, R. A. Kaindl, and W. P. Leemans, Opt. Quantum Electron. **36**, 681 (2004).
[4] Y.-S. Lee, *Principles of Terahertz Science and Technology* (Springer, 2010).
[5] E. Pickwell and V. P. Wallace, J. Phys. D: Appl. Phys. **02**, R301 (2009).
[6] D. M. Mittleman, R. H. Jacobsen, and M. C. Nuss, IEEE J. Sel. Top. Quantum Electron **2**(3), 679 (1996).
[7] K. J. Siebert, T. Loffler, H. Quast, M. Thomson, T. Bauer, R. Leonhardt, S. Czasch, and H. G. Roskos, Phys. Med. Biol. **47**, 3743 (2002).
[8] H. Zhong, A. Redo-Sanchez, and X.-C. Zhang, Int. J. High Speed Electron. Syst. **17**, 239 (2007).
[9] M. Theuer, S. S. Harsha, D. Molter, G. Torosyan, and R. Beigang, ChemPhysChem **12**, 2695 (2011).
[10] C. A. Schmuttenmaer, Chem. Rev. **104**, 1759 (2004).
[11] P. U. Jepsen, W. Schairer, I. H. Libon, U. Lemmer, N. Hecker, M. Birkholz, K. Lips, and M. Schall, Appl. Phys. Lett. **79**, 1291 (2001).
[12] T. Kampfrath, L. Perfetti, F. Schapper, C. Frischkorn, and M. Wolf, Phys. Rev. Lett. **95**, 187403 (2005).
[13] J. Zielbauer and M. Wegener, Appl. Phys. Lett. **68**, 1223 (1996).
[14] M. C. Nuss, D. H. Auston, and F. Capasso, Phys. Rev. Lett. **58**, 2355 (1987).
[15] B. N. Flanders, D. C. Arnett, and N. F. Scherer, IEEE J. Sel. Top. Quantum Electron **4**, 353 (1998).
[16] H. Němec, K. Kadlec, and P. Kužel, J. Chem. Phys. **117**, 8454 (2002).
[17] E. Knoesel, M. Bonn, J. Shan, F. Wang, and T. F. Heinz, J. Chem. Phys. **121**, 394 (2004).
[18] P. A. George, J. Strait, J. Dawlaty, S. Shivaraman, M. Chandrashekhar, F. Rana, and M. G. Spencer, Nano Lett. **8**, 4248 (2008).
[19] M. Breusing, C. Ropers, and T. Elsaesser, Phys. Rev. Lett. **102**, 086809 (2009).
[20] D. Polli, M. Rini, S. Wall, R. W. Schoenlein, Y. Tomioka, Y. Tokura, G. Cerullo, and A. Cavalleri, Nat. Mater. **6**, 643 (2007).
[21] K. W. Kim, A. Pashkin, H. Schaefer, M. Beyer, M. Porer, T. Wolf, C. Bernhard, J. Demsar, R. Huber, and A. Leitenstorfer, Nat. Mater. **11**, 497 (2012).
[22] G. Haran, W. D. Sun, K. Wynne, and R. M. Hochstrasser, Chem. Phys. Lett. **274**, 365 (1997).
[23] R. McElroy and K. Wynne, Phys. Rev. Lett. **79**, 3078 (1997).
[24] J. Savolainen, S. Ahmed, and P. Hamm, Proc. Natl. Acad. Sci. U.S.A. **110**, 20402 (2013).

A.2 The effect of the Gouy phase in optical-pump-THz-probe spectroscopy

Reprinted from ref. [61], with the permission of OSA Publishing Group.

A.2.1 Contribution to this paper

- Saima Ahmed performed the experiments with Dr. Janne Savolainen.
- Saima Ahmed analysed the experimental data.

The effect of the Gouy phase in optical-pump-THz-probe spectroscopy

Saima Ahmed, Janne Savolainen, and Peter Hamm[*]

Department of Chemistry, University of Zürich, Winterthurerstrasse 190, 8057 Zurich, Switzerland

[*]phamm@pci.uzh.ch

Abstract: We show theoretically as well as experimentally that the Gouy-phase shift, which depends on the exact positioning of a sample in relation to the focus of a probe beam in a pump-probe experiment, may have a pronounced effect on the shape of the pump-probe signal. The effect occurs only when single-cycle probe pulses are used, i.e. when the slowly varying envelope approximation breaks down, while it disappears for multi-cycle pulses. The effect is thus most relevant in THz time-resolved spectroscopy, where such single cycle pulses are most commonly used, but it should not be overlooked also in other spectral regimes when correspondingly short pulses are involved.

OCIS codes: (190.7110) Ultrafast nonlinear optics; (300.6270) Spectroscopy, far infrared; (300.6420) Spectroscopy, nonlinear; (350.5030) Phase.

References and links

1. B. Ferguson and X. C. Zhang, "Materials for terahertz science and technology," Nat. Mater. **1**, 26–33 (2002).
2. K. Reimann, "Table-top sources of ultrafast THz pulses," Rep. Prog. Phys. **70**, 1597–1632 (2007).
3. J. Faure, J. van Tilborg, R. A. Kaindl, and W. P. Leemans, "Modelling laser based table-top THz sources: Optical rectification, propagation and electro-optic sampling," Opt. Quantum Electron. **36**, 681–697 (2004).
4. Y.-S. Lee, *Principles of Terahertz Science and Technology* (Springer, 2010).
5. M. Theuer, S. S. Harsha, D. Molter, G. Torosyan, and R. Beigang, "Terahertz time-domain spectroscopy of gases, liquids, and solids," Chemphyschem **12**, 2695–2705 (2011).
6. C. A. Schmuttenmaer, "Exploring dynamics in the far-infrared with terahertz spectroscopy," Chem. Rev. **104**, 1759–1779 (2004).
7. E. Pickwell and V. P. Wallace., "Biomedical applications of terahertz technology," J. Phys. D Appl. Phys. **02**, R301 (2009).
8. D. M. Mittleman, R. H. Jacobsen, and M. C. Nuss, "T-ray imaging," IEEE J. Sel. Top. Quantum Electron. **2**(3), 679–692 (1996).
9. K. J. Siebert, T. Loffler, H. Quast, M. Thomson, T. Bauer, R. Leonhardt, S. Czasch, and H. G. Roskos, "All-optoelectronic continuous wave THz imaging for biomedical applications," Phys. Med. Biol. **47**, 3743–3748 (2002).
10. J. Zielbauer and M. Wegener, "Ultrafast optical pump THz-probe spectroscopy on silicon," Appl. Phys. Lett. **68**, 1223 (1996).
11. M. C. Nuss, D. H. Auston, and F. Capasso, "Direct subpicosecond measurement of carrier mobility of photoexcited electrons in gallium arsenide," Phys. Rev. Lett. **58**, 2355–2358 (1987).
12. B. N. Flanders, D. C. Arnett, and N. F. Scherer, "Optical pump-terahertz probe spectroscopy utilizing a cavity-dumped oscillator- driven terahertz spectrometer," IEEE J. Sel. Top. Quantum Electron. **4**, 353–359 (1998).
13. H. Němec, F. Kadlec, and P. Kužel, "Methodology of an optical pump-terahetz probe experiment: An analytical frequency domain approach," J. Chem. Phys. **117**, 8454 (2002).
14. E. Knoesel, M. Bonn, J. Shan, F. Wang, and T. F. Heinz, "Conductivity of solvated electrons in hexane investigated with terahertz time-domain spectroscopy," J. Chem. Phys. **121**, 394–404 (2004).
15. P. A. George, J. Strait, J. Dawlaty, S. Shivaraman, M. Chandrashekhar, F. Rana, and M. G. Spencer, "Ultrafast optical-pump terahertz-probe spectroscopy of the carrier relaxation and recombination dynamics in epitaxial graphene," Nano Lett. **8**, 4248–4251 (2008).

#201608 - $15.00 USD Received 19 Nov 2013; revised 10 Feb 2014; accepted 11 Feb 2014; published 18 Feb 2014

16. M. Breusing, C. Ropers, and T. Elsaesser, “Ultrafast carrier dynamics in graphite,” Phys. Rev. Lett. **102**, 086809 (2009).
17. P. U. Jepsen, W. Schairer, I. H. Libon, U. Lemmer, N. Hecker, M. Birkholz, K. Lips, and M. Schall, “Ultrafast carrier trapping in microcrystalline silicon observed in optical pumpterahertz probe measurements,” Appl. Phys. Lett. **79**, 1291 (2001).
18. T. Kampfrath, L. Perfetti, F. Schapper, C. Frischkorn, and M. Wolf, “Strongly coupled optical phonons in the ultrafast dynamics of the electronic energy and current relaxation in graphite,” Phys. Rev. Lett. **95**, 187403 (2005).
19. D. Polli, M. Rini, S. Wall, R. W. Schoenlein, Y. Tomioka, Y. Tokura, G. Cerullo, and A. Cavalleri, “Coherent orbital waves in the photo-induced insulator-metal dynamics of a magnetoresistive manganite,” Nat. Mater. **6**, 643–647 (2007).
20. K. W. Kim, A. Pashkin, H. Schaefer, M. Beyer, M. Porer, T. Wolf, C. Bernhard, J. Demsar, R. Huber, and A. Leitenstorfer, “Ultrafast transient generation of spin-density-wave order in the normal state of bafe2as2 driven by coherent lattice vibrations,” Nat. Mater. **11**, 497–501 (2012).
21. G. Haran, W. D. Sun, K. Wynne, and R. M. Hochstrasser, “Femtosecond far-infrared pump-probe spectroscopy: a new tool for studying low-frequency vibrational dynamics in molecular condensed phases,” Chem. Phys. Lett. **274**, 365–371 (1997).
22. R. McElroy and K. Wynne, “Ultrafast dipole solvation measured in the far infrared,” Phys. Rev. Lett. **79**, 3078–3081 (1997).
23. D. You and P. H. Bucksbaum, “Propagation of half-cycle far infrared pulses,” J. Opt. Soc. Am. B **14**, 1651–1655 (1997).
24. C. R. Gouy, “Sur une propriete nouvelle des ondes lumineuses,” Acad. Sci. Paris **110**, 1251 (1890).
25. S. Feng, H. G. Winful, and R. W. Hellwarth, “Gouy shift and tempral reshaping of focused single-cycle electromagnetic pulses,” Opt. Lett. **23**, 385–387 (1998).
26. P. Kužel, M. A. Khazan, and J. Kroupa, “Spatiotemporal transformations of ultrashort terahertz pulses,” J. Opt. Soc. Am. B **16**, 1795–1800 (1999).
27. A. B. Ruffin, J. V. Rudd, J. F. Whitaker, S. Feng, and H. G. Winful, “Direct observation of the Gouy physe shift with single-cycle terahertz pulses,” Phys. Rev. Lett. **83**, 3410–3413 (1999).
28. T. Feurer, N. S. Stoyanov, D. W. Ward, and K. A. Nelson, “Direct visualization of the Gouy physe by focusing phonon polaritons,” Phys. Rev. Lett. **88**, 257402 (2002).
29. T. Tritschler, K. D. Hof, M. W. Klein, and M. Wegener, “Variation of the carrier-envelope phase of few-cycle laser pulses owing to the Gouy phase: a solid-state-based measurement,” Opt. Lett. **30**, 753–755 (2005).
30. L. Zhang, H. Zhong, K. Mu, C. Zhang, and Y. Zhao, “Phase characterization in broadband THz wave detection through field-induced second harmonic generation,” Opt. Express **20**, 75–80 (2012).
31. R. W. Boyd, *Nonlinear Optics* (Academic, 1992).
32. N. Lastzka and R. Schnabel, “The Gouy phase shift in nonlinear interactions of waves,” Opt. Express **15**, 7211–7217 (2007).
33. C.-Y. Chung, J. Hsu, S. Mukamel, and E. O. Potma, “Controlling stimulated coherent spectroscopy and microscopy by a position-dependent phase,” Phys. Rev. A **87**, 033833 (2013).
34. J. T. Kindt and C. A. Schmuttenmaer, “Theory for determination of the low-frequency time-dependent response function in liquids using time-resolved terahertz pulse spectroscopy,” J. Chem. Phys. **110**, 8589 (1999).
35. P. Kužel, H. Němec, and F. Kadlec, “Propagation of THz pulses in photoexcited media: Analytical theory for layered systems,” J. Chem. Phys. **127**, 024506 (2007).
36. P. Kužel, H. Němec, F. Kadlec, and C. Kadlec, “Gouy shift correction for highly accurate refractive index retrieval in time-domain terahertz spectroscopy,” Opt. Express **18**, 15338–15348 (2010).
37. J. Savolainen, S. Ahmed, and P. Hamm, “2D Raman-Thz spectroscopy of water,” Proc. Natl. Acad. Sci. U. S. A. **110**, 20402–20407 (2013).
38. P. Hamm and J. Savolainen, “2D-Raman-THz spectroscopy of water: Theory,” J. Chem. Phys. **136**, 094516 (2012).
39. F. Krausz and M. Ivanov, “Attosecond physics,” Rev. Mod. Phys. **81**, 163–234 (2009).
40. L. Gallmann, J. Herrmann, R. Locher, M. Sabbar, A. Ludwig, M. Lucchini, and U. Keller, “Resolving intraatomic electron dynamics with attosecond transient absorption spectroscopy,” Molecular Physics, in press, DOI:10.1080/00268976.2013.799298 (2013).
41. N. Shivaram, A. Roberts, L. Xu, and A. Sandhu, “In situ spatial mapping of Gouy phase slip for high-detail attosecond pumpprobe measurements,” Opt. Lett. **35**, 3312–3314 (2010).
42. G. Cerullo, M. Nisoli, S. Stagira, and S. D. Silvestri, “Sub-8-fs pulses from an ultrabroadband optical parametric amplifier in the visible,” Opt. Lett. **23**, 1283-1285 (1998).
43. D. Herrmann, C. Homann, R. Tautz, M. Scharrer, P. S. J. Russell, F. Krausz, L. Veisz, and E. Riedle, “Approaching the full octave: Noncollinear optical parametric chirped pulse amplification with two-color pumping,” Opt. Express **18**, 18752–18762 (2010).
44. T. Kobayashi, J. Liu, and K. Okamura, “Applications of parametric processes to high-quality multicolour ultrashort pulses, pulse cleaning and cep stable sub-3fs pulse,” J. Phys. B At. Mol. Opt. Phys. **45**, 074005 (2012).

#201608 - $15.00 USD Received 19 Nov 2013; revised 10 Feb 2014; accepted 11 Feb 2014; published 18 Feb 2014

45. P. B. Petersen and A. Tokmakoff, “Source for ultrafast continuum infrared and terahertz radiation,” Opt. Lett. **35**, 1962–1964 (2010).
46. M. Cheng, A. Reynolds, H. Widgren, and M. Khalil, “Generation of tunable octave-spanning mid-infrared pulses by filamentation in gas media,” Opt. Lett. **37**, 1787–1789 (2012).

---

1. Introduction

Over the last two decades, there has been a tremendous development in THz technology [1–4] in different areas of science in both spectroscopy [5, 6] and imaging [7–9]. Optical pump-THz-probe spectroscopy has been widely applied to study e.g. the ultrafast carrier dynamics in various materials [10–16], phonon dynamics [17,18] and other excitations in strongly correlated materials [19,20], as well as low frequency vibrational dynamics in molecular liquids [6,21,22].

Short THz pulses change spatially and temporally as they propagate through a measurement setup [23]. One such important process is the Gouy phase shift [24, 25]. That is, when a laser pulse travels through a focus, it experiences a phase shift from $+\pi/2$ before the focus, 0 in the focus, and $-\pi/2$ after the focus, and in fact THz pulses have been used elegantly to visualize the effect [26–30]. It is widely recognized that the Gouy phase shift may play a role in nonlinear optics [31, 32] as well as in nonlinear spectroscopy, e.g. when phase-sensitive heterodyning is applied [33]. In the present paper, we demonstrate that the Gouy phase shift can also have a pronounced effect on the outcome of optical pump-THz-probe experiments. Despite the fact that many such experiments have been performed in the past [10–22], we are not aware of any discussion of that effect.

We consider a prototype optical-pump-THZ-probe experiment as schematically shown in Fig. 1. A short THz pulse is generated by optical rectification in a non-linear crystal, imaged by some imaging optics onto the sample, where it is overlapped with an optical pump-pulse, and the generated 3rd-order field $E^{(3)}(t)$ is imaged onto the detection crystal. The nonlinear interaction in the sample can be describe by the usual convolution of the laser pulses with a system response function $R(t_1,t_2)$:

$$P^{(3)}(t) \propto \int_0^\infty \int_0^\infty E_{THz}(t-t_2) I_{pu}(t-t_1) R(t_1,t_2) dt_1 dt_2 \qquad (1)$$

with $I_{pu}(t) = |E_{pu}(t)|^2$ the intensity profile of the pump pulse. Deducing the system response function $R(t_1,t_2)$, which is ultimately what we want to measure, effectively requires a deconvolution of the measured field [13, 34, 35], which in turns requires that we very accurately know the THz pulse $E_{THz}(t)$ at the sample position including its phase. This is where the Gouy phase shift comes into play.

In a idealized realization of Fig. 1, the Gouy phase shift would not matter since both generation and detection crystal as well as the sample are in the focus of the imaging optics and typically are thin, so the Gouy phase is the same apart from alternating minus signs in all three positions. However, since one wants to achieve high intensities of the pump-light in the sample to explore its pump-probe response, the THz pulse is often imaged with high-aperture optics to achieve a small focus. The Gouy phase changes on a scale that equals the Rayleigh length, which in turns is of the order of the wavelength of the THz light if the aperture approaches 1. Consequently, the positioning of the crystals and the sample is critical within a few 100 μm for a typical THz experiment. While the alignment of the crystals can easily be checked by measuring the Gouy phase of the THz pulse itself (which also enters the detection crystal), the exact positioning of the sample in between is less easy to determine.

One is tempted to assume that the exact positioning of the sample does not matter, since a “wrong” Gouy phase in $E_{THz}(t)$ is compensated by the corresponding Gouy phase that the emitted field accumulates on its way from the sample to the detection crystal. Although the

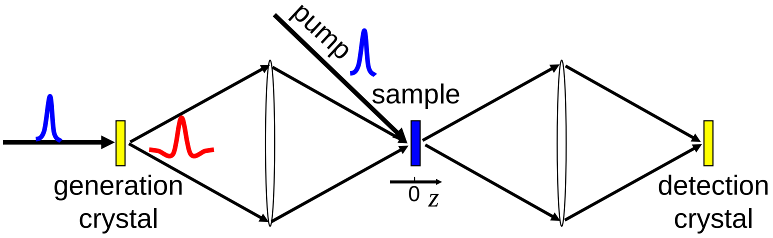

Fig. 1. Scheme of a optical-pump-THz-probe experiment. The displacement z is measured relative to the middle focus.

Gouy phase is a propagation effect, whose explanation requires the solution of the 3D Maxwell equations, it can be described by adding a phase ϕ to a propagating field in a 1D description. Hence, one might think that one can add a phase factor $e^{i\phi}$ to the input THz pulse in Eq. (1)

$$e^{i\phi}P^{(3)}(t) \propto \int_0^\infty \int_0^\infty e^{i\phi} E_{THz}(t-t_2) I_{pu}(t-t_1) R(t_1,t_2) dt_1 dt_2 \tag{2}$$

which of course can be pulled in front of the integral, and hence would cancel with a compensating phase $e^{-i\phi}$ for the emitted field. However, physical electric fields are real-valued. Using complex electric fields is a mathematical trick that simplifies many calculations, but is rigorously correct only as long as linear optics is considered. Despite the fact that the THz field $E_{THz}(t)$ enters in Eq. (1) in a linear fashion, the operation as a whole is nonlinear, which can be seen from the fact that the multiplication with a potentially much shorter pump-pulse $I_{pu}(t)$ can generate new frequency components in $P^{(3)}(t)$. Adding a phase factor in Eq. (2) inevitably results in a complex field which can be done only in certain limits.

For very short pulses, it is no longer meaningful to write them as an envelope times a carrier frequency:

$$E(t) = E_0(t)\cos(\omega_0 t) \tag{3}$$

which can be seen for example from the fact that such a pulse would have a non-vanishing amplitude at zero frequency (i.e. a DC component, which it cannot have in the far-field) whenever the time duration of $E_0(t)$ gets in the same order of magnitude as $1/\omega_0$. Consequently, one can also not introduce a phase by simply writing:

$$E(t) = E_0(t)\cos(\omega_0 t + \phi) \tag{4}$$

Alternatively, one may use a close analog of the Hilbert transformation to do so (while the common definition of the Hilbert transformation transforms a real field into its imaginary counterpart $\Re E(t) \to \Im E(t)$, we consider here the transformation of the real field into the complex field $\Re E(t) \to \Re E(t) + i\Im E(t)$). That is, the field is Fourier-transformed into the frequency domain, the negative frequencies are zeroed, and the field is Fourier-transformed back into the time-domain, which will result in a complex-valued representation of the field (in the following we will use a tilde to indicate a field is complex). The phase factor may then be added and the real part be taken:

$$E(t) \xrightarrow{FT} E(\omega) \to \Theta(\omega)E(\omega) \xrightarrow{FT^{-1}} \tilde{E}(t) \to \Re(e^{i\phi}\tilde{E}(t)) \tag{5}$$

where $\Theta(\omega)$ is the Heaviside step function. Not that this sequence of operations is not equivalent to Eq. (4), if the slowing varying envelope approximations doesn't apply.

#201608 - $15.00 USD Received 19 Nov 2013; revised 10 Feb 2014; accepted 11 Feb 2014; published 18 Feb 2014

The operations Eq. (1) and Eq. (5) do not commute. If they would commute, then one could first transform $E_{THz}(t)$ into a complex field $\tilde{E}_{THz}(t)$, plug it into Eq. (1) including the phase factor $e^{i\phi}$, add a phase factor $e^{-i\phi}$ to the generated 3-order polarization $\tilde{P}^{(3)}(t)$ in order to describe the compensating Gouy-phase, which then would cancel:

$$E_{THz}(t) \to e^{i\phi}\tilde{E}_{THz}(t) \xrightarrow{Eq.(1)} e^{i\phi}\tilde{P}^{(3)}(t) \to e^{-i\phi}e^{i\phi}\tilde{P}^{(3)}(t) \to \Re(\tilde{P}^{(3)}(t)) \tag{6}$$

The correct treatment of the problem first transforms $E_{THz}(t)$ into a complex field $\tilde{E}_{THz}(t)$, adds a phase factor, but then plugs only the real part $\Re(e^{i\phi}\tilde{E}_{THz}(t))$ into Eq. (1), and finally repeats the compensating phase shift for $P^{(3)}(t)$:

$$E_{THz}(t) \to Re(e^{i\phi}\tilde{E}_{THz}(t)) \xrightarrow{Eq.(1)} P^{(3)}(t) \to e^{-i\phi}\tilde{P}^{(3)}(t) \to \Re(e^{-i\phi}\tilde{P}^{(3)}(t)) \tag{7}$$

Both lines of operations do not necessarily reveal the same result.

It is instructive to see in the next section why and how a "wrong" Gouy phase is indeed compensated in linear response. We will furthermore show that a Gouy phase is still compensated also in a pump-probe response as long as multi-cycle pulses are used, which is why this problem is not relevant for most applications of femtosecond spectroscopy. However, in THz pump-probe spectroscopy, where single-cycle pulses are most common, the Gouy-phase has to be taken into account for a quantitative interpretation of the data. To that end, we will show both theoretically and experimentally that the outcome of a optical-pump-THz-probe experiment does in fact depend on the exact position of the sample relative to the focus.

2. Linear response

In the most simple approximation, linear response is described as:

$$P^{(1)}(t) \propto \int_0^\infty E_{THz}(t-t_1)R(t_1)dt_1 \tag{8}$$

As the integral is a convolution of 1D functions, the convolution theorem applies and it is advantageous to treat the problem in frequency domain:

$$\tilde{P}^{(1)}(\omega) \propto \tilde{E}_{THz}(\omega)\tilde{R}(\omega) \tag{9}$$

where $\tilde{E}(\omega)$ and $\tilde{R}(\omega)$ are the Fourier transformations of the corresponding functions in Eq. (8). Along the lines of Eq. (5), the negative frequencies are then zeroed:

$$\tilde{P}^{(1)}(\omega) \propto \Theta(\omega)\tilde{E}_{THz}(\omega)\tilde{R}(\omega) \tag{10}$$

All operations in Eq. (10) are simple products in frequency domain that of course do commute, and hence they will also commute in the time domain. Consequently, the equivalents of Eqs. (6) and (7) do indeed reveal the same results and a Gouy phase in the input field will be compensated by that of the emitted field, so the measured linear response does of course *not* depend on the exact positioning of the sample in the focus in Fig. 1.

It should however be added that when including the fact that a THz pulse undergoes multiple reflections at the sample surfaces, then different terms with changing Gouy phases add up (an effect that goes beyond Eq. (8)) and the Gouy phase has in fact a subtle effect even on the linear response [36]. This is yet another effect of the Gouy phase on spectroscopy that is however distinctively different from the one discussed here.

#201608 - $15.00 USD Received 19 Nov 2013; revised 10 Feb 2014; accepted 11 Feb 2014; published 18 Feb 2014

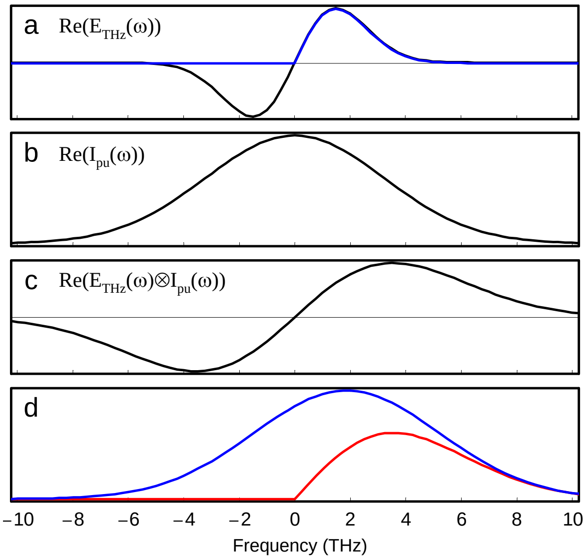

Fig. 2. (a) Spectrum of the THz pulse $\tilde{E}_{THz}(\omega)$ (Eq. (14), black) and with negative frequencies zeroed (blue). (b) Fourier transformation of the pump pulse intensity profile $\tilde{I}_{pu}(\omega)$ (Eq. (15)). (c) Convolution $\tilde{E}_{THz}(\omega) \otimes \tilde{I}_{pu}(\omega)$ and (d) convolution with zeroing negative frequencies of the THz pulse $\tilde{E}_{THz}(\omega)$ before the convolution (blue) and after the convolution (red). The pump-probe delay between the center of both pulses was set to $t_{pp} = 0$.

3. Pump-probe response

To simplify matters, we first consider a system response function that is faster than any other timescale of the system (e.g. a polarisibility that is exclusively electronic), so that it can be approximated as a δ-function:

$$R(t_1, t_2) = \delta(t_1)\delta(t_2) \tag{11}$$

In this case, Eq. (1) reduces to:

$$P^{(3)}(t) \propto E_{THz}(t) I_{pu}(t), \tag{12}$$

It is a simple product in time domain, so it will be a convolution in frequency domain:

$$\tilde{P}^{(3)}(\omega) \propto \tilde{E}_{THz}(\omega) \otimes \tilde{I}_{pu}(\omega). \tag{13}$$

Note that here $\tilde{I}_{pu}(\omega)$ is the Fourier transformation of the intensity profile of the pump pulse, and not that of its field, and thus it is centered around $\omega = 0$. Figure 2 shows the result of that convolution for a typical situation in a THz pump-probe experiment. To that end, we assumed a half-cycle THz pulse (see Fig. 3, top-middle panel):

$$E_{THz}(t) \propto \Re \int_0^\infty \omega e^{-\tau_1^2 \omega^2 / 4} e^{i\omega t} d\omega \tag{14}$$

where $\tau_1 = 150$ fs is a measure of the pulse duration (the pulse is constructed as the time-derivative of a generating Gaussian pulse together with a $\pi/2$ phase shift). For the pump pulse,

#201608 - $15.00 USD Received 19 Nov 2013; revised 10 Feb 2014; accepted 11 Feb 2014; published 18 Feb 2014

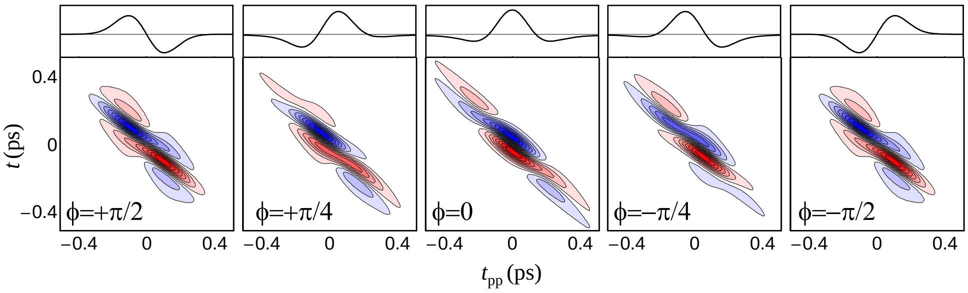

Fig. 3. Outcome of a hypothetical pump probe experiment of a sample with infinitesimally fast response function as a function of THz detection time t, pump-probe delay time t_{pp} between the center of both pulses, and the Gouy-phase error of the sample. Red and blue depict positive and negative fields, respectively. The top panels show the corresponding input THz pulse $E_{THz}(t)$.

we assumed a Gaussian pulse:

$$I_{pu}(t) \propto e^{-t^2/\tau_2^2} \tag{15}$$

with τ_2=70 fs. Figure 2(a), black, shows the spectrum of the resulting THz pulse $\tilde{E}_{THz}(\omega)$, Fig. 2(b) that of the pump pulse intensity profile $\tilde{I}_{pu}(\omega)$ and Fig. 2(c) the convolution Eq. (13). Applying the Hilbert transformation after the convolution, which simply zeros the negative frequencies (Fig. 2(d), red), obviously gives a different result as compared to applying the Hilbert transformation before the convolution. The latter is shown in Fig. 2(d), blue line, which results from the convolution of the blue line in Fig. 2(a) with Fig. 2(b). In other words, the Hilbert transformation and the nonlinear interaction in Eq. (1) do not commute:

$$\Theta(\omega)\left(\tilde{E}_{THz}(\omega)\otimes\tilde{I}_{pu}(\omega)\right) \neq \left(\Theta(\omega)\tilde{E}_{THz}(\omega)\right)\otimes\tilde{I}_{pu}(\omega) \tag{16}$$

Figure 3 shows the effect of a Gouy phase for a hypothetical pump probe experiment of a sample with infinitesimally fast response function (Eq. (11)), using Eqs. (12), (14) and (15) together with

$$E^{(3)}(t) \propto \frac{dP^{(3)}(t)}{dt} \tag{17}$$

which connects the emitted 3rd-order field to the 3rd-order polarization in the most simple case when dispersion and absorption can be neglected and the process is quasi-phasematched [13, 34, 35]. In addition, a Gouy phase ϕ is added along the lines of Eq. (7). These plots can be considered to be the instrument response of such an experiment. Identical responses are obtained for Gouy phases $\phi = +\pi/2$ and $\phi = -\pi/2$, which however clearly differs from that for $\phi = 0$. It should be noted that the effects are the stronger the shorter the pump pulse duration is compared to the THz pulse duration.

If, on the other hand, we write the probe pulse as a carrier wave times a pulse envelope:

$$E_{THz}(t) = \cos(\omega_0 t)e^{-t^2/\tau_1^2} \tag{18}$$

with $\omega_0 = 20$ THz (and leave the pump pulse as in Eq. (15)), the situation shown in Fig. 4 is obtained. In this case, the positive frequency and negative frequency contribution of $\tilde{E}_{THz}(\omega)$

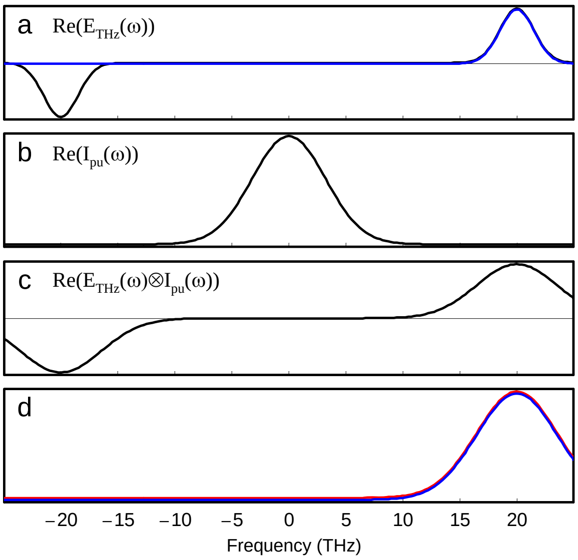

Fig. 4. Same as in Fig. 2, but for a THz pulse according to Eq. (18). The red line in (d) has been offset a little bit to make it visible.

do not overlap with $\tilde{I}_{pu}(\omega)$, which is centered around $\omega = 0$, and Hilbert transformation and the nonlinear interaction in Eq. (1) do commute to a very good approximation (compare red and blue line in Fig. 4(d), which is hardly different):

$$\Theta(\omega)\left(\tilde{E}_{THz}(\omega)\otimes\tilde{I}_{pu}(\omega)\right) \approx \left(\Theta(\omega)\tilde{E}_{THz}(\omega)\right)\otimes\tilde{I}_{pu}(\omega) \qquad (19)$$

In this case, a Gouy phase in the input field will be compensated by that of an outgoing field since Eq. (6) would be correct. We see that it is the spectrum of a typical THz pulse that covers all frequencies down to zero, or in other words, the break-down of the slowly varying envelope approximation, that makes the difference to “normal” femtosecond spectroscopy.

Finally, we consider a general response function that is not necessarily infinitesimally fast. To that end, we start with an auxiliary function

$$P'(t',t'') \propto \int_0^\infty \int_0^\infty E_{THz}(t''-t_2)I_{pu}(t'-t_1)R(t_1,t_2)dt_1dt_2 \qquad (20)$$

which is in fact a 2D convolution of the response function with the laser pulses. Hence, we again can switch to the frequency domain

$$\tilde{P}'(\omega',\omega'') \propto \tilde{E}_{THz}(\omega'')\tilde{I}_{pu}(\omega')\tilde{R}(\omega',\omega'') \qquad (21)$$

The fact that we need to evaluate $P'(t',t'')$ only for $t' = t''$, $P(t) = P'(t,t)$, is equivalent to

$$\tilde{P}(\omega) \propto \int_{-\infty}^{\infty} \tilde{P}'(\omega',\omega-\omega')d\omega' \qquad (22)$$

in the frequency domain. This expression is tedious to visualize, but in essence the argument of Fig. 2 *versus* Fig. 4 remains.

#201608 - $15.00 USD Received 19 Nov 2013; revised 10 Feb 2014; accepted 11 Feb 2014; published 18 Feb 2014

4. Experimental verification

To demonstrate the effect of the Gouy phase on the outcome of a concrete pump-probe experiment, we use the Raman-pump-THz probe response of water as an illustrative example. The relevance of such an experiment for water structure and dynamics has been explored in detail in a separate publication [37]. To give a brief motivation of that experiment, a first Raman interaction induced by a 800 nm pulse excites a coherence in low-frequency intermolecular modes of the hydrogen-bonded water network that is switched into another coherence by the subsequent THz pulse and finally read out by the emission of a THz field. The experiment has been termed 2D-Raman-THZ-probe spectroscopy, as it allows one to measure correlations among the various degrees of freedom of water, and indeed, a very short lived THz photon-echo has been observed. In Ref. [37] a full 2D data set in analogy to Fig. 3 has been measured, while we show here only 1D scans along the pump-probe delay time t_{pp} with the detection time t kept fixed to the position where the signal is maximal.

The experiment was performed with a optical-pump-THz-probe setup that is similar to many such implementations described in the literature [10–22], and that is introduced in detail in Ref. [37]. In brief, a half-cycled THz pulse was generated in a 100 μm GaP [110] crystal by optical rectification [3, 4] and was imaged by a single home-machined elliptical mirror ($2f$=83 mm) onto a 40 μm thick water jet, which was pumped by an intense 800 nm pulse through a non-resonant Raman process. Due to the high-aperture of the elliptical mirror ($A \approx 1$), the THz pulse could be focused in a transform-limited manner onto a spot of diameter ≈ 240 μm. The generated 3rd-order field was imaged by another elliptical mirror onto a second GaP crystal for electro-optical sampling. The beam size of the Raman-pump pulse (diameter 300 μm) was adjusted to match that of the THz pulse in the focus. Due to its much shorter wavelength, the beam size can be considered to be essentially constant in the range around the focus which is relevant for the present discussion. Alternatively, the detection crystal was put at the sample position to measure the input THz field $E_{THz}(t)$ directly. In that case, the positioning of the detection crystal relative to the water jet was measured with the help of a confocal chromatic measurement sensor (ConfocalDT, micro-epsilon) that provides a few micrometers resolution.

Figure 5, top row, shows the input THz pulse at various positions relative to the focus from z=-500 μm to z=500 μm, where we assumed the focus z=0 μm to be the position where the pulse is symmetric (the displacement z is defined in Fig. 1). As we move away from the focus in both directions, the phase of the THz pulse changes. The red lines in Fig. 5, top row, show the THz pulses measured at the various positions, while the black dotted lines take the pulse at z=0 μm and add a phase ϕ that was varied to give the best match with the red lines. As can be seen, a simple phase shift can very well describe the Gouy phase of the THz pulse as the crystal is moved through the focus. Between z=-500 μm to z=500 μm, the Gouy phase changes from $\approx 0.3\pi$ to $\approx -0.3\pi$. The fact that a simple Gouy phase shift can indeed describe the effect of moving the detection crystal through the focus quite well proves that effects of a changing frequency-dependent overlap between pump pulse and the THz probe pulse do play only a minor role, owing to the high-aperture THz optics (red and black dotted lines in Fig. 5 would match exactly if the spectral amplitude would not change at all.)

Figure 5, bottom row, shows the effect of the Gouy phase shift on the resulting Raman-pump-THz-probe signal. Between the various measurements of Fig. 5, bottom row, nothing has been touched in the experimental setup except of the crystal or the jet that has been moved by the indicated distance. As a trivial result, when the water jet is moved off-focus, the signal size diminishes due to the smaller spatial overlap between pump and probe pulses. More importantly, however, the shape of the response changes quite a bit, significantly more than the small deviations between red and black dotted lines in Fig. 5, top row, would suggest. For example, while

#201608 - $15.00 USD Received 19 Nov 2013; revised 10 Feb 2014; accepted 11 Feb 2014; published 18 Feb 2014

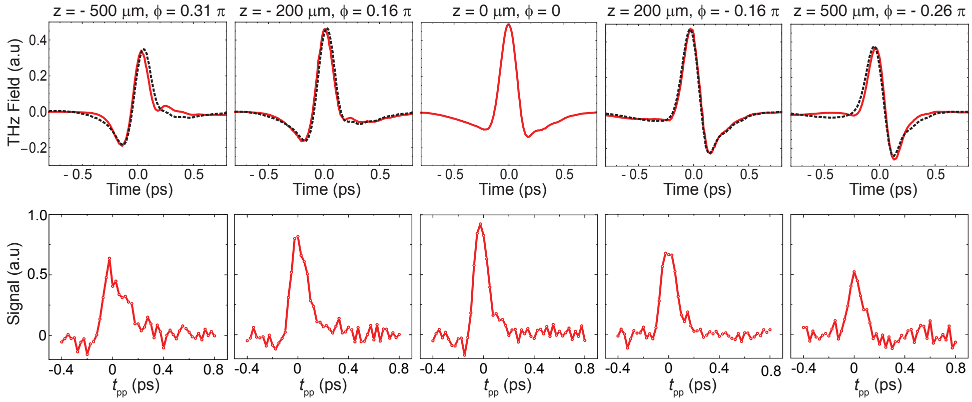

Fig. 5. Top panels: THz pulses (red) at various positions relative to the focus from -500 μm to +500 μm. The phases ϕ of these pulses have been estimated by taking the pulse at z=0 μm and adding a phase that has been varied to give the best fit (black dotted lines). Bottom panels: Raman-pump-THz-probe signal from water at various z-positions in dependence of pump-probe delay t_{pp} between the peaks of the Raman-pump and the THz probe pulse. The detection time t was kept fixed at 50 fs relative to the peak of the transmitted THz pulse, where the signal is maximal.

a quite sharp response is found at z=0 μm, the signal at z=-500 μm might be misinterpreted as relatively slow decay. Interestingly, it is these z=-500 μm data which exhibit the slowest decay, despite the fact that the THz pulse is slightly shorter (Fig. 5, top row) due to a somewhat smaller overlap of the lower frequency components when being off-focus. Hence the effect is opposite to what would be expected if a frequency-dependent overlap would be the origin.

Despite the fact that the Raman-pump-THz probe response of water includes a relatively large instantaneous contribution, originating from the electronic polarisibility and fast librational motions, the cuts in Fig. 5, bottom row, cannot be directly compared to Fig. 3, because slower components from hydrogen bond rearrangements exist in the water response function as well [37]. Nonetheless, Fig. 5, bottom row, clearly shows that the exact positioning of the sample does matter for the outcome of optical-pump-THz-probe experiments, for the reasons discussed in the previous section.

5. Discussion and conclusion

The Raman-pump-THz probe response of water is quite short lived [37, 38]. That is, the response function $R(t_1,t_2)$ in Eq. (1) indeed adds new frequency components to the emitted THz field that might not be present in the input field E_{THz}. This is the situation when the effect discussed in this paper is most relevant. When the response function varies slowly, then Eq. (1) represents a quasi-linear response which does not change during the duration of the THz pulse, in which case effectively the situation described in Sec. 2 would apply.

In conclusion, we discussed the effect of the Gouy phase on optical-pump-THz-probe experiments. In particular when high-aperture imaging optics is used, great care should be taken to precisely position the generation and detection crystals as well as the sample in their corresponding foci, in order to avoid severe perturbations of the measured signal. We have shown that the effect is related to the single-cycle pulses typically used in THz spectroscopy, whose spectral width is comparable to their center frequency, so that they span everything down to zero frequency. The effect is not relevant in most pump-probe studies in the visible or mid-IR

#201608 - $15.00 USD Received 19 Nov 2013; revised 10 Feb 2014; accepted 11 Feb 2014; published 18 Feb 2014

spectral range, where typically multi-cycle pulses are used. But when very short pulses are employed in attosecond spectroscopy [39–41], or in the visible [42–44] or mid-IR [45,46] spectral range, the effect should not be overlooked.

Acknowledgments

We thank Thomas Feurer and Jan Helbing for many insightful discussions. The work has been supported by the Swiss National Science Foundation (SNF) through the National Center of Competence and Research (NCCR) MUST.

A.3 Aqueous Solvation from the Water Perspective

This paper is submitted.

A.3.1 Contribution to this paper

Saima Ahmed performed the UV-pump-THz probe experiments.

Aqueous Solvation from the Water Perspective

Saima Ahmed, Andrea Pasti, Ricardo J. Fernández-Terán, Gustavo Ciardi, Andrey Shalit, Peter Hamm
Department of Chemistry, University of Zurich, Switzerland

(Dated: April 10, 2018)

Abstract: The response of water re-solvating a charge-transfer dye (deprotonated Coumarin 343) after photoexcitation has been measured by means of transient THz spectroscopy. Two steps of increasing THz absorption are observed, the first on the timescale of Debye relaxation of bulk water (∼10 ps) and the second upon electronic relaxation of the dye (3.9 ns). As a reference experiment, the hydroxyl vibration of water has been excited directly by a short IR pulse, establishing that the THz signal measures an elevated temperature within ∼1 ps. Comparison of the two experiments reveals that the late-time signal after pumping the charge-transfer dye indeed reflects heating of the bulk solution. However, the timescale of the first step is not limited by the response time of the THz signal, rather, it reflects reorientation of water molecules in the solvation layer. The apparent discrepancy between the relatively slow reorientation time and the general notion that water is among the fastest solvents with a solvation time in the sub-picosecond regime is discussed. Furthermore, non-equilibrium MD simulations have been performed, revealing close-to-quantitative agreement with experiment, that allow one to disentangle the contribution of heating to the overall THz response from that of water orientation.

I. INTRODUCTION

Dynamic Stokes shift experiments have been among the first ultrafast experiments in the solution phase and have been pursued on numerous molecular systems whenever corresponding nano- [1], pico- [2] and eventually femtosecond lasers [3, 4] became available. This work cumulated in a seminal review article by Maroncelli and coworkers [5]. The common picture of the dynamic Stokes shift is shown in Fig. 1. One starts from a thermalized (Gaussian) ensemble in the electronic ground state S_0 of a dye molecule and vertically promotes it to the electronically excited state S_1 with an ultrashort laser pulse according to the Franck-Condon principle. In the S_1, the ensemble will be in a non-equilibrium situation, since the free energy curves are displaced with respect to each other. The ensemble therefore relaxes on the S_1 free energy curve on a timescale that we will denote as solvation time τ_S. As the ensemble relaxes, the energy gap between the S_1 and S_0 free energy surfaces decreases, which can be observed experimentally as a time-dependent red-shift of the fluorescence or stimulated emission.

For rigid dye molecules with high fluorescence quantum yield in a polar solvent such as water, the dynamic Stokes shift is dominated by the relaxation of solvation degrees of freedom, rather than by intramolecular degrees of freedom, which is why it doesn't really matter which particular dye is used as a sensor of the solvent response [6]. Even though these experiments measure the dynamics of the solvent, they do it from a solute perspective. In the contrary, here we set out to measure solvation dynamics from the solvent perspective by transient THz spectroscopy. Both perspectives might actually be very different, which can be seen from the in principle well established, but often overlooked and rather non-intuitive fact that the solvation time τ_S and the Debye relaxation time τ_D may deviate significantly. The Debye relaxation time is related to orientational relaxation in the bulk. In the most simple theoretical approach, assuming a continuum model for solvation, a spherical non-polarizable solute molecule and a single Debye process of the solvent, solvation is predicted to occur with the so-called "longitudinal relaxation time" τ_L [6–10]:

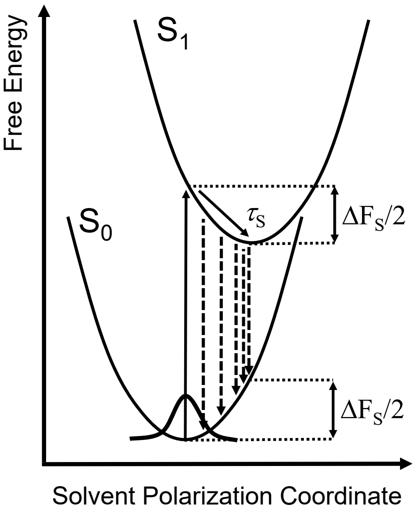

FIG. 1. The textbook picture describing the dynamic Stokes shift of a dye molecule in a polar solvent after electronic excitation. After promoting a thermalized ensemble onto the excited S_1 state, it relaxes with the solvation time τ_S, resulting in a time-dependent red-shift of the fluorescence (dashed arrows).

$$\tau_L = \frac{2\epsilon_\infty + 1}{2\epsilon_0 + 1}\tau_D \tag{1}$$

where ϵ_∞ is the dielectric constant from only the electronic polarizability, while ϵ_0 also includes orientational polarizability. In polar solvents, the latter dominates, i.e., $\epsilon_0 \gg \epsilon_\infty$, and Eq. 1 predicts a large separation of timescales between solvation dynamics τ_L and Debye relaxation τ_D. The origin of that timescale separation lies in the very nonlinear dependence of the reaction field R on the dielectric constant ϵ in Onsager's reaction field model:

$$R = \frac{2}{r^3}\frac{\epsilon - 1}{2\epsilon + 2}\mu. \tag{2}$$

where r is the radius of the assumed Onsager sphere and μ the dipole of the molecule. That is, Eq. 1 can be derived from Eq. 2 by plugging in a frequency dependent dielectric constant of a single Debye process [8]:

$$\epsilon(\omega) = \epsilon_\infty + \frac{\epsilon_0 - \epsilon_\infty}{1 - i\omega\tau_D}. \tag{3}$$

In simple words, the nonlinear dependence in Eq. 2 reflects the saturation of the solvent response due to screening; i.e., if the dielectric constant is very much larger than 1 (like for water), already a thin layer solvates a solute by generating a reaction field R in such a way that the field of the solute's dipole is in essence no longer seen by molecules beyond that layer. If the dielectric constant gets smaller, the size of the solvation layer will get larger, but in a way that the reaction field will stay almost the same – unless the dielectric constant gets close to 1.

While the continuum theory of Eq. 1 predicts a single exponential solvation process, it is very well established that solvation occurs in a multi-exponential manner [4–6, 11]. The multi-exponential response is attributed to many factors, such as the fact that the solvent cannot be described by a single Debye process [12, 13], the inertial component of solvation [7, 14], the non-spherical shape of the solute molecule [12], the failure of the continuum model to account for the discreetness of solvent molecules [15, 16] and translational degrees of freedom that contribute to solvation as well [7, 13, 14].

Water is considered to be among the "fastest" solvents with a dominating sub-100 fs inertial component of solvation and a subsequent 800 fs decay, as measured by the dynamic Stokes shift [4]. Somewhat later, the solvation dynamics of water have also been measured by a complementary technique, the photon-echo peak shift, revealing three kinetic components (17 fs, 400 fs and 2.7 ps) and an average solvation time of 400 fs [11]. Given the simplicity of the continuum model, it is remarkable that Eq. 1 predicts a longitudinal relaxation time for water τ_L=240 fs (with $\epsilon_0 \approx 80$, $\epsilon_\infty \approx 1.8$ and $\tau_D = 8.3$ ps [17]), which is quite close the experimentally observed average solvation time of 400 fs [11]. From that, one may conclude that the reason for the fast solvation time in water is in fact its large dielectric constant, and not its orientational dynamics *per se*, the latter of which not being particularly fast with $\tau_D = 8.3$ ps [17]. A recent comprehensive review of the current view of solvation is given in Ref. [6].

To study aqueous solvation from the water perspective, we optically excite a dye molecule and observe the response of the solvent water by transient THz spectroscopy. The THz spectrum of water is related to the dipole-dipole correlation function, whose long-time tail decays exponentially with the Debye relaxation time τ_D. When transiently measuring the THz spectrum of water after exciting a dissolved dye molecule, the expectation is that we observe τ_D rather than τ_S, based on the arguments given above. The present work is in the same spirit as Refs. [18, 19], which however studied solvation in organic solvents (probably for reasons of better solubility of the investigated dye molecules), in which case the expected timescale separation according to Eq. 1 is relatively small.

Looking at the problem from a very different angle, the present work is also motivated by the recent observation that solutes, very universally, seem to affect the THz spectrum of a solvation layer that is much larger than commonly assumed (≈10 Å) [20–22]. While this interpretation has been strongly challenged, for example by measuring the mobility of individual water molecules with the help of NMR spectroscopy [23], it has been proposed that the controversy can be resolved by the very delocalized character of THz vibrational modes, which results in correlated motion of many water molecules [24]. If that interpretation is correct, it may be expected that switching the dipole moment of a solute should affect also these delocalized THz modes, resulting in a transient THz signal.

II. METHODS

A. Sample

As sample molecule for this purpose, we chose Coumarin 343, whose solubility in water *per se* is very low (≪ 1 mM). To increase its solubility to 5 mM, we deprotonated, and thereby charged, the dye by addition of a base (1,4-diazabicyclo[2.2.2]octane, DABCO, 10 mM) to the solution (this base is less nucleophilic than NaOH and thereby prevents degradation of the coumarin due to ring opening). The Stokes shift is 3200 cm^{-1}, as determined from the peaks of the absorption and fluorescence spectra (see Fig. S1 in Supplementary Materials). The fluorescence quantum yield of a dilute solution of deprotonated Coumarin 343 has been determined to Φ_F=85% with the help of a Quanta-ϕ integrating sphere calibrated with respect to the reported quantum yield of Coumarin 153 in air-saturated ethanol at room temperature ($\Phi_F = 53 \pm 4\%$) [25]. A fluorescence lifetime of τ_F=4.7 ns has been measured by time-correlated single photon counting (Horiba Scientific, DeltaDiode DD-395L) in the dilute limit, and we found that it reduces to τ_F=3.9 ns at the concentration of the actual THz experiment (5 mM, see Fig. S2 in Supplementary Materials). We could not reliably measure the quantum yield at these high concentrations due to reabsorption of the emitted light, but we assume that it is reduced by the same factor as the fluorescence lifetime, i.e., $\Phi'_F \approx$70%. Finally, we calculated with TDDFT at the B3LYP/6-311++G(d,p) level of theory in IEF-PCM water [26] that the dipole changes by ≈5.3 D when exciting from the ground to the electronically excited state, which agrees well with values reported for the protonated form [27–29]. Note that the absolute dipole-moments of ground and excited state are ill-defined since the molecule is charged; when one chooses the center of nuclear charge as origin, the dipole increases from 35.2 D in the S_0 to 40.5 D in the S_1 and both are essentially parallel.

B. Transient THz Spectroscopy

For the transient THz experiments, we used essentially the same setup as previously described [30]. In brief, pump pulses (400 nm, energy 3.5 μJ) were derived from a 2.5 kHz Ti:S amplifier system (pulse width 120 fs) by frequency doubling in a 0.5 mm thick BBO crystal. THz probe pulses were produced by optical rectification in a 0.1 mm thick GaP (110) crystal, generating an almost perfect half-cycle pulse with a FWHM of ≈180 fs (see Fig. S3 in Supplementary Materials), and detected by electro-optic sampling in a 0.5 mm thick ZnTe (110) crystal, including a recently published concept based on four ZnSe Brewster windows to enhance the detectivity [31]. For a close to diffraction limited imaging of the probe pulses into the sample and into the detection crystal, two CNC-machined, large-aperture ellipsoidal mirrors have been used. The pump and probe spot sizes in the focus were ≈ 200 μm. The experimental layout introduces two delay times, the delay t_1 between optical pump-pulse and THz probe pulse, and time t_2 that scans the THz pulse. The Coumarin 343/DABCO solution was measured in a 40 μm thick wire-guided water (H_2O) jet [32] to avoid any contamination of the signal from window materials.

As a reference, we also performed an IR-pump-THz-probe experiment, exciting directly the OD band of neat D_2O at 2500 cm^{-1} with 0.7 μJ pulses derived from an IR OPA [33]. In that case, the sample was held in a cuvette constructed with two 100 μm thin sapphire windows and a spacer of 6 μm. All experiments were performed at room temperature.

Two different pump-sources have been used. For experiments with high time resolution, as well as for the IR pump experiment, pump and probe pulses were derived from the same Ti:S laser system, running the former over an optical delay line. For experiments with long delay times t_1 up to 50 ns, on the other hand, two Ti:S amplifier system have been electronically synchronized [34], revealing an effective time resolution of 10 ps due to the jitter in the synchronization.

C. Simulations

The molecular dynamics (MD) simulation setup is similar to Ref. [15] with a large Lennard-Jones sphere solvated in water, thereby mimicking Onsager's solvation model, albeit with a realistic description of the solvent both in terms of its discreteness and dynamics. TIP4P/2005 was used as water model, whose dielectric constant is ϵ_0=60 [35]. The Lennard-Jones parameters of the sphere were set to $\epsilon = 0.7794$ kJ/mol and $\sigma = 7.8$ Å, the former being the same as for TIP4P/2005 water and the latter resulting in a sphere radius of 3.9 Å, when considering the corresponding value of TIP4P/2005 (3.2 Å) and the usual combination rule. The sphere was placed in the center of a cubic box with size 25 Å and solvated with 505 water molecules at roughly the experimental density of water. The dipole of the Lennard-Jones sphere was approximated by two point charges separated by 0.8 Å, and the orientation of the dipole was kept fixed during the simulation by restraining these points with harmonic springs. Lennard-Jones interactions were smoothly switched to zero between 10.6 Å and 11.7 Å, and the Coulomb interactions were modelled with the reaction field (r_c=10.7 Å, $\epsilon = \infty$). A time step of 2.5 fs was chosen. The simulation box was equilibrated at 295 K in a 100 ps NVT simulation, thermostated by velocity-rescaling with a coupling constant of 0.5 ps. All simulations were performed with Gromacs [36].

In order to calculate the non-equilibrium dipole-dipole correlation function of Eq. 4, the following simulation protocol was subsequently used: A 1 ps NVT simulation, introduced to stabilize the temperature, was followed by a 1 ps NVE simulation. From that point on, two 21 ps NVE trajectories were run in parallel: an equilibrium trajectory with the dipole of the Lennard-Jones sphere unchanged and a non-equilibrium trajectory with the dipole changed. In order to accumulate statistics, that protocol was cycled many times (ca. 600000), continuing from the 21 ps NVE equilibrium trajectory. The simulation parameters were optimized for energy stability during the NVE simulations in order to ensure that the observed temperature change (see Fig. 3b below) reflects the solvation of the switched dipole, and not any energy drift.

The transient THz response has been calculated from the non-equilibrium dipole-dipole correlation function:

$$c(t_1, t_2) = \Delta\langle\dot{\mu}(t_1)\mu(t_1 + t_2)\rangle \tag{4}$$

where the Δ denotes the difference between non-equilibrium and equilibrium trajectory, t_1 is the pump-probe delay time after switching the dipole of the Lennard-Jones sphere, and t_2 the time for the THz free induction decay. Time t_1 was evaluated up to 20 ps (of which only 15 ps are shown in Fig. 3 below) and t_2 up to 1 ps. The dipole $\mu(t)$ contained the contribution of both the Lennard-Jones sphere and all water molecules in the simulation box. That correlation function was subsequently convoluted with the laser pulses to reveal the 3rd-order polarization:

$$\begin{aligned} P^{(3)}(t_1, t_2) = \int_0^\infty \int_0^\infty & dt' dt'' E_{THz}(t_2 - t'') \\ & \cdot I_{pu}(t_2 + t_1 - t'' - t')c(t', t''), \end{aligned} \tag{5}$$

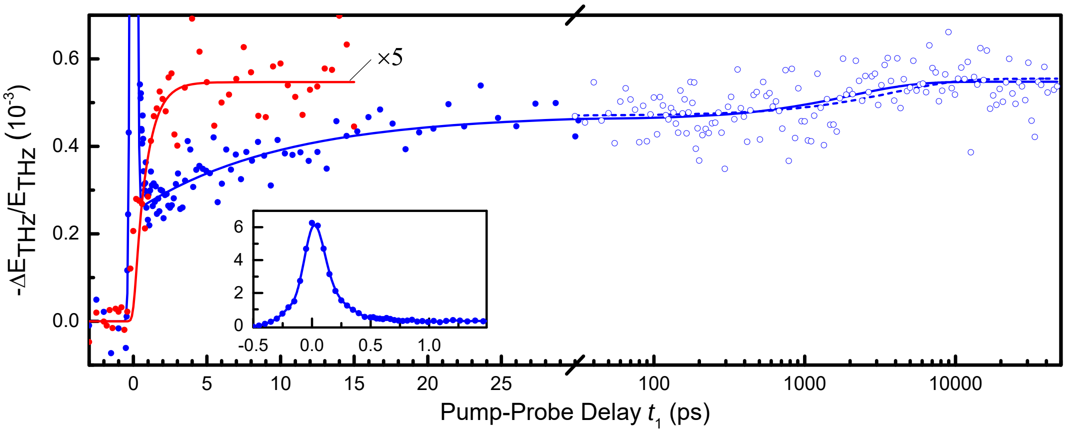

FIG. 2. Relative change of the transmitted THz field E_{THz} measured at the peak of the half-cycle THz pulse. Shown is the response after photoexcitation of Coumarin 343 in water at 400 nm (blue data), or, after pumping the hydroxyl vibration of water (D_2O) directly with an IR pulse (red data, smoothed with a 5-point quadratic Savitzky–Golay filter and scaled up by a factor 5 to match the late time temperature jump in the blue data). The blue filled circles show the data measured with high time resolution up to 30 ps plotted on a linear scale, and the blue open circles those measured with two synchronized laser systems from 30 ps up to 50 ns plotted on a logarithmic scale (both data sets were stitched together by slightly scaling the second one). The solid lines show exponential fits, leaving all time constants as free fit parameters, while the fit shown as dashed blue line fixes the slowest time constant to 3.9 ns, as determined from the fluorescence decay (see Fig. S2 in Supplementary Materials). The insert shows the spike around delay zero.

where a Gaussian was assumed for the pump pulse I_{pu} and the second derivative of a Gaussian for the THz pulse E_{THz} (in both cases with a width that matches the experimental pulses). Finally, a time-derivative with respect to t_2 was taken in order to model the emitted 3rd-order THz field [30]:

$$E^{(3)}(t_1, t_2) = \frac{d}{dt_2} P^{(3)}(t_1, t_2). \tag{6}$$

III. RESULTS AND DISCUSSION

Fig. 2 (blue) shows the transient THz signal after photoexcitation of the dye molecule, measured at the peak of the half-cycle THz pulse ($t_2 = 0$). Two data sets are stitched together in this plot, obtained with the two different pump sources described in Methods, thereby covering the time range from 100 fs to 50 ns. Around delay zero, a pulse-width-limited spike of increased THz absorption is observed (see Fig. 2, insert). The spike does not decay to zero completely, but leaves a small pedestal, which is hardly seen in the insert of Fig. 2, and which is what the main panel of Fig. 2 focuses on. That pedestal increases in two steps. The first step, occurring with a time constant of 10 ± 3 ps, agrees within error with the Debye relaxation time of water [17], while the second step can be fit to a process with 1.9 ns (Fig. 2, solid blue line). The signal stays constant from there on.

It can be safely assumed that water fully thermalizes on a nanosecond timescale over distances, which exceed that between neighboring dye molecules [37], and we attribute the final pedestal after the second step to the heating of the sample. Indeed, it is known from stationary spectroscopy that the THz absorption cross section of water increases as a function of temperature [38]. To calibrate the effect for our concrete experimental conditions, we measured the transmission of the THz pulse through a thermostated water cuvette of equal thickness at various temperatures, and observed a linear dependence with a slope $\Delta T/T = -7.5 \cdot 10^{-3}$ K^{-1} (see Fig. S3 in Supplementary Materials). With that, one can estimate a total temperature jump of ≈ 0.07 K from the size of the late-time pedestal of the transient THz data (Fig. 2). That number agrees very well with an independent estimate (0.06 K) obtained from the number of absorbed photons per sample volume, their energy, the heat capacity of water and the fluorescence quantum yield of the dye.

Based on this discussion, we conclude that the second step observed in the transient THz response reflects electronic relaxation of the dye. Since its fluorescence quantum yield is not 100% (we determined a quantum yield of $\Phi_F = 70\%$, see Methods), the remaining fraction of dye molecules dissipate their electronic excitation energy into the solvent upon radiationless relaxation, thereby heating the solvent. The fluorescence lifetime, which can be measured much more accurately (3.9 ns, see Fig. S2 in Supplementary Materials), deviates from the value obtained from the fit of the transient THz data (1.9 ns). We therefore also show in Fig. 2 a fit that fixes the time constant of that process to 3.9 ns (blue dashed line), evidencing that this is still consistent with the relatively poor signal-to-noise ratio of the transient THz data.

In light of the Introduction, we consider the first step, occurring with a time constant that agrees well with the Debye relaxation time of water, the most important result of this study. Before we continue with its discussion, we need to establish the timescale, on which the THz absorption responds to an elevated temperature. To that end, we also performed an IR-pump-THz-probe experiment, in which the hydroxyl vibration of water (D_2O) is excited directly (Fig. 2, red data). It is well established from IR-pump-IR-probe as well as from 2D IR experiments that the lifetime of that vibration is ultrafast, in particular in isotope-pure D_2O as well as H_2O, and that energy thermalizes on a ∼1 ps timescale [39–46]. And indeed, the THz-absorption rises very quickly with the fit revealing a time constant of 1 ± 0.3 ps (a complementary experiment, THz-pump-IR-probe, highlighting the coherence in the coupling between inter- and intramolecular modes on sub-picosecond timescales, has recently been performed by Bonn and coworkers [47]). Experimental [38] as well as simulation data (Fig. S4 in Materials and Methods) show that the THz absorption increases with temperature throughout the whole frequency range from 0-600 cm^{-1}, resulting from a red-shift of the librational mode at 600 cm^{-1}. Its low-frequency wing extends into the 100 cm^{-1} regime, where the THz pulses peak, indicating that the mode is almost critically damped. This also explains why the librational mode can respond to an elevated temperature so quickly, since a close-to-critical damping is the situation with the fastest possible relaxation. We conclude that the observation of a 10 ps timescale for the first step after photo-excitation of the coumarin dye is not limited by the response time of the THz signal, but rather evidences that the solvent response indeed occurs on that slower timescale.

To get deeper insights into this process, we performed non-equilibrium MD simulations, considering a large Lennard-Jones sphere as solute in water (see Methods for details). Fig. 3 (blue) shows the result when first equilibrating the system with the dipole of the Lennard-Jones sphere set to zero, and then instantaneously switching it on to 7.5 D at $t_1 = 0$, while the red data show the results for the opposite process switching from 7.5 D to 0. When switching the dipole on, the reaction field shown in Fig. 3a (blue) can be fit to three exponentials with 7 fs (37%), 210 fs (31%) and 1.6 ps (32%) and an average relaxation time of 590 fs. When switching off the dipole (Fig. 3a, red), the response is a bit faster with 8 fs (42%), 150 fs (34%) and 1.1 ps (23%) and an average decay time of 310 fs. The slightly different timescale indicates that the system is not quite in a linear response regime, yet, in either case the result is in very good agreement with the experimental solvation time (400 fs) [11], despite the crudeness of the model.

Fig. 3b shows the "non-equilibrium temperature" after switching, as determined from the total kinetic energy of the simulation box. When the dipole is switched on (blue), we observe an instantaneous temperature jump followed by a partial decay that can be fit to a single-exponential function with time constant of 2.2 ps. On the other hand, when switching off the dipole (red), about the same initial temperature jump is observed, but the temperature subsequently increases further with a time constant of 3.6 ps. The total amount of dissipated energy upon solvation of the dipole, as measured by the late-time temperature change, is different from that upon re-solvation of the Lennard-Jones sphere without any dipole. Based on Fig. 1, these results might seem surprising. That is, solvation and re-solvation is the equivalent of what would happen on the S_1 electronic state upon electronic excitation, and subsequently on the S_0 after emission of a fluorescence photon. Fig. 1 would suggest

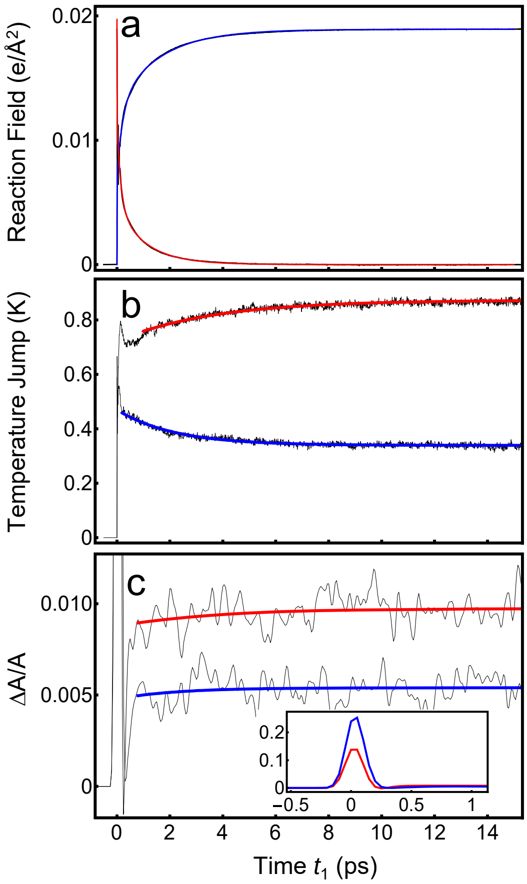

FIG. 3. Simulation results. Panel (a) shows the reaction field $R(t)$ when switching the dipole of the Lennard-Jones sphere on (blue) or off (red), panel (b) the solvent temperature in response to the switching (same color code), and panel (c) the simulated THz signal in units of relative absorbance change $\Delta A/A$. In either case, the thin black lines present data and the colored lines single exponential fits. The insert in panel (c) shows the spike around time t_1 zero.

that both events release about the same amount of free energy (which is a result of the linear response assumption that renders the curvatures of the S_0 and S_1 free energy surfaces the same). To understand this discrepancy, one must keep in mind that Fig. 1 plots "free energy", while temperature measures "energy". Since solvation is entropy-driven to a significant extent, both terms may be very different. For example, it is a freshman Chemistry experiment to observe that dissolution of NaCl in water is endothermic (e.g., temperature may indeed decrease upon solvation, as shown in Fig. 3b, blue). Nevertheless, entropy is a function only of the "solvent polarization coordinate" shown in Fig. 1, hence free energy differences at a given position of that coordinate are in fact the same as energy differences [7]. This is why the dashed arrows in Fig. 1 indeed indicate the energy of the emitted fluorescence photons. Also the total solvation free energy ΔF_S is the same as the Stokes shift ΔE_S. However, while the total solvation free energy splits half/half for the solvation of the excited state and the re-solvation of the ground state, the same is not necessarily true for the splitting of the total solvation energy.

Finally, Fig. 3c shows the transient THz response for both switching events, i.e., the result of Eq. 6 along t_1 at the peak of the signal with $t_2 = -50$ fs (the full 2D data set is shown in Fig. S5 in Supplementary Materials). Around delay zero ($t_1 = 0$), a pulse-width limited spike is observed, just like in experiment (inserts of Fig. 3c and Fig. 2), which represents the electronic contribution from the instantaneous switching of the dipole of the Lennard-Jones sphere. That can be verified by removing its contribution to $\mu(t)$ in Eq. 4, in which case that spike is inverted (and smaller). After the spike, a small pedestal of increased absorbance remains (Fig. 3c, main panel), that slightly increases further as a function of time in either case (the fit in Fig. 3c fixes the time constants to the values obtained from Fig. 3b, since the data are too noisy and the effect is too small to extract the timescale independently). While that second step in the simulation results is faster than the Debye relaxation (which is 14 ps for the current simulation setup, see Fig. S6 in Supplementary Materials), it is still slower than the solvation response (310 fs or 590 fs, see Fig. 3a).

Even though Fig. 3b and Fig. 3c resemble each other to a certain extent, evidencing that the THz response can indeed be considered an ultrafast thermometer, they don't do so in all aspects. First, trivially, the initial spike in the THz response is hardly present in the temperature data, as it originates directly from the THz field emitted upon switching the dipole of the Lennard Jones sphere. Second, while the temperature decreases again after the initial jump when switching on the dipole (Fig. 3b, blue), the THz absorption continues to increase (Fig. 3c, blue). Third, while the ratio of final temperatures is 2.6 after switching off the dipole (Fig. 3b, red) *versus* switching it on (Fig. 3b, blue), the corresponding factor is only 1.8 for the THz response (Fig. 3c, red *versus* Fig. 3c, blue). Points two and three emphasize that a sizable contribution to the THz response, that reflects the different structuring of water around solutes with different dipoles, exists as well. This is expected, since it has been shown that certain solutes affect the THz absorption of solvating water [20–22, 48]. For the case when the dipole is switched on, the kinetic response from water orientation actually overcompensates that of the temperature effect. Water reorients on the timescale of Debye relaxation, hence, it appears meaningful that we see that timescale in the THz response. We have no evidence, however, that the orientational response has a different spectral dependence than the temperature response, which would show up as a variation of the t_2-dependence of the THz signal as a function of t_1 (see full 2D data in Fig. S5, Supplementary Materials).

With the dipole switched off, the Lennard-Jones sphere is a very hydrophobic particle. Even in that most simple case, the solvation energy and solvation entropy are complicated and not necessarily intuitive functions of parameters such as sphere radius [49] or temperature [50, 51], and one might expect that the situation is even more involved for a real molecule with a complex charge distribution. Anyhow, the simulation of Fig. 3c is in very good agreement with the experimental results of Fig. 2, regardless whether the solute turns into more polar or more apolar upon switching, suggesting that these results are rather universal.

IV. CONCLUSION

In conclusion, we have measured aqueous solvation from a water perspective by means of transient THz spectroscopy. We indeed observe that the timescale of the water response is closer to the Debye relaxation time than it is to the solvation time in water; this is definitely seen in the experimental results, and to a lesser extent also in the simulation results. We have also shown that the THz response, for the most part, can be interpreted as an ultrafast thermometer with a response time of ∼1 ps, but the restructured water around the solute contributes as well to a smaller extent. While the sub-picosecond solvation of the excited state of the coumarin dye must imply a partial rearrangement of water molecules in the solvation layer, the timescale separation implies that this happens in a way that strain is built up within the solvation layer. Releasing that strain, apparently, requires an essentially complete reorientation of some of the water molecules in the solvation layer, which is why the Debye relaxation time is the relevant timescale. We consider this experiment to be a direct observation of the very non-intuitive timescale separation between solvation time and Debye relaxation (Eq. 1).

Acknowledgments: The work has been supported by the Swiss National Science Foundation (SNF) through the NCCR MUST as well as Grant 200021_165789/1.

---

[1] T. Azumi, K.-I. Itoh, and I. Hiroshi, J. Chem. Phys. **65**, 2550 (1976).

[2] L. A. Haliidy and M. R. Topp, J. Phys. Chem. **82**, 2415 (1978).

[3] W. Jarzeba, G. C. Walker, A. E. Johnson, M. A. Kahlow, and P. F. Barbara, J. Phys. Chem. **92**, 7039 (1988).

[4] R. Jimenez, G. R. Fleming, P. V. Kumar, and M. Maroncelli, Nature **369**, 471 (1994).

[5] M. L. Horng, J. A. Gardecki, A. Papazyan, and M. Maroncelli, J. Phys. Chem. **99**, 17311 (1995).

[6] B. Bagchi and B. Jana, Chem Soc. Rev. **39**, 1936 (2010).

[7] G. Van der Zwan and J. T. Hynes, J. Phys. Chem. **89**, 4181 (1985).

[8] B. Bagchi, D. W. Oxtoby, and G. R. Fleming, Chem. Phys. **86**, 257 (1984).

[9] R. F. Loring and S. Mukamel, J. Chem. Phys. **87**, 1272 (1986).

[10] D. Kivelson and H. Friedman, J. Phys. Chem. **93**, 7026 (1989).

[11] M. J. Lang, X. J. Jordanides, X. Song, and G. R. Fleming, J. Chem. Phys. **110**, 5884 (1999).

[12] B. Bagchi, E. W. Castner, and G. R. Fleming, J. Mol. Struct. **194**, 171 (1989).

[13] L. E. Fried and S. Mukamel, J. Chem. Phys. **93**, 932 (1990).

[14] A. Chandra and B. Bagchi, J. Chem. Phys. **94**, 3177 (1991).

[15] M. Maroncelli and G. R. Fleming, J. Chem. Phys **89**, 5044 (1988).

[16] M. Maroncelli, J. Chem. Phys. **94**, 2084 (1991).

[17] T. Fukasawa, T. Sato, J. Watanabe, Y. Hama, W. Kunz, and R. Buchner, Phys. Rev. Lett. **95**, 197802 (2005).

[18] G. Haran, W. D. Sun, K. Wynne, and R. M. Hochstrasser, Chem. Phys. Lett. **274**, 365 (1997).

[19] R. McElroy and K. Wynne, Phys. Rev. Lett. **79**, 3078 (1997).

[20] S. Ebbinghaus, S. J. Kim, M. Heyden, X. Yu, U. Heugen, M. Gruebele, D. M. Leitner, and M. Havenith, Proc. Natl. Acad. Sci USA **104**, 20749 (2007).

[21] M. Heyden, E. Bründermann, U. Heugen, G. Niehues, D. M. Leitner, and M. Havenith, J. Am. Chem. Soc. **130**, 5773 (2008).

[22] K. Meister, S. Ebbinghaus, Y. Xu, J. G. Duman, A. DeVries, M. Gruebele, D. M. Leitner, and M. Havenith, Proc. Natl. Acad. Sci USA **110**, 1617 (2013).

[23] L. R. Winther, J. Qvist, and B. Halle, J. Phys. Chem. B **116**, 9196 (2012).

[24] M. Heyden, J. Chem Phys **141**, 22D509 (2014).

[25] C. Würth, M. Grabolle, J. Pauli, M. Spieles, and U. Resch-Genger, Nat. Protoc. **8**, 1535 (2013).

[26] M. J. Frisch, G. W. Trucks, H. B. Schlegel, G. E. Scuseria, M. A. Robb, J. R. Cheeseman, G. Scalmani, V. Barone, B. Mennucci, G. A. Petersson, H. Nakatsuji, M. Caricato, X. Li, H. P. Hratchian, A. F. Izmaylov, J. Bloino, G. Zheng, J. L. Sonnenberg, M. Hada, M. Ehara, K. Toyota, R. Fukuda, J. Hasegawa, M. Ishida, T. Nakajima, Y. Honda, O. Kitao, H. Nakai, T. Vreven, J. A. Montgomery Jr., J. E. Peralta, F. Ogliaro, M. Bearpark, J. J. Heyd, E. Brothers, K. N. Kudin, V. N. Staroverov, R. Kobayashi, J. Normand, K. Raghavachari, A. Rendell, J. C. Burant, S. S. Iyengar, J. Tomasi, M. Cossi, N. Rega, J. M. Millam, M. Klene, J. E. Knox, J. B. Cross, V. Bakken, C. Adamo, J. Jaramillo, R. Gomperts, R. E. Stratmann, O. Yazyev, A. J. Austin, R. Cammi, C. Pomelli, J. W. Ochterski, R. L. Martin, K. Morokuma, V. G. Zakrzewski, G. A. Voth, P. Salvador, J. J. Dannenberg, S. Dapprich, A. D. Daniels, . Farkas, J. B. Foresman, J. V. Ortiz, J. Cioslowski, and D. J. Fox, *Gaussian 09* (Gaussian Inc. Wallingford CT, 2009).

[27] N. Nemkovich, H. Reis, and W. Baumann, J. Lumin. **71**, 255 (1997).

[28] R. J. Cave and E. W. Castner, J. Phys. Chem. A **106**, 12117 (2002).

[29] R. Kanya and Y. Ohshima, Chem. Phys. Lett. **370**, 211 (2003).

[30] J. Savolainen, S. Ahmed, and P. Hamm, Proc. Natl. Acad. Sci. **110**, 20402 (2013).

[31] S. Ahmed, J. Savolainen, and P. Hamm, Rev. Sci. Instrum. **85**, 13114 (2014).

[32] M. J. Tauber, R. A. Mathies, X. Chen, and S. E. Bradforth, Rev. Sci. Instrum. **74**, 4958 (2003).

[33] P. Hamm, R. A. Kaindl, and J. Stenger, Opt. Lett. **25**, 1798 (2000).

[34] J. Bredenbeck, J. Helbing, and P. Hamm, Rev. Sci. Instrum. **75**, 4462 (2004).

[35] J. L. Abascal and C. Vega, J. Chem. Phys. **123**, 234505 (2005).

[36] D. Van Der Spoel, E. Lindahl, B. Hess, G. Groenhof, A. E. Mark, and H. J. C. Berendsen, J. Comput. Chem. **26**, 1701 (2005).

[37] T. Lian, B. Locke, Y. Kholodenko, and R. M. Hochstrasser, J. Phys. Chem. **98**, 11648 (1994).

[38] H. R. Zelsmann, J. Mol. Struct. **350**, 95 (1995).

[39] A. J. Lock, S. Woutersen, and H. J. Bakker, J. Phys. Chem. A **105**, 1238 (2001).

[40] A. J. Lock and H. J. Bakker, J. Chem. Phys. **117**, 1708 (2002).

[41] A. Pakoulev, Z. Wang, and D. D. Dlott, Chem. Phys. Lett. **371**, 594 (2003).

[42] T. Steinel, J. B. Asbury, J. Zheng, and M. D. Fayer, J. Phys. Chem. A **108**, 10957 (2004).

[43] M. L. Cowan, B. D. Bruner, N. Huse, J. R. Dwyer, B. Chugh, E. T. J. Nibbering, T. Elsaesser, and R. J. D. Miller, Nature **434**, 199 (2005).

[44] L. Piatkowski, K. B. Eisenthal, and H. J. Bakker, Phys. Chem. Chem. Phys. **11**, 9033 (2009).

[45] J. Lindner, P. Vöhringer, M. S. Pshenichnikov, D. Cringus, D. A. Wiersma, and M. Mostovoy, Chem. Phys. Lett. **421**, 329 (2006).

[46] S. T. Van Der Post, C. S. Hsieh, M. Okuno, Y. Nagata, H. J. Bakker, M. Bonn, and J. Hunger, Nat. Commun. **6**, 8384 (2015).

[47] M. Grechko, T. Hasegawa, F. D'Angelo, H. Ito, D. Turchinovich, Y. Nagata, and M. Bonn, Nat. Commun. **9**, 885 (2018).

[48] D. A. Schmidt, S. Funkner, B. P. Born, R. Gnanasekaran, G. W. Schwaab, D. M. Leitner, and M. Havenith, J. Am. Chem. Soc. **131**, 18512 (2009).

[49] D. Chandler, Nature **437**, 640 (2005).

[50] N. T. Southall, K. A. Dill, and A. D. J. Haymet, J. Phys. Chem. **106**, 521 (2002).

[51] K. A. Dill and T. M. Truskett, Annu. Rev. Biophys.

Biomol. Struct **34**, 173 (2005).

Supplementary Material: Aqueous Solvation from the Water Perspective

Saima Ahmed, Andrea Pasti, Ricardo J. Fernández-Terán, Gustavo Ciardi, Andrey Shalit, Peter Hamm
Department of Chemistry, University of Zurich, Zurich, Switzerland

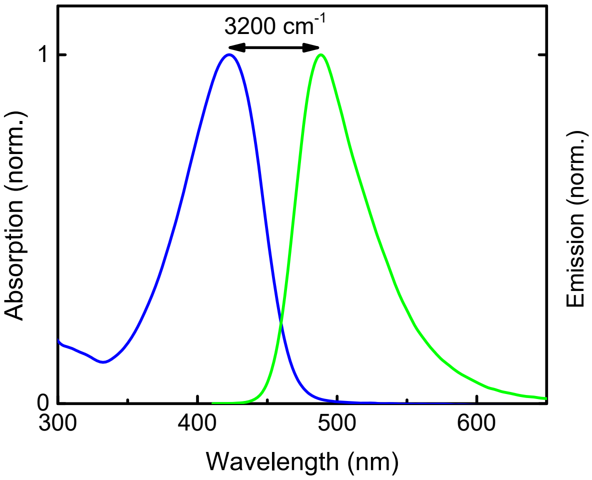

FIG. S1. Normalized absorption (blue) and emission (green) spectra of a solution of deprotonated Coumarin 343 (5 mM) in the presence of 10 mM DABCO in water at room temperature. The Stokes shift, as determined of the peaks of the spectra, is 3200 cm^{-1}.

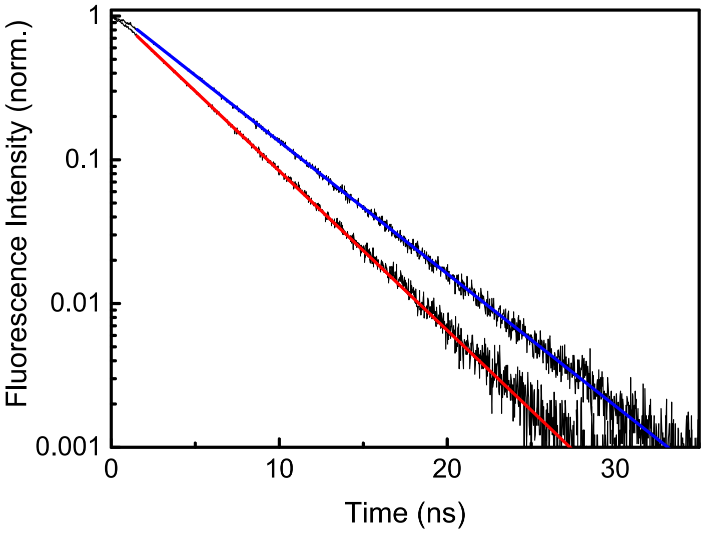

FIG. S2. Fluorescence decay of deprotonated Coumarin 343 in the dilute case (blue) and at the concentration used in the transient THz experiment (red, 5 mM Coumarin 343 and 10 mM DABCO). The data are fit to single exponential functions (thick lines), revealing lifetimes of 4.7 ns and 3.9 ns, respectively.

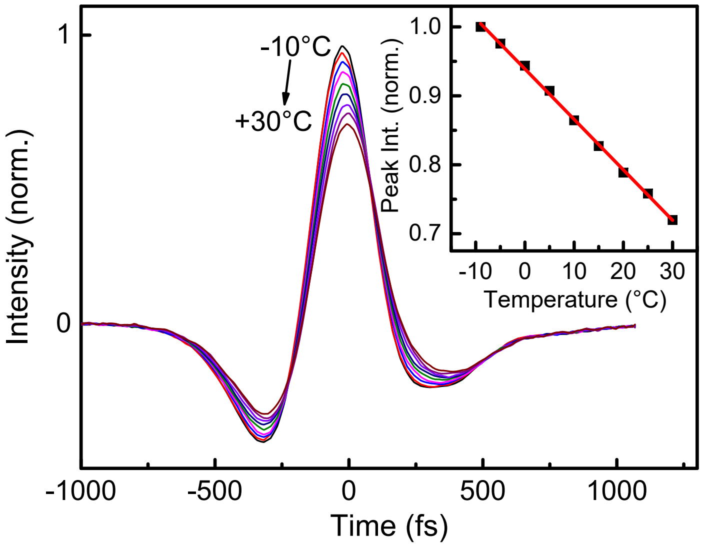

FIG. S3. Normalized THz pulse after transmitting through a thermalized 40 μm water cuvette with the temperature varied from -10°C to 30°C in steps of 5°C. The inset shows the peak intensity of the THz pulse together with a linear fit (red line) that reveals a slope of $\Delta T/T = -7.5 \cdot 10^{-3}$ K^{-1}.

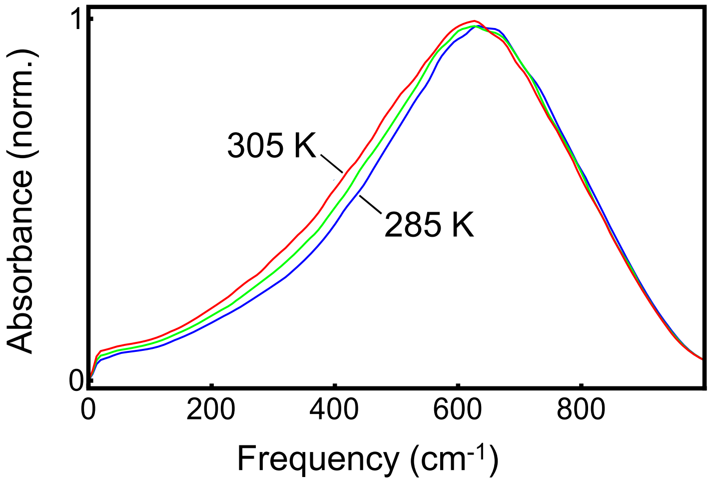

FIG. S4. Normalized THz absorption spectrum of water for the current MD simulation setup with the dipole of the Lennard-Jones sphere set to zero at 285 K (blue), 295 K (green) and 305 K (red). The absorption rise in the 100 cm^{-1} region with temperature results from a red-shift of the librational mode at 600 cm^{-1} due to its anharmonicity, whose wing extends to very low frequencies. This explains why the TIP4P/2005 water model, which as a non-polarizable water model does not reproduce the hydrogen-bond stretching mode at 200 cm^{-1}, still captures the temperature effect reasonably well.

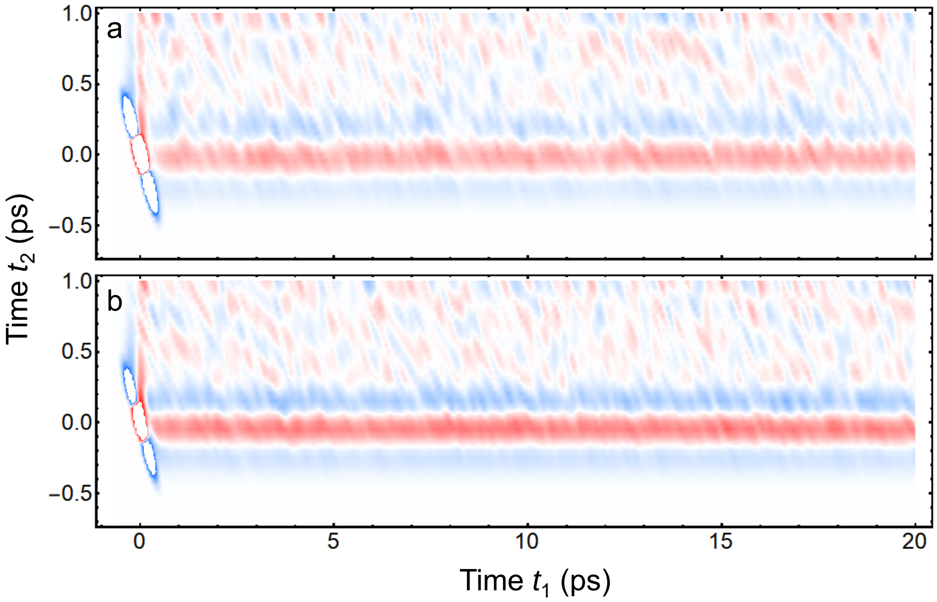

FIG. S5. Full 2D data of the simulation, the result of Eq. 6 along t_1 and t_2 for (a) switching on the dipole of the Lennard Jones sphere and (b) switching if off.

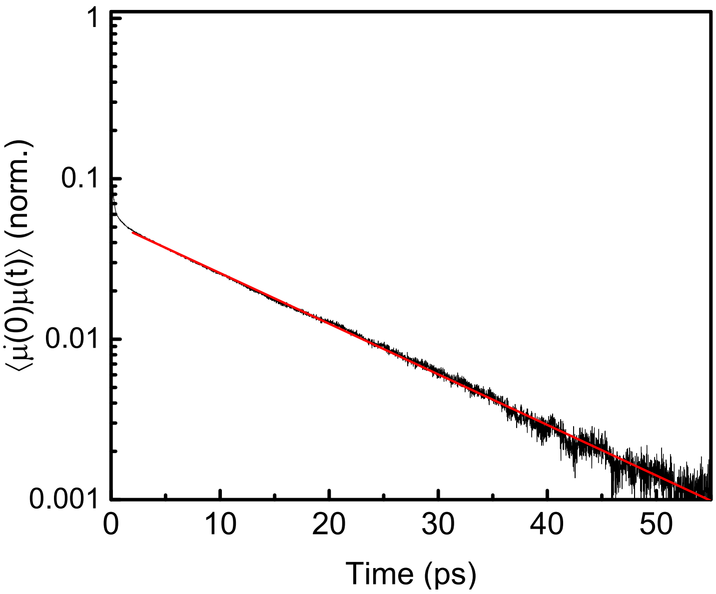

FIG. S6. Dipole-dipole correlation function $\langle \dot{\mu}(0)\mu(t) \rangle$ of water (normalized to the short-time peak, which is not visible on the scale of the plot) for the current MD simulation setup with the dipole of the Lennard-Jones sphere set to zero. An exponential fit of the long-time tail (red line) reveals a Debye relaxation time of 14 ps.

A.4 Two-dimensional Raman-terahertz spectroscopy of water

Reprinted from ref. [82], with the permission of copyright National Academy of Sciences.

A.4.1 Contribution to this paper

- Saima Ahmed performed the experiments with Dr. Janne Savolainen.
- Saima Ahmed helped in analysing the experimental data.

Two-dimensional Raman-terahertz spectroscopy of water

Janne Savolainen, Saima Ahmed, and Peter Hamm[1]

Department of Chemistry, University of Zurich, CH-8057 Zurich, Switzerland

Edited by Andrei Tokmakoff, The University of Chicago, Chicago, IL, and accepted by the Editorial Board November 10, 2013 (received for review September 16, 2013)

Two-dimensional Raman-terahertz (THz) spectroscopy is presented as a multidimensional spectroscopy directly in the far-IR regime. The method is used to explore the dynamics of the collective intermolecular modes of liquid water at ambient temperatures that emerge from the hydrogen-bond networks water forming. Two-dimensional Raman-THz spectroscopy interrogates these modes twice and as such can elucidate couplings and inhomogeneities of the various degrees of freedoms. An echo in the 2D Raman-THz response is indeed identified, indicating that a heterogeneous distribution of hydrogen-bond networks exists, albeit only on a very short 100-fs timescale. This timescale appears to be too short to be compatible with more extended, persistent structures assumed within a two-state model of water.

Water forms local structures due to the directionality of hydrogen bonding, and it is generally accepted that the emerging hydrogen-bond network is ultimately responsible for the many anomalies in the macroscopic thermodynamic properties of water (1). The consequences of that statement are however still discussed in an extremely controversial manner (2–11). For example, an increasing scattering amplitude for small angles in X-ray scattering experiments of room-temperature water has been interpreted in terms of the so-called "two-state model" of water with patches of a low-density liquid (LDL) and a high-density (HDL) liquid (5), whereas other researchers have interpreted essentially the same experimental result as continuous—in contrast with bimodal—density fluctuations, as they are expected from the isothermal compressibility (6). From a theoretical point of view, the hypothesized liquid-to-liquid phase transition in the deeply supercooled regime is discussed as either separating two metastable thermodynamic states of the liquid (2, 3, 8, 10) or as an artifact from nonequilibrated molecular dynamics simulations (7, 11). These two problems are related because two-state behavior at ambient temperatures is thought to be a reminiscence of the liquid-to-liquid phase transition in the deeply supercooled regime. It is currently not clear whether a liquid-to-liquid phase transition exists [neither for computer models (2, 3, 7, 8, 10, 11) nor for real water], and even if it does exist, it is not clear whether two-state behavior survives into ambient conditions. To provide unique experimental input to these types of questions, we present a 2D spectroscopy directly in the low-frequency terahertz (THz) regime, where the intermolecular motions of water are detected. The method can elucidate the heterogeneity and lifetimes of the hydrogen-bond networks of liquid water.

In contrast with any X-ray experiment performed so far (4–6), all of which take essentially an instantaneous snapshot (10), multidimensional IR spectroscopies (12–17), as well as related hole-burning or photon echo experiments (18–21), interrogate the molecular system at least twice and thus can deduce time correlations of interconverting structures. These experiments have been performed on the OH (or its deuterated version OD) intramolecular stretch vibration of water, which serves as a local sensor making use of the fact that its frequency is a sensitive probe of the strength of hydrogen bonding to the environment (22–24). Due to the multiple interactions with the sample, these spectroscopic techniques can reveal the inhomogeneous broadening of the OH or OD stretch vibration and thus the heterogeneity in hydrogen-bond strengths. Water as a liquid is of course not static, as such the inhomogeneous broadening is not static, but it is nevertheless meaningful to define an inhomogeneity on a certain timescale. It is very well established from these IR experiments that the OH or OD stretch vibration of liquid water is inhomogeneously broadened on an ~1-ps timescale, which is interpreted as the typical lifetime of the hydrogen bonds.

At this point, we need to introduce the concept of hierarchy of inhomogeneities. To that end, consider water dimers with short and long hydrogen bonds shown in Fig. 1*A*. The length or strength of a hydrogen bond modulates the OH stretch potential and as such the OH stretch vibrational frequency (22–24). The nonlinear experiments mentioned above (12–21) would thus interpret the OH stretch vibration as inhomogeneously broadened. However, now consider these two structures to be just the turning points of a lower-frequency intermolecular hydrogen-bond stretch vibration. If the water dimers were in the gas phase, literally as depicted in Fig. 1*A*, that hydrogen-bond stretch vibration per se would be perfectly homogeneous, and yet, a nonlinear IR experiment on the OH stretch vibration would misinterpret the system as inhomogeneously broadened on the timescale of the hydrogen-bond stretch vibration. Indeed, the hydrogen-bond stretch vibration has been observed as modulation in photon echo experiments on the OH stretch vibration (21) as well as in related simulation works (22, 23). When we talk about inhomogeneous water structures, we have in mind more extended hydrogen-bond networks, as for example those proposed for LDL and HDL water (Fig. 1*B*) (3). These hydrogen-bond networks will not necessarily differ greatly with respect to the OH stretch vibrations, but might with

Significance

The discussion about the structure of water becomes increasingly more controversial, and appears to be stuck because the major techniques used to study it (small-angle X-ray scattering emphasizing the structure, multidimensional infrared spectroscopy emphasizing the dynamics, and molecular dynamics simulations using questionable force fields) do not seem to provide mutually converging results. This calls for a different experimental approach, which we offer here with 2D Raman-terahertz spectroscopy. The work extends multidimensional vibrational spectroscopy into the far-IR regime where thermally excited soft modes are found that are directly responsible for molecular dynamics (in contrast with the high-frequency spectator modes investigated in 2D-IR spectroscopy, which per se are quiet at room temperature and sense the environment only indirectly).

Author contributions: J.S. and P.H. designed research; J.S. and S.A. performed research; J.S., S.A., and P.H. analyzed data; and J.S. and P.H. wrote the paper.

The authors declare no conflict of interest.

This article is a PNAS Direct Submission. A.T. is a guest editor invited by the Editorial Board.

[1] To whom correspondence should be addressed. E-mail: phamm@pci.uzh.ch.

This article contains supporting information online at www.pnas.org/lookup/suppl/doi:10.1073/pnas.1317459110/-/DCSupplemental.

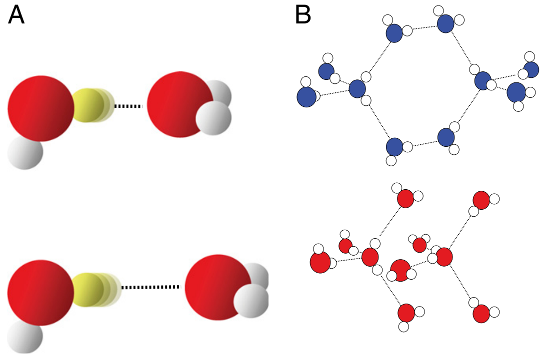

Fig. 1. Hierarchy of inhomogeneities. (*A*) Two configurations of a single hydrogen bond and (*B*) two extended hydrogen-bond networks proposed to explain LDL (*Upper*) and HDL (*Lower*) water (3).

respect to the collective intermolecular modes, which include the hydrogen-bond stretch vibration at about 6 THz (i.e., 200 cm^{-1}) and the hydrogen-bond bend vibration at about 2 THz (i.e., 60 cm^{-1}), the latter of which has been shown to extend over three solvation shells by ab initio molecular dynamics (MD) simulations (25). Both 1D-Raman (26–31) and 1D-THz (27, 32) spectroscopy in this low-frequency range have been used extensively to study pure water as well as water with various solutes. In fact, a recent 1D-Raman experiment of supercooled water has been fitted in terms of two spectrally distinguishable components underneath the 200-cm^{-1} band (31), which coincide with corresponding bands in high- and low-density amorphous ice (33). The fitting was performed using a line-shape analysis (which is not trivial including mode coupling theory) (31), but to unambiguously unravel that type of inhomogeneity, one needs a multidimensional spectroscopy of the low-frequency intermolecular modes directly.

With exactly that objective in mind, 2D Raman spectroscopy was proposed by Tanimura and Mukamel quite some time ago (34). That proposal initiated a great deal of theoretical (35–42) work. The experimental implementation, however, turned out to be exceptionally difficult (43–48), because cascaded third-order processes contaminate the desired fifth-order Raman signal (49). The fifth-order Raman signal could be isolated for certain liquids like CS$_2$ or formamide (44–48), but not yet for water due to its very weak Raman cross-section. On the other hand, 2D THz spectroscopy has also been demonstrated (50, 51), but due to the limited THz pulse energies that are currently available it is so far applicable only to low-lying strong electronic resonances with huge collective transition dipoles. Based on MD simulations, we have recently proposed a hybrid 2D Raman-THz spectroscopy (52, 53), which circumvents the technological limitations of both 2D Raman and 2D THz spectroscopy.

In 2D Raman-THz spectroscopy, two short laser pulses hit the sample: a nonresonant 800-nm pulse and a resonant half-cycle THz pulse. The first laser pulse excites a coherence of an intermolecular vibrational mode through either a Raman or a direct THz interaction, depending on which of these pulses hits the sample first. After time t_1, the second pulse (THz or Raman, respectively) interrogates the molecular system a second time, and the resulting coherence state is read out at time $t_1 + t_2$ by the emission of a THz field. We will refer to the two possibilities as the Raman-THz-THz and THz-Raman-THz pulse sequences, respectively (Fig. 2*A*). Both pulse sequences, as well as the Raman-Raman-Raman pulse sequence of 2D Raman spectroscopy (34), may in principle induce the same coherence pathways, albeit with varying probabilities due to the different selection rules of Raman and THz interactions (53). The most significant aspect of any of these pulse sequences is the switching of coherences induced by the second pulse, which ultimately allows one to correlate various degrees of freedom with each other. Most importantly in the context of the discussion above, if the spectrum of collective intermolecular modes is inhomogeneously broadened due to hydrogen-bond

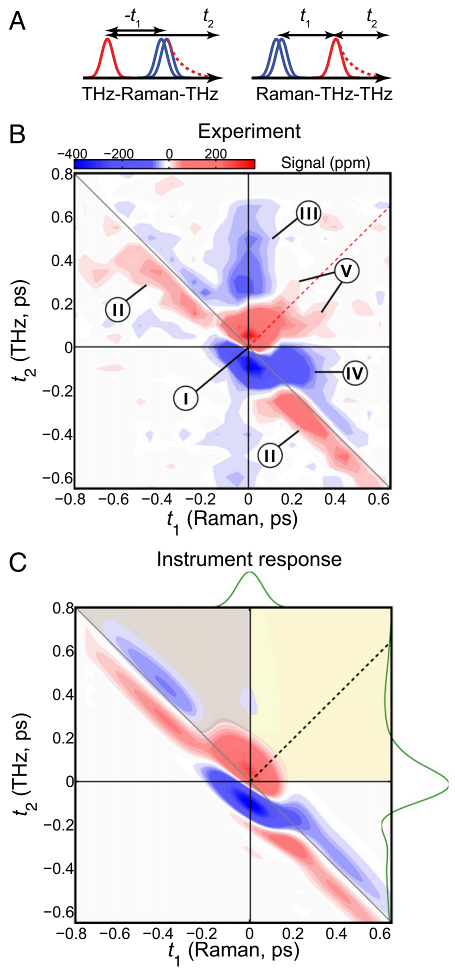

Fig. 2. Two-dimensional Raman-THz response of water. (*A*) Pulse sequences and (*B*) the experimental 2D Raman-THz signal of water. The intensity scale is given in parts per million (ppm) with respect to the maximum of the THz pulse field transmitted through the water sample. The red dotted line indicates the diagonal ($t_1 = t_2$), where an echo is potentially expected. The origin $t_2 = 0$ is defined as the peak of the transmitted THz pulse, which is also measured during scanning. The origin $t_1 = 0$ has been adjusted to fit with the instrument response function. Labels I–V indicate features discussed in the text. (*C*) The IRF. Raman ($I_{Raman}(t)$) and input THz ($E_{THz}(t)$) pulses have been determined experimentally and are shown as green lines on the top and left side, respectively (see *SI Materials and Methods* for details). The black dotted line indicates the diagonal, the gray shaded area is where the THz-Raman-THz sequence is expected, and the yellow-shaded area is where the Raman-THz-THz sequence is expected.

network patterns that are stable on the timescale of the experiment, the second pulse may rephase the coherence induced by the first pulse, giving rise to an echo (39).

Results

In the present work, we measured the 2D Raman-THz response of liquid water at ambient conditions. Conceptually, our experimental setup is not different from an optical-pump-THz-probe experiment (54, 55), just that the Raman pump pulse is nonresonant and as such excites a vibrational coherence. The setup had to be optimized for a high detection sensitivity (the peak of the emitted third-order field is only $\sim 4\times 10^{-4}$ of that of the input THz pulse) and low dispersion for a clean instrument response function (IRF; see *Materials and Methods* for details). The half-cycle THz pulses with a duration of ∼140 fs (i.e., the FWHM of the positive spike) peak at ∼1.4 THz and extend from ∼0.3 THz to ∼6 THz (200 cm^{-1}) with an almost flat phase across the spectrum (Fig. S1*A*), and thus cover the hydrogen-bond bend mode at 60 cm^{-1} and a significant part of the hydrogen-bond stretch mode at 200 cm^{-1}. They however miss the librational band at 600 cm^{-1}. The Raman pump pulses with a length of 110 fs FWHM (Fig. S1*B*) cover a somewhat larger frequency range up to ∼9 THz (300 cm^{-1}).

Fig. 2*B* shows the 2D Raman-THz response of liquid water, which reveals a rich set of features with good signal-to-noise ratio. Before discussing the 2D Raman-THz signal in detail, we need to investigate its dependence on the Raman pump-pulse irradiance. The high irradiance required to obtain a measurable signal is a major concern because it may photoionize water and lead to the generation of solvated electrons, which in turn may interact with the sample and/or with the probing THz pulses and lead to an unwanted signal. As the generation of solvated electrons is a multiphoton process, its appearance depends highly nonlinearly on pump-pulse intensity. The 2D Raman-THz signal, in contrast, has two field interactions with the Raman pulse and therefore should depend only linearly on the Raman pulse intensity. We thus critically verified the linearity of the signal by varying the Raman pulse intensity with an adjustable neutral density filter. The result in Fig. 3 indeed reveals a linear behavior in a regime below *ca.* 1 TW/cm^2, indicating that the signal is the desired 2D Raman-THz response. When increasing the Raman pump-pulse irradiance beyond that regime, we do observe a signal that depends nonlinearly on the pump irradiance (Fig. S2*A*) and looks qualitatively very different from the Raman signal. This signal is due to the solvated electrons upon photoionization of water with a threshold of above 1 TW/cm^2 for 800-nm pulses (as a side remark, we note that photoionization of neat water probed by THz radiation is in itself an interesting result, which will be investigated in detail in a separate publication). We also explored the polarization dependence of the signal. Whereas the 2D Raman-THz signal in the linear regime has a pronounced polarization effect (Fig. S2*B*), as expected for a Raman effect, the solvated electron signal at higher pump fluency is polarization independent, because the solvated electron is essentially spherical. We thus conclude that it is possible to detect the 2D Raman-THz signal that is not contaminated by the presence of solvated electrons in the water sample. The 2D Raman-THz response of Fig. 2*B* has been measured at a pump irradiance of 0.6 TW/cm^2, which is safely within the linear regime.

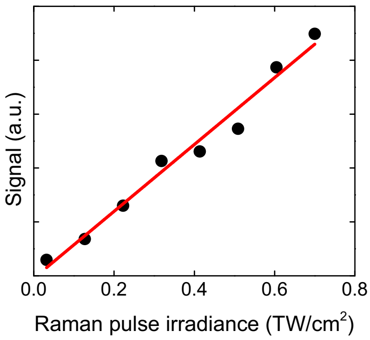

Fig. 3. Raman-pulse irradiance dependency of the peak of the 2D Raman-THz signal.

For the 2D Raman-THz response shown in Fig. 2*B*, we control two delay stages in the experimental setup (*Materials and Methods*): Delay 1 scans the delay between the Raman and THz pulses at the sample t_1, and delay 2 scans the delay between the THz input pulse at the sample and the emitted field t_2. The two possible pulse sequences for the 2D Raman-THz signal (53) are shown in Fig. 2*A*. In the experiment we scan t_1 from negative to positive times, which switches the signal from the THz-Raman-THz sequence to the Raman-THz-THz sequence. The time t_2 is defined as the delay between the THz input pulse and the emitted field, and not necessarily between the second pulse and the emitted field, so that $t_2 \leftarrow t_1 + t_2$ for $t_1 < 0$. Therefore, the Raman-THz-THz sequence appears in the upper-right quadrant with $t_1 > 0$ and $t_2 > 0$ (shaded in yellow in Fig. 2*B*), whereas the THz-Raman-THz sequence appears in the upper triangle of the upper-left quadrant with $t_1 < 0$ and $t_1 + t_2 > 0$ (shaded in gray in Fig. 2*B*).

The signal extends beyond these regions, because the molecular response function $R(t'',t')$ is convoluted with laser pulses that are not infinitesimally short:

$$P^{(3)}(t_2;t_1)=\int_0^\infty\int_0^\infty dt'dt''E_{THz}(t_2-t'')\cdot I_{Raman}(t_2+t_1-t''-t')R(t'',t'). \qquad [1]$$

Here, $E_{THz}(t_2-t'')$ is the THz pulse in the sample, $I_{Raman}(t)$ the intensity profile of the Raman pump pulse, and t_1 accounts for the experimentally controlled delay time between the peaks of the two pulses (*Materials and Methods*). The molecular response function $R(t'',t')$ is the property we ultimately want to measure because it contains the molecular information, and also because it can be compared with all-atom MD simulations (52, 53). To extract $R(t'',t')$, we need to precisely know the input THz and Raman pulses entering Eq. **1**, as well as how the emitted field propagates to the detection crystal (56) (Fig. S3). For the latter, we describe the generated third-order field as a time derivative of the third-order polarization:

$$E^{(3)}(t_2;t_1)=\frac{d}{dt_2}P^{(3)}(t_2;t_1), \qquad [2]$$

which is a good approximation for the most simple case when dispersion and absorption can be neglected and the process is quasi–phase-matched (57, 58). We subsequently introduce the effect of dispersion and absorption of the water jet via a linear transfer function in the frequency domain. That transfer function can be combined with those of the imaging optics and the detection crystal (56, 59), revealing a total transfer function $T_{total}(\omega_2)$, with which we obtain for the detected field

$$E_{det}(\omega_2;t_1)=T_{total}(\omega_2)E^{(3)}(\omega_2;t_1). \qquad [3]$$

The input pulses $E_{THz}(t)$ and $I_{Raman}(t)$, as well as the transfer function $T_{total}(\omega)$, have been determined experimentally, as discussed in detail in *SI Materials and Methods* (Figs. S1, S4, and S5). Whereas methods to invert Eqs. **1–3** have been worked out (56, 58), we chose here a forward strategy, i.e., simulate the measured signal from a given response function $R(t'', t')$, so future theoretical work can still be compared with our experiment.

Evaluating Eqs. **1–3** for a hypothetical instantaneous response function $R(t'', t') = -\delta(t'')\delta(t')$ reveals the IRF (Fig. 2*C*) of the setup, for which the integrals in the convolution Eq. **1** disappear:

$$P^{(3)}(t_2; t_1) = -E_{THz}(t_2) \cdot I_{Raman}(t_2 + t_1). \qquad \textbf{[4]}$$

The third-order polarization will then be a product of the two pulses, which extends along the antidiagonal in the 2D representation of Fig. 2*C* due to the argument $t_2 + t_1$ in I_{Raman}, reflecting the arrangement of delay lines in the experimental setup (*Materials and Methods*). The time derivative Eq. **2** is responsible for the minus–plus (blue–red) pattern in the IRF in the t_2 direction. Eq. **3** stretches it toward positive t_2 (because T_{total} is causal) with only a little bit of ringing (which is the reward for keeping dispersion low in the thin sample jet and generation and detection crystals as well as the high-aperture imaging optics). Note that the IRF stays quite narrow in the diagonal direction with $t_1 = t_2$, because the Raman pump pulse is significantly shorter than the THz pulse and because it is clean without wings (Fig. S1 and the pulses shown in green in Fig. 2*C*). This feature is a manifestation of the fact that the time resolution of an optical-pump-THz-probe experiment is not limited by the THz pulse length, but rather by the pump pulse and the bandwidth of the gated detection process (58).

Discussion

Certain parts of the experimental data (Fig. 2*B*) very closely resemble the IRF (Fig. 2*C*), indicating that we can determine the laser pulses and the transfer function with high accuracy. Any feature in the experimental data that is observed also in the IRF, i.e., in particular the spikes around $t_1 = t_2 = 0$ labeled as "I" in Fig. 2*B* and the antidiagonal ridge labeled as "II," originates from a part of the water response that is much faster than our laser pulses. Presumably, this fast response is due to the electronic polarizability as well as librational motion of water with a typical frequency of 600 cm^{-1}. In contrast, any feature beyond the IRF originates from water response that is slow enough to be observed with our time resolution. Three such features labeled III–V can indeed be identified. Features III and IV extend along the positive t_1 and t_2 axes, and the simulation results from ref. 52 suggest that these features essentially reflect the 1D Raman and 1D THz responses, respectively. The long time relaxation tail of the 1D-Raman response decays on a typical timescale of 350 fs at room temperature (albeit in a nonexponential manner) (26), in reasonable agreement with the decay of features III. The long time relaxation tail of the 1D-THz response, on the other hand, decays much slower with 8 ps (27). Due to the time derivative in Eq. **2**, we are very insensitive to such slow processes, so feature IV probably reflects some of the oscillatory contribution of the 1D-THz response. It has also been shown in ref. 52 that the 2D response is not just a simple product of these 1D responses; as such, the 2D response contains additional information.

In this regard, the most interesting is feature V, which extends along the diagonal $t_1 = t_2$ in the upper-right quadrant and contains additional substructure. Fig. 4 highlights that feature by showing a cut along the diagonal with the decay of the experimental data (red) being slower than that of the IRF (black). The diagonal $t_2 = t_1$ is where an echo is expected. Echoes appear when a multimode system gets synchronized twice by two perturbations separated by a time t_1. Whenever the character of the various modes persists for sufficiently long time and thus keeps a memory about their oscillation frequency, as they do for a heterogeneous set of oscillators, an echo is emitted at $t_2 = t_1$ when the modes rephase upon a second perturbation. That is, the various modes run out of phase during time t_1, and rephase during time t_2 because the second perturbation may "invert the coherence." As such, echoes are indicative for inhomogeneous broadening. The process of de- and rephasing is relatively intuitive to visualize in the case of the spins echo (Hahn echo) (60) as well as for electronic and vibrational photon echoes (21, 61–63), but the concept is much more general; for example, echoes upon multiple temperature jumps have been proposed as well (64, 65). Also in the context of 2D Raman spectroscopy, echoes have been discussed extensively (36, 39, 40). In comparison with conventional photon echo spectroscopy (21, 61–63), it is less obvious to identify the coherence pathways that invert the coherence upon the second pulse, but they do exist (39). Traces of a photon echo indeed appear in simulations of the 2D Raman spectroscopy of water as a ridge along the diagonal, but only when approximating the signal with instantaneous or quenched normal modes (figure 3 in ref. 36). The mechanism of the flow of coherence pathways is the same for 2D Raman and 2D Raman-THz spectroscopy, albeit with different selection rules. We therefore propose that feature V is related to an echo, which in contrast with the discussion of ref. 53 would actually be more evident for the Raman-THz-THz pulse sequence. Note, however, that the response functions reported in refs. 52, 53, based on a simple nonpolarizable point charge water model, cannot reproduce the experimental results, for reasons that are currently not clear.

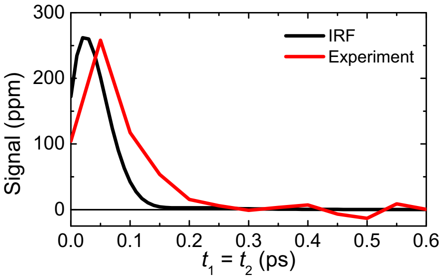

Fig. 4. Cuts along the diagonal for the Raman-THz-THz pulse sequence, red for the experimental data and black for the IRF. The data beyond 0.3 ps give an idea of the signal-to-noise ratio.

With that in mind, we turn to a discussion of the implications of these results in the context of the introduction. The appearance of an echo hints toward an inhomogeneous distribution among the collective intermolecular hydrogen-bond modes. Certainly, verifying this interpretation needs further theoretical attention, but if it turns out to be correct, this inhomogeneity would live for only a few hundred femtoseconds, in fair agreement with conclusions drawn from 3D-IR spectroscopy of the OD stretch vibration of water (17). In particular, it would live significantly shorter than the typical lifetime of a single hydrogen bond of about 1 ps, which has been concluded from 2D-IR and related experiments on the OH-stretch (or OD-stretch) vibration (12–21). Not unreasonably, the lifetime of a single hydrogen bond seems to be an upper limit for the lifetime of more extended hydrogen-bond networks. In ref. 25, the 200-cm^{-1} band has been dissected into the various hydrogen-bond stretching modes of a tetrahedral water cluster, which is the most common structural motive in liquid water up to the first solvation shell. Three distinguishable subbands have been identified, a situation which would indeed give rise to an echo. If the lifetime of a single hydrogen bond is 1 ps, then the lifetime of a tetrahedral water cluster with four hydrogen bonds can be as short as 250 fs, assuming that the various hydrogen bonds evolve statistically independently from each other. That simple estimate reveals a timescale that is in good agreement with the echo decay time we observe in Fig. 4. In essence, the low-frequency modes are quite fragile.

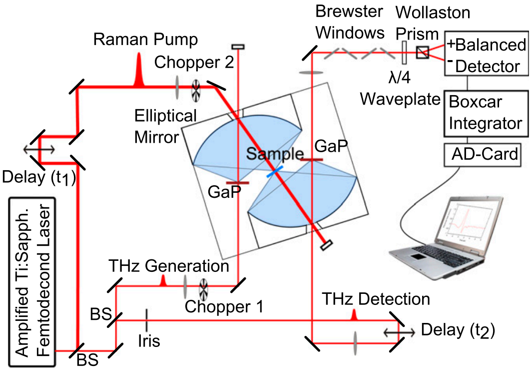

Fig. 5. 2D Raman-THz experimental setup.

The 100-fs timescale appears to be too short to be compatible with more extended, persistent structures assumed within a two-state model of water, as they have been deduced from X-ray scattering experiments (5). Either such extended structures do not exist at room temperature, or their low-frequency intermolecular spectra are so similar that they cannot be distinguished spectroscopically. Simulation work along the lines of refs. 52, 53 will be able to answer questions of that kind.

In conclusion, we believe that 2D Raman-THz spectroscopy, which we have shown to be experimentally accessible with good signal-to-noise ratio (Fig. 2*B*), is the most decisive spectroscopy as of today of the intermolecular structure and dynamics of liquid water. In combination with refined computer models of water, it will lead to a better understanding of the microscopic structure of water. Shorter Raman and THz pulses would certainly be desirable in an improved instrument using, e.g., a plasma generation and detection scheme (66) to fully cover the 200-cm^{-1}- band as well as the librational band. Furthermore, the 2D Raman-THz response of supercooled water would be rewarding because the dynamics is going to be slower and thus easier to measure (16), because two-state behavior—if it exists at all—will be more pronounced, and because evidence for the existence of two subbands underneath the hydrogen-bond stretching band at 200 cm^{-1} has recently been given by 1D-Raman spectroscopy (31). Finally, an extension of this work to study solute–water interactions will be most interesting; for example, proteins (32) or salts (29) have been shown to modify the THz or Raman water spectrum, respectively.

Materials and Methods

The setup used in the 2D Raman-THz experiment is essentially a standard optical-pump–THz-probe spectrometer (Fig. 5) (54). A commercial Ti:sapphire oscillator and a chirped-pulse amplifier (Spectra Physics) delivered 110-fs, 800-nm pulses at 5-kHz repetition rate. With beamsplitters, a small portion of the laser output was split in two parts that are used to generate and detect the THz pulses by optical rectification and electrooptic sampling, respectively (55). We used two identical 0.1-mm-thick (110) GaP crystals for both processes. Pulses with 10 μJ of energy were focused onto the generation crystal with a spot size of 50 μm (intensity just below the damage threshold). The THz pulses from the GaP generation crystal were collected and focused onto the sample and then onto the detection crystal by two custom-made elliptical aluminum mirrors ($2f = 83$ mm). This arrangement has a numerical aperture of about 1 and provides a near-diffraction limited spot size of 200 μm for the THz field at the sample and at the detection crystal. The detecting 800-nm beam passed through an iris for spatial mode cleaning, and was subsequently coupled to the detecting crystal via an optical delay stage (t_2) and through a small hole in the second elliptical mirror. It then passed through four ZnSe Brewster-angle windows, a quarter-wave plate, and a Wollaston polarizer followed by two balanced photodiodes detecting the difference between *s*- and *p* polarizations in the measuring 800-nm beam. The sensitivity of the electrooptic detection was enhanced by introducing the four properly mounted ZnSe Brewster windows before the quarter-wave plate. This arrangement increases the ratio between the measured signal and the amount of light on the detector (the details of this detection enhancement will be discussed in a separate publication). The photodiode signals were then amplified, integrated in a boxcar integrator, and recorded in a computer on a single-shot basis.

Approximately 200 μJ per pulse of the laser output was used as Raman pump pulses, which were passed through an optical delay stage controlling t_1. The Raman pulses were focused with a lens ($f = 1$ m) and coupled onto the sample collinearly with the THz pulses through a small hole in the first elliptical mirror. The spot size at the sample was adjusted to about 250 μm by keeping the focus ∼8 cm after the sample. An autocorrelation measurement (using an AC-1PS autocorrelator from UVisIR Inc.) and a Gaussian fit with an FWHM of about 150 fs of the Raman pulse are shown in Fig. S1*B*. Assuming Gaussian pulses, this corresponds to a pulse duration of ∼110 fs FWHM. Importantly, the Raman pulses are very clean with essentially no wings. If wings were present, they would show up in the diagonal cut of the IRF in Fig. 4. The same pulse was also used to generate the THz pulse in the first GaP crystal.

The Raman pump pulses were modulated at half of the laser frequency and the THz creation pulses at a quarter of the laser frequency using two optical choppers. Electrooptic sampling directly measures the THz field rather than its intensity. The transmitted THz field and the generated 2D Raman-THz field are additive and thus the 2D Raman-THz signal could be calculated as a difference between pumped and unpumped sample:

$$\begin{aligned} E_{det} \propto &+ (S_{\mathrm{RamanOnTHzOn}} - S_{\mathrm{RamanOnTHzOff}}) \\ &- (S_{\mathrm{RamanOffTHzOn}} - S_{\mathrm{RamanOffTHzOff}}). \end{aligned} \qquad \textbf{[5]}$$

All four types of data were recorded independently so that the THz pulse itself was also measured constantly during scanning:

$$E_{\mathrm{II}} = S_{\mathrm{RamanOffTHzOn}} - S_{\mathrm{RamanOffTHzOff}}. \qquad \textbf{[6]}$$

The setup was optimized for a high detection sensitivity to be able to measure the very small 2D Raman-THz signal. Further, we optimized the setup for low dispersion to obtain as short and clean an IRF as possible (Fig. 2*C*). Measures to achieve a high sensitivity include the high repetition rate of the laser system (5 kHz), the ZnSe Brewster windows, high numerical aperture optics, careful positioning of the crystals and water sample at the foci of the setup, as well as the long scanning time for the 2D data set of Fig. 2*B* of about 2 wk. The IRF was optimized by using thin 100-μm GaP crystals, which give an almost perfect half-cycle THz pulse with hardly any ringing (Fig. S1*A*) that would have complicated the discussion of the difference between IRF and water response significantly (Figs. 2 and 4). GaP produces significantly less THz light than the more commonly used ZnTe, making it harder to measure the small signal, but we considered the cleanness of the pulses to be most important. Finally, the high-aperture optics proves to be relevant as well because it provides a very flat transmission function down to quite low frequencies of ∼0.3 THz (Fig. S5*B*). We verified that the signal is not contaminated by a χ_2 -response from the water-jet surfaces.

The water sample (triple-distilled water) flowed in a windowless 40-μm-thick gravity-driven jet to avoid any extra artifacts from windows as well as any accumulative thermal effects in the excitation volume. The arrival time of the THz pulse Eq. **S6** was used as a measure of the thickness of that jet. Modulation of the thickness of the jet during the time of data scanning due to water evaporation, which changed the water level in the reservoir and hence the pressure of the water delivered to the jet, was controlled by continuously adding small amounts of water with a syringe pump. The THz section of the setup was sealed in a nitrogen-purged box to remove water vapor. All measurements were performed at room temperature.

ACKNOWLEDGMENTS. We thank Thomas Feurer and Sean Garrett-Roe for many insightful discussions. The work was supported by the Swiss National Science Foundation through the National Center of Competence and Research (NCCR) Molecular Ultrafast Science and Technology (MUST).

1. Debenedetti PG (2003) Supercooled and glassy water. *J Phys Condens Matter* 15:R1669–R1726.
2. Poole P, Sciortino F, Essmann U, Stanley H (1992) Phase behaviour of metastable water. *Nature* 360(6402):324–328.

3. Mishima O, Stanley HE (1998) The relationship between liquid, supercooled and glassy water. *Nature* 396(6709):329–335.
4. Wernet P, et al. (2004) The structure of the first coordination shell in liquid water. *Science* 304(5673):995–999.
5. Huang C, et al. (2009) The inhomogeneous structure of water at ambient conditions. *Proc Natl Acad Sci USA* 106(36):15214–15218.
6. Clark GNI, Hura GL, Teixeira J, Soper AK, Head-Gordon T (2010) Small-angle scattering and the structure of ambient liquid water. *Proc Natl Acad Sci USA* 107(32):14003–14007.
7. Limmer DT, Chandler D (2011) The putative liquid-liquid transition is a liquid-solid transition in atomistic models of water. *J Chem Phys* 135(13):134503.
8. Liu Y, Palmer JC, Panagiotopoulos AZ, Debenedetti PG (2012) Liquid-liquid transition in ST2 water. *J Chem Phys* 137(21):214505.
9. Poole PH, Bowles RK, Saika-Voivod I, Sciortino F (2013) Free energy surface of ST2 water near the liquid-liquid phase transition. *J Chem Phys* 138(3):034505.
10. Kühne TD, Khaliullin RZ (2013) Electronic signature of the instantaneous asymmetry in the first coordination shell of liquid water. *Nat Commun* 4:1450.
11. Limmer DT, Chandler D (2013) The putative liquid-liquid transition is a liquid-solid transition in atomistic models of water. II. *J Chem Phys* 138(21):214504.
12. Asbury JB, et al. (2004) Dynamics of water probed with vibrational echo correlation spectroscopy. *J Chem Phys* 121(24):12431–12446.
13. Yeremenko S, Pshenichnikov MS, Wiersma DA (2003) Hydrogen-bond dynamics in water explored by heterodyne-detected photon echo. *Chem Phys Lett* 369(1-2): 107–113.
14. Cowan ML, et al. (2005) Ultrafast memory loss and energy redistribution in the hydrogen bond network of liquid H_2O. *Nature* 434(7030):199–202.
15. Eaves JD, et al. (2005) Hydrogen bonds in liquid water are broken only fleetingly. *Proc Natl Acad Sci USA* 102(37):13019–13022.
16. Perakis F, Hamm P (2011) 2D IR spectroscopy of supercooled water. *J Phys Chem B* 115: 5289–5293.
17. Garrett-Roe S, Perakis F, Rao F, Hamm P (2011) 3D-IR spectroscopy of isotope-substituted liquid water reveals heterogeneous dynamics. *J Phys Chem B* 115:6976–6984.
18. Woutersen S, Emmerichs U, Bakker HJ (1997) Femtosecond mid-infrared pump-probe spectroscopy of liquid water: Evidence for a two-component structure. *Science* 278(5338):658–660.
19. Laenen R, Rauscher C, Laubereau A (1998) Dynamics of local substructures in water observed by ultrafast infrared hole burning. *Phys Rev Lett* 80(12):2622–2625.
20. Gale GM, et al. (1999) Femtosecond dynamics of hydrogen bonds in liquid water: A real time study. *Phys Rev Lett* 82(5):1068–1071.
21. Fecko CJ, Eaves JD, Loparo JJ, Tokmakoff A, Geissler PL (2003) Ultrafast hydrogen-bond dynamics in the infrared spectroscopy of water. *Science* 301(5640):1698–1702.
22. Lawrence CP, Skinner JL (2002) Vibrational spectroscopy of HOD in liquid D2O. II. Infrared line shapes and vibrational stokes shift. *J Chem Phys* 117(18):8847–8900.
23. Moller KB, Rey R, Hynes JT (2004) Hydrogen bond dynamics in water and ultrafast infrared spectroscopy: A theoretical study. *J Phys Chem A* 108:1275–1289.
24. Smith JD, et al. (2005) Unified description of temperature-dependent hydrogen-bond rearrangements in liquid water. *Proc Natl Acad Sci USA* 102(40):14171–14174.
25. Heyden M, et al. (2010) Dissecting the THz spectrum of liquid water from first principles via correlations in time and space. *Proc Natl Acad Sci USA* 107(27):12068–12073.
26. Torre R, Bartolini P, Righini R (2004) Structural relaxation in supercooled water by time-resolved spectroscopy. *Nature* 428(6980):296–299.
27. Fukasawa T, et al. (2005) Relation between dielectric and low-frequency Raman spectra of hydrogen-bond liquids. *Phys Rev Lett* 95(19):197802.
28. Hunt NT, Kattner L, Shanks RP, Wynne K (2007) The dynamics of water-protein interaction studied by ultrafast optical Kerr-effect spectroscopy. *J Am Chem Soc* 129(11):3168–3172.
29. Heisler IA, Meech SR (2010) Low-frequency modes of aqueous alkali halide solutions: Glimpsing the hydrogen bonding vibration. *Science* 327(5967):857–860.
30. Mazur K, Heisler IA, Meech SR (2011) THz spectra and dynamics of aqueous solutions studied by the ultrafast optical Kerr effect. *J Phys Chem B* 115(11):2563–2573.
31. Taschin A, Bartolini P, Eramo R, Righini R, Torre R (2013) Evidence of two distinct local structures of water from ambient to supercooled conditions. *Nat Commun* 4:2401.
32. Ebbinghaus S, et al. (2007) An extended dynamical hydration shell around proteins. *Proc Natl Acad Sci USA* 104(52):20749–20752.
33. Suzuki Y, Takasaki Y, Tominaga Y, Mishima O (2000) Low-frequency Raman spectra of amorphous ices. *Chem Phys Lett* 319(1-2):81–84.
34. Tanimura Y, Mukamel S (1993) 2-Dimensional femtosecond vibrational spectroscopy of liquids. *J Chem Phys* 99(12):9496–9511.
35. Palese S, et al. (1994) Femtosecond two-dimensional Raman spectroscopy of liquid water. *J Phys Chem* 98(48):12466–12470.
36. Saito S, Ohmine I (1998) Off-resonant fifth-order nonlinear response of water and CS$_2$: Analysis based on normal modes. *J Chem Phys* 108(1):240–251.
37. Ma A, Stratt RM (2000) Fifth-order Raman spectrum of an atomic liquid: Simulation and instantaneous-normal-mode calculation. *Phys Rev Lett* 85(5):1004–1007.
38. Jansen TL, Snijders JG, Duppen K (2000) The third- and fifth-order nonlinear Raman response of liquid CS$_2$ calculated using a finite field nonequilibrium molecular dynamics method. *J Chem Phys* 113(1):307–311.
39. Fourkas JT (2001) Multidimensional Raman spectroscopies. *Adv Chem Phys* 117: 235–273.
40. Saito S, Ohmine I (2003) Off-resonant two-dimensional fifth-order Raman spectroscopy of liquid CS2: Detection of anharmonic dynamics. *J Chem Phys* 119(17):9073–9087.
41. DeVane R, Kasprzyk C, Space B, Keyes T (2006) Theoretical investigation of the temperature dependence of the fifth-order Raman response function of fluid and liquid xenon. *J Phys Chem B* 110(8):3773–3781.
42. Hasegawa T, Tanimura Y (2006) Calculating fifth-order Raman signals for various molecular liquids by equilibrium and nonequilibrium hybrid molecular dynamics simulation algorithms. *J Chem Phys* 125(7):074512.
43. Tokmakoff A, et al. (1997) Two-dimensional Raman spectroscopy of vibrational interactions in liquids. *Phys Rev Lett* 79(14):2702–2705.
44. Blank DA, Kaufman LJ, Fleming GR (2000) Direct fifth-order electronically nonresonant Raman scattering from CS$_2$ at room temperature. *J Chem Phys* 113(2): 771–778.
45. Kaufman LJ, Heo J, Ziegler LD, Fleming GR (2002) Heterodyne-detected fifth-order nonresonant Raman scattering from room temperature CS$_2$. *Phys Rev Lett* 88(20): 207402.
46. Kubarych KJ, Milne CJ, Miller RJD (2003) Fifth-order two-dimensional Raman spectroscopy: A new direct probe of the liquid state. *Int Rev Phys Chem* 22:497–532.
47. Golonzka O, Demirdöven N, Khalili M, Tokmakoff A (2000) Separation of cascaded and direct fifth-order Raman signals using phase-sensitive intrinsic heterodyne detection. *J Chem Phys* 113(22):9893–9896.
48. Li YL, Huang L, Dwayne Miller RJ, Hasegawa T, Tanimura Y (2008) Two-dimensional fifth-order Raman spectroscopy of liquid formamide: Experiment and theory. *J Chem Phys* 128(23):234507.
49. Blank DA, Kaufman LJ, Fleming GR (1999) Fifth-order two-dimensional Raman spectra of CS$_2$ are dominated by third-order cascades. *J Chem Phys* 111(7):3105–3114.
50. Kuehn W, Reimann K, Woerner M, Elsaesser T (2009) Phase-resolved two-dimensional spectroscopy based on collinear n-wave mixing in the ultrafast time domain. *J Chem Phys* 130(16):164503.
51. Kuehn W, et al. (2011) Strong correlation of electronic and lattice excitations in GaAs/AlGaAs semiconductor quantum wells revealed by two-dimensional terahertz spectroscopy. *Phys Rev Lett* 107(6):067401.
52. Hamm P, Savolainen J (2012) 2D-Raman-THz spectroscopy of water: Theory. *J Chem Phys* 136(9):094516.
53. Hamm P, Savolainen J, Ono J, Tanimura Y (2012) Note: Inverted time-ordering in two-dimensional-Raman-terahertz spectroscopy of water. *J Chem Phys* 136(23):236101.
54. Schmuttenmaer CA (2004) Exploring dynamics in the far-infrared with terahertz spectroscopy. *Chem Rev* 104(4):1759–1779.
55. Lee Y-S (2010) *Principles of Terahertz Science and Technology* (Springer, Berlin).
56. Němec H, Kadlec K, Kužel P (2002) Methodology of an optical pump-terahertz probe experiment: An analytical frequency domain approach. *J Chem Phys* 117(18): 8454–8466.
57. Kindt JT, Schmuttenmaer CA (1999) Theory for determination of the low-frequency time-dependent response function in liquids using time-resolved terahertz pulse spectroscopy. *J Chem Phys* 110(17):8589–8596.
58. Kužel P, Kadlec F, Němec H (2007) Propagation of terahertz pulses in photoexcited media: Analytical theory for layered systems. *J Chem Phys* 127(2):024506.
59. Faure J, van Tilborg J, Kaindl RA, Leemans WP (2004) Modelling laser based table-top THz sources: Optical rectification, propagation and electro-optic sampling. *Opt Quantum Electron* 36:681–697.
60. Hahn EL (1950) Spin echoes. *Phys Rev* 80:580–594.
61. de Boeij WP, Pshenichnikov MS, Wiersma DA (1998) Ultrafast solvation dynamics explored by femtosecond photon echo spectroscopies. *Annu Rev Phys Chem* 49: 99–123.
62. Fayer MD (2001) Fast protein dynamics probed with infrared vibrational echo experiments. *Annu Rev Phys Chem* 52:315–356.
63. Hamm P, Zanni MT (2011) *Concepts and Methods of 2D Infrared Spectroscopy* (Cambridge Univ Press, Cambridge, UK).
64. Grest G, Nagel S, Rahman A (1980) Quench echoes in molecular dynamics–a new phonon spectroscopy. *Solid State Commun* 36(10):875–879.
65. Becker OM, Karplus M (1993) Temperature echoes in molecular dynamics simulations of proteins. *Phys Rev Lett* 70(22):3514–3517.
66. Matsubara E, Nagai M, Ashida M (2012) Ultrabroadband coherent electric field from far infrared to 200 THz using air plasma induced by 10 fs pulses. *Appl Phys Lett* 101(1): 011105.

Supporting Information

Savolainen et al. 10.1073/pnas.1317459110

SI Text

Fig. S1*A* shows the terahertz (THz) pulse in time and in frequency domain (*Inset*) and Fig. S1*B* an autocorrelation of the Raman pump pulse.

Fig. S2*A* shows a 1D cut along t_1 when increasing the Raman-pump intensity beyond the threshold for the generation of a solvated electron. Fig. S2*B* shows the polarization dependence of the 2D Raman-THz signal for 1D cut along t_1 with the Raman-pump intensity below that threshold.

SI Materials and Methods

Transfer Functions and Pulses. The calculation of the detected signal from a molecular response function $R(t', t'')$ using Eqs. **1** and **3** requires the precise knowledge of the input THz field E_{THz}, as well as the propagation effects for the emitted third-order field to the detection crystal (1). The latter is described on the level of a linear transfer function in the frequency domain $T_{total}(\omega)$. The schematic Fig. S3 shows that this total transfer function $T_{total}(\omega)$ includes contributions from the water jet $T_{water}(\omega)$, from the imaging optics $T_{image}(\omega)$, and the detection crystal $T_{crystal}(\omega)$. The experimental determination of all transfer functions as well as of the input THz field E_{THz} will be discussed below. The 800-nm Raman pump pulse I_{Raman}, which also enters Eq. **1**, experiences only negligible dispersion and absorption in the thin water jet, and has been modeled as a Gaussian pulse with FWHM of 110 fs (Fig. 1*B*).

The transfer function $T_{water}(\omega)$ can be determined experimentally by measuring the pulses transmitted through the whole setup with and without water jet, revealing E_{II} (Fig. S4*B*) and E_{I} (Fig. S4*A*), respectively:

$$T_{water}(\omega) = \frac{E_{\mathrm{II}}(\omega)}{E_{\mathrm{I}}(\omega)}. \qquad \textbf{[S1]}$$

The temporal shift of the pulse peak due to the index of refraction of water, resulting in a linear spectral phase, has been removed before Fourier transforming $E_{\mathrm{II}}(t)$ and $E_{\mathrm{I}}(t)$. As a good approximation of propagation effects within the water jet, we assume that the input THz pulse interacts in the middle of the water jet after propagating through its first half, and likewise, the emitted field is generated in the middle of the jet and propagates through the second half. Hence, one part of the water transfer function, modeled as $\sqrt{T_{water}(\omega)}$, will contribute to the input THz pulse (see Eq. **S5** below), and the second part $\sqrt{T_{water}(\omega)}$ to $T_{total}(\omega)$ (see Eq. **S4** below). A more accurate description of propagation effects of the interaction in the water jet would require a split-step Fourier method that models the water jet as even smaller slices, but because the water jet is already quite thin (40 µm), the present approximation is believed to capture the essence of the propagation effect well enough.

Subsequently, the emitted signal propagates from the sample position to the detection position experiencing $T_{image}(\omega)$, which can be determined by moving the detection crystal precisely at the sample position and measuring the THz field there (E_{III}, Fig. S4*C*), and then comparing it to the THz field measured at the detection crystal position (E_{I}, Fig. S4*A*):

$$T_{image}(\omega) = \frac{E_{\mathrm{I}}(\omega)}{E_{\mathrm{III}}(\omega)}. \qquad \textbf{[S2]}$$

Due to the high-aperture optics used, this transfer function is quite flat down to 0.3 THz.

Determining $T_{crystal}(\omega)$ is less straightforward. To obtain this transfer function, we generated a THz pulse at the sample position by moving the generation crystal, and by reducing the pump intensity dramatically to about 100 nJ, so that saturation effects in the generation process can be neglected. In that case, the emitted field would just be the first derivative of the generating pulse (a Gaussian pulse with 110-fs FWHM; Fig. S1*B*), if the generation crystal were free of dispersion and absorption (1–3). The measured field E_{IV} (Fig. S4*D*) is thus compared with such an idealized pulse E_{V} (Fig. S4*E*). In addition, we have to remove the effect of $T_{image}(\omega)$ from that measurement, so that we obtain for $T_{crystal}(\omega)$

$$T_{crystal}(\omega) = \frac{E_{\mathrm{IV}}(\omega)}{E_{\mathrm{V}}(\omega)} \cdot \frac{1}{T_{image}(\omega)}. \qquad \textbf{[S3]}$$

That procedure reveals the combined effect of both the generation and detection crystals. As we use identical crystals for both, we assume that $\sqrt{T_{crystal}(\omega)}$ describes the detection process and thus contributes to the total transfer function. With these ingredients, the total transfer function becomes

$$T_{total}(\omega) = \sqrt{T_{water}(\omega)} \cdot T_{image}(\omega) \cdot \sqrt{T_{crystal}(\omega)}. \qquad \textbf{[S4]}$$

All of the resulting transfer functions obtained from Eqs. **S1–S4** are presented in Fig. S5.

With the known transfer functions, we can also calculate the input THz pulse $E_{THz}(t)$ in the middle of the water jet, which enters Eq. **1**. To that end, we start from the pulse E_{III} measured at the sample position without water jet, propagate it through half the water jet, and take out the effect of the detection crystal (Fig. S4*F*, gray line):

$$E_{THz}(\omega) = E_{\mathrm{III}}(\omega) \frac{\sqrt{T_{water}(\omega)}}{\sqrt{T_{crystal}(\omega)}}. \qquad \textbf{[S5]}$$

The measurement of the transfer functions is noisy in regions where the spectral intensity of the pulses is low, i.e., below ~0.3 THz and above ~6 THz. We therefore fitted, and effectively extrapolated to zero and toward higher frequencies, the total transfer function T_{total} from Eq. **4**. We used a phenomenological function:

$$|T_{total}(\omega)| \propto \left(1 - e^{-\omega/\omega_1}\right) \frac{\omega_2^2}{\omega^2 + \omega_2^2} \qquad \textbf{[S6]}$$

for the amplitude, revealing $\omega_1 = 1.4$ THz and $\omega_2 = 1.9$ THz. The phase was fitted to a quadratic function:

$$\arg(T_{total}(\omega)) = \phi_0 + d\phi(\omega - \omega_0)^2, \qquad \textbf{[S7]}$$

with $\phi_0 = 0.25$, $d\phi_0 = -0.073$, and $\omega_0 = 1.0$ THz. The fits are shown in Fig. S4*D* (gray lines). Similarly, the transfer function in Eq. **S5** was fit to a phenomenological function:

$$\left| \frac{\sqrt{T_{water}(\omega)}}{\sqrt{T_{crystal}(\omega)}} \right| \propto a_1 e^{-\omega/\omega_1'} + e^{-\omega/\omega_2'}, \qquad \textbf{[S8]}$$

revealing $\omega_1' = 0.23$ THz, $a_1 = 5$, $\omega_2' = 7.2$ THz, and again to a quadratic function for the phase with $\phi_0' = 0.24$, $d\phi_0' = -0.13$, and $\omega_0' = 1.9$ THz.

Control of the Gouy Phase Shift. In the construction of the instrument response function, we must consider the well-known effect of the Gouy phase shift that varies the phase of a pulse when it passes through a focus (4–7). Unlike in conventional nonlinear spectroscopy, where many-cycle pulses are most commonly used, the absolute phase of the THz field in Eq. **1** in fact matters in 2D Raman-THz spectroscopy with half-cycle THz pulses. That is, the accumulated Gouy phase shift in the input THz field $E_{THz}(t)$ before the sample does not cancel out in the signal propagation after the sample (this effect will be discussed in detail in a separate publication). The Gouy phase modulates the THz field on a scale that equals the Rayleigh length, which in our case is of the order of only a few hundreds of micrometers because we use a small focus with high numerical aperture optics to achieve field amplitudes as high as possible. Consequently, the positioning of the crystals and the sample is critical within ∼100 μm. In the present work, we take care of the Gouy phase shift by precisely positioning the water jet and the crystals in the foci of the imaging optics.

The two elliptical mirrors were machined and mounted (without possibility of further alignment) in a way that we know the position of their foci with the help of an additionally designed alignment tool (i.e., a thin Al plate with a small pinhole of ∼200 μm positioned on a magnetic retention base). The estimated error in the positioning of the mirrors and the alignment tools is on the order of 100 μm. Further uncertainties originate from the additional optical path lengths introduced by the generation and detection crystals, both with thickness $d = 100$ μm and index of refraction of $n \sim 3$, which amounts to a shift of foci of $d(n-1) = 200$ μm in either case. As a starting point, we assumed that the nonlinear processes happen effectively in the middle of the crystals, but that assumption is weak in particular for the THz generation process, for which the GaP crystal is strongly pumped so that depletion effects due to two-photon absorption can no longer be neglected. The effect of the water jet ($d = 40$ μm, $n = 2$) on the optical path length is negligible.

With these uncertainties in mind, we positioned the crystals and the water jet in the following way. We first placed generation and detection crystals precisely at their predetermined foci using the alignment tool together with a confocal sensor (ConfocalDT, microepsilon, resolution ∼5 μm). The positioning was then optimized by observing the Gouy phase at the detection crystal position and trying to get a pulse $E_{\mathrm{I}}(t)$ as symmetric as possible (Fig. S4*A*), resulting in a shift of the latter of ∼130 μm toward the elliptical mirror, which is consistent with the effect of the additional optical path length introduced by both crystals. The detection crystal was subsequently moved to the sample position at its predetermined focus, where the pulse entering the sample $E_{\mathrm{III}}(t)$ (Fig. S4*C*) was measured. The pulse is slightly asymmetric, in contrast with $E_{\mathrm{I}}(t)$ (Fig. S4*A*), whose Gouy phase has been optimized, and we assume the asymmetry to be the result of the combined uncertainties in the determination of the positions of the foci. We therefore allowed for a small correcting phase ϕ for the input THz pulse and replaced Eq. **S5** by

$$E_{THz}(\omega) = e^{i\phi} E_{\mathrm{III}}(\omega) \frac{\sqrt{T_{water}(\omega)}}{\sqrt{T_{crystal}(\omega)}}. \qquad \textbf{[S9]}$$

The resulting pulse is shown in Fig. S4*F*, black line. We also added a compensating phase to the emitted field:

$$T_{total}(\omega) = e^{-i\phi} \sqrt{T_{water}(\omega)} \cdot T_{image}(\omega) \cdot \sqrt{T_{crystal}(\omega)}. \qquad \textbf{[S10]}$$

The value of that phase, $\phi = 0.4$, has been determined by matching the antidiagonal ridge of the instrument response function (IRF) and the amplitude ratio of its positive and negative peaks around $t_1 = t_2 = 0$ (Fig. 2*C*) to the corresponding features I and II in the experimental data (Fig. 2*B*). We thereby assumed that these features originate from an essentially instantaneous part of the water response function such as from the electronic polarizability or the librational modes of water. We independently measured that a Gouy phase of $\phi = 0.4$ corresponds to a shift of the foci of 150 μm, which is well within the uncertainty of our alignment procedure. Note that even substantially larger phase corrections have no effect on the comparison shown in Fig. 4; the diagonal decay of the experimental data will always remain significantly slower than that of the IRF.

1. Němec H, Kadlec K, Kužel P (2002) Methodology of an optical pump-terahertz probe experiment: An analytical frequency domain approach. *J Chem Phys* 117(18):8454–8466.
2. Faure J, van Tilborg J, Kaindl RA, Leemans WP (2004) Modelling laser based table-top THz sources: Optical rectification, propagation and electro-optic sampling. *Opt Quantum Electron* 36:681–697.
3. Kindt JT, Schmuttenmaer CA (1999) Theory for determination of the low-frequency time-dependent response function in liquids using time-resolved terahertz pulse spectroscopy. *J Chem Phys* 110(17):8589–8596.
4. Feng S, Winful HG, Hellwarth RW (1998) Gouy shift and temporal reshaping of focused single-cycle electromagnetic pulses. *Opt Lett* 23(5):385–387.
5. Kužel P, Khazan MA, Kroupa J (1999) Spatiotemporal transformations of ultrashort terahertz pulses. *J Opt Soc Am B* 16:1795–1800.
6. Ruffin AB, Rudd JV, Whitaker JF, Feng S, Winful HG (1999) Direct observation of the Gouy phase shift with single-cycle terahertz pulses. *Phys Rev Lett* 83(17):3410–3413.
7. Feurer T, Stoyanov NS, Ward DW, Nelson KA (2002) Direct visualization of the Gouy phase by focusing phonon polaritons. *Phys Rev Lett* 88(25):257402.

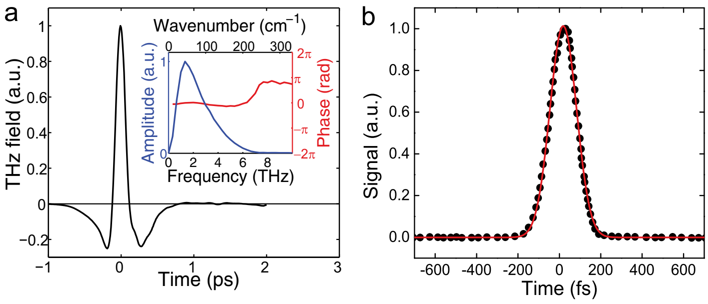

Fig. S1. (*A*) THz pulse in time domain. (*Inset*) Amplitude and phase in frequency domain. (*B*) Raman pulse autocorrelation (black dots) and Gaussian fit (red line).

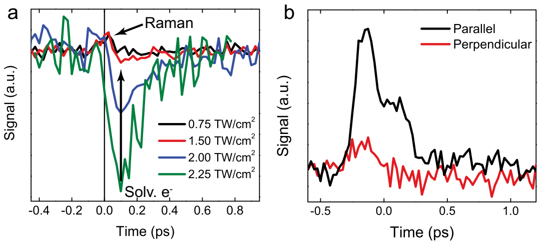

Fig. S2. Verifying the origin of the 2D Raman-THz signal. (*A*) The emerging Raman-induced signal and the vanishing solvated electron signal with decreasing Raman pulse fluency. (*B*) The dependency of the 2D Raman-THz signal on the polarization between the Raman and THz pulses. The transfer functions and the setting of the Gouy phase in these measurements were different from Fig. 2, but the data within one measurement series are self-consistent.

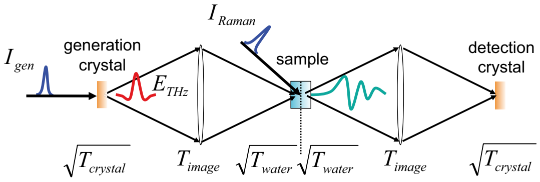

Fig. S3. Two-dimensional Raman-THz experimental scheme. Shown are the generated THz field (red), Raman pump pulse (blue), and the emitted field (green). Also shown are the transfer functions that describe the propagation effects in the sample (T_{water}), for either one of the imaging optics (T_{image}), and the combined effects of generation and detection in the crystals ($T_{crystal}$).

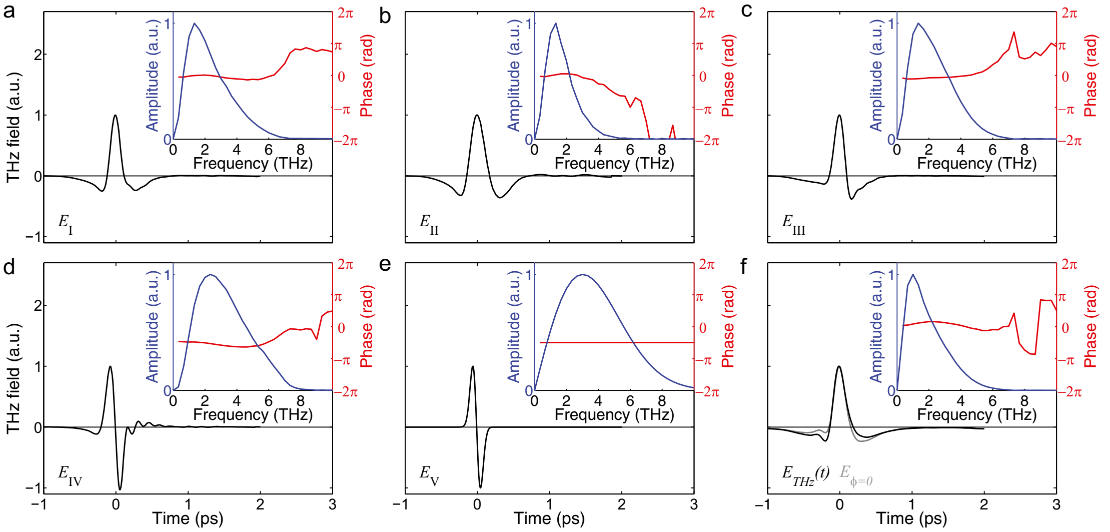

Fig. S4. (*Insets*) Electric fields of the THz pulses in time and frequency domain. (*A*) E_I, pulse measured at detection position. (*B*) E_II, pulse measured at detection position having the water sample in the beam. (*C*) E_III, pulse measured at the sample position. (*D*) E_IV, pulse created at the sample position with low energy. (*E*) E_V, idealized THz pulse without any propagation effects. (*F*) $E_{THz}(t)$ pulse halfway in the sample (black line, Eq. **S9**) and for comparison the pulse without any extra phase added (gray line, Eq. **S5**).

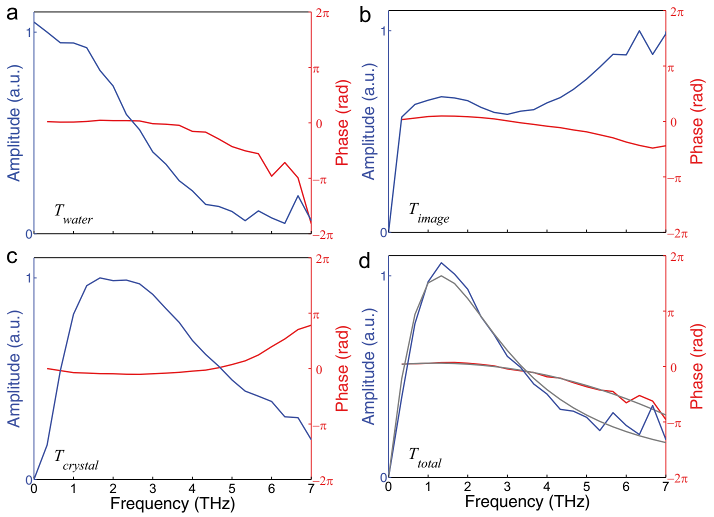

Fig. S5. Transfer functions. (*A*) $T_{water}(\omega)$, (*B*) $T_{image}(\omega)$, (*C*) $T_{crystal}(\omega)$, and (*D*) $T_{total}(\omega)$. The gray lines show the fitted amplitude and phase functions.

A.5 Direct observation of the collapse of the delocalized excess electron in water

Reprinted from ref. [101], with the permission of Nature Publishing Group (Macmillan Publishers Limited).

A.5.1 Contribution to this paper

- Saima Ahmed performed the experiments with Dr. Janne Savolainen.
- Saima Ahmed helped in analysing the experimental data.

nature chemistry

ARTICLES

PUBLISHED ONLINE: 6 JULY 2014 | DOI: 10.1038/NCHEM.1995

Direct observation of the collapse of the delocalized excess electron in water

Janne Savolainen[1]†, Frank Uhlig[2]†, Saima Ahmed[1], Peter Hamm[1]* and Pavel Jungwirth[2]*

It is generally assumed that the hydrated electron occupies a quasi-spherical cavity surrounded by only a few water molecules in its equilibrated state. However, in the very moment of its generation, before water has had time to respond to the extra charge, it is expected to be significantly larger in size. According to a particle-in-a-box picture, the frequency of its absorption spectrum is a sensitive measure of the initial size of the electronic wavefunction. Here, using transient terahertz spectroscopy, we show that the excess electron initially absorbs in the far-infrared at a frequency for which accompanying *ab initio* molecular dynamics simulations estimate an initial delocalization length of ≈40 Å. The electron subsequently shrinks due to solvation and thereby leaves the terahertz observation window very quickly, within ≈200 fs.

One of the simplest transient species—the hydrated, or aqueous electron (e^-_{aq})—is a highly reactive intermediate and, as such, an important entity in radiation chemistry[1,2]. Perhaps even more compellingly, e^-_{aq} is the simplest case of a quantum particle in a complex chemical and thermal environment, an object of great fundamental interest that has challenged researchers since its discovery[3,4]. To appreciate the system in full, it is vital to understand the initial steps from photodetachment to e^-_{aq} formation. Femtosecond pump–probe experiments have been used to unravel details of the equilibration processes following trapping by the solvent[5–12]. In addition, picosecond measurements on the recombination kinetics of e^-_{aq} have described the ejected electron's migration lengths from its geminate partners[13–22]. These studies evoke a picture of an excess electron that is first delocalized in the conduction band and then localizes to the hydrated electron e^-_{aq} within about a picosecond. According to a simple particle-in-a-box picture, such a localization should be accompanied by a shift in the absorption spectrum from potentially the terahertz or even gigahertz regions through the mid-infrared and to the visible (VIS) spectral range. Indeed, the latter stages of this process have been observed in femtosecond pump–probe experiments in the mid-infared[9–11,23,24] or near-infrared (NIR)/VIS regime[10,14,24], but the initial frequency at which this process starts, which is directly related to the initial degree of delocalization of the excess electron, has not yet been explored.

According to current knowledge there is a threshold in the photodetachment between molecular-based mechanisms and bulk excitation to delocalized states[17,21]. With high enough energies given to the ejected electron, the conduction band can be reached directly, leaving the nuclear positions unchanged. Given the inhomogeneity in the water hydrogen-bonding network, the threshold energy for this vertical ionization mechanism is ∼9.8–9.9 eV (ref. 21), ∼0.5–1 eV below the vacuum level (it should be added, however, that other works have estimated a much smaller width of the conduction band based on an extrapolation from clusters[25]). Below this threshold, the conduction band is not directly accessible and e_{aq} is formed via mechanisms involving nuclear degrees of freedom in the sense of solvation.

The electronic structure of e^-_{aq} is understood to be *s*-like in character, with the absorption relating primarily to the $s \rightarrow p$ transition. Rossky and co-workers have pioneered this interpretation based on pseudopotential calculations[26], revealing an e^-_{aq} that occupies a quasi-spherical cavity with a radius of ∼2.5 Å surrounded by four to six water molecules. Recent *ab initio* molecular dynamics simulations have shown that e^-_{aq} has a rather complex structure. Its largest part resides in a cavity, but there is also a sizeable diffuse part, as well as a significant part that overlaps with the surrounding water molecules[27]. This picture lies somewhere between the consensus based on most pseudopotential calculations[26,28] and a rival new pseudopotential model that predicts a significantly larger strongly delocalized hydrated electron, even in the equilibrated ground state[29,30]. Note that an *ab initio* molecular dynamics approach by construction accounts for more quantum electronic structure effects than pseudopotentials, with the latter also being more prone to potential parameterization artefacts.

The terahertz response of a solvated electron has been exploited before, but only in *n*-hexane, in which solvation is so weak that the electron remains delocalized for a very long time[31]. Here, we extend the concept to water. That is, we present direct evidence of a (very short-lived) delocalized electron immediately after photoionization using optical-pump–terahertz-probe spectroscopy, and follow its localization upon solvation. Corresponding *ab initio* molecular dynamics simulations capture the subsequent stages of electron localization, thereby bridging the domains of the present time-resolved terahertz measurement and the previous ultrafast experiments in the mid-infrared to VIS spectral regimes[9–11,14,23,24].

Results

Experimental. Figure 1 presents the terahertz response of the excess electron in water as a function of the pump–probe delay time t_{pp}, with the terahertz scanning time t_{THz} kept fixed to the peak of the terahertz probe field. Pump pulses at 266 nm, 400 nm and 800 nm were used with irradiances of 0.08 TW cm^{-2}, 0.3 TW cm^{-2} and 1.9 TW cm^{-2}, respectively, which resulted in e^-_{aq} concentrations of 20 μM, 110 μM and 65 μM, as determined from accompanying experiments using a 800 nm probe pulse (Supplementary Fig. 4)[32]. Although it is well established that pumping at 266 nm and 400 nm generates e^-_{aq} by multiphoton processes, the photolysis of neat water with 800 nm (1.54 eV) pulses has been explored much less[33,34], because the ionization process is not nearly as well characterized. The matching

---

[1]Department of Chemistry, University of Zurich, Winterthurerstrasse 190, CH-8057 Zurich, Switzerland, [2]Institute of Organic Chemistry and Biochemistry, Academy of Sciences of the Czech Republic, Flemingovo nam. 2, 16610 Prague 6, Czech Republic; †These authors contributed equally to this work. *e-mail: phamm@pci.uzh.ch; pavel.jungwirth@marge.uochb.cas.cz

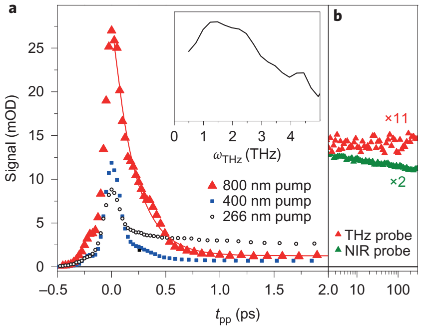

Figure 1 | Terahertz response to photoionization of neat water. a, The 800 nm pump (red triangles) with a single exponential fit (200 fs, red line), 400 nm pump (blue filled squares) and 266 nm pump (open black circles). The 400 and 266 nm pump traces are scaled to the e^-_{aq} concentration in the 800 nm pump measurement. Inset: spectral signature of the excess electron upon 800 nm pumping deduced from a two-dimensional scan. This initial spectrum peaks at ~1.5 THz. **b**, The long-time terahertz response with the 800 nm pump (red, scaled by factor of 11) remains constant, whereas the response probed at NIR shows clearly the geminate recombination kinetics (green).

irradiance dependencies of the terahertz and NIR responses shown in Supplementary Fig. 2 prove that the terahertz signal indeed originates from excess electrons for all pump wavelengths. The 266 nm and 400 nm pump data follow the expected second- and third-order power laws[24,35], whereas the 800 nm pump signal depicts a threshold behaviour with ~1 TW cm^{-2} as the onset of ionization. Such a threshold behaviour indicates that a strong-field ionization rather than a multiphoton mechanism is behind the photo detachment with 800 nm photons, in accordance with the conclusions from ref. 34. The signal drop with circularly polarized pump light shown in Supplementary Fig. 3 also provides strong evidence for that interpretation[36].

Geminate recombination of e^-_{aq} proceeds in a diffusive manner and hence is a measure of the initial delocalization length, which in turn has been shown to depend on the excitation energy[14,18–21,37,38]. Supplementary Fig. 4 shows the recombination kinetics measured for 266 nm, 400 nm and 800 nm pumping, respectively. Comparing the recombination kinetics with refs 20 and 21, we estimate that 800 nm pumping results in an effective excitation energy of 12.4 eV and an average ejection length of ~38 Å. At this energy the electron reaches the conduction band vertically[19], or even states above the vacuum level (which we expect to relax very quickly in bulk solution).

With this in mind, we return to the discussion of the terahertz response (Fig. 1). During the first few hundred femtoseconds, the terahertz responses for all pump wavelengths exhibit a fast rise to a peak value followed by a decay (Fig. 1a). The 800 nm pump trace has the largest amplitude and an initial decay with a time constant of ~0.2 ps down to a small offset that remains constant until the end of the scanning range (Fig. 1b, red). The asymmetric shape of the initial signal indicates that the decay is not instrument-response-limited. The 266 nm pump trace, in contrast, initially exhibits a much sharper symmetric spike, which we consider to represent the instrument response. The long-term offset decays gradually afterwards. The 400 nm pump trace has an intermediate behaviour with some sub-picosecond decay after the instrument-response-limited peak. With respect to the initial evolution of the ejected electron, the 800 nm pump data are the most conclusive, and will be the subject of further discussion here.

The inset of Fig. 1a shows the spectral signature of the water response upon 800 nm pumping, which has been extracted from a full two-dimensional data set along both the pump–probe delay time t_{pp} and terahertz scanning time t_{THz} (Supplementary Fig. 5 see Supplementary Information for details, Fig. 1a)[39,40]. The spectral response shows a broad band peaking at ~1.5 THz, with a long tail towards larger frequencies. In essence, the band shown in the inset of Fig. 1a decays according to the red line of Fig.1a, but the sensitivity of the method to details of the data does not allow us to extract an additional time evolution of the spectral response as it decays.

The terahertz response could be of an electronic nature or due to a change in the nuclear spectrum of a perturbed water network. For example, the change in the molar extinction coefficient of water induced by dissolving NaCl is $\sim 1 \times 10^{-2}\ mM^{-1}\ cm^{-1}$ (ref. 41). Assuming that e^-_{aq} and the geminate partners have a similar effect on the terahertz water spectrum, the induced absorption change would be as small as <0.05 mOD at the concentration of e^-_{aq} generated in our experiment—several orders of magnitude smaller than the detected signal. The temperature jump induced by the pump process also disturbs the water network to a certain extent, but we estimate a temperature jump of ~0.2 °C, which in turn would result in an increase in terahertz water absorption of ~0.4 mOD (ref. 42), again not sufficient to explain the detected signal peaking at ~27 mOD.

On the other hand, the ~1 mOD signal size of the long-time offset (Fig. 1b, red) is in fair agreement with our estimate of a temperature effect. Indeed, that signal stays constant in time up to 300 ps, as expected for a temperature jump, whereas the NIR-probe signal (Fig. 1b, green), which probes geminate recombination of e^-_{aq} , does decay a little. However, it should be noted that a long-time signal is also observed for 266 nm and 400 nm pumping, which is larger and not constant in time but instead parallels geminate recombination, so it cannot be due exclusively to heating. The effect is not understood at present, and is probably related to the smaller ejection length and different detachment mechanisms at these pump wavelengths.

Nonetheless, the large amplitude of the initial terahertz signal upon 800 nm pumping can only be explained as an electronic response. The signal size of the initial peak for terahertz probing and that observed after equilibration in the NIR regime are of similar magnitudes (that is, ~27 mOD and 7 mOD, respectively, Fig. 1a and Supplementary Fig. 4). This equivalence is expected for a particle-in-a-box description with an oscillator strength $f \propto \nu\ |\mu|^2$, whose transition frequency ν scales as $1/r_g^2$ (where r_g is the dimension of the box) and the transition dipole μ as r_g. Hence, as the initially delocalized electron localizes, its frequency and thus its size vary over a wide range (by factors of 300 or 0.06, respectively), while its oscillator strength stays constant (within a factor of 4). Another interesting aspect of the terahertz response is the complete lack of anisotropy (Supplementary Fig. 3) indicating that the ejected electron has spherical symmetry from the very beginning, as expected for an *s*-like wavefunction.

Computational. To aid the interpretation of the experiment and to put it onto more quantitative grounds, we modelled the localization process with *ab initio* molecular dynamics (AIMD) simulations. The averaged time evolution of r_g and of the lowest excitation energy are shown in Fig. 2 together with the mean deviations. An exponential fit of the averaged r_g reveals a time constant of 1 ps. At the moment of electron attachment to the neutral water system, the excitation energies for the excess electron are strongly redshifted compared to the optical absorption of a hydrated electron in equilibrium. However, as the excess electron localizes and shrinks, the optical spectrum converges to that of a hydrated electron.

The maximum size of the attached electron in our simulations is limited by the size of the quantum-mechanical (QM) subsystem to ~7 Å. The simulations thus aim at filling the gap between the

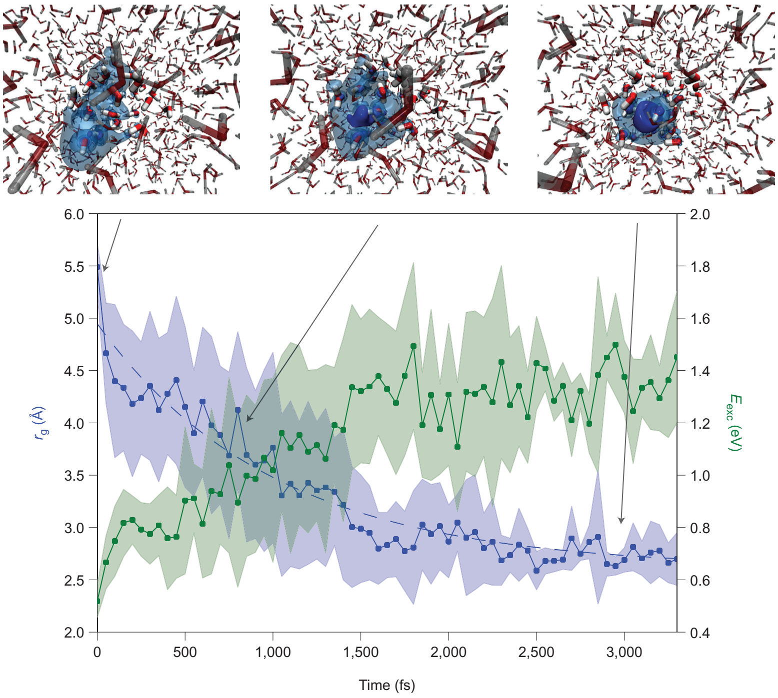

Figure 2 | Averaged radius of gyration r_g (blue) and lowest excitation energy (green) of an excess electron attached to neat water system as a function of time. Data are calculated every 50 fs using time-dependent density functional theory (TD-DFT) and are presented together with shading depicting the corresponding mean deviations and an exponential fit with a 1 ps time constant (dashed line). Three exemplary snapshots along a representative trajectory are presented above the plot, with isosurfaces of the spin density shown in blue (transparent at 0.0001 and opaque at 0.001 Bohr^{-3}). The QM water molecules are shown in an opaque licorice representation and MM water molecules in a transparent licorice representation.

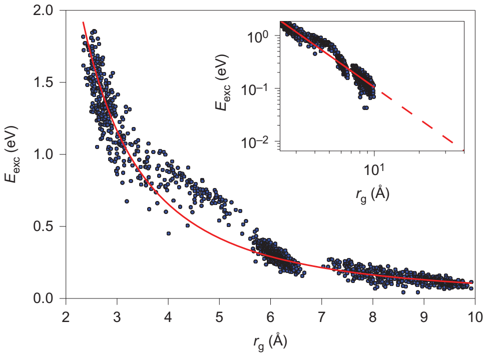

Figure 3 | Correlation between radius of gyration r_g of the spin density and first excitation energy (blue dots). Red line shows fit of data to a/r_g^2 with $a = 10.5$ eV Å^2 (covariance $\sigma = 2 \times 10^{-3}$ eV Å^2). This fit is very close to that obtained using parameters for a three-dimensional particle-in-a-box with the mass of an electron (Supplementary Section II.B and Supplementary Fig. 6) Inset: the same data in a log–log plot with extended r_g axis and correspondingly extended fit curve (dashed).

initially strongly delocalized electron absorbing in the terahertz region and the (practically) localized electron probed in the NIR spectral region. To get even closer to the experimentally measured absorption in the terahertz region, additional electron attachment calculations to neat water systems with larger QM subsystems (either 64 QM and 960 molecular mechanical (MM) H_2O, or 256 QM and 3886 QM H_2O) have been performed. In this case, we recorded only the initial size ($t = 0$) of an excess electron attached to snapshots sampled from six trajectories of neat water covering almost 30 ps, yielding electron sizes of around 7 Å.

Figure 3 depicts the first excitation energy plotted against the r_g of the excess electron from all the above simulations. The dependence is reminiscent of the behaviour of a particle-in-a-box system. However, we have shown previously that the hydrated electron is of a much more complex nature[27]. Nevertheless, it is still possible to fit the data accurately using a particle-in-a-box formula, that is, the a/r_g^2 relationship, which indicates that this behaviour of the hydrated electron is rather robust with respect to the particular model employed for its description[28]. The present fitting allows us to extrapolate to size and excitation energy ranges that are not directly accessible to the AIMD simulations. Although the simulated data exhibit a certain spread, they can clearly be fitted to a straight line in the log–log plot, and faithfully extended to electron sizes pertinent to the terahertz region. From such an extrapolation, the radius of gyration of an excess electron with a first excitation

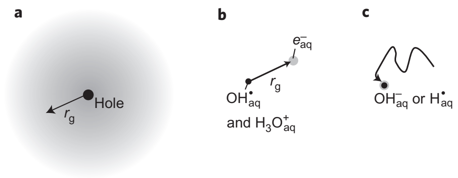

Figure 4 | Schematic depiction of excess electron formation and localization process in water. a, Ejected delocalized excess electron (in grey) with radius r_g. **b**, Collapse of the electron wavefunction, which will result in an average ejection length r_g. **c**, Diffusive geminate recombination.

energy of 1.5 THz, as determined experimentally (Fig. 1a, inset), would be ~40 Å (see fit in Fig. 3). It is remarkable that this number is very close to the ejection length, which has been estimated independently from the recombination kinetics (Supplementary Fig. 4) along the lines of ref. 21.

Discussion

The picture that emerges from our combined experimental–theoretical study is depicted schematically in Fig. 4. The initially generated electron is rather delocalized with a radius r_g of at least 40 Å (we cannot entirely rule out that electron delocalization is even larger at the very moment of the photoionization event). It is reasonable to assume that the initially generated electron is essentially centred around the ionized water molecule (Fig. 4a). The water molecules then solvate the electron and its size reduces considerably. If the probability of becoming trapped at a particular position is proportional to the initial electron density, then the mean distance of the localized electron from the origin roughly equals its original radius of gyration (Fig. 4b), explaining why initial delocalization length and final ejection length are the same, within error. During the complete collapse of the electron wavefunction (occurring on a 1 ps timescale; Fig. 2), the absorption sweeps from the terahertz into the NIR regime. That is, it leaves our terahertz observation window after ~200 fs (Fig. 1), then appears in the mid-IR[9–11,23,24] and eventually the NIR spectral range upon full solvation[10,14,24]. Subsequently, the hydrated electron recombines in a diffusive process on a much slower timescale (Fig. 4c).

In conclusion, time-resolved terahertz spectroscopy captures the early stages of the photodetached electron and furthermore provides a direct measure of its initial size. The ejection length after solvation agrees extremely well with the initial size of the electron estimated from the terahertz experiment and *ab initio* molecular dynamics simulations. To date, the only experimental measure of the initial size of the electron has used the geminate recombination kinetics of the e^-_{aq}/hole pair as an indirect 'ruler', the standing hypothesis being that the ejection length is directly related to the initial size of the electron's wavefunction[19]. However, seeing is believing, and we can now conclude that this assumption is indeed correct, at least in the case of above-threshold photolysis. Thus, our experimental and computational studies paint a more complete picture of the initial steps involved in e^-_{aq} formation, with the electron resonance sweeping continuously through the spectrum from the terahertz regime into the NIR regime as the electron localizes. The work paves the way towards understanding water's character as a temporary liquid semiconductor.

Methods

The response of the excess electron in water was measured using an optical-pump terahertz-probe set-up[43] with the spectrum of the terahertz pulses peaking at ~1.0 THz and covering a bandwidth of ~0.3–5 THz. For the AIMD simulations an electron was vertically attached into the conduction band (which is 0.5–1 eV below the vacuum level according to our AIMD model) to a neat water system of 32 QM water molecules surrounded by 992 MM water molecules with periodic boundary conditions. Data were collected from seven independent trajectories. The optical spectrum was calculated along the trajectories every 50 fs. The size of the excess electron during localization was taken as the radius of gyration of the spin density (see Supplementary Information Section II for details).

Received 19 December 2013; accepted 4 June 2013;

References

1. Garrett, B. C. *et al.* Role of water in electron-initiated processes and radical chemistry: issues and scientific advances. *Chem. Rev.* **105,** 355–389 (2005).
2. Young, R. M. & Neumark, D. M. Dynamics of solvated electrons in clusters. *Chem. Rev.* **112,** 5553–5577 (2012).
3. Hart, E. J. & Boag, J. W. Absorption spectrum of hydrated electron in water and in aqueous solutions. *J. Am. Chem. Soc.* **84,** 4090–4095 (1962).
4. Boag, J. W. & Hart, E. J. Absorption spectra in irradiated water and some solutions—absorption spectra of hydrated electron. *Nature* **197,** 45–47 (1963).
5. Chase, W. J. & Hunt, J. W. Solvation time of electron in polar liquids—water and alcohols. *J. Phys. Chem.* **79,** 2835–2845 (1975).
6. Wiesenfeld, J. M. & Ippen, E. P. Dynamics of electron solvation in liquid water. *Chem. Phys. Lett.* **73,** 47–50 (1980).
7. Migus, A., Gauduel, Y., Martin, J. L. & Antonetti, A. Excess electrons in liquid water—first evidence of a prehydrated state with femtosecond lifetime. *Phys. Rev. Lett.* **58,** 1559–1562 (1987).
8. McGowen, J. L., Ajo, H. M., Zhang, J. Z. & Schwartz, B. J. Femtosecond studies of hydrated electron recombination following multiphoton ionization at 390-nm. *Chem. Phys. Lett.* **231,** 504–510 (1994).
9. Pepin, C., Goulet, T., Houde, D. & Jay-Gerin, J. P. Observation of a continuous spectral shift in the solvation kinetics of electrons in neat liquid deuterated water. *J. Phys. Chem. A* **101,** 4351–4360 (1997).
10. Laenen, R., Roth, T. & Laubereau, A. Novel precursors of solvated electrons in water: evidence for a charge transfer process. *Phys. Rev. Lett.* **85,** 50–53 (2000).
11. Vilchiz, V. H., Kloepfer, J. A., Germaine, A. C., Lenchenkov, V. A. & Bradforth, S. E. Map for the relaxation dynamics of hot photoelectrons injected into liquid water via anion threshold photodetachment and above threshold solvent ionization. *J. Phys. Chem. A* **105,** 1711–1723 (2001).
12. Laenen, R. & Roth, T. Generation of solvated electrons in neat water: new results from femtosecond spectroscopy. *J. Mol. Struct.* **598,** 37–43 (2001).
13. Crowell, R. A. & Bartels, D. M. Multiphoton ionization of liquid water with 3.0–5.0 eV photons. *J. Phys. Chem.* **100,** 17940–17949 (1996).
14. Thomsen, C. L., Madsen, D., Keiding, S. R., Thogersen, J. & Christiansen, O. Two-photon dissociation and ionization of liquid water studied by femtosecond transient absorption spectroscopy. *J. Chem. Phys.* **110,** 3453–3462 (1999).
15. Bartels, D. M. & Crowell, R. A. Photoionization yield vs energy in H_2O and D_2O. *J. Phys. Chem. A* **104,** 3349–3355 (2000).
16. Sander, M. U., Gudiksen, M. S., Luther, K. & Troe, J. Liquid water ionization: mechanistic implications of the H/D isotope effect in the geminate recombination of hydrated electrons. *Chem. Phys.* **258,** 257–265 (2000).
17. Son, D. H., Kambhampati, P., Kee, T. W. & Barbara, P. F. Delocalizing electrons in water with light. *J. Phys. Chem. A* **105,** 8269–8272 (2001).
18. Kee, T. W., Son, D. H., Kambhampati, P. & Barbara, P. F. A unified electron transfer model for the different precursors and excited states of the hydrated electron. *J. Phys. Chem. A* **105,** 8434–8439 (2001).
19. Kambhampati, P., Son, D. H., Kee, T. W. & Barbara, P. F. Solvation dynamics of the hydrated electron depends on its initial degree of electron delocalization. *J. Phys. Chem. A* **106,** 2374–2378 (2002).
20. Lian, R., Oulianov, D. A., Shkrob, I. A. & Crowell, R. A. Geminate recombination of electrons generated by above-the-gap (12.4 eV) photoionization of liquid water. *Chem. Phys. Lett.* **398,** 102–106 (2004).
21. Elles, C. G., Jailaubekov, A. E., Crowell, R. A. & Bradforth, S. E. Excitation-energy dependence of the mechanism for two-photon ionization of liquid H_2O and D_2O from 8.3 to 12.4 eV. *J. Chem. Phys.* **125,** 044515 (2006).
22. Kratz, S., Torres-Alacan, J., Urbanek, J., Lindner, J. & Vöhringer, P. Geminate recombination of hydrated electrons in liquid-to-supercritical water studied by ultrafast time-resolved spectroscopy. *Phys. Chem. Chem. Phys.* **12,** 12169–12176 (2010).
23. Hertwig, A., Hippler, H. & Unterreiner, A. N. Transient spectra, formation, and geminate recombination of solvated electrons in pure water UV-photolysis: an alternative view. *Phys. Chem. Chem. Phys.* **1,** 5633–5642 (1999).
24. Birkedal, V. *et al.* Observation of a persistent infrared absorption following two photon ionization of liquid water. *Chem. Phys.* **328,** 119–124 (2006).
25. Coe, J. V. *et al.* Using cluster studies to approach the electronic structure of bulk water: reassessing the vacuum level, conduction band edge, and band gap of water. *J. Chem. Phys.* **107,** 6023–6031 (1997).
26. Turi, L. & Rossky, P. J. Theoretical studies of spectroscopy and dynamics of hydrated electrons. *Chem. Rev.* **112,** 5641–5674 (2012).
27. Uhlig, F., Marsalek, O. & Jungwirth, P. Unraveling the complex nature of the hydrated electron. *J. Phys. Chem. Lett.* **3,** 3071–3075 (2012).

28. Jacobson, L. D. & Herbert, J. M. Theoretical characterization of four distinct isomer types in hydrated-electron clusters, and proposed assignments for photoelectron spectra of water cluster anions. *J. Am. Chem. Soc.* **133,** 19889–19899 (2011).
29. Larsen, R. E., Glover, W. J. & Schwartz, B. J. Does the hydrated electron occupy a cavity? *Science* **329,** 65–69 (2010).
30. Casey, J. R., Kahros, A. & Schwartz, B. J. To be or not to be in a cavity: the hydrated electron dilemma. *J. Phys. Chem. B* **117,** 14173–14182 (2013).
31. Knoesel, E., Bonn, M., Shan, J. & Heinz, T. F. Charge transport and carrier dynamics in liquids probed by THz time-domain spectroscopy. *Phys. Rev. Lett.* **86,** 340–343 (2001).
32. Hare, P. M., Price, E. A. & Bartels, D. M. Hydrated electron extinction coefficient revisited. *J. Phys. Chem. A* **112,** 6800–6802 (2008).
33. Brown, M. S., Erickson, T., Frische, K. & Roquemore, W. M. Hot electron dominated rapid transverse ionization growth in liquid water. *Opt. Express* **19,** 12241 (2011).
34. Li, J., Nie, Z., Zheng, Y. Y., Dong, S. & Loh, Z-H. Elementary electron and ion dynamics in ionized liquid water. *J. Phys. Chem. Lett.* **4,** 3698–3703 (2013).
35. Crowell, R. A. *et al.* Light-induced temperature jump causes power-dependent ultrafast kinetics of electrons generated in multiphoton ionization of liquid water. *J. Phys. Chem. A* **108,** 9105–9114 (2004).
36. Mics, Z. *et al.* Nonresonant ionization of oxygen molecules by femtosecond pulses: plasma dynamics studied by time-resolved terahertz spectroscopy. *J. Chem. Phys.* **123,** 104310 (2005).
37. Pimblott, S. M. Independent pairs modeling of the kinetics following the photoionization of liquid water. *J. Phys. Chem.* **95,** 6946–6951 (1991).
38. Goulet, T. & Jay-Gerin, J. P. On the reactions of hydrated electrons with $OH^{\bullet}$ and H_3O^+—analysis of photoionization experiments. *J. Chem. Phys.* **96,** 5076–5087 (1992).
39. Němec, H., Kadlec, K. & Kužel, P. Methodology of an optical pump–terahertz probe experiment: an analytical frequency domain approach. *J. Chem. Phys.* **117,** 8454 (2002).
40. Kužel, P., Němec, H. & Kadlec, K. Propagation of THz pulses in photoexcited media: analytical theory for layered systems. *J. Chem. Phys.* **127,** 024506 (2007).
41. Xu, J., Plaxco, K. W., Allen, S. J., Bjarnason, J. E. & Brown, E. R. 0.15–3.72 THz absorption of aqueous salts and saline solutions. *Appl. Phys. Lett.* **90,** 031908 (2007).
42. Zelsmann, H. R. Temperature-dependence of the optical-constants for liquid H_2O and D_2O in the far IR region. *J. Mol. Struct.* **350,** 95–114 (1995).
43. Savolainen, J., Ahmed, S. & Hamm, P. Two-dimensional Raman-terahertz spectroscopy of water. *Proc. Natl Acad. Sci. USA* **110,** 20402–20407 (2013).

Acknowledgements

The authors thank S. Bradforth and P. Kužel for discussions. The work was supported in part by the Swiss National Science Foundation (SNF) through the NCCR MUST. P.J. acknowledges the Czech Science Foundation (grant P208/12/G016) for support and thanks the Academy of Sciences for the Praemium Academie award. F.U. and P.J. also acknowledge the computing time granted by the John von Neumann Institute for Computing (NIC) and provided on the supercomputer JUROPA at Jülich Supercomputing Centre (JSC).

Author contributions

J.S. and P.H. designed the experiments and analysed the data. J.S. and S.A. performed the experiments. P.J. and F.U. designed and analysed the computational part of the study and FU performed the calculations. P.H., P.J. and J.S. co-wrote the paper. J.S. and F.U. contributed equally to this work.

Additional information

Supplementary information is available in the online version of the paper. Reprints and permissions information is available online at www.nature.com/reprints. Correspondence and requests for materials should be addressed to P.H. and P.J.

Competing financial interests

The authors declare no competing financial interests.

nature chemistry
SUPPLEMENTARY INFORMATION
DOI: 10.1038/NCHEM.1995

Direct Observation of the Collapse of the Delocalized Excess Electron in Water

Janne Savolainen[1*], Frank Uhlig[2*], Saima Ahmed[1], Peter Hamm[1#], Pavel Jungwirth[2#]

[1]*Department of Chemistry, University of Zurich,*
Winterthurerstrasse 190, CH-8057 Zurich, Switzerland
[2]*Institute of Organic Chemistry and Biochemistry,*
Academy of Sciences of the Czech Republic,
Flemingovo nam. 2, 16610 Prague 6, Czech Republic

Contents

I. EXPERIMENTAL PROCEDURES

A. Experimental Setup

A schematic representation of the optical-pump THz-probe spectrometer used in the experiments is presented in Supplementary Figure 1. The setup is driven by an amplified 5-kHz laser system (Spectra Physics) that provided 110-fs, 800-nm pulses for all the experiments. A small portion of the laser output was used to create and detect the THz probing pulses in two 0.1-mm-thick (110)GaP crystals by optical rectification and electro-optic sampling, respectively. THz generation beam was chopped at a quarter of the laser frequency and focused to the generation crystal to a spot size of 50 μm. Pulse energy was 10 μJ resulting in a clean half-cycle THz pulse. The pulse transmitted through the water sample is shown in Supplementary Figure 1b; the spectrum peaks at $\approx$1.0 THz and extends from $\approx$0.3 THz to $\approx$5 THz with almost a flat phase across the spectrum.

The THz pulses were collected and focused onto the sample and then onto the detection crystal by two custom-made elliptical aluminium mirrors ($2f = 83$ mm) to a diffraction limited spot size of $\approx$150 μm. The detecting 800-nm beam was coupled to the detecting crystal via a delay stage (gating delay, t_{THz}) and through a small hole in the second elliptical mirror. After the detection crystal, the detection beam passed first through a set of four ZnSe Brewster-angle windows, a quarter-wave plate and a Wollaston polarizer and then fell on two balanced photodiodes that detected the difference between s and p polarizations. The ZnSe Brewster windows enhance the sensitivity of the electro-optic detection by increasing the ratio between the measured signal and the amount light on the detector (the details of this detection enhancement will be discussed in a separate publication). The photodiode signals were then amplified, integrated in a boxcar integrator and recorded in a computer on a single-shot basis.

Approximately 200 μJ/pulse of the laser output was used for the photoionizing pulses. These pump pulses were passed through an optical delay stage controlling pump-probe delay (t_{pp}) and then modulated at half of the laser frequency with a chopper. For 800-nm pumping the pulses were used as such. For the 400 nm pumping a 100 μm BBO crystal was used, and for the 266-nm pump pulses, a frequency doubling and a mixing BBO crystals were in use. The pump pulses were focused with a lens ($f = 1$ m) and coupled onto the sample collinearly

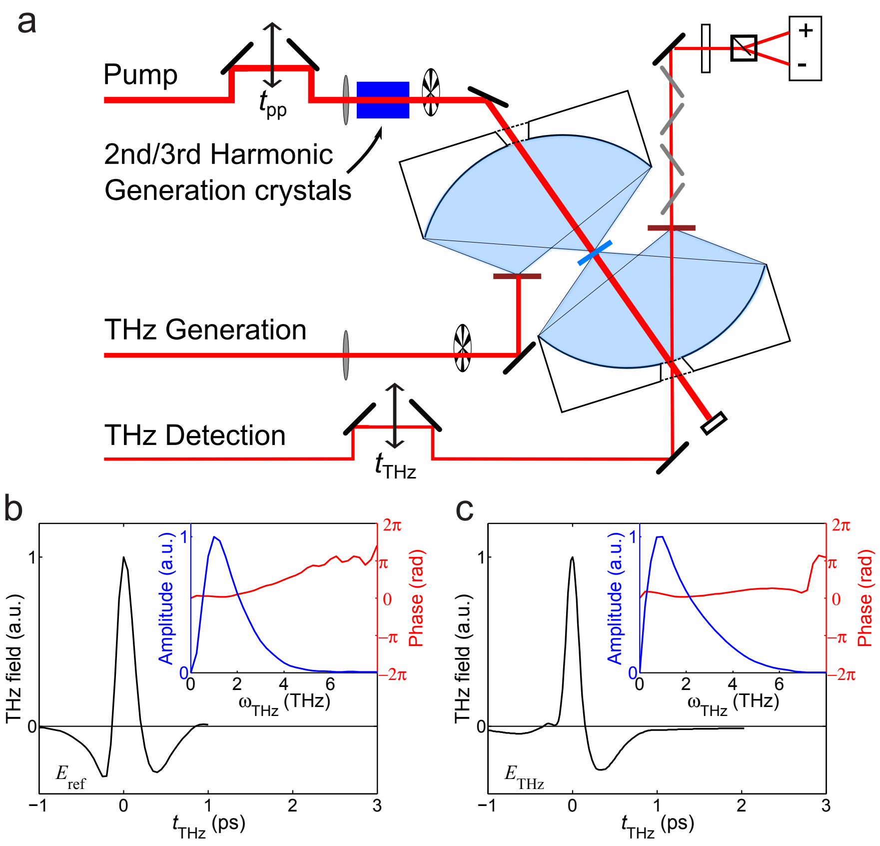

Supplementary Figure 1: (a) The optical pump THz probe experiment.(b) THz reference pulse E_{ref} and (c) THz input pulse E_{THz}, which have been determined as discussed in the text. The insets show frequency domain representation of the pulses.

with the THz pulses through a small hole in the first elliptical mirror. The spot size at the sample was adjusted to about 150 μm by keeping the focus ≈4 cm after the sample. We verified that no distortions in the jet nor in the 800-nm 200-μJ/pulse beam occurred, and that no white light was created in the jet. In the irradiance dependency measurements we used an adjustable neutral density filter to control the pump irradiance at the sample.

Electro-optic sampling measures directly the transmitted THz field and the generated pump-probe field. Fields are additive and thus the signal was calculated as the difference between pumped and un-pumped sample:

$$S(t_{\mathrm{pp}}, t_{\mathrm{THz}}) = (S_{\mathrm{PumpOnTHzOn}} - S_{\mathrm{PumpOnTHzOff}}) - (S_{\mathrm{PumpOffTHzOn}} - S_{\mathrm{PumpOffTHzOff}}) \qquad 1$$

In the NIR-probing experiments, the GaP generation crystal was removed, and the 800-nm pulses were used as probe light by detecting their transmission directly the sample by a single photodiode (PDA55, ThorLabs inc.).

In all the experiments, the water sample (triple-distilled water) flowed in a 50-μm-thick wire-guided, gravity-driven jet having no windows. Hence, artifacts from windows as well as any accumulative thermal effects in the excitation volume were avoided. The thin jet also provided a uniform excitation across the water sample as well as prevented any white-light generation when using the high irradiance needed in the 800-nm pumping measurements. The THz section of the setup was purged by nitrogen to completely remove water vapour. All measurements were performed at room temperature.

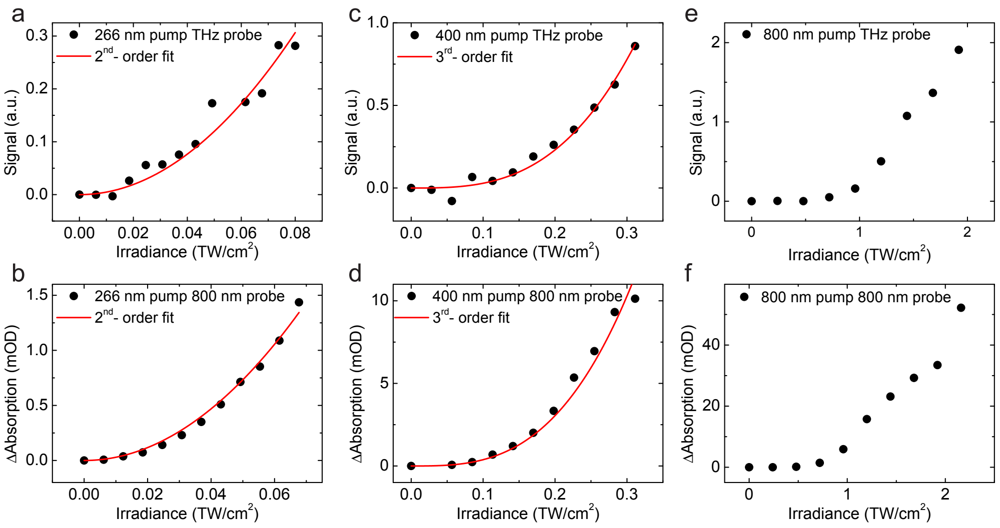

Supplementary Figure 2: Irradiance dependencies of the signals probed with THz (top row) and 800-nm pulses (bottom row). All irradiance responses were determined at the peak of the signals.

B. Irradiance and Polarization Dependence

For additional confirmation of the origin of the detected THz signals, we performed irradiance dependency measurements by varying the pump-pulse energies and compared the results between NIR and THz probing. As shown in Supplementary Figure 2, the signals probed in NIR and in THz show matching irradiance dependencies, evidencing that both signals stem from the created excess electrons. The 266-nm and 400-nm pump signals follow second-order an third-order power laws, respectively, indicating a two-photon and a three-photon process, respectively. In contrast, the 800-nm-pump data does not fit well with a power law but instead shows a threshold-like behavior with ≈1 TW/cm^2 as the ionization threshold.

Finally, we measured the THz response varying the polarization of the pump pulse as parallel or perpendicular with respect to the THz probing pulse. As can be seen in Supplementary Figure 3 the traces measured with parallel and perpendicular polarizations between the 800 nm pump and THz probe pulses overlap perfectly showing no anisotropy even at the earliest times. On the other hand, with circular polarization the signal size drops significantly to about 30%. The decrease is seen also in the long time signal, which we attribute to a heating of the bulk solution, suggesting that less 800 nm light in total is absorbed as the photo-ionization process becomes less efficient.

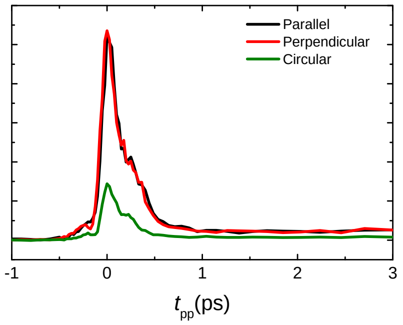

Supplementary Figure 3: Polarization dependencies of the 800-nm-pump THz-probe signal. Parallel pump and probe polarizations (black line), perpendicular pump and probe polarizations (red line) and circular pump polarization (green line).

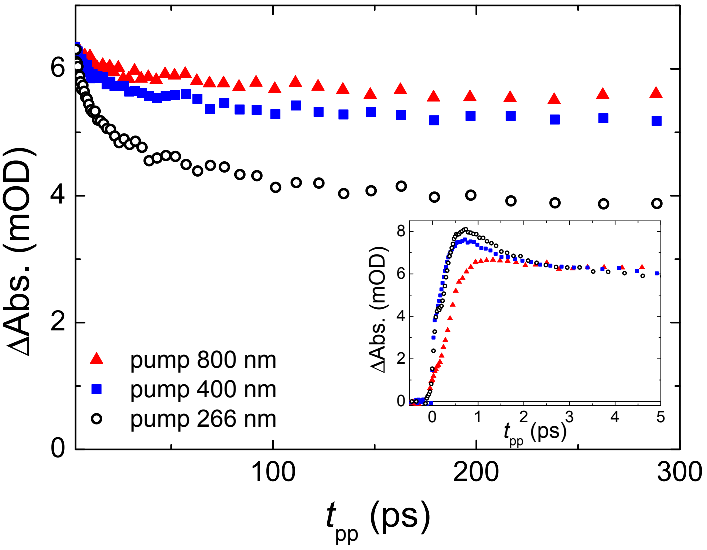

Supplementary Figure 4: Solvated electron recombination kinetics and early-time dynamics probed at 800 nm. The induced absorption signals probed at near infrared (NIR, 800 nm) with excitation wavelengths of 266-nm (black circles), 400-nm (blue squares) and 800-nm (red triangles) pump pulses are shown. The inset shows the 800-nm probing traces in the first 5 ps time window. The 266-nm and 400-nm traces are scaled to the same concentration of hydrated electrons as the 800 nm trace at $t_{pp} = 3$ ps.

C. Ejection Length

The ejection lengths of the hydrated electrons were estimated by monitoring the decay of e^-_{aq} concentrations from the NIR response due to geminate recombination with $H_3O^+_{aq}$ and $OH^\bullet_{aq}$ (Supplementary Figure 4). The 400-nm and the 266-nm data have been normalized to the 800-nm data at 3 ps delay, when e^-_{aq} is already in its fully relaxed and solvated form. The 266-nm-pump data shows approximately 62% survival yield after 300 ps, which agrees well with Refs. [1, 2]. Assuming a diffusive process, an ejection length of about 1.4 nm has been estimated from that drop of the signal [2]. The 400-nm-pump trace shows a slower decay and the comparison with Elles *et al.* [2] reveals an average ejection length in the order of 2.4 nm. The 800-nm-pump trace shows clearly the slowest recombination rate and closely matches with the 12.4-eV data in Lian *et al.*, having an approximate survival yield of 90%

at 300 ps [3].

D. Equilibration of the Hydrated Electron

The inset of Supplementary Figure 4 shows the 800-nm probing traces within the first 5 picoseconds. Again, the 400-nm and the 266-nm data have been normalized to the 800-nm data at 3 ps t_{pp} delay. The traces show how the excess electron absorption spectrum arrives from lower frequencies to the equilibrium spectrum that peaks at 720 nm. The 800-nm pump trace clearly rises slower and depicts less of an initial decay. These features are in agreement with the picture of larger initial delocalization with 800-nm strong-field ionization that results in a delayed arrival of the spectrum at 800 nm as well as reduced fraction of fast recombination processes occurring before the equilibration is complete.

E. Extracting the Spectral Response

The measured signal originates from a 3rd-order polarization that can be expressed as a convolution of a response function with the laser pulses:

$$\begin{aligned} P^{(3)}(t_{\mathrm{THz}};t_{\mathrm{pp}}) \;=\; & \int_0^\infty \int_0^\infty dt'_{\mathrm{pp}} dt'_{\mathrm{THz}} E_{\mathrm{THz}}(t_{\mathrm{THz}} - t'') \\ & \cdot I_{\mathrm{pump}}(t_{\mathrm{THz}} + t_{\mathrm{pp}} - t'_{\mathrm{THz}} - t'_{\mathrm{pp}}) R(t'_{\mathrm{THz}}, t'_{\mathrm{pp}}). \end{aligned} \qquad 2$$

where the pump-pulse I_{pump}, which is much shorter and simpler in structure than the THz probe pulse E_{THz}, is typically convoluted into an effective response function [4]. The response function $R(t_{\mathrm{THz}}, t_{\mathrm{pp}})$ is the property we ultimately want to determine because it contains the molecular information. In order to extract it, Supplementary Equation 2 needs to be deconvoluted and propagation effects within the sample, which ultimately translate the 3rd-order polarization $P^{(3)}(t_{\mathrm{THz}}; t_{\mathrm{pp}})$ into a 3rd-order field $E^{(3)}(t_{\mathrm{THz}}; t_{\mathrm{pp}})$, as well as those from the sample to the detection crystal need to be taken into account. Kužel and coworkers [4, 5] have worked out how to do that, and we essentially follow their approach. That is, we calculated the frequency domain response along the lines of Eq. 42 of Ref. [4]:

$$R(\omega_{\mathrm{THz}}, \omega_{\mathrm{pp}}) = \frac{1}{i\omega_{\mathrm{THZ}}} \cdot \frac{S(\omega_{\mathrm{THz}}, \omega_{\mathrm{pp}})}{E_{\mathrm{ref}}(\omega_{\mathrm{THz}})} \cdot \frac{E_{\mathrm{THz}}(\omega_{\mathrm{THz}})}{E_{\mathrm{THz}}(\omega_{\mathrm{THz}} - \omega_{\mathrm{pp}})} \qquad 3$$

where $S(\omega_{\mathrm{THz}}, \omega_{\mathrm{pp}})$ is the two-dimensional Fourier-transformation of the time-domain data shown in Supplementary Figure 5a. $E_{\mathrm{ref}}(\omega_{\mathrm{THz}})$ is the THz pulse transmitted through the

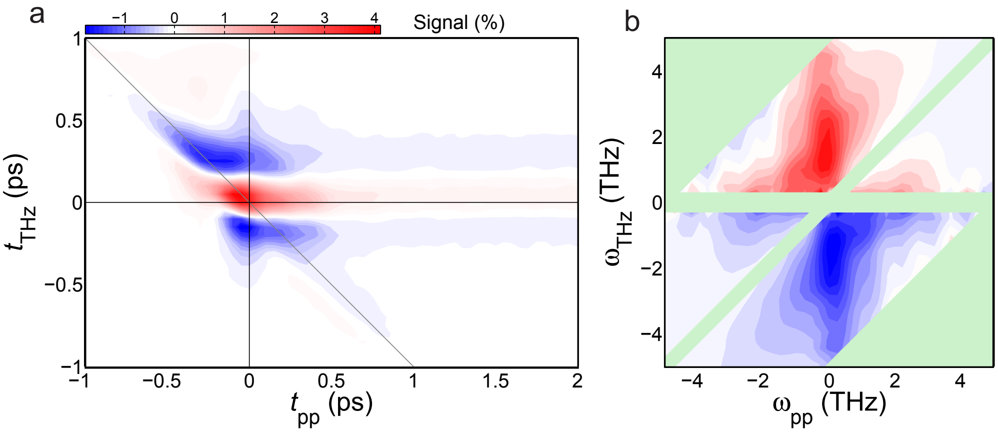

Supplementary Figure 5: (a) 2D time-domain and (b) 2D frequency-domain representation of the measured response function. In the latter, case the imaginary part of $R(\omega_{\mathrm{THz}}, \omega_{\mathrm{pp}})$ is shown as calculated from Supplementary Equation 3. Regions where the data are not meaningful, i.e., where the terms in the denominators of Supplementary Equation 3 are too small, are blanked out. In the left panel, the signal size is given as a percentage of the THz-pulse field transmitted through the water sample.

sample to the detection crystal (Supplementary Figure 1b) and $E_{\mathrm{THz}}(\omega_{\mathrm{THz}})$ is the pulse at the input of Supplementary Equation 2 (Supplementary Figure 1c). $E_{\mathrm{ref}}(\omega_{\mathrm{THz}})$ is continuously measured during data acquisition by calculating $E_{\mathrm{ref}}(t_{\mathrm{THz}}) = S_{\mathrm{PumpOffTHzOn}} - S_{\mathrm{PumpOffTHzOff}}$, and normalizes out propagation effects from the sample to the detector [4]. $E_{\mathrm{THz}}(\omega_{\mathrm{THz}})$ has been measured independently by moving the detection crystal to the sample position, and by removing the spectral response of the detection crystal using the same procedure as described in detail in Ref. [6].

With the factor $i\omega_{\mathrm{THz}}$ in Supplementary Equation 3 we take a simpler approach than Ref. [4]. That is, rather than taking dispersion and absorption effects into account explicitly during the non-linear interaction in the sample, we treat them as a linear response. To that end, we effectively split the water jet into two halves and assume that the nonlinear interaction happens in the middle of the jet. We then group the first half of the dispersion and the absorption into $E_{\mathrm{THz}}(\omega_{\mathrm{THz}})$ and the second half into the propagation of the emitted field to the detector (the procedure is described in more detail in Supporting Information of

Ref. [6]). This simplifying approach is justified since the dispersion and the absorption are kept small in the thin water jet. The process is thus quasi-phase-matched and the generated 3rd-order field $E^{(3)}(t_{\mathrm{THz}}; t_{\mathrm{pp}})$ is connected to the 3rd-order polarization $P^{(3)}(t_{\mathrm{THz}}; t_{\mathrm{pp}})$ by a simple time-derivative that, in these limits, is expressed by the factor $i\omega_{\mathrm{THz}}$ in Supplementary Equation 3 (see Eq. 54 of Ref. [5]).

Supplementary Figure 5b shows the resulting response function $\Im R(\omega_{\mathrm{THz}}, \omega_{\mathrm{pp}})$ calculated from Supplementary Equation 3. Regions where the data are not meaningful, i.e., where the terms in the denominators of Supplementary Equation 3 are too small, are blanked out. A peak centered at $\omega_{\mathrm{pp}} = 0$ can clearly be identified; Fig. 1 shows a vertical cut through that peak along $\omega_{\mathrm{pp}} = 0$. Even though the peak is phase twisted with absorptive and dispersive components, for $\omega_{\mathrm{pp}} = 0$ only the absorptive component contributes along ω_{THz}. We consider the 1D cut in the inset of Fig. 1 to be the spectral response of the excess electron. The sensitivity of the method to details of the data (2D scan as well as pulses and transfer functions) does not allow us to extract a time evolution of that spectral response as a function of t_{pp}.

II. COMPUTATIONAL METHODOLOGY

We performed combined quantum mechanics/molecular mechanics (QM/MM) molecular dynamics simulation of aqueous bulk water after vertical attachment of an electron, further denoted as electron localization dynamics. Furthermore, we computed the vertical attachment of an excess electron along trajectories from molecular dynamics of neutral water systems (electron attachment simulations).

Initial structures for all simulations were generated from classical molecular dynamics (CMD) simulations with an extended, simple point charge model (SPC/E) [7] in an NpT ensemble at p=1bar. Seven configuration with 1024 water molecules in total were taken as input for the electron localization dynamics. 32 water molecules spherically surrounding the center of the unit cell were assigned as QM region. The structures were periodically replicated with a cubic unit cell of 3.1 nm length. All systems were equilibrated in an NVT ensemble at 300 K. Then, the charge of the (QM) system was decreased by one and molecular dynamics simulations were run until the excess electron localized and formed a hydrated electron. This happened on a 1 ps timescale, as is shown in Figure 2. Here, the radius of gyration of the spin density r_g is plotted as a function of time for all trajectories (in gray) and the average r_g from all trajectories (in black). At t=0 the electron reaches the boundaries of the QM region, however, only about 5% of the electron density leaks out of the QM region. Moreover, within few femtoseconds the electron shrinks enough such that it does not touch the QM/MM boundary and from that moment on this problem disappears.

For electron attachment simulations two system sizes, 1024 water molecules in a periodic 3.1 nm box and 4142 water molecules in a periodic 5.0 nm box, were considered. Five systems with 64 QM and 960 MM water molecules and one system with 256 QM and 3886 MM water molecules were equilibrated in an NVT ensemble with QM/MM and then structures were sampled for 5 ps (64QM/960MM) and 2 ps (256QM/3886MM). The electronic structure setup is similar to that of our previous simulations of a bulk-hydrated electron [8]. The setup allows for reproducing well properties of the hydrated electron.

Simulations were performed with the QM/MM module of CP2K. [9] The density functional used for calculating energies and forces is the combined Becke exchange [10] and Lee, Yang, Paar correlation [11] functional. An additional spin-density dependent term was added to correct for the spurious self-interaction error of the unpaired electron. [12] A pairwise-additive potential was added to effectively account for dispersion effects. [13] A moleculary optimized triple-ζ basis set with two polarization functions [14] was used to expand the Kohn-Sham orbitals plus an auxiliary plane-wave basis with a kinetic energy cutoff of 280 Ry to describe the electron density. Norm-conserving pseudopotentials of Goedecker-Teter-Hutter type replaced core-electrons. [15] Poisson's equation for the QM system is solved using density-derived atomic point charges [16] in the field of the periodically surrounding MM nuclei represented as Gaussian charge distributions. [17, 18] The QM periodicity is explicitly taken into account. [18] Forces on the MM system were obtained from a flexible SPC/E model. The smooth particle mesh technique was used to evaluate the electrostatic potential of the periodically replicated MM system.

A. Evaluation of Optical Properties

The first three lowest excitation energies were evaluated along the localization trajectories with a stride of 50 fs using time-dependent density functional theory (TD-DFT) in its linear response formulation [19] using the NWChem program package. [20] In these calculations the unit cell was replicated once in each direction to avoid spurious effects at the boundaries. The MM atoms were represented by point charges according to the SPC/E parametrization. The B3LYP functional [11, 21–23] in combination with an atom-centered double-ζ basis set with diffuse and polarization functions [24, 25] on all QM nuclei was chosen as it reproduces spin densities closely to the QM/MM molecular dynamics setup. For the systems with larger QM subsystems (either 64 QM or 256 QM atoms) calculating the excitation energies explicitly is computationally too demanding. We thus calculated the gap between highest occupied molecular orbital (HOMO) and lowest unoccupied molecular orbital (LUMO). The gap energy was then scaled to obtain an estimate for the first excitation energy. The scaling factor was taken as the ratio between HOMO/LUMO gap and the excitation energy in the smallest system were we calculated both excitation and gap explicitly. This scaling factor was on average 0.79. As the HOMO/LUMO gap employing the before-mentioned self-interaction correction resulted in unrealistic, negative HOMO/LUMO gaps, we used the plain BLYP functional to calculate the HOMO/LUMO gaps. The HOMO/LUMO gaps between the BLYP and B3LYP setup differ by a factor of 1.64, which has been accounted for.

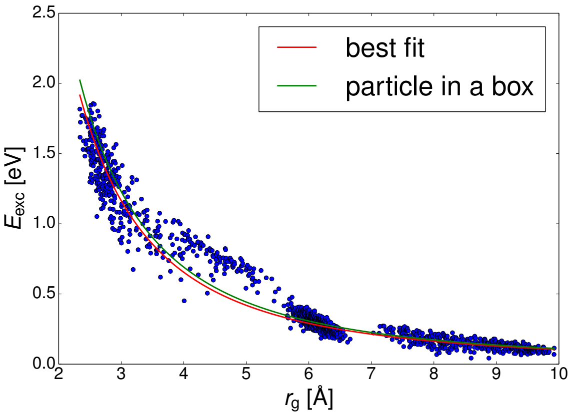

Supplementary Figure 6: Red line: Best fit of the dependence of the first excitation energy on the radius of gyration to a a/r_g^2 relationship (same as in Fig. 3) and green line: particle-in-a-box relationship.

B. Particle-in-a-box fit

Supplementary Figure 6 shows the best fit of the dependence of the first excitation energy on the radius of gyration to a a/r_g^2 relationship (same as in Fig. 3) as well as the analytical result for a particle in a 3D box (i.e., Eq. 8 from Ref. [26]). The fit reveals $a = 10.5$ eVÅ^2 while the corresponding value for a particle in a 3D box is 11 eVÅ^2.

[1] Crowell, R. A. and Bartels, D. M. Multiphoton ionization of liquid water with 3.0-5.0 eV photons. *J. Phys. Chem.* **100**, 17940–17949 (1996).

[2] Elles, C. G., Jailaubekov, A. E., Crowell, R. A., and Bradforth, S. E. Excitation-energy dependence of the mechanism for two-photon ionization of liquid H_2O and D_2O from 8.3 to 12.4 eV. *J. Chem. Phys.* **125**, 044515 (2006).

[3] Lian, R., Oulianov, D. A., Shkrob, I. A., and Crowell, R. A. Geminate recombination of electrons generated by above-the-gap (12.4 eV) photoionization of liquid water. *Chem. Phys. Lett.* **398**, 102–106 (2004).

[4] Němec, H., Kadlec, K., and Kužel, P. Methodology of an optical pump-terahertz probe experiment: An analytical frequency domain approach. *J. Chem. Phys.* **117**, 8454 (2002).

[5] Kužel, P., Němec, H., and Kadlec, K. Propagation of THz pulses in photoexcited media: Analytical theory for layered systems. *J. Chem. Phys.* **127**, 024506 (2007).

[6] Savolainen, J., Ahmed, S., and Hamm, P. Two-dimensional Raman-terahertz spectroscopy of water. *Proc. Natl. Acad. Sci. USA* **110**, 20402–20407 (2013).

[7] Berendsen, H. J. C., Grigera, J. R., and Straatsma, T. P. The missing term in effective pair potentials. *J. Phys. Chem.* **91**, 6269–6271 (1987).

[8] Uhlig, F., Marsalek, O., and Jungwirth, P. Unraveling the complex nature of the hydrated electron. *J. Phys. Chem. Lett.* **3**, 3071–3075 (2012).

[9] VandeVondele, J., Krack, M., Mohamed, F., Parrinello, M., Chassaing, T., and Hutter, J. Quickstep: fast and accurate density functional calculations using a mixed gaussian and plane waves approach. *Comput. Phys. Commun.* **167**, 103–128 (2005).

[10] Becke, A. D. Density-functional exchange-energy approximation with correct asymptotic-behavior. *Phys. Rev. A* **38**, 3098–3100 (1988).

[11] Lee, C. T., Yang, W. T., and Parr, R. G. Development of the colle-salvetti correlation-energy formula into a functional of the electron-density. *Phys. Rev. B* **37**, 785–789 (1988).

[12] VandeVondele, J. and Sprik, M. A molecular dynamics study of the hydroxyl radical in solution applying self-interaction-corrected density functional methods. *Phys. Chem. Chem. Phys.* **7**, 1363–1367 (2005).

[13] Grimme, S., Antony, J., Ehrlich, S., and Krieg, H. A consistent and accurate ab initio parametrization of density functional dispersion correction (DFT-D) for the 94 elements H-Pu. *J. Chem. Phys.* **132**, 154104–154123 (2010).

[14] VandeVondele, J. and Hutter, J. Gaussian basis sets for accurate calculations on molecular systems in gas and condensed phases. *J. Chem. Phys.* **127**, 114105–114114 (2007).

[15] Goedecker, S., Teter, M., and Hutter, J. Separable dual-space gaussian pseudopotentials. *Phys. Rev. B* **54**, 1703–1710 (1996).

[16] Blochl, P. E. Electrostatic decoupling of periodic images of plane-wave-expanded densities and derived atomic point charges. *J. Chem. Phys.* **103**, 7422–7428 (1995).

[17] Laino, T., Mohamed, F., Laio, A., and Parrinello, M. An efficient real space multigrid QM/MM electrostatic coupling. *J. Chem. Theory Comput.* **1**, 1176–1184 (2005).

[18] Laino, T., Mohamed, F., Laio, A., and Parrinello, M. An efficient linear-scaling electrostatic coupling for treating periodic boundary conditions in QM/MM simulations. *J. Chem. Theory Comput.* **2**, 1370–1378 (2006).

[19] Casida, M. Time-dependent density-functional response theory for molecules. In *Recent Advances in Density Functional Methods, Part I,* Chong, D., editor. World Scientific, Singapore (1995).

[20] Valiev, M., Bylaska, E., Govind, N., Kowalski, K., Straatsma, T., Dam, H. V., Wang, D., Nieplocha, J., Apra, E., Windus, T., and de Jong, W. Nwchem: A comprehensive and scalable open-source solution for large scale molecular simulations. *Comput. Phys. Commun.* **181**, 1477–1489 (2010).

[21] Becke, A. D. Density-functional thermochemistry. III. The role of exact exchange. *J. Chem. Phys.* **98**, 5648–5652 (1993).

[22] Vosko, S. H., Wilk, L., and Nusair, M. Accurate spin-dependent electron liquid correlation energies for local spin density calculations: a critical analysis. *Can. J. Phys.* **58**, 1200–1211 (1980).

[23] Stephens, P. J., Devlin, F. J., Chabalowski, C. F., and Frisch, M. J. Ab initio calculation of vibrational absorption and circular dichroism spectra using density functional force fields. *J. Phys. Chem.* **98**, 11623–11627 (1994).

[24] Hehre, W., Ditchfield, R., and Pople, J. Self-consistent molecular-orbital methods. 12. Further extensions of gaussian-type basis sets for use in molecular-orbital studies of organic-molecules. *J. Chem. Phys.* **56**, 2257–2261 (1972).

[25] Krishnan, R., Binkley, J., Seeger, R., and Pople, J. Self-consistent molecular-orbital methods. 20. Basis set for correlated wave-functions. *J. Chem. Phys.* **72**, 650–654 (1980).

[26] Jacobson, L. D. and Herbert, J. M. Theoretical characterization of four distinct isomer types in hydrated-electron clusters, and proposed assignments for photoelectron spectra of water cluster anions. *J. Am. Chem. Soc.* **133**, 19889–19899 (2011).

A.6 THz echoes reveal the inhomogeneity of aquaous salt solution

Reprinted from the ref. [99], with the permission of Nature Publishing Group (Macmillan Publishers Limited).

A.6.1 Contribution to this paper

Saima Ahmed performed the experiments with Dr. Andrey Shalit.

nature chemistry
ARTICLES
DOI: 10.1038/NCHEM.2642

Terahertz echoes reveal the inhomogeneity of aqueous salt solutions

Andrey Shalit, Saima Ahmed, Janne Savolainen and Peter Hamm*

The structural and dynamical properties of water are known to be affected by ion solvation. However, a consistent molecular picture that describes how and to what extent ions perturb the water structure is still missing. Here we apply 2D Raman–terahertz spectroscopy to investigate the impact of monatomic cations on the relaxation dynamics of the hydrogen-bond network in aqueous salt solutions. The inherent ability of multidimensional spectroscopy to deconvolute heterogeneous relaxation dynamics is used to reveal the correlation between the inhomogeneity of the collective intermolecular hydrogen-bond modes and the viscosity of a salt solution. Specifically, we demonstrate that the relaxation time along the echo direction $t_1 = t_2$ correlates with the capability of a given cation to 'structure' water. Moreover, we provide evidence that the echo originates from the water–water modes, and not the water–cation modes, which implies that cations can structure the hydrogen-bond network to a certain extent.

Despite significant experimental and theoretical efforts over several decades, the microscopic mechanisms that lead to the various anomalous properties of water, whether as the neat substance or as a primary biological solvent, are far from being fully understood. The general consensus nowadays is that the ability of water to form complex hydrogen-bond networks is primarily responsible for the discrepancies in its various dynamical and thermodynamical properties compared with those of simple liquids[1,2]. However, the exact structure of these hydrogen-bond networks, the spatial extent to which they persist as well as the relevant timescales are not known. Nevertheless, the language of 'water structure' has been widely adopted on a rather empirical level, particularly when attempting to elucidate the effect of ions on the surrounding water molecules upon solvation.

It was first observed by Poiseuille in 1847[3] that the viscosity of water (η) changes upon the solvation of simple inorganic salts in an ion-specific manner. Later, the semi-empirical Jones–Dole equation[4]

$$\eta/\eta_w = 1 + Ac^{1/2} + Bc + Dc^2 \dots \quad (1)$$

was put forward to quantify this behaviour, where η_w is the viscosity of neat water and c the ion concentration. Coefficients A and D result from the long-range Coulombic forces and ion pairing, respectively, whereas B, which depends on ion–water interaction, has remained largely empirical up to now[5]. Depending on the sign of the B coefficient, ions are usually categorized as either 'structure makers' ($B > 0$) or 'structure breakers' ($B < 0$) (refs 6,7), again without a comprehensive molecular picture behind these terms. At least for simple monatomic ions, the viscosity effect correlates with the charge density, that is, with an increasing charge and decreasing size of an ion the viscosity effect increases. Although it is quite clear that solvated ions dramatically affect the hydrogen-bond network in their immediate vicinity because of electrostatic interactions, the question remains whether this effect extends beyond the first solvation shell.

The extensive experimental and computational studies, which include NMR spectroscopy[8], dielectric relaxation[9–11], diffraction methods[12–14], ultrafast vibrational spectroscopies[11,15–19] and molecular dynamics (MD) simulations[20,21], over the years have resulted in very diverse and sometimes conflicting interpretations of ion solvation. For example, neutron-scattering experiments by Soper and co-workers have indicated an influence of ions on the second peak of the oxygen–oxygen radial distribution function, which reflects the tetrahedral hydrogen-bond structure of water[13]. However, these experiments revealed no difference when comparing monovalent Na^+ with divalent Mg^{2+} cations[14], and thus they do not follow the macroscopic viscosity trend discussed above. On the other hand, ultrafast infrared measurements of isotope-diluted water (HOD in H_2O) by Bakker and co-workers demonstrated that the orientational relaxation of waters beyond the first solvation shell is not affected by ion solvation, even at very high salt concentrations[15]. Later, this claim was somewhat softened when longer-range effects were observed for specific combinations of strongly hydrated ions[19]. The seemingly contradicting interpretations might stem from the fact that each of these technique is sensitive only to a specific property of the hydrogen-bond network. That is, diffraction methods can capture only the average structure, omitting any dynamical aspect, whereas ultrafast infrared spectroscopy, which possesses the necessary time resolution, is able to measure the hydrogen-bond dynamics only indirectly and only very locally by typically monitoring the intramolecular hydroxyl-stretch vibration of the water molecule.

A more direct measurement of the effect of salts on the hydrogen-bond network was performed by Meech and co-workers[22,23]. They applied ultrafast heterodyne-detected optical Kerr effect (OKE) spectroscopy to study the influence of hydrated ions on the collective intermolecular modes of water in the low-frequency spectral region below 1,000 cm^{-1}. Various terahertz (THz) absorption[24,25] and Raman-scattering techniques[26,27] established that the spectral response in this region is governed by the water's intermolecular degrees of freedom and consists mainly of three broad peaks around 600 cm^{-1} (hindered rotations), 200 cm^{-1} (hydrogen-bond stretch) and 60 cm^{-1} (hydrogen-bond bend). The polarization sensitivity as well as the time resolution offered by OKE allows one to disentangle the water-ion contribution (isotropic response) from the collective response of the hydrogen-bond network (anisotropic response). It has been shown that the decay time of the anisotropic signal correlates with viscosity, where aqueous salt solutions with strongly hydrated ions show significantly slower relaxation dynamics[23]. Nevertheless, OKE spectroscopy as a one-dimensional (1D) technique

Department of Chemistry, University of Zurich, Winterthurerstrasse 190, CH-8057 Zurich, Switzerland. *e-mail: peter.hamm@chem.uzh.ch

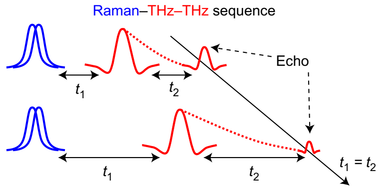

Figure 1 | Raman–THz–THz pulse sequence. The appearance of an echo at $t_2 = t_1$ reflects the ability of the system to rephase the coherence after the second light perturbation.

is unable to provide information regarding the inhomogeneity of the vibrational dynamics[28] that reflects the structural heterogeneity induced by solvated ions.

To resolve such an inhomogeneous distribution, a measurement of higher-order correlation functions is required, which is usually achieved by means of multidimensional spectroscopy, in which the system is subjected to multiple perturbations[29]. Low-frequency molecular resonances can be probed either directly by THz electromagnetic fields through the dipole moment or indirectly by Raman interaction through a molecular polarizability. Following the advances in the generation of strong THz fields[30] required for a nonlinear interaction, various multidimensional THz techniques have emerged recently, but their applicability is currently limited to semiconductor solids[31] or molecules in the gas phase[32]. To investigate intermolecular collective modes of liquids in the low-frequency range of a few 100 cm^{-1}, over 20 years ago Tanimura and Mukamel proposed fifth-order 2D Raman spectroscopy[33]; however, the realization of that experiment turned out to be exceptionally difficult because of the cascading of lower-order nonlinear processes[34]. The fifth-order Raman signal could be isolated for certain liquids, such as CS_2 or formamide[35–38], but not yet for water because of its very weak Raman cross-section. Only very recently was the cascading problem overcome in a single-beam spectrally controlled technique[39].

Our group has proposed a hybrid method, denoted 2D Raman–THz spectroscopy[40,41]. Although it reveals similar information, the new approach is experimentally more feasible than 2D Raman spectroscopy because of the inherent elimination of cascading effects and the large THz cross-section of water; indeed, very recently the first 2D Raman–THz experiment of neat water at ambient conditions was carried out[42]. In the so-called Raman–THz–THz pulse sequence shown in Fig. 1, two non-resonant field interactions induce a Raman transition and excite an intermolecular vibrational coherence, which quickly dephases because of homogeneous as well as inhomogeneous line broadening. After a time t_1, the system is perturbed a second time by a THz field interaction, and is then read out along t_2 by the emission of a THz field. The amount of inhomogeneity can be monitored through the extent of the signal along the diagonal $t_1 = t_2$. That signal, usually denoted as an 'echo', reflects the ability of the system to rephase the coherence after the second perturbation[29].

In the current work, we exploit the unique capabilities of this new spectroscopic tool to investigate how the 'structure-making' capability of certain cations affects the 2D Raman–THz response. We present a systematic study of a series of aqueous solutions of chloride salts $M^{n+}Cl_n$, where M^{n+} is the cation varied from 'structure breaking' (Cs^+, $B = -0.047\ M^{-1}$) to structure making (Mg^{2+}, $B = 0.385\ M^{-1}$) (ref. 5). The Cl^- anion was kept constant in this series, because its B coefficient is very close to 0 ($B = -0.005\ M^{-1}$; B factors of cations and anions are essentially additive)[5]. We restrict our study to simple monatomic cations, because the range of B coefficients that can be covered is much larger than would be possible with the monatomic halide anions Cl^- and Br^- (ref. 5). (I^- would not be possible because of its low ionization threshold that leads to dominating THz signals from solvated electrons[43].) We use the same cation concentration of 2 M throughout, which is not an uncommon concentration range for these types of studies[13,15,19,21,22,44]. In this concentration range the B term in equation (1) dominates, whereas ion pairing and clustering, described by the D term, do not yet play a significant role. We show that the inhomogeneity of the intermolecular hydrogen-bond vibrations, measured via the extent of the echo signals along the $t_1 = t_2$ diagonal, increases as the structure-making property of the cation becomes larger.

Results

Figure 2a–d presents a series of 2D Raman–THz signals of 2 M aqueous chloride salt solutions with Cs^+ (Fig. 2a), Na^+ (Fig. 2b), Sr^{2+} (Fig. 2c) and Mg^{2+} (Fig. 2d) in an increasing order of water structure-making capabilities. In our specific experimental layout, the Raman–THz–THz pulse appears in the upper-right quadrant of the 2D response, and the THz–Raman–THz pulse sequence in the upper triangle of the upper-left quadrant (the third THz–THz–Raman pulse sequence has recently been implemented by others as well[45]). As has been discussed in our previous publication[42], the molecular response is significantly smeared out by the convolution with the THz and Raman pulses, both having a finite duration, which makes the interpretation of the observed signal quite difficult. Nevertheless, owing to the shorter duration of the Raman pulse compared with the THz pulse, the Raman–THz–THz pulse sequence is less susceptible to contamination from the instrument-response function (see the instrument-response function shown as Figure 2C in Savolainen *et al.*[42]), and thus will be considered from this point on.

A clear trend between the temporal extent of the diagonal signal in the upper-right quadrant and the B coefficient of the considered cation is immediately noticeable. Whereas the 2D Raman–THz response of CsCl in Fig. 2a strongly resembles that of neat water (Supplementary Information and Supplementary Fig. 1), the increase in the structure-making ability of the cation, as in the case of Na^+, is clearly accompanied with a longer relaxation along the main diagonal, $t_1 = t_2$, in the upper-right quadrant (Fig. 2b). This effect becomes much more pronounced for the stronger structure modifiers Sr^{2+} and Mg^{2+}, that is, for the divalent cations, for which a ridge along the diagonal is formed (Fig. 2c,d).

The insets in Fig. 2 highlight the signals along the diagonal (red solid line) and compare it with that of neat water (black dashed line). Although the latter has been reported before[42], the measurement has been repeated for consistency and is presented in the Supplementary Information and Supplementary Fig. 1, where possible sources of small discrepancies in the instrument-response functions are discussed as well. For a quantitative analysis, the averaged relaxation time has been calculated for each diagonal cut, defined as:

$$\langle \tau \rangle \equiv \int_{t_0}^{\infty} (\tau - t_0) g(\tau) \mathrm{d}\tau \Big/ \int_{t_0}^{\infty} g(\tau) \mathrm{d}\tau \qquad (2)$$

where $t_0 = 50$ fs represents the peak of the signal. An averaged relaxation time of $\langle \tau \rangle \approx 65 \pm 4$fs is revealed for neat water, which is the same as the value obtained from our previously published data (Supplementary Fig. 2)[42]. In the case of CsCl, the signal decays somewhat faster with $\langle \tau \rangle \approx 55 \pm 4$fs, whereas a slower relaxation with $\langle \tau \rangle \approx 80 \pm 7$fs is obtained for NaCl. The deviations from the neat-water signal are much stronger for $SrCl_2$ and $MgCl_2$ with relaxation times of $\langle \tau \rangle \approx 95 \pm 5$fs and $\langle \tau \rangle \approx 110 \pm 7$fs, respectively. In these two cases, an additional oscillatory feature evolves in the echo signal, which can be fitted by a damped oscillator with frequencies of $\sim 230 \pm 20$cm^{-1} for $SrCl_2$ and $\sim 150 \pm 15$cm^{-1} for $MgCl_2$. Figure 3 (red symbols) shows that the averaged relaxation time along the diagonal correlates very well with the B coefficient of the cation.

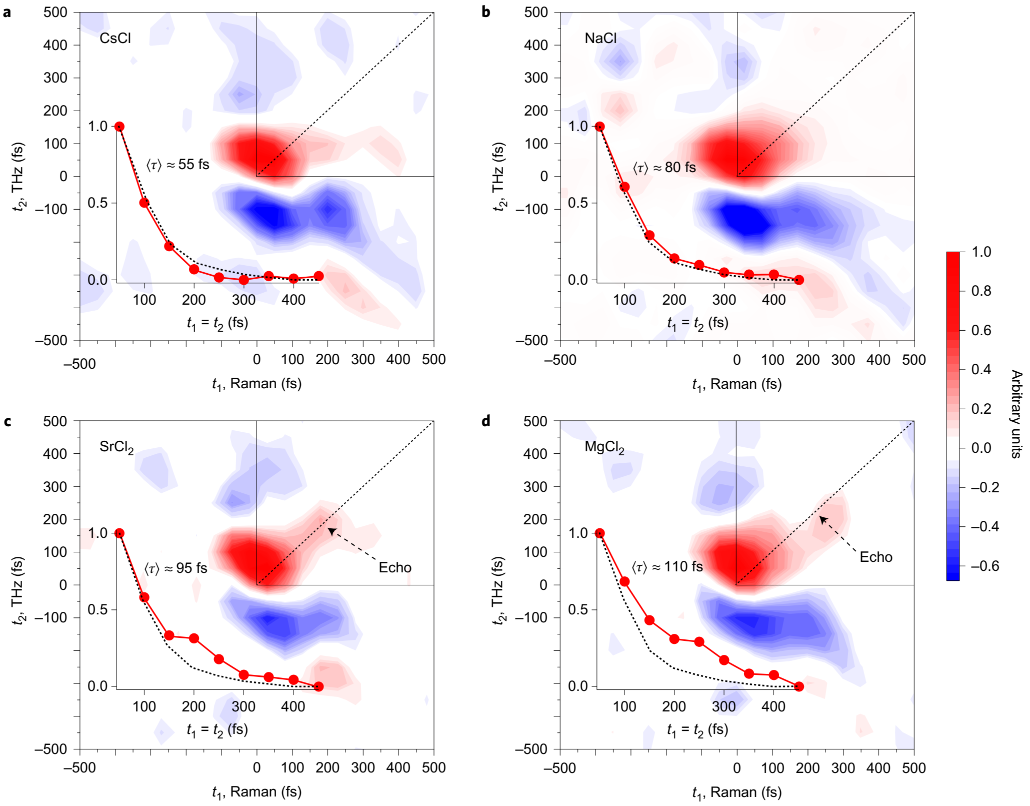

Figure 2 | 2D Raman–THz–THz responses of 2 M aqueous salt solutions. a–d, Experimental signals for CsCl (**a**), NaCl (**b**), $SrCl_2$ (**c**) and $MgCl_2$ (**d**). The upper-right quadrant corresponds to the Raman–THz–THz pulse sequence and the main diagonal (dashed line) is indicated. 1D cuts along the $t_1 = t_2$ diagonal for the corresponding salt (solid red line) and neat water (dashed black line) are shown in the insets. The 1D and 2D data are normalized to the maximum signal. The cation exhibits greater structure-making ability, as observed via an extended relaxation component along the main diagonal.

Discussion

An echo occurs if the memory to rephase persists for a time similar to the free-induction decay or longer. In that regard, it is interesting to compare the diagonal decay (Fig. 3, dashed red line) with that along the t_1 axis, which is shown in Fig. 3 in green (although we do observe an extended ridge along the t_1 axis, the same is suppressed in the t_2 direction because of the time derivative that occurs in the signal-generation process (see equation (2) of Savolainen *et al.*[42])). Both decay times approach each other for $MgCl_2$, hence one is definitely in the regime to call it an echo. Interestingly, the t_1-axis decay shows the opposite trend to that of the echo decay, that is, it becomes slightly faster for cations with larger *B* coefficients. That signal is related to the initial drop of the free induction in a 1D Raman experiment, and hence the speed-up indicates a broader overall (that is, combined homogeneous and inhomogeneous) linewidth. To the contrary, the echo decay along the diagonal reflects exclusively the homogeneous dephasing of the investigated vibrational modes, and thus the data in Fig. 3 present a trend of increasing inhomogeneity with increasing viscosity along the series $Cs^+ < Na^+ < Sr^{2+} < Mg^{2+}$. The longest echo lifetime we observed, 110 fs for Mg^{2+}, is still fast compared with the typical hydrogen-bond lifetime of 1 ps (refs 46–49). However, in the low-frequency range the collective, intermolecular modes of the hydrogen-bond networks involve more than one hydrogen bond, and hence the persistent time of these modes will be shorter.

It is important to stress that there are two possible types of low-frequency modes in aqueous salt solutions. That is, in addition to the water–water intermolecular modes, there is a new set of ion–water vibrational modes from the first solvation layer[22,23,44,50]. In the following, we provide three pieces of evidence that, taken together, make us believe that the enhanced diagonal feature originates from the intermolecular water–water vibrational modes, and not from the ion–water vibrational modes:

- First, the red dashed line in Fig. 3 shows a linear fit through the four salt measurements (red circles). Even though that fit did not include the water value (blue diamond), the latter falls on the fit with a deviation of only 3 fs. This emphasizes that both experiments, neat water versus salt solution, measure the inhomogeneity of the same set of vibrational modes, that is, the intermolecular water–water modes.
- As a second piece of evidence, we compare the frequency of the oscillatory feature in the photon echo signal observed for both Sr^{2+} and Mg^{2+} with what is known from 1D spectroscopy[22,23,44,50]. With regard to water–cation vibrations,

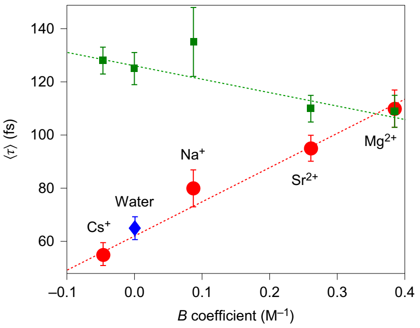

Figure 3 | Averaged relaxation time ⟨τ⟩ as a function of the *B* coefficient of the cation (from ref. 5). Experimental values for the diagonal decay of the aqueous salt solutions are shown as red circles, whereas the value for neat water is indicated as a blue diamond (assuming a *B* coefficient of 0). A linear fit, intersecting at ⟨τ⟩ = 62 fs for $B = 0$, is depicted. The green squares show the same for the signal decay along the t_1 axis for $t_2 = -100$ fs (fixed), which corresponds to the maximum of the blue ridge in the 2D data (see Fig. 2). Error bars (±1 s.d.) have been estimated by block averaging.

Havenith and co-workers[44] identified distinct vibrational bands for both $SrCl_2$ and $MgCl_2$ in linear THz absorption spectra, but with the opposite frequency ordering (~100 cm^{-1} for $SrCl_2$ versus ~200 cm^{-1} for $MgCl_2$, which in essence simply reflects the much larger mass of Sr^{2+}) as compared with our observation (~230 cm^{-1} for $SrCl_2$ versus ~150 cm^{-1} for $MgCl_2$, which can be discriminated within the error bars of the fitted beat frequencies).

- Finally, we substituted the Cl^- anion by Br^- while keeping the same strong structure-making Sr^{2+} cation (Fig. 4) to also test possible water–anion vibrations. Regarding 1D spectroscopy, conflicting results can be found in the literature, with frequencies that seem to depend on the spectroscopic method (THz absorption[44,50] versus Raman spectroscopy[22,23], which indicates a non-coincident effect from delocalized modes[51]) or on the charge of the cation (monovalent[22,23,44] versus divalent[50]). However, in any case, the frequency of the anion–water vibration depends on the nature of the ion, in some cases as extremely as ~200 cm^{-1} for Cl^- to ~50 cm^{-1} for Br^- (ref. 44), again following the mass of the anion. In contrast, Fig. 4 shows that the 2D Raman–THz responses of both $SrCl_2$ and $SrBr_2$ are virtually the same with a significant prolongation of the diagonal signal and a profound oscillatory contribution in the echo signal, with a frequency of ~230 cm^{-1} in both cases.

Hence, the echo signal does not seem to stem from water–ion vibrations. Although a detailed explanation of the oscillatory feature in the echo signal is currently missing, it is very suggestive to see that its frequency falls into the broad hydrogen-bond-stretch vibration of liquid water, which is centred at ~200 cm^{-1}.

A full understanding of the 2D Raman–THz response will require extensive theoretical and simulation work. Such work has, indeed, identified echo features for neat water[41,52–55], but, contrary to our observation, only for the THz–Raman–THz pulse sequence, which would lie in the upper-left quadrant along $-2t_1 = t_2$ in our representation of the data (that is, along the blue line of Supplementary Fig. 1). Tanimura and co-workers have explained that effect by the larger anharmonicity of the Raman interaction, resulting in a more-efficient two-quantum transition that is needed to obtain an ‘inversion of coherence’ that eventually results in rephasing[56]. However, the simulated echo features are very short-lived and originate from the librational modes of water that are completely suppressed in our experiment because of a limited time resolution. The only simulation work we are aware of that includes ions is by Zhuang and co-workers[57], who saw a slight prolongation of the main peak around $t_1 = t_2 = 0$ in the Raman–THz–THz echo direction for a 3.5 M $MgCl_2$ solution. That effect is also extremely short-lived and would not be observable with our current time resolution. Unfortunately, the limited simulation time of Zhuang and co-workers[57] does not allow for any conclusions on the slower dynamics observed here (as a general remark, the convergence of the multitimepoint correlation functions needed to calculate a 2D Raman–THz signal from MD simulations becomes exponentially more computer-time expensive when longer times for t_1 and t_2 are considered).

It has been shown[58] that the 2D Raman–THz signal of neat water is an extremely sensitive probe of the level of accuracy with which the polarizability of a water model is described, and this is expected to become even more relevant once the charge of an ion is introduced. From the water models considered in Hamm[58], by far the best agreement with the experimental 2D Raman–THz response was achieved with the TL4P water model recently put forward by Tavan and co-workers[59]. This is a rigid four-point model that features a Gaussian-shaped inducible dipole, which allows one to realize a transferable model that describes both the gas- and the solution-phase dipole moment and polarizability correctly, avoiding the usual problems of the polarization catastrophe. It will be interesting to see whether ions parametrized consistently to the TL4P water model can reproduce the experimental results reported here.

Conclusion

In conclusion, we have identified an extended relaxation component along the $t_1 = t_2$ direction by comparing the 2D Raman–THz response of neat water with that of a series of chloride salts. As the structure-making ability of the cation increases, the echo feature becomes longer and evolves an oscillatory contribution. As in the case of the conceptually similar 2D Raman spectroscopy, such an echo reflects the amount of inhomogeneity of the corresponding degrees of freedom. The echo decay time correlates very well with the Jones–Dole *B* coefficient. This observation connects

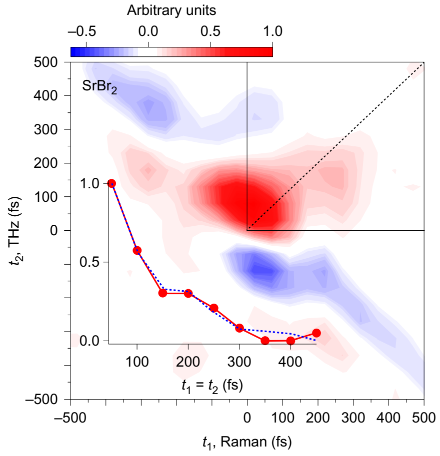

Figure 4 | 2D Raman–THz response of a 2 M $SrBr_2$ solution. 1D cuts along the $t_1 = t_2$ diagonal for $SrBr_2$ (solid red line) and for $SrCl_2$ taken from Fig. 2c (dashed blue line) are shown in the insets. The relaxation along the diagonal does not depend on the counteranion.

a macroscopic property (viscosity) to the microscopic heterogeneity of hydrogen-bond networks. We find the slight speed up of the echo decay for Cs^+ rather remarkable, as to the best of our knowledge such an acceleration has not been observed before by any other spectroscopic technique. Moreover, we provide evidence that the enhanced structural heterogeneities do not originate from water–ion vibrations but are related to water–water modes. This observation implies structural effects on the hydrogen-bond networks, and thus confirms the empirically used concept of structure makers or structure breakers on a molecular level.

Given the extraordinary sensitivity of the method to detect the polarizability of the various molecular constituents[58], we believe that these experiments are the most-decisive experiments of ion solvation to date, even though currently the full information cannot be retrieved. A more-thorough interpretation of the experimental results will require massive support from theory, and we hope that our current interpretation will serve as a working hypothesis for theoretical work to come.

Methods

The experimental set-up for 2D Raman–THz spectroscopy is described in detail elsewhere[42]. Briefly, a train of short (~100 fs) 800 nm pulses with a bandwidth of 300 cm^{-1} (~9 THz) delivered from a 5 kHz amplified Ti:sapphire laser was split into three beams. The first beam, denoted as a Raman pump, was used to excite a vibrational coherence in the sample through two field interactions. Before hitting the sample, the Raman-pump pulses passed through an optical delay stage, which defines time t_1. Their energy was varied from 200 μJ for neat water (Supplementary Fig. 1) down to 40 μJ for $SrBr_2$ to avoid the otherwise strong contributions from a hydrated electron generated by multiphoton processes[43]. The second beam was used to generate short THz pulses by means of optical rectification, and these were focused onto the sample by means of an elliptical mirror, and the third beam was used to detect the transmitted THz pulses by electro-optic sampling. Before hitting the detection crystal, the detection beam was passed through another delay stage, which defines time t_2. For both THz generation and detection, a 100 μm thick (110) GaP crystal was used, which gave a higher bandwidth than the more-common ZnTe crystal and very clean half-cycle pulses with essentially no ringing. The pulse duration of the THz pulse was ~140 fs, peaking at ~1.4 THz and extending to ~7 THz, which is sufficient to excite and probe the water's hydrogen-bond-stretch band at ~200 cm^{-1}. The foci of both THz and Raman pulses were matched at ~250 μm on a ~40 μm thick wire-guided gravity-driven jet to avoid any undesired extra signals from the windows. Each measurement consisted of ~100 individual 2D scans, each scanning t_1 and t_2 on a 50 fs grid. The total averaging time of each measurement amounted to ~60 h. All the measurements were performed at room temperature.

Received 8 April 2016; accepted 9 September 2016;

References

1. Debenedetti, P. G. Supercooled and glassy water. *J. Phys. Condens. Matter* **15,** R1669–R1726 (2003).
2. Stanley, H. E. *et al.* Liquid polyamorphism: possible relation to the anomalous behaviour of water. *Eur. Phys. J. Special Topics* **161,** 1–17 (2008).
3. Sutera, S. P. & Skalak, R. The history of Poiseuille's law. *Annu. Rev. Fluid Mech.* **25,** 1–20 (1993).
4. Jones, G. & Dole, M. The viscosity of aqueous solutions of strong electrolytes with special reference to barium chloride. *J. Am. Chem. Soc.* **51,** 2950–2964 (1929).
5. Jenkins, H. D. B. & Marcus, Y. Viscosity *B*-coefficients of ions in solution. *Chem. Rev.* **95,** 2695–2724 (1995).
6. Gurney, R. W. *Ionic Processes in Solution* (McGraw–Hill, 1953).
7. Frank, H. S. & Wen, W.-Y. Ion–solvent interaction. Structural aspects of ion–solvent interaction in aqueous solutions: a suggested picture of water structure. *Discuss. Faraday Soc.* **24,** 133–140 (1957).
8. Struis, R. P. W. J., Bleijser, J. D. & Leyte, J. C. $^{25}Mg^{2+}$ and $^{35}Cl^-$ quadrupolar relaxation in aqueous $MgCl_2$ solutions at 25 °C. 2. Relaxation at finite $MgCl_2$ concentrations. *J. Phys. Chem.* **93,** 7943–7952 (1989).
9. Buchner, R., Chen, T. & Hefter, G. Complexity in 'simple' electrolyte solutions: ion pairing in $MgSO_4$(aq). *J. Phys. Chem. B* **108,** 2365–2375 (2004).
10. Wachter, W., Kunz, W., Buchner, R. & Hefter, G. Is there an anionic Hofmeister effect on water dynamics? Dielectric spectroscopy of aqueous solutions of NaBr, NaI, $NaNO_3$, $NaClO_4$, and NaSCN. *J. Phys. Chem. A* **109,** 8675–8683 (2005).
11. Turton, D. A., Hunger, J., Hefter, G., Buchner, R. & Wynne, K. Glasslike behavior in aqueous electrolyte solutions. *J. Chem. Phys.* **128,** 161102 (2008).
12. Näslund, L.-Å. *et al.* X-ray absorption spectroscopy study of the hydrogen bond network in the bulk water of aqueous solutions. *J. Phys. Chem. A* **109,** 5995–6002 (2005).
13. Mancinelli, R., Botti, A., Bruni, F., Ricci, M. A. & Soper, A. K. Perturbation of water structure due to monovalent ions in solution. *Phys. Chem. Chem. Phys.* **9,** 2959–2967 (2007).
14. Bruni, F., Imberti, S., Mancinelli, R. & Ricci, M. A. Aqueous solutions of divalent chlorides: ions hydration shell and water structure. *J. Chem. Phys.* **136,** 064520 (2012).
15. Omta, A. W., Kropman, M. F., Woutersen, S. & Bakker, H. J. Negligible effect of ions on the hydrogen-bond structure in liquid water. *Science* **301,** 347–349 (2003).
16. Kropman, M. F. & Bakker, H. J. Effect of ions on the vibrational relaxation of liquid water. *J. Am. Chem. Soc.* **126,** 9135–9141 (2004).
17. Park, S. & Fayer, M. D. Hydrogen bond dynamics in aqueous NaBr solutions. *Proc. Natl Acad. Sci. USA* **104,** 16731–16738 (2007).
18. Moilanen, D. E., Wong, D., Rosenfeld, D. E., Fenn, E. E. & Fayer, M. D. Ion–water hydrogen-bond switching observed with 2D IR vibrational echo chemical exchange spectroscopy. *Proc. Natl Acad. Sci. USA* **106,** 375–380 (2009).
19. Tielrooij, K. J., Garcia-Araez, N., Bonn, M. & Bakker, H. J. Cooperativity in ion hydration. *Science* **328,** 1006–1009 (2010).
20. Stirnemann, G., Wernersson, E., Jungwirth, P. & Laage, D. Mechanisms of acceleration and retardation of water dynamics by ions. *J. Am. Chem. Soc.* **135,** 11824–11831 (2013).
21. Zhang, R. & Zhuang, W. Cation effect in the ionic solution optical Kerr effect measurements: a simulation study. *J. Chem. Phys.* **140,** 054507 (2014).
22. Heisler, I. A. & Meech, S. R. Low-frequency modes of aqueous alkali halide solutions: glimpsing the hydrogen bonding vibration. *Science* **327,** 857–860 (2010).
23. Heisler, I. A., Mazur, K. & Meech, S. R. Low-frequency modes of aqueous alkali halide solutions: an ultrafast optical Kerr effect study. *J. Phys. Chem. B* **115,** 1863–1873 (2011).
24. Bertie, J. E. & Lan, Z. Infrared intensities of liquids XX. The intensity of the OH stretching band of liquid water revisited, and the best current values of the optical constants of H_2O(l) at 25 °C between 15,000 and 1 cm^{-1}. *Appl. Spectrosc.* **50,** 1047–1057 (1996).
25. Mazur, K., Heisler, I. A. & Meech, S. R. Thz spectra and dynamics of aqueous solutions studied by the ultrafast optical Kerr effect. *J. Phys. Chem. B* **115,** 2563–2573 (2011).
26. Torre, R., Bartolini, P. & Righini, R. Structural relaxation in supercooled water by time-resolved spectroscopy. *Nature* **428,** 296–299 (2004).
27. Fukasawa, T. *et al.* Relation between dielectric and low-frequency Raman spectra of hydrogen-bond liquids. *Phys. Rev. Lett.* **95,** 197802 (2005).
28. Loring, R. F. & Mukamel, S. Selectivity in coherent transient Raman measurements of vibrational dephasing in liquids. *J. Chem. Phys.* **83,** 2116–2128 (1985).
29. Hamm, P. & Zanni, M. T. *Concepts and Methods of 2D Infrared Spectroscopy* (Cambridge Univ. Press, 2011).
30. Hwang, H. Y. *et al.* A review of non-linear terahertz spectroscopy with ultrashort tabletop-laser pulses. *J. Mod. Opt.* **62,** 1447–1479 (2015).
31. Kuehn, W. *et al.* Strong correlation of electronic and lattice excitations in GaAs/AlGaAs semiconductor quantum wells revealed by two-dimensional terahertz spectroscopy. *Phys. Rev. Lett.* **107,** 067401 (2011).
32. Fleischer, S., Field, R. W. & Nelson, K. A. Commensurate two-quantum coherences induced by time-delayed THz fields. *Phys. Rev. Lett.* **109,** 123603 (2012).
33. Tanimura, Y. & Mukamel, S. Two-dimensional femtosecond vibrational spectroscopy of liquids. *J. Chem. Phys.* **99,** 9496–9511 (1993).
34. Blank, D. A., Kaufman, L. J. & Fleming, G. R. Fifth-order two-dimensional Raman spectra of CS_2 are dominated by third-order cascades. *J. Chem. Phys.* **111,** 3105–3114 (1999).
35. Golonzka, O., Demirdöven, N., Khalil, M. & Tokmakoff, A. Separation of cascaded and direct fifth-order Raman signals using phase-sensitive intrinsic heterodyne detection. *J. Chem. Phys.* **113,** 9893–9896 (2000).
36. Kaufman, L. J., Heo, J., Ziegler, L. D. & Fleming, G. R. Heterodyne-detected fifth-order nonresonant Raman scattering from room temperature CS_2. *Phys. Rev. Lett.* **88,** 207402 (2002).
37. Kubarych, K. J., Milne, C. J. & Miller, R. J. D. Fifth-order two-dimensional Raman spectroscopy: a new direct probe of the liquid state. *Int. Rev. Phys. Chem.* **22,** 497–532 (2003).
38. Li, Y. L., Huang, L., Miller, R. J. D., Hasegawa, T. & Tanimura, Y. Two-dimensional fifth-order Raman spectroscopy of liquid formamide: experiment and theory. *J. Chem. Phys.* **128,** 234507 (2008).
39. Frostig, H., Bayer, T., Dudovic, N., Eldar, Y. C. & Silberberg, Y. Single-beam spectrally controlled two-dimensional Raman spectroscopy. *Nat. Photon.* **9,** 339–343 (2015).
40. Hamm, P. & Savolainen, J. Two-dimensional-Raman–terahertz spectroscopy of water: theory. *J. Chem. Phys.* **136,** 094516 (2012).

41. Hamm, P., Savolainen, J., Ono, J. & Tanimura, Y. Note: inverted time-ordering in two-dimensional-Raman–terahertz spectroscopy of water. *J. Chem. Phys.* **136,** 236101 (2012).
42. Savolainen, J., Ahmed, S. & Hamm, P. Two-dimensional Raman–terahertz spectroscopy of water. *Proc. Natl Acad. Sci. USA* **110,** 20402–20407 (2013).
43. Savolainen, J., Uhlig, F., Ahmed, S., Hamm, P. & Jungwirth, P. Direct observation of the collapse of the delocalized excess electron in water. *Nat. Chem.* **6,** 697–701 (2014).
44. Funkner, S. *et al.* Watching the low-frequency motions in aqueous salt solutions: the terahertz vibrational signatures of hydrated ions. *J. Am. Chem. Soc.* **134,** 1030–1035 (2012).
45. Finneran, I. A., Welsch, R., Allodi, M. A., Miller III, T. F. & Blake, G. A. Coherent two-dimensional terahertz–terahertz–Raman spectroscopy. *Proc. Natl Acad. Sci. USA* **113,** 6857–6861 (2016).
46. Asbury, J. B. *et al.* Dynamics of water probed with vibrational echo correlation spectroscopy. *J. Chem. Phys.* **121,** 12431–12446 (2004).
47. Yeremenko, S., Pshenichnikov, M. S. & Wiersma, D. A. Hydrogen-bond dynamics in water explored by heterodyne-detected photon echo. *Chem. Phys. Lett.* **369,** 107–113 (2003).
48. Cowan, M. L. *et al.* Ultrafast memory loss and energy redistribution in the hydrogen bond network of liquid H_2O. *Nature* **434,** 199–202 (2005).
49. Eaves, J. D. *et al.* Hydrogen bonds in liquid water are broken only fleetingly. *Proc. Natl Acad. Sci. USA* **102,** 13019–13022 (2005).
50. Schmidt, D. A. *et al.* Rattling in the cage: ions as probes of sub-picosecond water network dynamics. *J. Am. Chem. Soc.* **131,** 18512–18517 (2009).
51. Torii, H. Ultrafast anisotropy decay of coherent excitations and the non-coincidence effect for delocalized vibrational modes in liquids. *Chem. Phys. Lett.* **323,** 382–388 (2000).
52. Ito, H., Hasegawa, T. & Tanimura, Y. Calculating two-dimensional THz–Raman–THz and Raman–THz–THz signals for various molecular liquids: the samplers. *J. Chem. Phys.* **141,** 124503 (2014).
53. Ito, H., Jo, J.-Y. & Tanimura, Y. Notes on simulating two-dimensional Raman and terahertz–Raman signals with a full molecular dynamics simulation approach. *Struct. Dyn.* **2,** 054102 (2015).
54. Ikeda, T., Ito, H. & Tanimura, Y. Analysis of 2D THz–Raman spectroscopy using a non-Markovian Brownian oscillator model with nonlinear system–bath interactions. *J. Chem. Phys.* **142,** 212421 (2015).
55. Ito, H. & Tanimura, Y. Simulating two-dimensional infrared–Raman and Raman spectroscopies for intermolecular and intramolecular modes of liquid water. *J. Chem. Phys.* **144,** 074201 (2016).
56. Fourkas, J. T. Multidimensional Raman spectroscopies. *Adv. Chem. Phys.* **117,** 235–273 (2001).
57. Pan, Z. *et al.* Low frequency 2D Raman–THz spectroscopy of ionic solution: a simulation study. *J. Chem. Phys.* **142,** 212419 (2015).
58. Hamm, P. 2D-Raman–THz spectroscopy: a sensitive test of polarizable water models. *J. Chem. Phys.* **141,** 184201 (2014).
59. Tröster, P., Lorenzen, K., Schwörer, M. & Tavan, P. Polarizable water models from mixed computational and empirical optimization. *J. Phys. Chem. B* **117,** 9486–9500 (2013).

Acknowledgements

We thank P. J. M. Johnson for many insightful discussions. The work has been supported by the Swiss National Science Foundation (SNF) through the NCCR MUST.

Author contributions

A.S., J.S and P.H. conceived and designed the experiments. A.S. and S.A. performed the experiments. A.S analysed the data. A.S. and P.H. co-wrote the paper. All the authors discussed the results and commented on the manuscript.

Additional information

Supplementary information is available in the online version of the paper. Reprints and permissions information is available online at www.nature.com/reprints. Correspondence and requests for materials should be addressed to A.S and P.H.

Competing financial interests

The authors declare no competing financial interests.

nature chemistry
SUPPLEMENTARY INFORMATION
DOI: 10.1038/NCHEM.2642

Terahertz Echoes Reveal the Inhomogeneity of Aqueous Salt Solutions

Andrey Shalit, Saima Ahmed, Janne Savolainen, and Peter Hamm
Department of Chemistry, University of Zurich, Winterthurerstrasse 190,
CH-8057 Zurich, Switzerland, peter.hamm@chem.uzh.ch
(Dated: September 8, 2016)

Supplementary Figure 1 shows the 2D Raman-THz response of neat water, which is qualitatively similar to the previously reported one of Fig. 2b in Ref. [1]. As discussed in detail in Ref. [1] and its Supplementary Materials, many of the features in the observed 2D Raman-THz response originate from the convolution of the molecular response function with the THz and Raman pulses. In particular the THz pulse is time-resolution limiting and furthermore has a rather complicated shape. We defined the instrument response function (IRF) as the response we would expect to get if the molecular response function would be $\delta-$shaped, i.e., in essence the product of the Raman and the THz pulse with some slight additional modifications, which originate from the dispersion the emitted THz field undergoes on its way to the detection crystal.

We have shown in Ref. [1] that in particular the signal along the anti-diagonal of the 2D data is related to the IRF. Comparing that part of the signal in Supplementary Figure 1 with Fig. 2b of Ref. [1], some discrepancies in the IRF can be identified, which we attribute mostly to Gouy-phase shifts due to the uncertainty of the alignment of the sample with respect to the THz focus, which is extremely critical [2]. Nevertheless, the comparison of the 1D cuts along the main diagonal of the upper-right quadrant containing the Raman-THz-THz pulse sequence, shown in Supplementary Figure 2, reveals practically identical signal decays with $\langle\tau\rangle\approx65$ fs in both cases. The similarity of these decays emphasizes the reduced effect of the IRF on the measured molecular response for the Raman-THz-THz pulse sequence. Nevertheless, we took extreme care to obtain a self-contained data set in the present paper. That is, the various salt measurements have been interleaved with neat water measurements in order to exclude drifts in the IRF. As a result, the neat water (Supplementary Figure 1) measurement together with the series of chloride salt measurement depicted in Fig.1b–e show a high degree of reproducibility with respect to the IRF (i.e., mainly the anti-diagonal signal).

Small remaining deviations are attributed to the change in the surface quality of our gravity driven sample jet. We have verified that a decrease in the jet smoothness mediates a scattering of the intense Raman beam into the

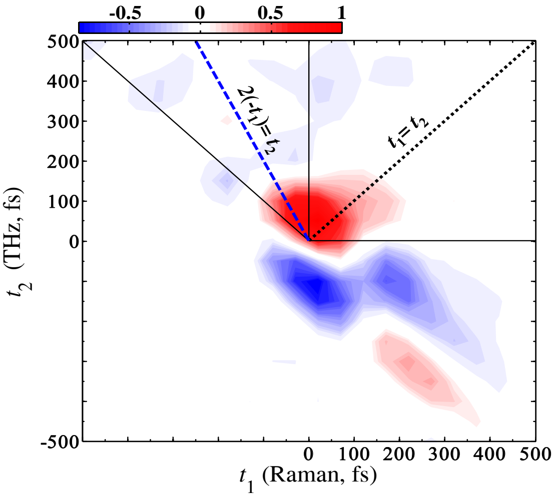

Supplementary Figure 1: 2D Raman-THz response of neat water. The upper-right quadrant corresponds to the Raman-THz-THz pulse sequence, while upper left triangle (above $-t_1=t_2$) corresponds to the THz-Raman-THz pulse sequence. For both pulse sequences the main diagonals where an echo is potentially expected are indicated with black dotted line and blue dashed line, respectively.

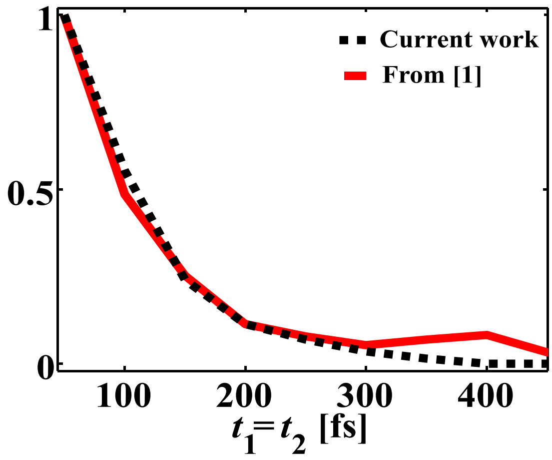

Supplementary Figure 2: Comparison of the 1D cut along the diagonal of the upper-right quadrant for neat water from the current work (black dashed line) with that from the data reported in Ref. [1] (red solid line).

detection crystal, which might give rise to an undesired signal along -t_1=t_2 direction (due to the cross-correlation of the Raman and the gated beams). In addition, we noticed that the stability and quality of the jet is degrading with increasing viscosity of the aqueous salt solution. Thus, the gradual change in the signal shape particulary in the lower right quadrant of the 2D map, along the measurements shown in Fig. 2a–d can be ascribed, at least partially, to the increased scattering contributions to the total signal.

---

[1] Savolainen, J., Ahmed, S. & Hamm, P. Two-dimensional Raman-terahertz spectroscopy of water. *Proc. Natl Acad. Sci. USA* **110**, 20402–20407 (2013).

[2] Ahmed, S., Savolainen, J. & Hamm, P. The effect of the Gouy phase in optical-pump-THz-probe spectroscopy. *Opt. Express* **22**, 4256–4266 (2014).

Bibliography

[1] L. Pauling. *General chemistry.* Dover Publications,INC., New York, 1969.

[2] Anders Nilsson and Lars G.M. Pettersson. The structural origin of anomalous properties of liquid water. *Nat.Comm.*, 6(8998), 2015.

[3] H. Eugene Stanleya Kevin Stokelya, Marco G. Mazzaa and Giancarlo Franzeseb. Effect of hydrogen bond cooperativity on the behavior of water. *Proc. Natl. Acad. Sci. USA*, 107:1301–1306, 2010.

[4] P. G. Debenedetti. Supercooled and glassy water. *J. Phys.- Condens Matter*, 15:R1669, 2003.

[5] J. Morgan and B. E. Warren. X-ray analysis of the structure of water. *J. Phys. Chem*, 6(666), 1938.

[6] K. B. Moller, R. Rey, and J. T. Hynes. Hydrogen bond dynamics in water and ultrafast infrared spectroscopy: A theoretical study. *J. Phys. Chem. A*, 108:1275–1289, 2004.

[7] J. B. Asbury, T. Steinel, K. Kwak, S. A. Corcelli, C. P. Lawrence, J. L. Skinner, and M.D. Fayer. Dynamics of water probed with vibrational echo correlation spectroscopy. *J. Chem. Phys.*, 121:12431–12446, 2004.

[8] S. Yeremenko, M. S. Pshenichnikov, and D. A. Wiersma. Hydrogen-bond dynamics in water explored by heterodyne-detected photon echo. *Chem. Phys. Lett.*, 369:107–113, 2003.

[9] M. L. Cowan, B. D. Bruner, N. Huse, J. R. Dwyer, B. Chugh, E. T. J. Nibbering, T. Elsaesser, and R. J. D. Miller. Ultrafast memory loss and energy redistribution in the hydrogen bond network of liquid H_2O. *Nature*, 434:199–202, 2005.

[10] J. D. Eaves, J. J. Loparo, C. J. Fecko, S. T. Roberts, A. Tokmakoff, and P. L. Geissler. Hydrogen bonds in liquid water are broken only fleetingly. *Proc. Natl. Acad. Sci. USA*, 102:13019–13022, 2005.

[11] F. Perakis and P. Hamm. 2D IR spectroscopy of supercooled water. *J. Chem. Phys. B*, 115:5289–5293, 2011.

[12] S. Garrett-Roe, F. Perakis, F. Rao, and P. Hamm. 3D-IR spectroscopy of isotope-substituted liquid water reveals heterogeneous dynamics. *J. Phys. Chem. B*, 115:6976–6984, 2011.

[13] W. Jarzeba, G. C. Walker, A. E. Johnson, M. A. Kahlow, and P. F. Barbara. Femtosecond microscopic solvation dynamics of aqueous solutions. *J. Phys. Chem*, 92(7039), 1988.

[14] R. Jimenez, G. R. Fleming, P. V. Kumar, and M. Maroncelli. Femtosecond solvation dynamics of water. *Nature*, 369:471–473, 1994.

[15] U. W. Schmitt and G. A. Voth. The computer simulation of proton transport in water. *J. Chem. Phys*, 111:9361–9381, 1999.

[16] P. L. Geissler, C. Dellago, D. Chandler, J. Hutter, and M. Parrinello. Autoionization in liquid water. *Science*, 291:2121, 2001.

[17] H. J. C. Berendsen, J. P. M. Postma, W. F. van Gunsteren, and J. Hermans. *Intermolecular Forces.* Reidel, Dortrecht, Netherland, 1981.

[18] Christian Reichardts. *Solvent and solvent effects in Organic Chemistry.* John Wiley and Sons, Netherland, 2006.

[19] D. Hadži and S. Bratos. Vibrational spectroscopy of the hydrogen bond. In P. Schuster, G. Zundel, and C. Sandorfy, editors, *The Hydrogen Bond*, volume II, chapter 12. Elsevier, Amsterdam, 1976.

[20] M. Maroncelli and G. R. Fleming. Comparison of time-resolved fluorescence stokes shift measurements to a molecular theory of solvation dynamics. *J. Phys. Chem*, 89(875), 1988.

[21] B. Bagchi. Polar solvent dynamics and electron-transfer reactions. *Annu. Rev. Phys. Chem.*, 40(115), 1989.

[22] S. Mukamel. Femtosecond optical spectroscopy: A direct look at elementary chemical events. *Ann. Rev. Phys. Chem.*, 41:647–681, 1990.

[23] G. Van der Zwan and J. T. Hynes. Time-dependent fluorescence solvent shifts, dielectric friction, and nonequilibrium solvation in polar solvents. *J. Phys. Chem*, 89(4181), 1985.

[24] J. L. Skinner and P.G. Wolynes. Relaxation processes and chemical-kinetics. *J. Phys. Chem*, 69(5), 1978.

[25] R. F. Grote and J. T. Hynes. Stable states picture of chemical-reactions .2. rate constants for condensed and gas-phase reaction models. *J. Phys. Chem*, 73(6), 1980.

[26] D.Chandler. Statistical-mechanics of isomerization dynamics in liquids and transition-state approximation. *J. Phys. Chem*, 68(6), 1978.

[27] L. A. Halliday and M. R. Topp. Time-resolved fluorescence spectroscopy of 2-amino-7-nitrofluorene in two-solvent solutions. *J. Chem. Phys.*, 82:2415–2419, 1978.

[28] H. E. Lessing and M. Reichert. Kinetics of fluorescence solvatochromism. *Chem. Phys. Lett.*, 46:111–116, 1977.

[29] M. Maroncelli. Computer-simulations of solvation dynamics in acetonitrile. *J. Chem. Phys*, 94(2084), 1994.

[30] M. Maroncelli E. Castner and G. R. Fleming. Subpicosecond resolution studies of solvation dynamics in polar aprotic and alcohol solvents. *J. Chem. Phys*, 86(1090), 1987.

[31] M. J. Lang, X. J. Jordanides, X. Song, and G. R. Fleming. Aqueous solvation dynamics studied by photon echo spectroscopy. *J. Phys. Chem*, 10(5884), 1999.

[32] W. C. Röntgen. Ueber die Constitution des flüssigen Wassers. *Annal. Phys. Chem.*, 281:91–97, 1892.

[33] O. Mishima and H. E. Stanley. The relationship between liquid, supercooled and glassy water. *Nature*, 396:329–335, 1998.

[34] P. Poole, F. Sciortino, U Essmann, and H. Stanley. Phase behaviour of metastable water. *Nature*, 360:324, 1992.

[35] P. Wernet, D. Nordlund, U. Bergmann, M. Cavalleri, M. Odelius, H. Ogasawara, L. A. Näslund, T. K. Hirsch, L. Ojamäe, P. Glatzel, L. G. M. Pettersson, and A. Nilsson. The structure of the first coordination shell in liquid water. *Science*, 304:995–999, 2004.

[36] T.Tokushima, Y.Harada, O.Takahashi, Y.Senba, H.Ohashi, L.G.M.Pettersson, A.Nilsson, and S.Shin. High resolution x-ray emission spectroscopy of liquid water: The observation of two structural motifs. *Chem. Phys. Lett*, 460:387–400, 2008.

[37] C. Huang, K. T. Wikfeldt, T. Tokushima, D. Norlund, Y. Harada, U. Bergmann, M. Niebuhr, T. M. Weiss, Y. Horikawas, M. Leetmaa, M. P. Ljundberg, O. Takahashi, A. Lenz, L. Ojamäe, A. P. Lubartsev, S. Shin, L. G. M. Pettersson, and A. Nilsson. The inhomogeneous structure of water at ambient conditions. *Proc. Natl. Acad. Sci. USA*, 106:15214–15218, 2009.

[38] Gary N. I. Clark, Greg L. Hura, Jose Teixeira, Alan K. Soper, and Teresa Head-Gordon. Small-angle scattering and the structure of ambient liquid water. *Proc. Natl. Acad. Sci. USA*, 107:14003–14007, 2010.

[39] S. Woutersen, U. Emmerichs, and H. J. Bakker. Femtosecond mid-infrared pump-probe spectroscopy of liquid water: evidence for a two-component structure. *Science*, 278:658–660, 1997.

[40] C. J. Fecko, J. D. Eaves, J. J. Loparo, A. Tokmakoff, and P. L Geissler. Ultrafast hydrogen-bond dynamics in the infrared spectroscopy of water. *Science*, 301:1698–1702, 2003.

[41] G. M. Gale, G. Gallot, F. Hache, N. Lascoux, S. Bratos, and J-Cl. Leicknam. Femtosecond dynamics of hydrogen bonds in liquid water: A real time study. *Phys. Rev. Lett.*, 82:1068–1071, 1999.

[42] S. Mukamel. *Principles of Nonlinear Optical Spectroscopy.* Oxford University Press, Oxford, 1995.

[43] P. F. Barbara and W. Jarzeba. Dynamic solvent effects on polar and nonpolar somerizations. *Acc. Chem. Res.*, 21(195), 1988.

[44] J. McInnis M. Maroncelli and G. R. Fleming. Polar solvent dynamics and electron-transfer reactions. *Science*, 243(1674), 1989.

[45] N. Nandi and B. Bagchi. Dielectric relaxation of biological water. *J. Phys. Chem.*, 101(10954), 1997.

[46] M. M. Teeter. Water-protein interactions: theory and experiment. *Annu. Rev. Biophys. Chem.*, 20(577), 1991.

[47] Nuss MC Smith PR, Auston DH. Subpicosecond photoconducting dipole antennas. *IEEE J. Quantum Elec.*, 24:255–260, 1989.

[48] D Grischkowsky, Soren Keiding, Martin Van Exter, and Ch Fattinger. Far-infrared time-domain spectroscopy with terahertz beams of dielectrics and semiconductors. *J. Opt. Soc. Am. B*, 7:2006–2015, 1990.

[49] B. M. Fischer, M. Walther, and P. U. Jepsen. Far-infrared vibrational modes of dna components studied by terahertz time-domain spectroscopy. *Phys. Med. Biol.*, 47:3807–3814, 2002.

[50] M. Walther, B. M. Fischer, and P. U. Jepsen. Noncovalent intermolecular forces in polycrystalline and amorphous saccharides in the far infrared. *Chem. Phys.*, 288:261–268, 2003.

[51] Matthew C. Beard, Gordon M. Turner, and Charls A. Schmuttenmaer. Terahertz spectroscopy. *J. Phys. Chem. B*, 106:7146–7159, 2002.

[52] K. Wynne, , and John J. Carey. An integrated description of terahertz generation through optical rectification, charge transfer, and current surge. *Opt. Comm.*, 256:400–413, 2005.

[53] K. Y. Kim, B. Yellampalle, J. H. Glownia, A. J. Taylor, and G. Rodriguez. Measurements of terahertz electrical conductivity of intense laser-heated dense aluminum plasmas. *Phys. Rev. Lett.*, 100(135002), 2008.

[54] C. A. Schmuttenmaer. Exploring dynamics in the far-infrared with terahertz spectroscopy. *Chem. Rev.*, 104(4):1759–1779, 2004.

[55] J. E. Bertie and Z. Lan. Infrared intensities of liquids xx: The intensity of the OH stretching band of liquid water revisited and the best current values of the of the optical constants of $h_2o(l)$ at 25° bewteen 25000 cm^{-1} and 1 cm^{-1}. *Appl. Spectroscopy*, 50:1047–1057, 1996.

[56] M. Heyden, J. Sun, S. Funker, G. Mathies, H. Forbert, M. Havenith, and D. Marx. Dissecting the THz spectrum of liquid water from first principles via correlations in time and space. *Proc. Natl. Acad. Sci. USA*, 107:12068–12073, 2010.

[57] Andrey Shalit, Fivos Perakis, and Peter Hamm. Two-dimensional infrared spectroscopy of isotope-diluted low density amorphous ice. *J.Phys.ChemB*, 40:15512–15518, 2013.

[58] Yun-Shik Lee. *Principles of Terahertz Science and Technology.* Springer, 2010.

[59] Saima Ahmed, J. Savolainen, and P. Hamm. Detectivity enhancement in thz electrooptical sampling. *Rev. of Sci. Instr.*, 85(013114), 2014.

[60] R. Menzel. *Photonics.* Springer, Berlin, 2001.

[61] Saima Ahmed, J. Savolainen, and P. Hamm. Detectivity enhancement in thz electrooptical sampling. *Opt.Exp.*, 22, 2014.

[62] D. You and P. H. Bucksbaum. Propagation of half-cycle far infrared pulses. *J. Opt. Soc. Am. B*, 14:1651–1655, 1997.

[63] L. G. Gouy. Sur une propriété nouvelle des ondes lumineuses. *Acad. Sci. Paris*, 110:1251–1253, 1890.

[64] S. Feng, H. G. Winful, and R. W. Hellwarth. Gouy shift and tempral reshaping of focused single-cycle electromagnetic pulses. *Opt. Lett.*, 23:385–387, 1998.

[65] A. B. Ruffin, J. V. Rudd, J. F. Whitaker, S. Feng, and H. G. Winful. Direct observation of the Gouy physe shift with single-cycle terahertz pulses. *Phys. Rev. Lett.*, 83:3410–3413, 1999.

[66] T. Feurer, N. S. Stoyanov, D. W. Ward, and K. A. Nelson. Direct visualization of the Gouy physe by focusing phonon polaritons. *Phys. Rev. Lett.*, 88:257402, 2002.

[67] K.-i. Itoh T. Azumi and I. Hiroshi. Shift of emission band upon the excitation at the long wavelength absorption edge. iii. temperature dependence of the shift and correlation with the time dependent spectral shift. *J. Chem. Phys.*, 65(2550), 1976.

[68] R. F. Loring and S. Mukamel. Selectivity in coherent transient Raman measurements of vibrational dephasing in liquids. *J. Chem. Phys.*, 83:2116–2128, 1985.

[69] D. W. Oxtoby B. Bagchi and G. R. Fleming. Theory of the time development of the stokes shift in polar media. *J. Phys. Chem*, 86(257), 1984.

[70] L. Onsager. Effects of phase density on ionization processes and electron localization in fluids: Discussion. *Can. J. Chem.*, 55(1819), 1977.

[71] Ilya Rips, Joseph Klafter, , and Joshua Jortner. Solvation dynamics in polar liquids. *J. Chem. Phys*, 89(4288), 1988.

[72] T. Fukasawa, T. Sato, J. Watanabe, Y. Hama, W. Kunz, and R. Buchner. Relation between dielectric and low-frequency Raman spectra of hydrogen-bond liquids. *Phys. Rev. Lett.*, 95:197802, 2005.

[73] M. L. Horng, J. A. Gardecki, A. Papazyan, and M. Maroncelli. Subpicosecond measurements of polar solvation dynamics: Coumarin 153 revisited. *J. Phys. Chem.*, 99:17311–17337, 1995.

[74] X. G. Liu, J. M. Cole, P. C. Chow, L. Zhang, Y. Z. Tan, and T. Zhao. Dye aggregation and complex formation effects in 7-(diethylamino)-coumarin-3-carboxylic acid. *J. Mod. Opt.*, 118:13042–13051, 2014.

[75] R. J. Cave and E. W. Castner. Theoretical investigation of the ground and excited states of coumarin 151 and coumarin 120. *J. Phys. Chem. A*, 106(12117), 2002.

[76] R. Kanya and Y. Ohshima. Determination of dipole moment change on the electronic excitation of isolated coumarin 153 by pendular-state spectroscopy. *Chem. Phys. Lett.*, 370(211), 2003.

[77] C. Würth, M. Grabolle, M. Spieles J. Pauli, and U. Resch-genger. Relative and absolute determination of fluorescence quantum yields of transparent samples. *Nat. Protoc.*, 8(1535), 2013.

[78] X. Chen M. J. Tauber, R. A. Mathies and S. E. Bradforth. Flowing liquid sample jet for resonance raman and ultrafast optical spectroscopy. *Rev. Sci. Instr.*, 74(4958), 2003.

[79] J. Bredenbeck, J. Helbing, and P. Hamm. Continuous scanning from picoseconds to microseconds in time resolved linear and nonlinear spectroscopy. *Rev. Sci. Instrum.*, 75(11):4462, 2004.

[80] T. Lian, B. Locke, Y. Kholodenko, and R. M. Hochstrasser. Energy flow from solute to solvent probed by femtosecond IR spectroscopy: Malachite green and heme protein solutions. *J. Phys. Chem.*, 98:11648–11656, 1994.

[81] H. R. Zelsmann. Temperature dependence of the optical constants for liquid h_2o and d_2o in the far IR region. *J. Mol. Struct.*, 350:95–114, 1995.

[82] J. Savolainen, S. Ahmed, and P. Hamm. 2D Raman-THz spectroscopy of water. *Proc. Natl. Acad. Sci. USA*, 110:20402–20407, 2013.

[83] C. P. Lawrence and J. L. Skinner. Vibrational spectroscopy of HOD in liquid D2O. II. infrared line shapes and vibrational stokes shift. *J. Chem. Phys.*, 117:8847, 2002.

[84] T. Torre, P. Bartolini, and R. Righini. Structural relaxation in supercooled water by time-resolved spectrsocopy. *Nature*, 428:296–299, 2004.

[85] I. A. Heisler and S. R. Meech. Low frequency modes of aqueous alkali halide solutions: Glimpsing the hydrogen bond vibration. *Science*, 327:857, 2010.

[86] S. Ebbinghaus, S. J. Kim, M. Heyden, X. Yu, U. Heugen, M. Gruebele, D. M. Leitner, and M. Havenith. An extended dynamical hydration shell around proteins. *Proc. Natl. Acad. Sci USA*, 104:20749, 2007.

[87] P. Hamm and M. T. Zanni. *Concepts and Methods of 2D Infrared Spectrsocopy.* Cambridge University Press, Cambridge, 2011.

[88] Y. Tanimura and S. Mukamel. 2-Dimensional femtosecond vibrational spectroscopy of liquids. *J. Chem. Phys.*, 99:9496–9511, 1993.

[89] Laura J. Kaufman, Jiyoung Heo, Larry D. Ziegler, and Graham R. Fleming. Heterodyne-detected fifth-order nonresonant Raman scattering from room temperature CS_2. *Phys. Rev. Lett.*, 88:207402, 2002.

[90] K. J. Kubarych, C. J. Milne, and R. J. D. Miller. Fifth-order two-dimensional Raman spectroscopy: a new direct probe of the liquid state. *Int. Rev. Phys. Chem.*, 22:497–532, 2003.

[91] O. Golonzka, N. Demirdöven, M. Khalili, and A. Tokmakoff. Separation of cascaded and direct fifth-order Raman signals using phase-sensitive intrinsic heterodyne detection. *J. Chem. Phys.*, 113:9893–9896, 2000.

[92] Y. L. Li, L. Huang, R. J. D. Miller, T. Hasegawa, and Y. Tanimura. Two-dimensional fifth-order Raman spectroscopy of liquid formamide: Experiment and theory. *J. Chem. Phys.*, 128:234507, 2008.

[93] Harold Y. Hwang, Sharly Fleischer, Nathaniel C. Brandt, Bradford G. PerkinsJr., Mengkun Liu, Kebin Fan, Aaron Strnbach, Xin Zhang, Richard D. Averitt, and Keith Nelson. A review of non-linear terahertz spectroscopy with ultrashort tabletopp-laser pulses. *J. Phys. Chem.*, 62:1447–1479, 2015.

[94] W. Kuehn, K. Reimann, M. Woerner, and T. Elsaesser ad R. Heyand U. Schade. Strong correlation of electronic and lattice excitations in gaas/algaas semiconductor quantum wells revealed by two-dimensional terahertz spectroscopy. *Phys. Rev. Lett.*, 107(067401), 2011.

[95] S. Fleischer, R. W. Field, and K. A. Nelson. Commensurate two-quantum coherences induced by time-delayed thz fields. *Phys. Rev. Lett.*, 109(123603), 2012.

[96] P. Hamm and J. Savolainen. 2D-Raman-THz spectroscopy of water: Theory. *J. Chem. Phys.*, 136:094516, 2012.

[97] P. Hamm, J. Savolainen, J. Ono, and Y. Tanimura. Note: Inverted time-ordering in two-dimensional-Raman-terahertz spectroscopy of water. *J. Chem. Phys.*, 136:236101, 2012.

[98] J. T. Fourkas. Multidimensional Raman spectroscopies. *Adv. Chem. Phys.*, 117:235–273, 2001.

[99] Janne Savolainen Andrey Shalit, Saima Ahmed and Peter Hamm. Terahertz echoes reveal the inhomogeneity of aqueous salt solutions. *Nat.Chem.*, 9:273–278, 2017.

[100] Dr. Michael Theuer, Srikantaiah Sree Harsha, Daniel Molter, Dr. Garik Torosyan, and Prof. Dr. Rene Beigang. Terahertz time-domain spectroscopy of gases, liquids and solids. *ChemPhysChem*, 12:2695–2705, 2011.

[101] Janne Savolainen1, Frank Uhlig, Saima Ahmed, Peter Hamm, and Pavel Jungwirth. Direct observation of the collapse of the delocalized excess electron in water. *Nat.Chem.*, 6:697–701, 2014.

[102] H. Němec, F. Kadlec, and P. Kužel. Methodology of an optical pump-terahertz probe experiment: An analytical frequency domain approach. *J. Chem. Phys.*, 117:8454, 2002.

[103] J. Faure, J. van Tilborg, R. A. Kaindl, and W. P. Leemans. Modelling laser based table-top THz sources: Optical rectification, propagation and electro-optic sampling. *Optical and Quantum Electronics*, 36:681–697, 2004.

[104] E. Matsubara, M. Nagai, and Masaaki Ashida. Ultrabroadband coherent electric field from far infrared to 200 Ãűthz using air plasma induced by 10 fs pulses. *Appl. Phys. Lett.*, 101:011105, 2012.

[105] B. Buchli, S. A. Waldauer, R. Walser, M. L. Donten, R. Pfister, N. Blöchliger, A. Caflish, O. Zerbe, and P. Hamm. Kinetic response of a photoperturbed allosteric protein. *Proc. Natl. Acad. Sci. USA*, 110:11725–11730, 2013.

Acknowledgments

UZH has been an exceptional experience for me in terms of my scientific as well as personal development, for which I owe my deepest gratitude to many individuals.

I would like to thank Prof. Peter Hamm, for the support and encouragement throughout the course of my research. His ability to extract the fundamental question from an ambiguous scientific problem and his pursuit for intuitive physical explanation taught me a lot. Once he told me, that there is always a solution to a problem, you just have to find it. I can never forget that statement which has been the motivation for me all along these years.

I was fortunate to start my research career with Dr. Janne Savolainen, who taught me all necessary skills required to survive in an ultrafast laser lab. His excellent experimental proficiency has contributed enormously to the work presented in this thesis. Alternately we maintained the water jet on weekends, during the course of measurements, which was not only fun but also resulted in fruitful results. After his departure, I enjoyed working with Dr. Andrey Shalit. While working on the experimental set up, Andrey always used to ask primary and essential questions which actually steered my thought process in the right direction. He taught me that "every misalignment is a step towards better alignment!".

Having Dr. Jan Helbing around is such a pleasure as he saved me and Margherita from many laser mishaps in lab 2. He set high standard of scientific excellence in the labs of the K-floor and his efforts continue till today.

I spent many memorable days together with Dr. Halina Tran and Dr. Biplab Dutta in 34-K-90. Our coffee breaks comprising of series of discussion on science, history, politics and feminism often led to moments of sheer hilarity which formed the basis of a wonderful friendship through the years. During the last year of my PhD, these places were taken over by Dr. Kerstin Oppelt and Ricardo Fernández-Terán. I have enjoyed being around them, talking with them and learning from them. It has also been fun to work with the remaining past and present members of the Hamm's group: Arian, David S., Andrea, Gustavo, Claudio, Olga, Brankica, Jasmin, David P., Gökçen and Rolf; (past members: Shabir, Joanna, Brigitte, Klemens, Philip, Robert, Margherita and Alex) Thank you all. The shared laughter, tears, food and dreams have been a source of sustenance during these past years and I wish you all the best.

I would like to thank Ms. Maja Gossweiler and Ms. Fabienne Stutz for the administrative support and the cheers they bring to the offices on K floor.

The research presented in this dissertation would not have been possible without Roland Zehn-

der and Martin Haller's technical excellence. They were always available in the workshop with quick help, marvellous ideas and a warm smile.

The time that I have spent doing research at UZH has been supplemented and nourished by the CMSZH graduate school. I thank CMZH for establishing enthusiasm and a lively atmosphere among the PhD students of the chemistry department through aperos, retreats, soft skill courses and financial support.

CMSZH
CHEMICAL MOLECULAR SCIENCES ZURICH
GRADUATE SCHOOL

Farooques companionship has been and continues to be a great support by all means. His patience, care as well as scientific input have enriched my graduate school life beyond measure and I thank him for that. Mawra made my life more colourful and joyful during this time of intense personal growth.

I conclude by thanking the most essential part of my life: my family. They always encouraged and loved me unconditionally and I am sure they will continue to do so. My parents Akter and Akhlaque Ahmed are the most important teachers in my life. I owe my deepest gratitude to them.

Curriculum Vitae

Surname: NAFEES
Name: Saima
Place and date of birth: Nasik, India, 15.05.1984
Citizenship: Indian

Education and training:

2012–2017 Ph.D. Program in Physical Chemistry
Graduate School of Chemical and Molecular Sciences
University of Zurich, Zurich (Switzerland)

2009–2011 Junior Research Fellow(Plasma Physics)
Tata Institute of Funadamental Research
Mumbai, (India)

2006–2008 Masters of Science(Physics)
Material Science
University of Pune, Maharashtra (India)

2003–2006 Bachelor of Science, Physics (Hons)
S.P.H Mahila Collage, Malegaon (India)